Experimental study of angular-dependent magnetic properties of nanostructures: Influence of Magnetic Anisotropy

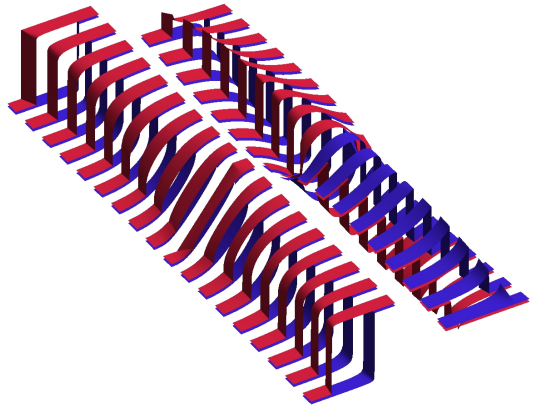

Memoria presentada por
Erika Jiménez Romero
para optar al título de Doctora en Ciencias Físicas
Dpto. de Física de la Materia Condensada
Universidad Autónoma de Madrid

Madrid
11 de octubre de 2011

Director de tesis:
Dr. J. Camarero De Diego

Fecha de la presentación:
11 de octubre de 2011

en memoria de mi Abuelo
con cariño a mi Abuela

Resumen

El vertiginoso avance en el campo del nanomagnetismo, esta motivado, primeramente, por la cantidad de áreas donde se encuentran aplicaciones con un enorme impacto social, la grabación magnética, los sensores y actuadores, la espintrónica o aplicacioes médicas como los sensores nanobiomagnéticos. Como resultado, la innovación y tecnología transferida a la tecnología magnética ha sido continua en las últimas décadas. En la práctica, los actuales y futuros dispositivos basados en nanoestructuras magnéticas son el resultados de una complicada nano-ingeniería, principalmente diseñando sistemas artificiales, intercaras y efectos debido a baja dimensionalidad. El total entendimiento de estos complicados materiales requiere, investigar el estado magnético de las nanoestructuras con diferentes técnicas experimentales donde se combinen diferentes habilidades para extraer los parámetros que definen las propiedades del sistema.

La anisotropía magnética es la propiedad más importante de los materiales magnéticos, tanto des del punto de vista tecnológico como fundamental. Ésta determina la orinetación de los ejes fáciles y difíciles de imanación, así como el comportamiento de la inversión de la imanación, y controlar importantes parámetros, tales como los campos de inversión, la imanación remanente (es decir, la imanación a campo magnético cero) y la estabilidad magnética. Así pues, es decisivo para la tecnología basada en el magnetismo y sus aplicaciones.

En esta tesis se presenta un estudio sistemático de la dependencia angular de las propiedades magnéticas de nanoestructuras modelo así como más complejas con una anisotropía bien definida (diseñada a voluntad). Con esta intención, se han desarrollado en paralelo dos técnicas experimentales, con las que se han identificado los procesos de inversión de la imanació, la estabilidad magnética y los campos de inversión, así como los parámetros claves que los determinan. La nanoestrucutras magnéticas se han clasificado según la simetría de su anisotropía, incluyendo anisotropía uniaxial (simetría de orden dos), biaxial (orden cuatro) y unidireccional (orden uno), así

como su combinación, incluyendo la combinación de anisotropias colineales y no-colineales.

El estudio experimental presentado en esta tesis demuestra la versatibilidad de las propiedades magnéticas a escala nanométrica. Factores como las condiciones de deposición (oblicua vs. incidencia normal), estructura del substrato (policristalina vs. monocristal), superficies artificiales (incluyendo sistemas con anisotropía en el plano, perpendicular y de polarización de canje (bicapas FM/AFM)) o la historia magnética (procedimientos de enfriamiento bajo campo) muestran un drástico efecto sobre la simetría de la anisotropía efectiva en láminas delgadas FM (Co, FeNi y Fe) y como consecuencia, sus propiedades magnéticas incluyendo, los procesos de inversión de la imanación, la estabilidad magnética y los campos de inversión. Este hecho enfatiza la necesidad de controlar estos factores así como la posibilidad de diseñar a voluntad la estructura, morfología y las propiedades magnéticas de las nanoestructuras. Los resultados revelan una nueva perspectiva, a nivel fundamental, de la propiedades magnéticas de las nanoestructuras especialmente en los sistemas que presentan polarización de canje. Este conocimiento, sin duda, abre la posibilidad de nuevas avenidas para el desarrollo de futuros dispositivos magnéticos.

Abstract

Nanomagnetism is a rapidly advancing field, primarily motivated by applications in many strategic areas with an enormous potential impact in society, as magnetic recording, sensors and actuators, spintronics, or medical applications for nanobiomagnetic sensing strategies. As a result, innovation and technology transfer in magnetic technology have been remarkably successful during the last two decades. In practice, the properties of current and future devices based in magnetic nanostructures are the outcome of complex material nanoengineering, mainly tailoring artificial systems, interfaces, and low dimensionality effects. The complete understanding of these complex systems requiresprobing the magnetic state of the nanostructures with different experimental techniques combining different capabilities to extract all parameters that define the system properties.

Magnetic anisotropy is the most important property of magnetic materials from both fundamental and technological point of view. It determines the orientation of the easy and hard magnetization axes as well as the magnetization reversal behavior, and controls relevant magnetic parameters, such as reversal fields, remanent magnetization (i.e., magnetization at zero magnetic field), and magnetic stability. Thus, it is crucial for magnetism-based technology and its applications.

This thesis provides a systematic study on the angular dependence of the magnetic properties of both model and complex magnetic nanostructures with well-defined (tailored) magnetic anisotropy. For this purpose, two specific photon-based experimental tools have been developed. Magnetization reversal processes, magnetic stability and reversal fields have been determined and the key parameters, which determine them, have been identified. The magnetic nanostructures studied have been classified according to their magnetic anisotropy symmetry, including two-fold (uniaxial anisotropy), four-fold (biaxial), and one-fold (unidirectional) symmetries, as well as the combination of them, including collinearly and non-collinearly combined anisotropies.

The experimental studies presented in this thesis illustrate how critical the magnetic properties at the nanoscale are. Factors like deposition conditions (i.e. oblique *vs.* normal incidence), substrate structure (i.e. polycrystal *vs.* single-crystal), artificial interfaces (including in-plane, perpendicular, and exchange-biased anisotropy systems), or like magnetic history (i.e. field-cooling procedures) have been shown to drastically affect the symmetry of the effective magnetic anisotropy of systems as simple as Co, FeNi and Fe ultrathin films and, as a consequence, their magnetic properties, including reversal fields, magnetic stability, and magnetization reversal processes. These facts immediately point out the need to control such factors and also to tailor the structure, morphology and magnetic properties of magnetic nanostructures according to a specific purpose. Our results provide new fundamental insights within nanomagnetism, with special emphasis on the exchange bias phenomenon. This knowledge will certainly open additional avenues to develop future advanced magnetic devices based on anisotropy-tailored magnetic nanostructures.

Contents

Chapter 1

Introduction

Finding the right answers starts with
asking the right questions.

This chapter gives an introduction to the research topic discussed in this thesis. The first section provides a short introduction into the research field of Nanomagnetism. In the second section the physical origin and the consequences of magnetic anisotropy are briefly described. The current knowledge for tuning the magnetic anisotropy in artificial magnetic nanostructures are presented in the third section, highlighting the effects of the magnetic anisotropy that have not been explored in detail. Finally, the outline of the thesis is given.

Magnetic nanostructures have generated an intense (and growing) research activity in the last years since they have many potential applications in many strategic areas, as e.g. magnetic recording, sensors and actuators, spintronics, biomedical applications or quantum effects that may lead to future quantum computation [1, 2].

The novel properties of nanostructures emerge as the sample size becomes comparable to or smaller than characteristic length scales of the system, such as spin diffusion length, carrier mean free path, magnetic domain wall width, exchange length etc. As a consequence, new magnetic phenomena appear, as quantum confinement, altered thermodynamics, exchange coupling between different magnetic phases, induced magnetic moments, magnetic reorientations, etc.

From the mutual stimulation of basic research, technical development, and technological application, a rich variety of novel experimental techniques and stunning

scientific discoveries have evolved, like the exchange-bias effect [3], perpendicular magnetic anisotropy [4], giant magneto-resistance effect [5–7] or spin-current induced magnetic switching [8] on the scientific side. From the application point of view, this process led to the new technology of spintronics [9]. Consequently, the challenge for the future is to understand and control the magnetism on very small length and time scales to be able to prepare custom-designed magnetic nanostructures for a given purpose [10].

Magnetic anisotropy is the most important property of magnetic materials from both fundamental and technological point of views. It determines the preferred orientation of the magnetization and the magnetization reversal behavior, and controls relevant magnetic parameters, such as reversal fields, remanent magnetization (i.e., magnetization at zero magnetic field), and magnetic stability. Thus, it is crucial for magnetic-based technology and its applications. Magnetic anisotropy is a consequence of different asymmetric effects like the crystalline structure and/or the shape of the magnetic material, as discussed below. The physical basis that underlies a preferred magnetic moment orientation in magnetic nanostructures, such as ultrathin films and multilayers, can be quite different from the factors that account for the alignment along a symmetry direction of a bulk material, and the strength can also be differ significantly. The low dimensionality and the layered form of these artificial systems presents symmetry-breaking elements such as planar interfaces and surfaces, which are the basic ingredients for this behavior [11]. In particular, breaking the symmetry of magnetic systems results in additional contributions to the magnetic anisotropy, which could alter the preferred direction of magnetization as well as reversal processes. For these reasons, the fundamental understanding of symmetry-breaking effects on magnetic anisotropy, and consequently on the magnetic properties, of artificial magnetic nanostructures has become a fascinating field in basic Condensed Matter Physics research, in particular in Nanomagnetism.

In the following of this chapter a short introduction into the basic concepts of magnetism and magnetic anisotropy are given. The current learning to control the magnetic anisotropy of artificial magnetic nanostructures is also described. The lack of experimental evidences regarding the magnetic anisotropy effects on the magnetic properties are briefly discussed before to present the scope of this thesis.

1.1. Magnetism: an old but exciting phenomenon

Magnetism is one of the oldest scientific disciplines, but is also one at the forefront of the emerging nanotechnology era. Nowadays, magnetism is a very broad scientific

discipline, ranging from theoretical physics to motor design, with active and emerging links to materials science, chemistry, engineering, biology, or medicine. The development, characterization, and technological exploitation of new artificial materials, particularly as components of smart devices, are key challenges in this millennium.

Magnetism has been part of our civilization since the Greek discovered that a piece of iron would itself become magnetic if touched, or rubbed with a natural stone, ferrite (Fe_3O_4 magnetite), called lodestone (Thales of Miletus (6th century BC)). The first culture finding an application were the Chinese, whom develop the earliest compass, also known as the South Pointer (5th century BC), by using a suspended piece of lodestone. However, over the next 20 centuries, very little progress was made, with the important exception of the use of magnetic compass in navigation (12th century AC). There is no known scientific investigation with respect to magnetism until the 17th century. William Gilbert is recognized as the first person who made a study about magnetism in the book "De Magnete" in 1600 [12] where all the knowledge about magnetism up to that date is collected. Until the second part of the 18th century, the only kind of magnetism known, was the permanent magnetism of iron or lodestone [13–15]). A new kind of physics was introduced by scientist as Coulomb, Oersted, Ampére, Faraday, Maxwell among others, who made important steps towards the "fundamental" understanding of (electro-) magnetism [16–18].

Only with the development of quantum mechanics, in th early of 20th century, it was possible to understand the phenomenon [16, 19]. From quantum mechanics it is known that magnetism is a complex many particle effect, with all electrons of a solid contributing. In brief, the source of magnetism in solid state materials relies in the orbital and spin motions of electrons and how the electrons interact with one another. In detail it is so complicated that its origins on the atomic scale can be calculated only in approximation, e.g., Density Functional Theory (DFT) methods. Due to the requirement of approximations one cannot claim that all accompanying effects are fully understood. Among these effects are phenomena originating from spin orbit coupling such as magnetocrystalline anisotropy and magnetostriction, not mentioning the impact of these atomistic effects on the macroscopic properties of long-range magnetically ordered materials.

In the 20th century the research in solid state magnetism was shifting from bulk materials towards smaller structures. The pioneering theoretical works of Louis Néel in 1954 [20] already predicted that reduced dimensions and the presence of interfaces should alter the magnetic properties of magnetic materials such as magnetic anisotropy and domain structure, for example, which could be useful for applications. However, at that time it was not possible to produce high quality ultrathin magnetic

structures mainly because of lacking technology, especially high vacuum deposition systems. Therefore, successful verification of most of these predictions was far out of reach. It was not until the first part of the 1980's that deposition techniques had improved, under the influence of the strong expansion of the semiconductor research and industry, to an extent that controlled deposition of ultrathin magnetic layers and multilayered nanostructures of high structural quality became possible [21]. During the last decades it has been shown that the "artificial" composition and structure of these systems as well as their low dimensionality give rise to a large number of interesting novel properties. This opened a whole new field of research dedicated to the physics of magnetic nanostructures called Nanomagnetism [22–24].

1.1.1. Different types of magnetic materials

The best way to introduce the different types of magnetism is to describe how materials respond to magnetic fields. All matter is magnetic, it is just that some materials are much more magnetic than others. For systems composed of a single lattice of identical atoms, the main distinction is that in some materials the present interaction do not result in a ground state with long range magnetic order (referred as diamagnetic and paramagnetic materials depending on a negative and positive response to magnetic fields, respectively), whereas in other materials strong exchange interaction between atomic moments is observed, resulting long-range magnetic order (referred as ferromagnets (FM) and antiferromagnets (AFM) depending on a parallel and antiparallel coupling between neighbor magnetic atoms, respectively). This is schematically shown in Fig. 1.1.

While diamagnetic and paramagnetic materials do not remember their magnetic history, i.e. zero remanent magnetization, ferromagnetic materials can present a net magnetization without applying external magnetic fields, i.e. non-vanishing remanent magnetization. Systems composed of different atomic sublattices with antiparallel coupling, referred as ferrimagnetic materials, can also present a net magnetization in remanence if the magnetic moments of each sublattice do not compensate each other. The long-range magnetic order occurs below the ordering temperature, called Curie temperature T_C (Néel temperature T_N) for ferromagnetic or ferrimagnetic (antiferromagnetic) materials. Above this critical temperature the materials become paramagnetic.

The magnetic response M of the sample to an external applied field H, i.e., magnetization curve $M(H)$, of a given system can provide information about its magnetic nature, since the magnetic responses differ greatly in strength and shape, Fig. 1.1. All materials exhibit Diamagnetism, i.e. they have a diamagnetic contribution to their

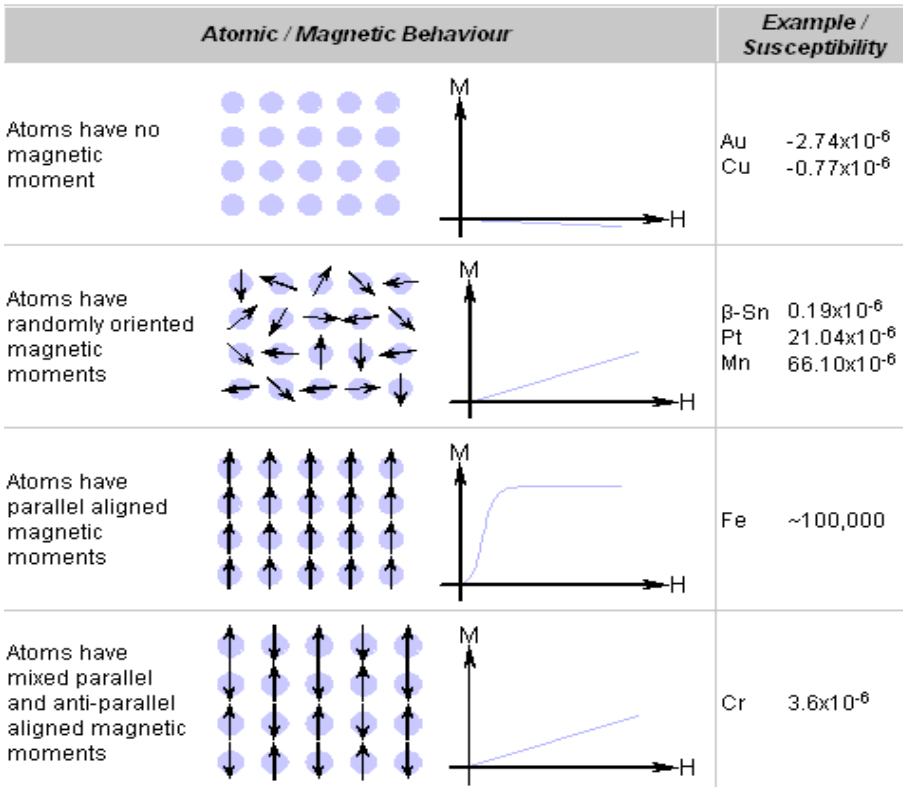

Figure 1.1: Local arrangement and magnetization curves for different types of materials. Both order of magnitude of susceptibility,i.e. M/H, and magnetization field-evolution provide the information about its magnetic nature ([23]).

magnetic response. Paramagnetism, when present, is stronger than diamagnetism and produces magnetization in the direction and proportional to the applied field. Antiferromagnetism presents a response similar to paramagnetic systems, although it posses long-range magnetic order. The total magnetic moment, however is zero as the magnetic moment of different "ionic" sublatices canceled each other. In contrast, ferromagnetic effects are very large, producing magnetizations sometimes orders of magnitude greater than the applied field. Hence, they are much larger than either diamagnetic, paramagnetic or antiferromagnetic effects. In addition, ferromagnetic (and ferrimagentic) materials present irreversible magnetic transitions at relatively low magnetic fields, whereas the systems present reversible ones.

The magnetization curve of a ferromagnetic (ferrimagnetic) material presents magnetic hysteresis. When the material is magnetized in one direction, it will not relax back to zero magnetization when the imposed magnetizing field is removed, i.e. non-vanishing remanent magnetization ($M_R \neq 0$). It must be driven back to zero by a magnetic field, called coercive field or coercivity and denoted $\mu_0 H_C$, in the opposite direction. If an alternating magnetic field is applied to the material, its magnetization will trace out an open loop called a hysteresis loop. This property is related to the existence of magnetic domains in the material and the origin can be understood taking into account magnetic anisotropy.

1.2. Magnetic anisotropy

Without the effect of the magnetic anisotropy, magnetism would have been hard to discover. From the technological point of view the existence of magnetic anisotropy is the most relevant property of magnetic materials. Almost all applications of magnetic materials, in some way or the other, depend on the fact that it is more favorable to magnetize a long-range order magnetic material in a certain direction than in another direction. This difference makes the material magnetically anisotropic. Magnetic anisotropy releases to the no homogeneity of the magnetic properties when measured in different spacial directions. Magnetically isotropic materials have no preferential direction of magnetization in the absence of an applied magnetic field, while magnetically anisotropic materials will align the magnetization along certain axes which correspond to an energy minimum and are called "easy axes" of magnetization (e.a.). The directions of the respective energy maxima are called "hard axes" of magnetization (h.a.). Therefore, the magnetic anisotropy energy is basically a measure for the resistance of the material to be magnetized in a specific direction by an external applied magnetic field.

The magnetic anisotropy manifests itself in magnets of any shape and dimensionality and stabilizes magnetic order in dimensions were the exchange interaction alone would not suffice. For instance, for bulk Fe (T_C = 1043 K) the exchange interaction would be strong enough (e.g., ≈ 0.1 eV/atom) to stabilize magnetic order against thermal fluctuations, but it is rather short-ranged and decays exponentially with the distance.

Magnetic anisotropy is thus related to the symmetry of the crystal lattice as well as the shape of a given specimen. A common and classical but still very important way to study magnetic anisotropy is by recording magnetization curves at different applied field directions [23]. For example, the e.a. directions for bulk bcc-Fe, hcp-Co,

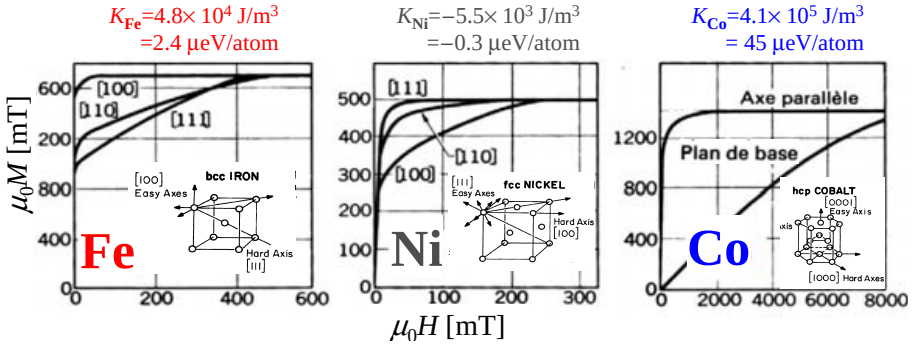

Figure 1.2: (a) Magnetization curves for bulk bcc-Fe, hcp-Co and fcc-Ni materials acquired along different crystal directions (adapted from [23]). The more energetically favorable magnetization curve refers to the e.a. direction.

and fcc-Ni are the [001], [0001], and [111] crystallographic directions, respectively, as show Fig. 1.2 a. The strength of the anisotropy is expressed by anisotropy constants (K) and it can be measured by the external field required to reverse the magnetization from an e.a. direction to a h.a. direction. Materials with small (large) anisotropy constants are called magnetically soft (hard). Depending on the strength of the anisotropy and its symmetry it is possible to observe different magnetization features. In addition, depending on the type of application, material with high, medium or low magnetic anisotropy will be required, for respective application as, for example, permanent magnets, information storage media, or magnetic cores in transformers and magnetic recording heads.

1.2.1. Origin of magnetic anisotropy

At the origin of magnetic anisotropy are crystal lattice, strain, artificial interfaces, and demagnetizing fields [25]. In general, two fundamental interactions are responsible for magnetic anisotropies: *dipolar interactions* between atomics moments are directly connected with the shape of a given ferromagnetic body (shape anisotropy), while *spin-orbit coupling* is the origin of all other anisotropies: magneto-crystalline, magneto-elastic [26, 27], surface/interface anisotropies, which are intimately related to the local symmetry of the atomic configuration. In addition, *interfacial exchange coupling* is at the origin of the exchange anisotropy in systems compose of magnetic layers of different nature, i.e., in soft/hard or FM/AFM systems. The effects of these

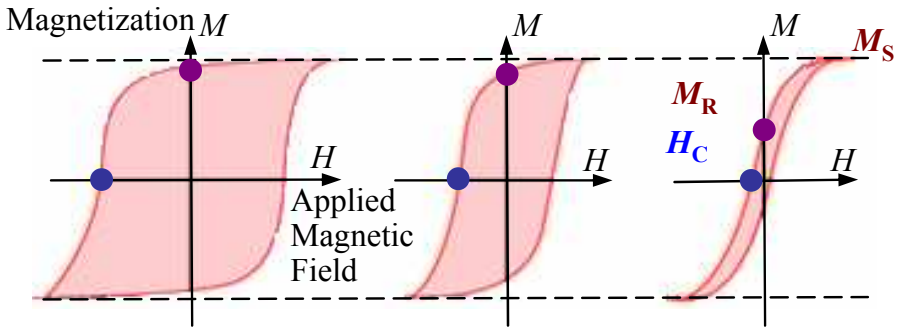

Figure 1.3: Typical magnetization curves of magnetically hard, medium, and soft systems. Both coercivity and remanent magnetization determine the final application.

interactions are briefly described in the following (see Fig. 1.4):

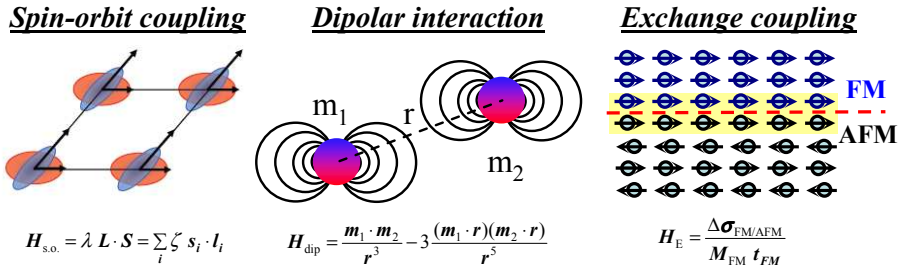

Figure 1.4: Schematic representation of the fundamental interactions responsible of magnetic anisotropy, as discussed in the text.

(a). Dipolar effects

The dipolar interaction is long range and so its contribution is dependent upon the shape of the sample (0.1 meV/atom). Hence, shape anisotropy becomes important when one of the dimensions of the magnetic material is reduced [16]. To minimize this energy contribution the magnetization tries to be aligned within the longest dimension. For example, the e.a. direction of thin magnetic films is typically with in the surface plane (in-plane anisotropy) whereas the magnetization of laterally reduced nanostructures e.g. magnetic nanostripes, is preferable aligned along the stripe direc-

tion.

Since the dipolar interaction has its origin in the shape of the specimen, it can be tailored starting from the early stages of sample growth via angle of deposition [28–31], via stressing the sample [32, 33], or by using self-organization processes [34], and after growth by using standard lithography techniques [35].

(b). Spin-orbit coupling effects

In bulk magnets, and following the work of van Vleck [36], orbital coupling involves in general not merely the orientation of the orbital angular momentum vectors relative to each other, but also their orientation relative to the axis joining the atoms. Since practically all ferromagnetism arises from Coulomb interaction, the symmetric form of the exchange interaction, i.e. $\vec{S}_i \cdot \vec{S}_j$ implies isotropic coupling, as it only depends on the relative angle between spins but not on the absolute angles in space. In contrast, spin-orbit interaction results in a term $H_{SO} \sim \vec{L} \cdot \vec{S}$. As the orbital momentum is influenced by real space properties such as crystal symmetry, the spin, i.e. the magnetization, is coupled to the space symmetry, which is anisotropic in single crystal systems. As a consequence the total energy of the magnetic system depends on the direction of the magnetization.

Spin-orbit coupling effects are also strongly affected by dimensional effects. This is a key parameter for ultrathin magnetic structures because it can determine the easy direction of the magnetization. The broken symmetry at the interface creates a new contribution, first introduced by Néel [20], that may overcome the in-plane (shape) anisotropy in the low coverage range leading to a perpendicular magnetization with respect to the film surface (perpendicular magnetic anisotropy (PMA)) [37].

(c). Exchange coupling effects

It is referred to the emergence of anisotropic interfacial exchange coupling between two different magnetically ordered systems. The magnetic layers may be ferromagnetic, ferrimagnetic, or antiferromagnetic, magnetically soft or hard. Of particular current technological interest is the unidirectional anisotropy, or exchange-bias field produced in a ferromagnetic film that is coupled to an appropriate antiferromagnetic film [38]. AFM/FM bilayer systems exhibit exchange bias phenomena after cooling through the order temperature of the AFM layer under an applied magnetic field [39]. A more detailed introduction is given in Chapter 4.

1.2.2. Consequences of magnetic anisotropy

Magnetic anisotropy not only defines the easy magnetization directions and the magnetic fields required to reverse the magnetization of a sample, as introduced above, but it is responsible also of the existence of magnetic domains as well as how the reversal itself takes place on the micrometer and nanometer scale [40, 41]. [1]. These are briefly introduced in the next.

(a). Magnetic Domains

A magnetic domain describes a region within a magnetic material which has uniform magnetization, as firstly postulated by Pierre-Ernest Weiss [42]. The regions separating magnetic domains are called domain walls, where the magnetization rotates coherently from the direction in one domain to that in the next domain.

The existence of magnetic domains is a result of energy minimization. A simple way to describe the energy reduction is depicted in Fig. 1.5. Note that the demagnetizing fields, coming from surface poles, are much larger in "large" domain (Fig. 1.5 a), that in long thin domains (Fig. 1.5 c), vanishing in the "closure" domain of Fig. 1.5 d. The question arises to what extend this subdivision process continues. With each subdivision there is a decrease in field energy, but there is also an increase in exchange energy, since more and more magnetic moments are aligning antiparallel. Finally a state is reached in which further subdivision would cause a greater increase in exchange energy than decrease in field energy, and the ferromagnet will assume this state of minimum total energy. In single crystals the magnetization direction is aligned along certain anisotropy axis. In polycrystals, i.e. randomly oriented single crystals, it varies from domain to domain in a more or less random manner.

There are many ways to observe magnetic domains [43]. Each method has a different application as domains show, depending on the material, a large variety of shapes and sizes. Domains can be circular, square, irregular, elongated, and striped, all of which have varied sizes and dimensions, but always related with the local effective magnetic anisotropy. Fig. 1.6 shows magnetic images and symmetries. These systems, the total magnetization is zero and could correspond with the magnetic structure at the coercive field (during reversal transition) or after removing the external field and waiting enough time to minimize the total magnetic free energy. Note that the magnetic domain structures are directly related with their corresponding magnetic anisotropy.

[1] Additionally it has an impact on the precession properties of electron spins, such that it not only influences the behavior on very short length scales, but also on very short time scales

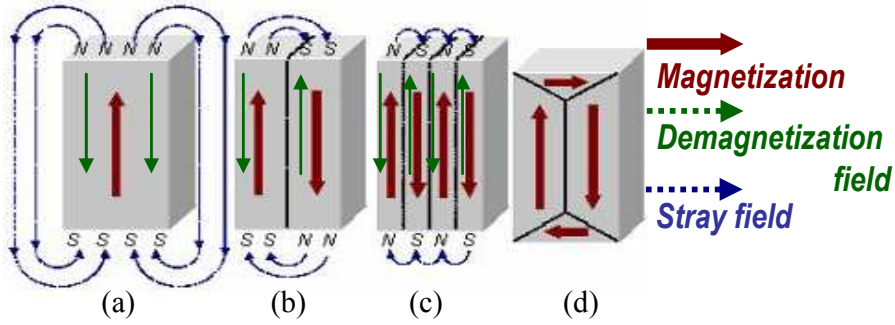

Figure 1.5: (Top) Schematic illustration of the break up of magnetization into domains (a) single domain, (b) two domains, (c) four domains and (d) closure domains. (Bottom) Magnetic domain structures of magnetic systems with well-defined magnetic anisotropy: in-plane uniaxial (c) and biaxial (b) and perpendicular (c). The images have been extracted from [43].

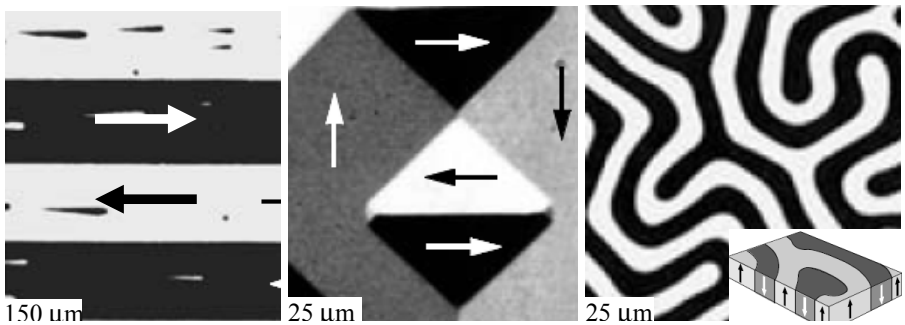

Figure 1.6

(b). Magnetization Reversal processes

Since magnetic anisotropy is at the origin of the magnetic domains and their orientation, as discussed above, it also influences the magnetization reversal processes. In the presence of magnetic anisotropy, which can be expressed as an angular-dependent energy, a field of finite size is needed to reverse the magnetization. In general, magnetization reversal can proceed by magnetization rotation and by nucleation of magnetic domains (usually on inhomogeneities or defects) and further propagation of the magnetic domain walls [44]. The relevant process depends on both dimensionality of the system and on the applied field angle.

The simplest model to explain magnetization switching is the uniform coherent rotation model, first described by Stoner and Wohlfarth [45], which consider uniform magnetization where all the atomic spins forced to be collinear. In the total energy E_{Total} competes the Zeeman energy, i.e. the energy of the magnetic material in the presence of an external applied magnetic field H, and the magnetic anisotropy energy. For the simplest case of a system with uniaxial magnetic anisotropy K_1:

$$E_{\text{Tot}} = -\mu_0 H M_{\text{S}} \cos(\theta_H - \varphi) + K_1 \sin^2 \varphi, \tag{1.1}$$

where M_{S} is the material spontaneous magnetization, θ_H and φ the angles between the applied field and the magnetization and the e.a. direction, respectively. For each angle θ_H, the hysteresis loops can be simulated numerically by minimizing eq. 1.1 with respect to φ. In the model the magnetization follows the local minimum via coherent rotation (see Sec. (a)). For magnetic systems with another magnetic anisotropy it is only necessary to modify the anisotropy energy term according symmetry (see Sec. 3.2 and 4.1). This model is rather rich and is generally used as a first theoretical approach to experimental data. For instance, it introduces the anisotropy field $\mu_0 H_{\text{K}} = 2K/M_{\text{S}}$, which compares the strength of the anisotropy energy and the Zeeman energy. However, in the last decade, it founded a good agreement for nanoparticles, with dimensions much smaller than any micromagnetic characteristic length scale and where the magnetization can be replaced by a single giant spin (macrospin model) [46], where nucleation processes cannot take place.

The uniform coherent rotation (SW) model is rarely relevant in magnetic systems with in-plane dimensions and predicts coercive fields several orders of magnitude higher than the experimental ones, an effect known as Brown's paradox [47]. Magnetic thin films and multilayered structures are considerably larger than the domain wall width and, normally, it is assumed that the reversal of magnetization is in general initiated by nucleation. Local moments start to rotate distorting the magnetic configuration, leading to small volumes of inverse magnetization (activation volume). These volumes are separated from the other magnetic phase by magnetic domain walls. A complete reversal is achieved by propagation of these domain walls The magnetization reversal properties of an extended material are determined by a combination of the properties of nucleation and domain wall propagation, with their associated energy barriers, which depend intrinsically on material constants like defects (i.e., inhomogeneities in magnetic, structural and chemical properties) and magnetic anisotropy symmetries. The latter would suggest that the angular dependence of the magnetic properties can be qualitatively reproduces with this simple model, taking into account that instead of coherent switching reversal must be considered nucleative and prop-

agative reversal processes.

1.3. Engineering magnetic anisotropy

The sources of magnetic anisotropy are crystal lattice (magnetocrystalline anisotropy), strain (magnetoelastic anisotropy), interfaces (surface anisotropy and exchange anisotropy) and demagnetizing fields (shape anisotropy). The latter originates from magnetostatic interactions whereas the others originate from electronic interactions, as discussed previously.

The advances made during the past decades on technological development as well as the improved understanding of growth processes have led to the fabrication of custom-designed multilayered systems. Nowadays, ultrathin films or more complex multilayered structures with tailored magnetic anisotropy can be engineered. First, we have to choose the growth method (e.g. epitaxial or sputtering), the substrates employed (single-crystals, anisotropic surfaces, oxides) and the multilayer structure in order to prepare artificial heterostructures with broken symmetries, reduced dimensionality, custom-engineered morphologies, or exotic crystallographic phases. Second, during the deposition of the different layers, we have to control the growth parameters (i.e. growth temperature, deposition rate, deposition angle, external fields). Finally, one can use different procedures after growth to modify the effective magnetic anisotropy. In this sense, for example, different field cooling procedures are presented in Chapter 4 in order to tailor the magnetic properties of exchange biased FM/AFM systems.

Figure 1.7 shows several examples for tuning the effective magnetic anisotropy of magnetic nanostructures by exploiting the electronic (top) or dipolar (center) interactions responsible for different anisotropy contributions, as described previously. In the case of the $[\text{FM/non magnetic}]_n$, multilayers, the interface anisotropy due to the spin-orbit coupling is strong enough to flip the e.a. direction of the FM layers into the perpendicular direction (perpendicular magnetic anisotropy), overcoming the large shape anisotropy trying to lie the magnetization within the surface plane. For FM/AFM bilayers, the exchange coupling at the interface induces an unidirectional anisotropy in the FM layer for temperatures bellow T_N. In both cases, interfacial phenomena play an important role. The thickness of the FM layers much be in the nanometer range because interfacial effects behaves inversely to the FM thickness. In turn, dipolar interaction effects can be exploited by, e.g., choosing grazing angle deposition or anisotropic surfaces for anisotropic adatom diffusion, or by using standard lithography techniques to reduce furthermore the dimensionality of the magnetic

nanostructure.

In summary, the broken symmetry at surfaces and/or interfaces and the low dimensionality of magnetic multilayered nanostructures can alter their magnetic behavior by inducing additional magnetic anisotropy contributions. It is well know that this can modify important properties such as, for example, e.a. direction, coercivity, and magnetic stability. These effects, as well as related phenomena for spintronic applications, have been widely studied [23, 25–27] but little efforts have been devoted to study how the magnetization reversal behaviors are affected. For instance, there are no systematic experimental angular dependence studies dealing with the symmetry effects of the magnetic anisotropy of magnetic nanostructures. The identification of the key parameters controlling these effects could be used for the further development of novel magnetic devices based on nanostructures with tailored magnetic properties.

1.4. The outline of this thesis

The aim of this thesis is to study the effects of the symmetry of the magnetic anisotropy on the magnetic properties of magnetic nanostructures, in order to prepare custom-designed systems for specific purposes. The angular dependence of the reversal fields, magnetic stability, and magnetization reversal processes have been investigated in magnetic nanostructures with tailored magnetic anisotropy with different symmetry, including onefold, twofold and fourfold symmetries as well as their combinations with different configurations (i.e. collinear and non-collinear cases) and strengths (i.e., different ratios between involved anisotropies).

The artificial magnetic nanostructures investigated have been prepared by standard Molecular Beam Epitaxy (MBE) or sputtering techniques in ultra-high vacuum chambers. The quality of the samples have been tested by standard surface science techniques, such as X-ray Photoemission Microscopy (XPS), Low Energy Electron Diffraction (LEED), atomic Force Microscopy (AFM), and Scanning Tunneling Microscopy (STM). Both preparation and characterization of the specific system are described in the corresponding Chapters.

Two new experimental setups have been developed in this thesis. An artefact-free vectorial- Magneto-Optic Kerr magnetometer (v-MOKE) for the angular-dependent measurements, and a unique soft x-ray based setup, which combines magnetic spectroscopy and holography measurements. The instrumentations, capabilities, experimental procedures, and the basics of these photon-based techniques are described in chapter 2.

In Chapter 3, first the studies performed in model systems exhibiting pure in-plane

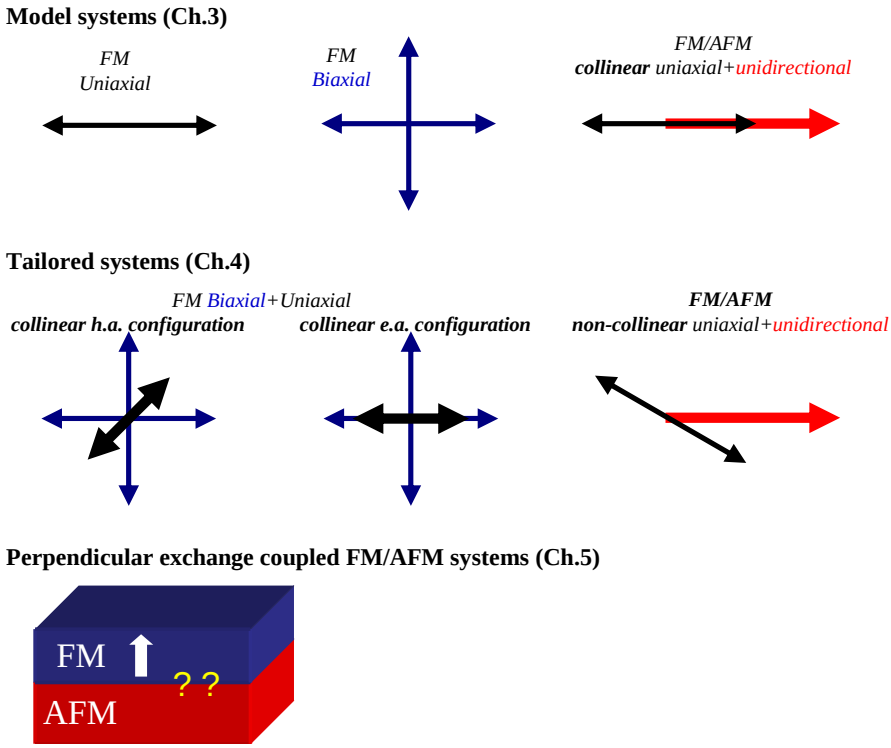

Figure 1.7: Schematic representation of the different magnetic anisotropy symmetries investigated in this thesis. (Interfacial) spin-orbit coupling effects are the responsible of perpendicular anisotropy in $[FM/non\ magnetic]_n$ multilayers (a), whereas the (interfacial) exchange coupling induced unidirectional anisotropy in FM/AFM systems (b). (Bottom) Magnetostatic effects become important in thin films and can be tuned by angle deposition (c), inducing stress(d), o by shaping the sample (e).

uniaxial and biaxial magnetic anisotropy one presented. These studies provide the reader with a simple introduction, showing the characteristic anisotropy directions, i.e. e.a. and h.a. directions how can be determined with a great accuracy, by performing angular-dependent *v*-MOKE measurements. In addition, the angular dependence of the magnetization reversal processes and reversal fields are determined and correlated with the symmetry of the magnetic anisotropy. Secondly, the exchange bias phenomena is investigated in in-plane exchange coupled FM/AFM bilayer systems. These systems combine the intrinsic uniaxial FM anisotropy and the induced interfacial uni-

directional anisotropy in, a priori, collinear configuration. Different FM materials and thickness are investigated in order to provide a general picture on the exchange bias phenomena. Remarkably, the emergence of a non-collinear anisotropy is found for the bilayer with small FM anisotropy. This intrinsic non-collinearity results with a peculiar asymmetric angle-dependent magnetic properties, including magnetization reversal processes as well as both coercive and exchange bias fields.

In Chapter 4, magnetic systems combining the symmetries studied in the precedent chapter are studied. First, single-crystal thin films combining biaxial and uniaxial anisotropy contributions with two different configurations are presented. In particular, a *collinear h.a. configuration*, where the hard axis direction of the uniaxial term coincides with one of the hard axis directions of the biaxial one, and a *collinear e.a. configuration*, where are the easy axis directions of both anisotropy terms thats coincide. In the former (latter) case the symmetry breaking of the biaxial anisotropy results in non-orthogonal e.a. (h.a.) directions and a peculiar asymmetric behavior of the reversal processes. In addition, different anisotropy ratio strengths are explored. Hysteresis loops with one, two, or three sharp irreversible magnetic transitions are demonstrated for just a single magnetic element. Second, non-collinear exchange biased FM/AFM bilayers are tailored extrinsically in systems with a hard FM anisotropy layer, in order to extend the study presented in the previous chapter on the intrinsic non-collinear configuration found in bilayers with a soft FM anisotropy layer.

Finally, the key parameters that control these special features are determined to be the anisotropy ratio and the configuration.

Using x-ray diffraction holography, it has been possible to image the magnetic states, corresponding to the discussions presented in the previous chapters, on the microscopic scale. This allows to correlate the macroscopic behavior, observed by hysteresis curves, with specific domains, domain walls, the wall propagation and, of course, the wall pinning, in chapter 5.

References

[1] J. Stöhr and H. C. Siegmann, *Magnetism, From Fundamentals to Nanoscale Dynamics* (Springer, Berlin, 2006).

[2] J. P. Liu, E. Fullerton, O. Gutfleisch, and D. J. Sellmyer, eds., *Nanoscale Magnetic Materials and Applications* (Springer, Berlin, 2009).

[3] J. Nogués and I. K. Schuller, J. Magn. Magn. Mater. **192**, 203 (1999).

[4] M. T. Johnson, P. J. H. Bloemen, F. J. A. den Broeder, and J. J. de Vries, Rep. Prog. Phys. **59**, 1409 (1996).

[5] M. N. Baibich, J. M. Broto, A. Fert, F. Nguyen Van Dau, F. Petroff, P. Etienne, G. Creuzet, A. Friederich, and J. Chazelas, Phys. Rev. Lett. **61**, 2472–2475 (1988).

[6] G. Binasch, P. Grünberg, F. Saurenbach, and W. Zinn, Phys. Rev. B **39**, 4828–4830 (1989).

[7] D. C. Ralph and M. D. Stiles, J. Magn. Mag. Mat. **320**, 1190 (2008).

[8] J. A. Katine, F. J. Albert, R. A. Buhrman, E. B. Myers, and D. C. Ralph, Phys. Rev. Lett. **84**, 3149–3152 (2000).

[9] A. Fert, Ange. Chem. Inter. Ed. **47**, 5956 (2008).

[10] S. D. Bader, Rep. Mod. Phys. **78**, 1 (2006).

[11] Stöhr, J. Magn. Mag. Mat. **200**, 470 (1999).

[12] W. Gilbert, *De Magnete* (Peter Short, London, 1600).

[13] I. Newton, *Opticks, Treatise of Light* (Dover, London, 1730).

[14] M. R. Cohen and I. E. Drabkin, *A Source Book in Greek Science* (Harvard University Press, Cambridge, 1966).

[15] W. C. Dampier, J. Hered. **21**, 436 (1930).

[16] B. D. Cullity and C. D. Graham, *Introduction to magnetic materials* (John Wiley & Sons, Inc., Hoboken, 2009).

[17] C. H. Durney and C. C. Johnson, *Introduction to modern electromagnetics* (McGraw-Hill, New York, 1969).

[18] R. K. Wangsness, *Electromagnetic Fields* (John Wiley & Sons, Inc., Hoboken, 1986).

[19] D. C. Mattis, *the theory of magnetism made syimple* (World Scientific, Singapore, 2006).

[20] L. Néel, J. Phys. Rad. **15**, 225 (1954).

[21] I. K. Schuller, S. Kim, and C. Leighton, J. Magn. Magn. Mater. **200**, 571 (1999).

[22] D. Jiles, *Introduction to magnetism and magnetic materials* (Chapman & Hall, London, 1991).

[23] C. Kittel, *Introduction to Solid State Physics* (John Wiley & Sons, Inc., New York, 1996).

[24] C. M. Schneider and J. Kirschner, *Electronic Structure* (Elsevier, Amsterdam, 2000), vol. 2, chap. 9, pp. 511–668.

[25] W. J. M. de Jonge, P. J. H. Bloemen, and F. J. A. der Broeder, *Ultrathin magnetic strucutes I* (Springer, Berlin, 1994), chap. 2.3, pp. 65–90.

[26] U. Nowak, J. Heimel, T. Kleinefeld, and D. Weller, Phy. Rev. B. **56** (1997).

[27] J. W. Lee, J. R. Jeong, S. C. Shin, J. Kim, and S. K. Kim, Phys. Rev. B **66**, 172409 (2002).

[28] D. Ecija, E. Jiménez, J. Camarero, J. M. Gallego, J. Vogel, N. Mikuszeit, N. Sacristán, and R. Miranda, Phy. Rev. B **77**, 024426 (2008).

[29] Y. Zhai, L. Shi, W. Zhang, Y. X. Xu, M. Lu, H. R. Zhai, W. X. Tang, X. F. Jin, Y. B. Xu, and J. A. C. Bland, J. Appl. Phys. **93**, 7622 (2003).

[30] U. Welp, V. K. Vlasko-Vlasov, X. Liu, J. K. Furdyna, and T. Wojtowicz, Phys. Rev. Lett. **90**, 167206 (2003).

[31] R. M. Osgood III, B. M. Clemens, and R. L. White, Phys. Rev. B **55**, 8990 (1997).

[32] P. Perna, C. Rodrigo, E. Jiménez, F. J. Teran, N. Mikuszeit, L. Méchin, J. Camarero, and R. Miranda, J. Appl. Phys. **110**, 013919 (2011).

[33] M. Mathews, F. M. Postma, J. C. Lodder, R. Jansen, G. Rijnders, and D. H. A. Blanka, Appl. Phys. Lett. **87**, 242507 (2005).

[34] T. Bobek, N. Mikuszeit, J. Camarero, S. Kyrsta, L. Yang, M. A. Nino, C. Hofer, L. Gridneva, D. Arvanitis, R. Miranda, et al., Adv. Mater. **19**, 4375 (2007).

[35] J. I. Martín, J. Nogués, K. Liu, J. L. Vicent, and I. K. Schuller, J. Mag. Mag. Mat. **256**, 449 (2003).

[36] J. H. van Vleck, Phys. Rev. **52**, 1178–1198 (1937).

[37] M. T. Johnson, P. J. H. Bloemenz, F. J. A. den Broeder, and J. J. de Vries, Rep. Prog. Phys. **59**, 1409 (1996).

[38] W. H. Meiklejohn and C. P. Bean, Phys. Rev. **102**, 1413 (1956).

[39] J. Nogués, J. Sort, V. Langlais, V. Skumryev, S. Suriñach, J. S. Muñoz, and M. D. Baró, Phys. Rep. **422**, 65 (2005).

[40] S. Krause, L. Berbil-Bautista, G. Herzog, M. Bode, and R. Wiesendanger, Science **317**, 1537 (2007).

[41] T. Stapelfeldt, R. Wieser, E. Y. Vedmedenko, and R. Wiesendanger, Phy. Rev. Lett. **107**, 027203 (2011).

[42] P. Weiss, Comptes Rendus **143**, 1136 (1906).

[43] A. Hubert and R. Schäfer, *Magnetic Domains. The analisis of magnetic microstructures* (Springer, Berlin, 1998).

[44] J. Vogel, J. Moritz, and O. Fruchart, C. R. Physique **7**, 977 (2006).

[45] E. C. Stoner and E. P. Wolfarth, Phil. Trans. Roy. Soc. **A240**, 599 (1948).

[46] W. Wernsdorfer, E. Bonet, K. Hasselbach, A. Benoit, B. Barbara, N. Demoncy, A. Loiseau, H. Pascard, and D. Mailly, Phy. Rev. L **78**, 1791 (1997).

[47] A. Aharoni, Phys. Rev. **119**, 127–131 (1960).

Chapter 2

Experimental Techniques

> Philosophy is written in the grand book, the universe, which stands continually open to our gaze. But the book cannot be understood unless one first learns to comprehend the language and read the letters in which it is composed. It is written in the language of mathematics,...
>
> Galileo Galilei,1570

Magnetic properties of the artificial nanostructures are investigated by magneto-optic techniques. An artefact-free vectorial magnetometer based on the Kerr effect has been implemented at LASUAM to study the angular dependence of magnetic properties. In addition, a unique setup combining element-selective soft x-ray magnetic spectroscopy and holography measurements has been developed at beamline ID08 of the ESRF. Soft x-ray absorption spectra collected simultaneously by recording both the total electron yield (TEY) and the transmitted photon intensity, provides quantified information about the magnetic properties as well as the possibility to exploit the dichroism in the transmitted beam intensity for imaging.

The huge technological development that has taken place over the last decades, allows to exploit the fundamental properties of nanoestructures. This thesis focuses on the magnetic properties of those structures. Hence, the most important measuring

techniques are those for magnetic characterization. The two exploit techniques are, vectorial magneto-optic Kerr effect (v-MOKE) and x-ray holography in combination with x-ray magnetic circular dichroism (XMCD).

To get further insight into the systems, additional techniques for structural and magnetic characterization have been used. Among others these techniques are x-ray diffraction (XRD) [1], transmission electron microscopy (TEM) [2, 3], scanning probe microscopy (SPM) [4, 5], Kerr microscopy (M-MOKE) [3] and vibration sample magnetometry (VSM) [6],[7].

Progress in nanomagnetism is particularly rapid at present, primarily motivated by applications in many strategic areas with an enormous potential impact in society, as magnetic recording, sensors and actuators, spintronics, or medical applications for nanobiomagnetic sensing strategies bader. As a result, innovation and technology transfer in magnetic technology have been remarkably successful during the last two decades. In practice, the final properties of current and future devices based in magnetic nanostructures are the outcome of complex materials nanoengineering, mainly tailoring artificial systems, interfaces, and low dimensionality effects. The complete understanding of these complex systems requires, in addition, probing the magnetic state of the nanostructures with different experimental techniques combining different capabilities with many degree of freedom.

The basic understanding starts with controlling the preparation of the system from the beginning. In this sense, huge technological development has taken place over the last decades. Standard techniques as molecular beam epitaxy (MBE), sputtering, inert gas condensation (IGC), plasma vapor deposition (PVD), pulsed laser deposition (PLD), chemical precipitation from solution, electrodeposition, nanoimprint lithography (NIL), self-assemble molayers (SAMs), made it possible to prepare magnetic nanostructures in a control way to study material properties. [8]. The challenge is to grow and prepare very high quality samples, i.e of high crystalline order and chemically clean, one can measure the magnetic properties of very well defined systems. This is not only crucial for basic research but also to understand the properties that are important for technical applications.

The magnetic nanostructures investigated in this thesis were grown by MBE (for single-crystal films) or sputtering (polycrystalline films) in several experimental systems that have not been developed during this thesis. The reader is thus referred to different documents for a detailed description of those experimental systems [ULA, Thesis David , SPINTEC, Thesis Cesar clavero]. Standard Surface Science techniques have been also used to perform the structural (by LEED and XRD), chemical (by XPS and XAS), and morphological (by AFM and STM) characterization of the systems.

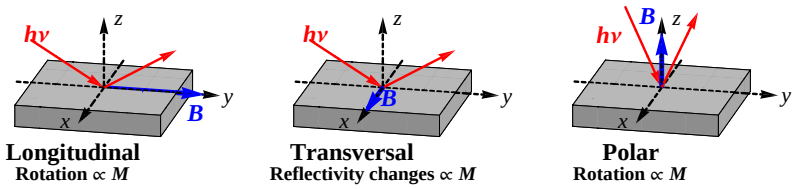

Figure 2.1: The three standard Kerr-setup geometries

The preparation and characterization of the different samples are described in the corresponding sections, highlighting the critical aspects for reaching our purpose. Within the scope of this thesis, the different routes employed to prepare controlled magnetic nanostructures with tailored magnetic anisotropy have been already described in the previous Chapter (see...). This relais on the right choice between different options, such as the growth process, substrates employed, and the parameters chosen during growth (i.e., growth temperature, deposition rate, deposition angle) or/and after growth (i.e., field cooling procedure).

Regarding to the technical development, two new experimental set-ups that have been developed in this thesis. An artefact-free *v*ectorial-resolved Magneto-Optic Kerr magnetometer (*v*-MOKE) for the angular-dependent measurements, and a unique soft x-ray based set-up which combines magnetic spectroscopy and holography measurements. The instrumentations, capabilities, experimental procedures, and the basics of these photon-based techniques are described in the following sections.

2.1. Vectorial-Magneto-optic Kerr Effect

Since 1876, when Sir John Kerr reported for the first time the magneto-optic effect known by his name, Kerr's effect [9], has become a powerful and easy to use surface technique. The phenomenon consist in a change of intensity or polarization of a light beam upon reflection at a magnetic surface. This technique allows studying magnetic properties such as magnetic ordering, magnetic anisotropy, exchange coupling, among others in systems as thin films, bilayer exchange-bias systems, multilayers such a tunnel junctions or spin valves, or last but not least nanoparticles. The first publication of the magneto-optic effect was presented in polar configuration in a setup where the magnetic field is applied normal to the sample, i.e. the setup is probing an out-of-plane magnetization, as shown in the Figure 2.1(polar geometry). Two more setup

configurations are possible, depending on the relative orientation of the applied field vector $\vec{B}$, the plane of incidence P_{I} and the plane of reflection P_{R}, i.e. the sample surface. Consequently, there are three configurations

- Longitudinal: $\vec{B} \in P_{\mathrm{I}} \wedge \vec{B} \in P_{\mathrm{R}}$
- Transversal: $\vec{B} \perp P_{\mathrm{I}} \wedge \vec{B} \in P_{\mathrm{R}}$
- Polar: $\vec{B} \in P_{\mathrm{I}} \wedge \vec{B} \perp P_{\mathrm{R}}$

All the data shown in this work are made in longitudinal configuration. The longitudinal component of the magnetization will always be presented as black line or symbol, and the transversal component as red line or symbols, unless mentioned otherwise.

With a proper measuring setup (chapter 2.1.1) the Kerr-effect allows to measure two independent components of the magnetization vector at the same time. To understand the Kerr-effect one has to mathematically describe the light beam as well as the process of reflection. The properties of the light beam are usually handled either with the Stokes or the Jones formalism [10]. In the following the Jones formalism is used, i.e. the polarization state is expressed as a two dimensional vector with complex entries. In this case the process of reflection is handled by a 2×2 complex matrix, the reflection matrix. An important point is that for many systems the components of the reflection matrix are, in good approximation, linear in the magnetization components. The reflection matrix can be calculated using the boundary matrix method of Zak *et al*. [11], meaning via 4×4 boundary and propagation matrices. In the following this method is used to calculate the reflection matrix of a single magnetic layer on a non-magnetic substrate. Within this framework one multiplies the medium boundary ($\mathbf{A}_i$) and medium propagation matrices ($\mathbf{D}_j$) to obtain the boundary condition matrix $\mathbf{M}$ defined by:[1]

$$\mathbf{M} = \mathbf{A}_{\mathrm{i}}^{-1}\mathbf{A}_{\mathrm{m}}\mathbf{D}_{\mathrm{m}}\mathbf{A}_{\mathrm{m}}^{-1}\mathbf{A}_{\mathrm{f}} \equiv \begin{pmatrix} \mathbf{G} & \mathbf{H} \\ \mathbf{I} & \mathbf{J} \end{pmatrix} \tag{2.1}$$

where the Fresnel reflection and transmission coefficients are defined as

$$\mathbf{G}^{-1} = \begin{pmatrix} t_{\mathrm{ss}} & t_{\mathrm{sp}} \\ t_{\mathrm{ps}} & t_{\mathrm{pp}} \end{pmatrix}; \; \mathbf{I}\mathbf{G}^{-1} = \begin{pmatrix} r_{\mathrm{ss}} & r_{\mathrm{sp}} \\ r_{\mathrm{ps}} & r_{\mathrm{pp}} \end{pmatrix} \tag{2.2}$$

In case of a thin magnetic film of thickness d (the thickness small compared to the wavelength λ) on top of a semi-infinite sample, the reflection coefficient can be ap-

[1] Indices i,m,f refer to the initial, magnetic and final medium, respectively.

proximated as

$$r_{\mathrm{ss}} = \frac{1}{(n_{\mathrm{i}}\cos\theta_{\mathrm{i}} + n_{\mathrm{f}}\cos\theta_{\mathrm{f}})^2}\left[n_{\mathrm{i}}^2\cos^2\theta_{\mathrm{i}} - n_{\mathrm{f}}^2\cos^2\theta_{\mathrm{f}} + \right. \\ \left. + 4\pi\mathrm{i}\frac{d}{\lambda}n_{\mathrm{i}}\cos\theta_{\mathrm{i}}\left(n_{\mathrm{m}}^2\cos^2\theta_{\mathrm{m}} - n_{\mathrm{f}}^2\cos^2\theta_{\mathrm{f}}\right)\right] \tag{2.3}$$

$$r_{\mathrm{sp}} = -\frac{4\pi d}{\lambda}\frac{n_{\mathrm{f}}^2\sin\theta_{\mathrm{f}}M_y + n_{\mathrm{m}}^2\cos\theta_{\mathrm{f}}M_z}{(n_{\mathrm{i}}\cos\theta_{\mathrm{i}} + n_{\mathrm{f}}\cos\theta_{\mathrm{f}})(n_{\mathrm{f}}\cos\theta_{\mathrm{i}} + n_{\mathrm{i}}\cos\theta_{\mathrm{f}})} \times \\ \times n_{\mathrm{i}}\cos\theta_{\mathrm{i}}Q \tag{2.4}$$

$$r_{\mathrm{ps}} = +\frac{4\pi d}{\lambda}\frac{n_{\mathrm{f}}^2\sin\theta_{\mathrm{f}}M_y - n_{\mathrm{m}}^2\cos\theta_{\mathrm{f}}M_z}{(n_{\mathrm{i}}\cos\theta_{\mathrm{i}} + n_{\mathrm{f}}\cos\theta_{\mathrm{f}})(n_{\mathrm{f}}\cos\theta_{\mathrm{i}} + n_{\mathrm{i}}\cos\theta_{\mathrm{f}})} \times \\ \times n_{\mathrm{i}}\cos\theta_{\mathrm{i}}Q \tag{2.5}$$

$$r_{\mathrm{pp}} = \frac{1}{(n_{\mathrm{f}}\cos\theta_{\mathrm{i}} + n_{\mathrm{i}}\cos\theta_{\mathrm{f}})^2}\left\{n_{\mathrm{f}}^2\cos^2\theta_{\mathrm{i}} - n_{\mathrm{i}}^2\cos^2\theta_{\mathrm{f}} - \right. \\ -4\pi\frac{d}{\lambda}\left[\mathrm{i}\left(n_{\mathrm{m}}^2\cos^2\theta_{\mathrm{f}} - n_{\mathrm{f}}^2\cos^2\theta_{\mathrm{m}}\right) + \right. \\ \left.\left. + n_{\mathrm{f}}^2\sin 2\theta_{\mathrm{f}}M_xQ\right]n_{\mathrm{i}}\cos\theta_{\mathrm{i}}\right\} \tag{2.6}$$

where n_{i}, n_{f} and n_{m} are the indicies of refraction of the initial, the final, and the magnetic medium, respectively. The incident angle is θ_{i}, while θ_{m} and θ_{f} are the (complex) angles of propagation in the magnetic layer and the substrate, respectively. The magneto-optic effect also depends on the material constant Q—the Voigt constant—that accounts for the off diagonal elements in the dielectric tensor.

Note that the components of the matrix contain either terms linear in the magnetization or constant terms. Hence, reflecting light with a known initial state of polarization and analyzing the state of polarization after reflection gives, in principle, access to the vector components of the magnetization. In practice, however, there are difficulties to overcome. Nevertheless, the next chapter presents a setup, the vectorial-MOKE setup, that is capable of measuring two of the three components at the same time.

2.1.1. The experimental setup

The vectorial-MOKE setup can be explained in three parts, the optical path, the mechanical sample stage, and the control unit. The optical part consists of (see Fig. 2.2)

- LASER
- polarizer
- lens
- sample
- lens
- $\lambda/2$-retarder
- Wollaston-prism
- photodiodes

The 5 mW HeNe laser ($\lambda = 632$ nm) is intensity stabilized, but has an undefined polarization such that a Glen-Thompson polarizer with extinction coefficient 5×10^{-5} is introduced. In the typical configuration it is set to p-polarization, although it also allows for measurements with incident s-polarization. Lenses are used to focus the light beam onto the sample as well as to focus the divergent beam after reflection. The $\lambda/2$ retarder, set to 22.5° of the optical axes, intermixes the outgoing s- and p-wave (see discussion Sec. 2.1.2). Finally, the s- and p-waves are split into two separate beams using a Wollaston prism with extinction coefficient 10^{-5}. The intensity is measured by two photodiods that work up to 1 MHz. The diodes are incorporated into a proper amplification electronics, which also contains some circuits for data post processing. The electronics is connected to an oscilloscope.

The mechanical part consists of

- *xyz*-sapmple stage for positioning
- eucentric goniometer, and motor
- rotatable electromagnet

The positioning stage in combination with the focused beam and a microscope allows to investigated specific areas of microstructured samples. Spot sizes down to 20 µm are possible. The sample is placed on an eucentric goniometer head to ensure a fixed

plane of reflection upon sample rotation. The whole head can be rotated by a stepping motor in steps of 0.9°. An additional rotation of the magnet allows a simple change from a longitudinal to a transverse field geometry. Furthermore, a polar field geometry can be mounted.

The control unit is formed by

- computer
- frequency generator and current source
- digital oscilloscope

Via the home made measurement software the computer controls the stepping motor of the goniometer as well as the applied magnetic field via frequency generator and connected current source. Additionally, it reads out the hysteresis data, i.e. the signals from the oscilloscope. These signals are

1. I_{Σ}^{DC}: the DC component of the sum of intensities, measured at both photodiods.
2. I_{Δ}: the difference of intensities of the diodes.
3. I_{Σ}^{AC}: the AC component of the added intensities
4. The applied voltage to the field coil, which—after calibration—can be directly transformed into the applied field.

The control program also allows to set minor loops. Therefore, in a single automated measurement procedure it is possible to acquire the hysteresis data—transverse and longitudinal—of a sample for the whole in-plane angular range. Due to the control of the frequency generator for each angle a frequency dependent study or FORC-measurements [12] can be performed.

2.1.2. Theoretical details of the setup

All Kerr measurements are based on the fact that the magnetization alters the dielectric tensor such making an otherwise isotropic material optically anisotropic. Proper considerations of the boundary conditions of Maxwell's equations enable the calculation of the corresponding reflection matrix of a magnetic material [13]. Typically, the symmetry breaking due to the magnetization results only in small modifications of the reflection matrix such that the optical anisotropy can be handled as a first

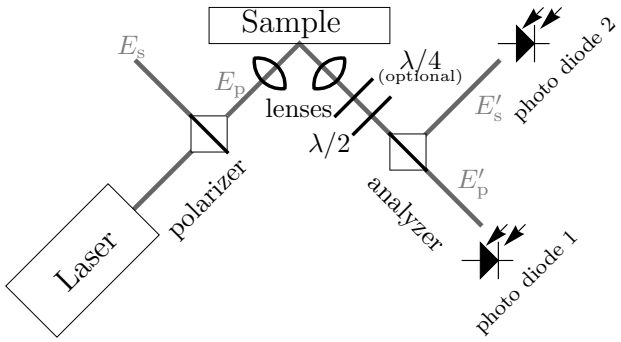

Figure 2.2: Optical part of the setup. Light from an intensity stabilized HeNe laser is polarized, focused by a lens, and reflected at the surface of a sample. The divergent reflected beam is focused by a second lens. It passes a $\lambda/2$-retarder to intermix the s- and p-wave. The two components are then split by a Wollaston prism. The according intensities of the beams are measured using photodiodes.

order perturbation. The components of the reflection matrix for a thin magnetic film are shown above. It is found that in first order the matrix is of the form[2]

$$\mathbf{r} = \begin{pmatrix} r_{ss} & r_{sp} \\ r_{ps} & r_{pp} \end{pmatrix} \approx \begin{pmatrix} a & b_1 M_y + b_2 M_z \\ -b_1 M_y + b_2 M_z & c + d M_x \end{pmatrix} \tag{2.7}$$

The directions x, y, and z as well as the incident angle θ_i are defined in Fig. 2.3. All calculations presented here are performed using the Jones formalism [10]. It is

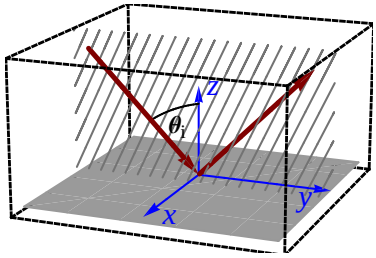

Figure 2.3: Typical Kerr geometry. The polar angle of the incident beam θ_i is around 45°. The plane of incidence (hatched) is the y-z-plane

important to note that r_{ss} is independent of the magnetization. The components r_{sp} and r_{ps} are proportional while r_{pp} contains an additional constant term. Upon reflection on the surface of the magnetic sample the electric field vector $\vec{E}$ of the incident light is

[2]This is still true for multilayers if the total thickness is small compared to the wavelength of the laser.

reflected and results in $\vec{E}'$ as

$$\vec{E}' = \mathbf{r}\vec{E} \tag{2.8}$$

Naturally, the final measuring procedure consists in measuring the intensity $I = \vec{E}' \cdot (\vec{E}')^*$, where the asterisk denotes the complex conjugate. It is easily seen that the intensity of s-polarized light due to incoming p-polarized light (or vise versa) results in a signal that is quadratic in m. Consequently, such a measurement does not give proper information on the magnetic state of the sample. However, the measurement of the reflected p-polarization of incoming p-polarized light gives

$$\begin{aligned} I_\mathrm{p} = E'_\mathrm{p}(E'_\mathrm{p})^* &= cc^* + 2\mathrm{Re}[cd^*]M_x + dd^*M_x^2 \\ &\approx cc^* + 2\mathrm{Re}[cd^*]M_x + \mathscr{O}(M_x^2), \end{aligned} \tag{2.9}$$

assuming the typical case where $\mathrm{Re}[cd^*] \gg dd^*$. Hence, the constant term in r_pp allows for easy measurement of M_x in a transverse Kerr setup.

The presented setup is based on the idea of introducing an additional constant term in the E_s component, therefore generating a linear term in the corresponding intensity. This goal is achieved by first introducing a $\lambda/2$-retarder $\mathbf{L}_2$, rotated by $\pi/8$ off the optical axes. As a consequence the reflected signal has the form

$$\begin{aligned} \begin{pmatrix} E''_\mathrm{s} \\ E''_\mathrm{p} \end{pmatrix} &= \mathbf{L}_2\mathbf{r}\begin{pmatrix} E_\mathrm{s} \\ E_\mathrm{p} \end{pmatrix} \\ &= \frac{\mathrm{i}}{\sqrt{2}}\begin{pmatrix} 1 & 1 \\ 1 & -1 \end{pmatrix}\begin{pmatrix} r_\mathrm{ss} & r_\mathrm{sp} \\ r_\mathrm{ps} & r_\mathrm{pp} \end{pmatrix}\begin{pmatrix} E_\mathrm{s} \\ E_\mathrm{p} \end{pmatrix}. \end{aligned} \tag{2.10}$$

For simplification let us assume $M_z = 0$ and incoming pure p-polarized light. The electric field vector after passing the retarder then has the form

$$\begin{pmatrix} E''_\mathrm{s} \\ E''_\mathrm{p} \end{pmatrix} = E_\mathrm{p}\begin{pmatrix} b_1 m_y + c + d m_x \\ b_1 m_y - c - d m_x \end{pmatrix} \tag{2.11}$$

and the intensities read

$$\begin{aligned} I_{\mathrm{s}} &= \frac{I_0}{2}\left\{|c|^2+|b_1|^2M_y^2+|d|^2M_x^2+2\mathrm{Re}[b_1d^*]M_xM_y+\right. \\ &\quad \left.+2\mathrm{Re}[b_1c^*]M_y+2\mathrm{Re}[dc^*]M_x\right\} \\ I_{\mathrm{p}} &= \frac{I_0}{2}\left\{|c|^2+|b_1|^2M_y^2+|d|^2M_x^2-2\mathrm{Re}[b_1d^*]M_xM_y-\right. \\ &\quad \left.-2\mathrm{Re}[b_1c^*]M_y+2\mathrm{Re}[dc^*]M_x\right\}, \end{aligned} \tag{2.12}$$

where I_0 is the intensity of the incident beam. Adding and subtracting the two intensities gives

$$\begin{aligned} I_\Delta = I_s - I_p &= 2I_0\left\{\mathrm{Re}[b_1c^*]M_y+\mathrm{Re}[b_1d^*]M_xM_y\right\} \\ &\approx 2I_0\mathrm{Re}[b_1c^*]M_y+\mathscr{O}(M_xM_y) \\ I_\Sigma = I_s + I_p &= I_0\left\{|c|^2+|b_1|^2m_y^2+|d|^2M_x^2+\right. \\ &\quad \left.+2\mathrm{Re}[b_1d^*]M_xM_y+2\mathrm{Re}[dc^*]M_x\right\} \\ &\approx I_0\left\{|c|^2+2\mathrm{Re}[dc^*]M_x\right\}+ \\ &\quad +\mathscr{O}(M_x^2,M_y^2,M_xM_y) \end{aligned} \tag{2.13}$$

As a result the difference signal is proportional to M_y, whereas the sum is linear in M_x, but has an additional DC-component, i.e. $I_\Sigma^{\mathrm{DC}}=|c|^2=|r_{\mathrm{pp}}^{\mathrm{DC}}|^2$. Note that due to this DC component one has

$$\begin{aligned} \frac{I_\Delta}{I_\Sigma^{\mathrm{DC}}} &= \frac{2\mathrm{Re}[r_{\mathrm{sp}}\left(r_{\mathrm{pp}}^{\mathrm{DC}}\right)^*]}{|r_{\mathrm{pp}}^{\mathrm{DC}}|^2}=\frac{2\mathrm{Re}[\frac{r_{\mathrm{sp}}}{r_{\mathrm{pp}}^{\mathrm{DC}}}r_{\mathrm{pp}}^{\mathrm{DC}}\left(r_{\mathrm{pp}}^{\mathrm{DC}}\right)^*]}{|r_{\mathrm{pp}}^{\mathrm{DC}}|^2} \\ &= 2\mathrm{Re}[\frac{r_{\mathrm{sp}}}{r_{\mathrm{pp}}^{\mathrm{DC}}}]\approx 2\theta_{\mathrm{K}}^{\mathrm{p}}, \end{aligned} \tag{2.14}$$

which is the Kerr-rotation for p-polarized light. By introducing an additional $\lambda/4$-retarder, which within the Jones formalism has the form

$$\frac{\mathrm{i}}{\sqrt{2}}\begin{pmatrix} 1+\mathrm{i} & 0 \\ 0 & 1-\mathrm{i} \end{pmatrix}, \tag{2.15}$$

one finally gets

$$\left.\frac{I_\Delta}{I_\Sigma^{\mathrm{DC}}}\right|_{\lambda/4} = 2\mathrm{Im}[\frac{r_{\mathrm{sp}}}{r_{\mathrm{pp}}^{\mathrm{DC}}}] \approx 2\varepsilon_{\mathrm{K}}^{\mathrm{p}}, \tag{2.16}$$

the Kerr ellipticity.

Choosing the incoming light as pure s-polarized, Eq. 2.11 changes to

$$\begin{pmatrix} E_{\mathrm{s}}'' \\ E_{\mathrm{p}}'' \end{pmatrix} = E_{\mathrm{s}} \begin{pmatrix} a+b_1 M_y \\ a-b_1 M_y \end{pmatrix}. \tag{2.17}$$

Following the same steps as before one eventually gets

$$\begin{aligned} I_\Delta = I_s - I_p &= 2I_0 \mathrm{Re}[b_1 a^*] M_y + \mathscr{O}(M_y^3) \\ I_\Sigma = I_s + I_p &= I_0 \left\{ |a|^2 + |b_1|^2 M_y^2 \right\} + \mathscr{O}(M_y^3) \end{aligned} \tag{2.18}$$

It follows that s-polarized light leads to a difference signal that is $\propto \theta_{\mathrm{K}}^s$ or including the $\lambda/4$-retarder $\propto \varepsilon_{\mathrm{K}}^s$. However, the sum I_Σ does not contain useful information other than $R_{\mathrm{ss}} = |r_{\mathrm{ss}}|^2$ plus higher order terms

2.1.3. Errors due to misaligned optical components

In the previous paragraph the ideal case has been discussed. In experiment, however, one has to assume small angular errors in the optical components, i.e. polarizer, $\lambda/2$-retarder, and analyzer. Let us assume that these components have angular errors of α_1, α_2, and α_3. In the following errors of the order $\alpha_i \alpha_j$ $(i, j = 1,2,3)$ as well as $\alpha_i M_\xi M_\zeta$ $(\xi, \zeta = x, y, z)$ are neglected. In this approximation the final intensities have the form

$$\begin{aligned} I_\Delta \propto\ & 2\mathrm{Re}[b_1 c^*] M_y + 2\mathrm{Re}[b_2 c^*] M_z + \\ & + 2\mathrm{Re}[b_1 d^*] M_x M_y + 2\mathrm{Re}[b_2 d^*] M_z M_x + \\ & + 2\alpha_1 \left(\mathrm{Re}[a c^*] + \mathrm{Re}[a d^*] M_x\right) + \\ & + 2(2\alpha_2 - \alpha_3) \left(|c|^2 + 2\mathrm{Re}[c d^*] M_x\right) \end{aligned} \tag{2.19}$$

and

$$\begin{aligned} I_\Sigma \quad \propto \quad & |c|^2 + 2\mathrm{Re}[cd^*]M_x + \\ & + |d|^2 M_x^2 + |b_1|^2 M_y^2 + |b_2|^2 M_z^2 + \\ & + 2\mathrm{Re}[b_1 b_2^*] M_y M_z + \\ & + 2\alpha_1 \left(\mathrm{Re}[a^* b_1 - b_1 c^*] M_y + \mathrm{Re}[a^* b_2 + b_2 c^*] M_z\right) - \\ & - 2\alpha_3 \left(\mathrm{Re}[b_1 c^*] M_y + \mathrm{Re}[b_2 c^*] M_z\right). \end{aligned} \tag{2.20}$$

The optional $\lambda/4$-retarder is not considered here. Furthermore, the summation and subtraction, resulting in I_Δ and I_Σ, are assumed to be without error. Note that α_2 does not effect I_Σ as its effect cancels out in the sum, but mixes I_Σ into I_Δ. Furthermore, α_3 intermixes I_Δ and I_Σ; however, due to the adding and subtracting of the signals, I_Δ is affected double.

Furthermore, one must keep in mind that the measured intensities, at both diodes, are dominated by the term $I_{\mathrm{p,s}} \approx |c|^2 I_0/2$. This term defines the photon noise. Assuming a Poisson statistic the resulting photon noise in each channel is proportional $|c|$. Hence, the linear approximation becomes better with increasing c and the relative photon noise decreases with $|c|^{-1}$.

2.1.4. The measuring and analysis procedure

A simple measurement procedure starts with a field calibration, as every sample needs different maximum fields. In a second step the eucentric goniometer is aligned to have a fixed sample plane upon sample rotation. In the beginning two measurements, one in longitudinal and one in transversal geometry, are performed. From these measurements one can extract the scale factor between the longitudinal and transverse channel of the setup. Afterwards the measurement parameters are set within the control program. From this point a full series of measurements is performed completely automatic. The sample is rotated automatically by the stepping motor. For each angle hysteresis loops with the given field parameters are recorded. It is important to mention that for each loop also the loop at 180° is recorded. This is necessary to eliminate quadratic effects. Assuming that there is no M_z-component, on can see from the previous paragraph that the linear terms will change sign upon rotation of 180° while the quadratic terms don't. Subtraction of these measurements contains only odd terms. Hence, quadratic terms are eliminated. If the reflection matrix is truly linear in M, there are, naturally, no third order terms due to the setup. There are, however,

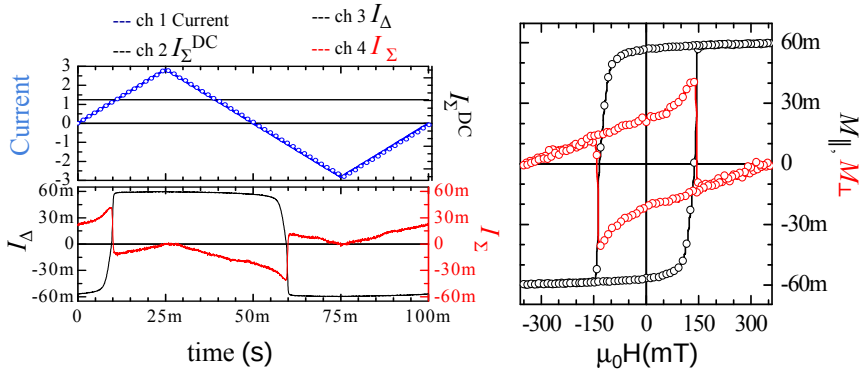

Figure 2.4: Typical image on the oscilloscope during a measurement. One channel shows the applied field (blue) while the second and third channels show the sum (black continuous) and difference (red dashed) signal of the signal processing electronics, i.e.—apart from higher order effects—the longitudinal and transversal hysteresis, respectively.

small second order corrections to the reflection matrix, such that third order terms may be present, even after the subtraction procedure. As the z-component of the magnetization also keeps its sign, any contribution to the signal due to the polar Kerr-effect is also eliminated [14]. The sum of the signals measured at θ_H and $\theta_H + 180°$, on the other hand, contains all quadratic terms as well as the polar Kerr-effect. Hence, this enables the measurement of an additionally z-component, although it is required that the linear signal of the polar Kerr-effect is significantly larger than the quadratic effects due to the setup.

2.1.5. Example Experiment

As an example a system with pure uniaxial magnetic anisotropy is presented. The control program uses the frequency generator to drive the current source and, hence, the coil with a linear ramp. After averaging several hundreds of loops, the averaged data is stored and the sample is automatically rotated by 0.9 degree. A typical data set for one angle is shown in Fig. 2.4. The applied current as a function of time is shown as triangular curve. Using the previously performed field calibration, this curve is transformed into the applied magnetic field. The two other curves present the output signals of the two photodiodes, or to be more precise, the output signals after data processing, i.e. I_Δ and I_Σ. For presentation reasons the curves are shifted in y-direction to be centered around the origin. It is, however, obvious—especially for the longitu-

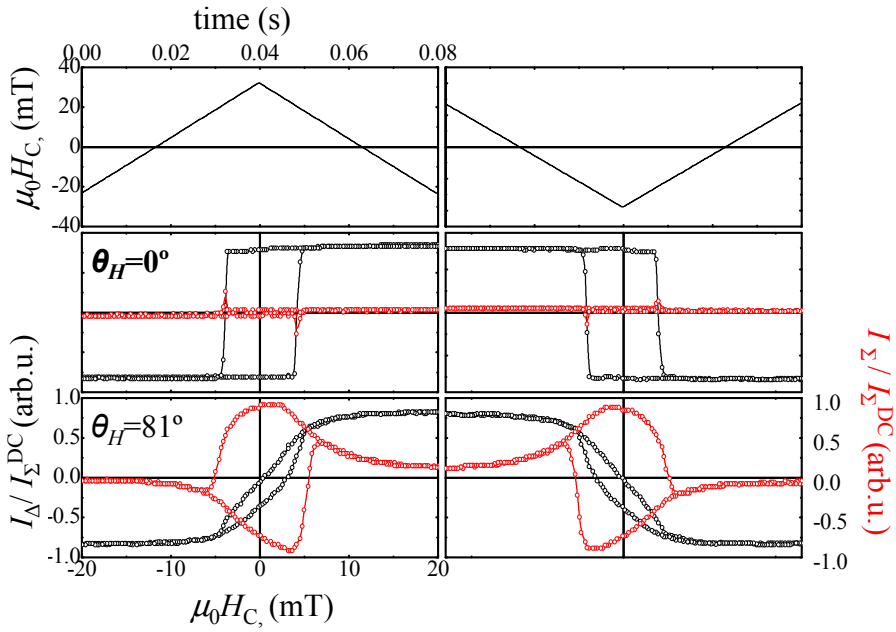

Figure 2.5: Hystersis curves measured near the easy and the hard axis, as well as the curves measured at $\theta_H + 180°$, respectively. Due to quadratic effects no curve shows the expected point symmetry. Curves measured at 180°, however, mutually show mirror symmetry.

dinal component—that the hysteresis curves are not fully point symmetric. The lack of symmetry is due to higher order effects of the setup, mentioned in the previous paragraphs. As the influence of quadratic effects are identical for the curve measured at θ_H and $\theta_H + 180°$ the corresponding hysteresis curves are similarly but oppositely distorted. This distortion disappear when one component is null. This can be seen easily from the sets of hysteresis curves presented in Fig. 2.5. As discussed before, the pure linear term is obtained by subtracting curves measured at opposite angles, while the quadratic terms are given by the sum. In Fig. 2.6 the difference is shown and it is obvious that the longitudinal as well as the transversal component are point symmetric within the precision of the experiment.[3] On the other hand, the sum of the curves, shown in Fig. 2.6 is basically axial symmetric, as is expected from theory. Although the precise values of b_1, c, and d, as introduced in Eq. 2.7 are not known,

[3] In some cases the point symmetric hysteresis curves contain an additional slope from a substrate's para- or diamagnetic signal. This slope must be subtracted from all curves.

the knowledge of the true shape of the transversal and longitudinal hysteresis allows to qualitatively compare the experimental quadratic signal with theory. According to Eq. 2.19 the non-linear term in I_Δ is proportional to $M_x M_y$, assuming $M_z = 0$. Multiplying the two point symmetric signals of Fig. 2.5 gives the continuous curve in Fig. 2.6. This curve is in very good agreement with directly extracted quadratic effect (symbols). Hence, this is a self-consistent proof of the applied procedure.

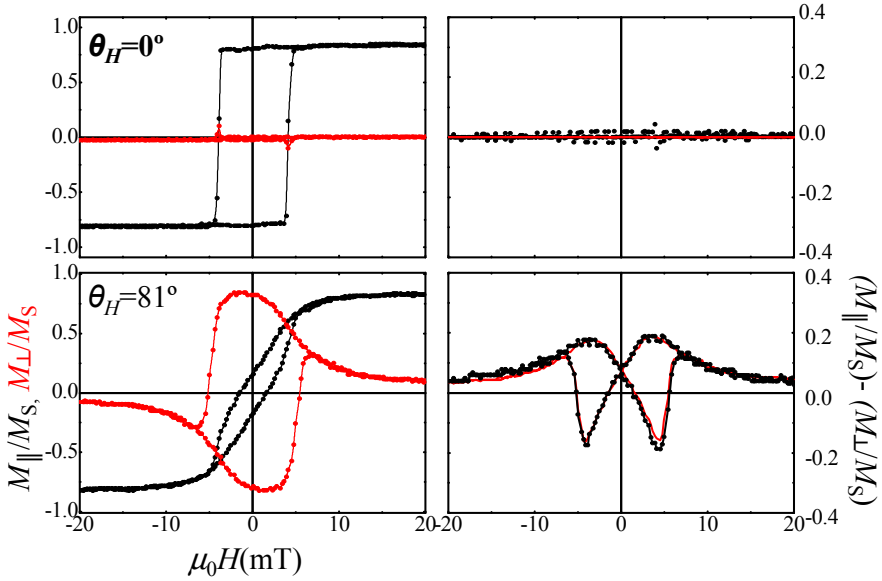

Figure 2.6: Subtracting hysteresis curves measured at θ_H and $\theta_H + 180^\circ$ one obtains the linear signal (left). Longitudinal and transversal curves are point symmetric. The sum, however, presents the setup's quadratic effects and shows axial symmetry. The quadratic terms (points) follow in good agreement the theoretical prediction (continuous line).

Only by applying this method to all data it is ensured that angular evolutions of the remanence, coercivity, switching field, exchange-bias, etc. is extracted properly.

Naturally, the strength of quadratic effects depends on the details of b_1, c, and d, but generally they must be considered.

Polar representation

The measurement of both vectorial components of the magnetization allows, not only verified the exact position of the characteristic axes, but to determine the rotation of the magnetization. In figure 2.7 the corresponding loops to e.a. and close to h.a. are

plot in polar representation. From the e.a. only nucleation and further propagation of domain walls processes take place, while close to h.a. both nucleation and propagation of domain wall and coherent rotation take place. The detection of both components is due to the fact the magnetization is not fully oriented in the direction of the applied field.

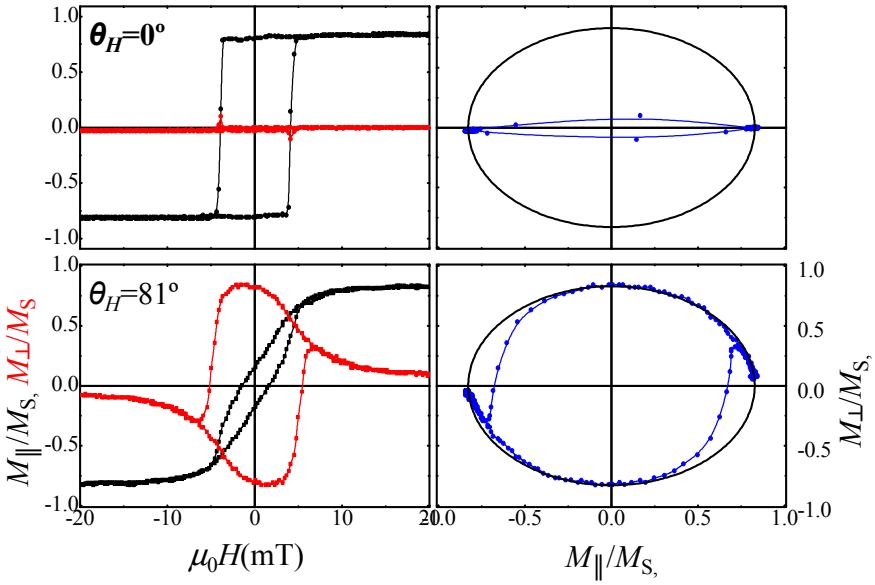

Figure 2.7: Vectorial representation of the hysteresis loops allows to polar plots where the reversal are shown, via coherent rotation and nucleation and propagation of domain walls.

2.2. X-Ray Magnetic Circular Dichroism, Spectroscopy and Imaging

Current applications related to nanomagnetism are generally based in more than one magnetic element and the resulting properties are not simply additive. Therefore is necessary use a technique with specific characteristics, we required:

- element and magnetic selectivity
- spatial resolution

- and have the possibility to applied magnetic fields

To do that already exist different approaches based in x-ray range, as XMCD and X-PEEM, (photon-in, electron-out technique), Transmission Microscopy (photon-in, photon-out technique, using lens), Resonant Magnetic Scattering (photon-in, photon-out technique), X-Ray holography (photon-in, photon-out technique, without lens). In this section is presented the later technique.

Brief history

Since 1947 when the synchrotron radiation was observed for the first time at General Electric, in United States, there has been a spectacular evolution in synchrotron radiation applications [15].

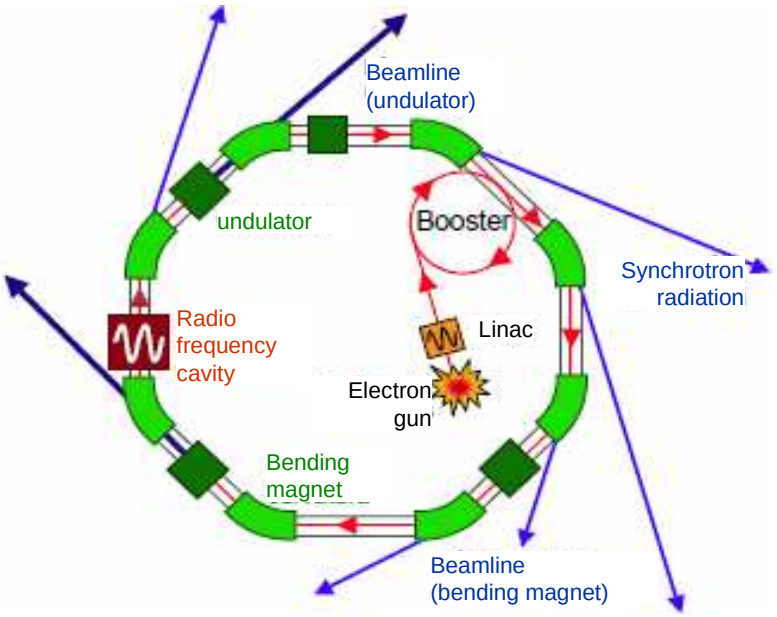

Figure 2.8: Scheme of a synchrotron ring [16]. The electrons are accelerated at the linear accelerator (linac) and introduced into the ring changing their trajectories trough bending magnets. The undulators accelerate the electrons in the straight regions of the ring to produce radiation in the x-ray range. The laboratories are settled at the tangential trajectory of the electrons, where the radiation is use to study a wide range of systems.

The radiation is due to the fact that an accelerated charged particle emits light, as

described by the Maxwell equations. For electrons accelerated in a synchrotron the light is known as synchrotron radiation. The radiation is tangential to the electron path. The electrons circle on a closed path consisting of straight lines connected by parts of small curvature (see Fig. 2.8) Bending magnets force the electrons to follow the curvature. Originally the radiation emitted in these curved parts was used as a light source to investigated physical properties. Nowadays, the straight parts have undulator magnets to produce even more photons. These photons propagate on the straight line to the experiment where samples are investigated even down to atomic scale. Synchrotron radiation provides [17]

- wide-range tunability of energies
- high brightness
- variable polarization
- well-defined time structure
- hight degree of coherence

Polarized synchrotron radiation gives the possibility to image magnetic materials with nanometer resolution [17]. Recently, soft x-ray holography was introduced as a powerful tool for the lensless imaging of magnetic systems [18]. The technique is based on Fourier Transform holography using a reference beam. The magnetic contrast is obtained by exploiting XMCD at the L_3 absorption edges of magnetic transition metals [18, 19]. As a pure photon-based technique, soft x-ray holography allows imaging samples with applied external magnetic fields [20].

2.2.1. Principles of x-ray holograph

In x-ray holography a hologram generated as the result of a coherent interference between a beam scattered by a semitransparent sample and a reference beam. Hence, coherent radiation is required.

(a). coherent x-ray radiation

Generally, light sources do not provide coherent electromagnetic waves. That means interference experiments with light can only be performed using one light source and producing coherent waves from it. The process of coherent filtering light is well known, but goes along with a significant decrease of photon flux. This is still

an issue in modern high brilliant synchrotron radiation sources [21], but will probably change with free electron lasers.

For the x-ray holography described in this chapter there are two types of coherences of concern, longitudinal and transverse coherence. These two will be explained in the following. The longitudinal coherence length is determined by the spectral resolution $E/\Delta E \propto \lambda/\Delta\lambda$. It is proportional to the distance along the propagation direction over which two beams of different wavelengths ($\Delta\lambda$) acquired a phase shift of π. For typical energy resolutions of synchrotron beamlines of about $E/\Delta E \approx 10^3 ... 10^5$ the longitudinal coherence length ξ_l for x-rays

$$\xi_l = \frac{\lambda^2}{2\Delta\lambda} \tag{2.21}$$

is in the range of $10^0 ... 10^2$ µm. In an interference experiment it is required that the maximum optical path difference is less than the longitudinal coherence length.

Transverse coherence varies along the path of the waves and is measured perpendicular to this direction. Perfect transverse coherence would be achieved by a point source emitting perfectly correlated spherical wavefronts. However, a true point source is impossible due to the uncertainty, $\Delta k \Delta x \geq 1/2$, where Δk is the uncertainty in wavenumber and Δx is the uncertainty in position, [21]. One has $k = 2\pi/\lambda$ and, if Δk is small, $\Delta k = k\Delta\Theta$. Here $\Delta\Theta$ is the uncertainty of the divergence angle Θ, [21]. If furthermore the diameter of the source is $d = 2\Delta x$ the transverse coherence length ξ_t reads

$$\xi_t = \frac{\lambda D}{2\pi d}. \tag{2.22}$$

The coherence area provided at ID08 is (17×307) µm^2 [22].

(b). small angle x-ray scattering

Soft x-rays that are scattered by a sample structure under a scattering angle $\Theta \lesssim 5^\circ$ have experienced so-called small angle scattering. In small angle scattering the intensity profile contains information on the size, shape, and distribution of the scattering objects. It therefore allows to obtain structural information about inhomogeneities in materials with a characteristic length on the order of tenth to hundredth of Angstroms.

For coherent illumination of the sample the region of interest d must be smaller than the coherent area spanned by the transverse coherent lengths. Fig. 2.10 illustrates the difference between incoherent and coherent small angle scattering (SAS) from a sample with characteristic structures of a certain correlation length. In the upper panel the transverse coherence length of the set up is appropriate for the scale of the sample

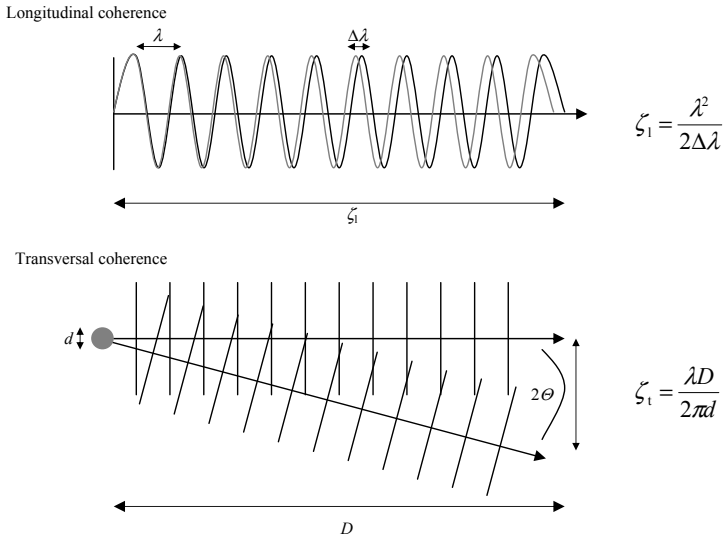

Figure 2.9: Sketch to the origin of a finite longitudinal and transversal coherence length.

structure but is smaller than the region of interest, i.e. the illuminated area. Hence, common incoherent SAS is observed. Statistical properties of the scattered intensity such as the average period of the black and white structures can be extracted. The panel below presents the same experiment where the coherent length is increased up to the size of the region of interest. Constructive and destructive interference occurs from the structure of the completely illuminated sample and causes maxima and minima in the intensity at the detector, known as speckle pattern. The scattered intensity provides information about the individual sample configuration. Objects with same statistical properties but different structure will naturally cause different speckle patterns.

Due to the possibility of tunning the photon energy at the synchrotron, it is possible to perform the SAS at the absorption edge of the studied element, i.e. performing resonant-magnetic scattering, therefore strongly amplifying the magnetic contribution to the total scattering.

2.2.2. X-ray magnetic circular dichroism

The use of the polarization properties of synchrotron radiation for studies on the magnetic properties of materials has its historical roots in the calculation by Ersk-

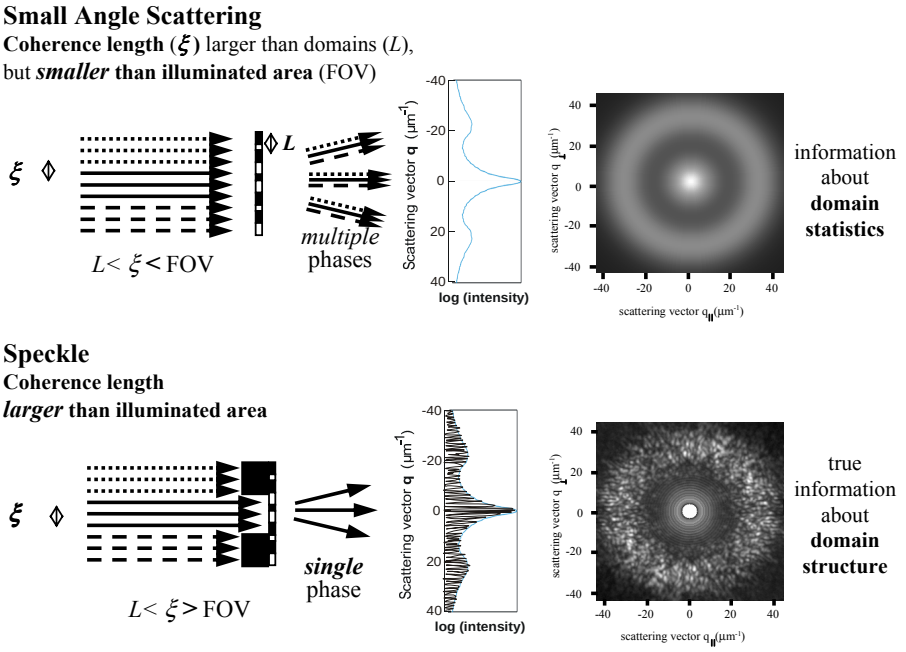

Figure 2.10: The coherence length of the waves determinate the information obtain from the scattered object. Only true magnetic information is obtain if the coherence length is larger than the illuminated area. The speckle pattern contains information of the domain structure and its configuration. (Images taken from the talk: *X-ray imaging of magnetic nanoestructures and their dynamics* by J. Stöhr

ine and Stern of the x-ray circular magnetic dichroism (XMCD) at the $M_{4,5}$ edges of Ni, published 30 years ago [23], which was followed, 10 years later, by a calculation by Thole and coworkers, on the magnetic linear dichroism (XMLD) at the $M_{4,5}$ edges of rare earth magnets [24]. In the meanwhile, x-ray magnetic scattering, both resonant and non-resonant had been discovered (by de Bergevin and Brunel with a home-laboratory source3) as a useful technique. Its theoretical description has been worked out in Refs. [25, 26]. It was in the late eighties, when second generation synchrotrons allowed to observe the predicted magnetic dichroic effects: as soon as one year after the prediction, G. van der Laan and coworkers observed the XMLD at the $M_{4,5}$ of Tb in a terbium-iron garnet [27]. XMCD was shown by G. Schütz soon after at the K absorption edge of iron [28]. Early in the nineties, the fundamental steps were

taken to develop XMCD as a unique measuring technique in magnetism:

- XMCD at the $L_{2,3}$ edges of Fe, Ni and Co were measured by C. T. Chen and coworkers in 1990 [29], finding a signal as high as 20% of the measured XAS, easy to observe and quantify, showing that its use as a new magnetometry is possible.
- The so-called sum rules were derived by T. Thole, P. Carra and coworkers [30, 31], allowing (in principle) to separate orbital and spin moments in the initial states from XMCD signals measured in a pair of well resolved $j = l \pm s$ absorption edges. Its experimental confirmation only needed to wait till 1995, and it was performed by C. T. Chen et al. [32].
- J. Stöhr and coworkers [33] did show that XMCD contrast allows to perform element-specific microscopy with high resolution and unique properties. After that seminal work, several magnetic microscopic techniques have been developed using synchrotron radiation, allowing to study ferro- as well as antiferromagnets, interfaces, buried layers, etc.

In 1994 ESRF opened their first beamlines to users, including two beamlines dedicated to XMCD from the very beginning and another one dedicated to magnetic diffraction shortly after. The American (APS) and Japanese (Spring 8) third generation high-energy synchrotrons opened later in the decade. Although the main magnetic dichroic effects were already demonstrated, thanks to those three, and other third-generation synchrotron radiation sources, not only large signals as those observed at the $L_{2,3}$ edges of Fe, Ni and Co can be studied today, but also XMCD from tiny induced magnetic moments (in O, Cu, S, etc.) and also other very small dichroic signals, as the K-edge XMCD from transition metals, etc.

Nowadays XMCD has become a well established experimental tools in advanced magnetism. This is partially due to the fact that at modern synchrotrons XMCD is a rather simple technique: In case of L-edge XMCD one selects from the wide range of energies provided by modern undulators the energy that drives an electron transition from a p-corelevel into the d-bands. In a ferromagnetic material the d-bands are split into spin-up and spin-down bands. Considering the selection rules of the transition and the corresponding transition matrix elements, the resonant absorption for circular polarized light depends on the angle between photon angular momentum and magnetization. Consequently, the absorption spectra of a ferromagnetic material for left and right circular light are, in general, different, as can be seen in Fig. 2.11. In fact XMCD probes the projection of the magnetization onto the photon k-vector. A detailed introduction to XMCD is given in Ref. [34].

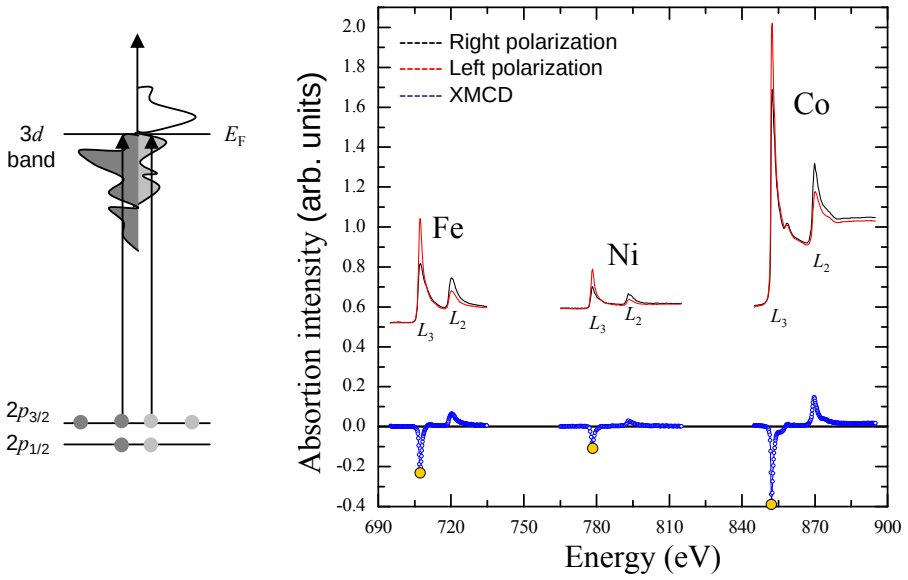

Figure 2.11: Scheme of a resonant electron transition from $2p$ states to $3d$ states (left). Due to the d-band splitting in ferromagnetes and the selection rules for transitions, the photon cross section is different for left and right circular light. Furthermore, the energy of the transition is strongly element dependent (right), such that element specific absorption asymmetries can be recorded, XMCD.

(a). Lensless imaging using x-ray magnetic circular dichroism

If the transverse coherence length is larger than the illuminated area, scattering reveals not only statistical properties, but also information about the sample's internal structure via a diffraction pattern. One could understand the spackle diffraction pattern as the real space structure *encoded* in frequency space. The frequency image is taken in the far field such that one is within the Fraunhofer limit. In this limit the transition to frequency space is approximately described by the Fourier transformation, assuming small scattering angles and perfect coherent conditions [35, 36]. Using inverse Fourier transform (IFT) it is then possible to retrieve the original real space structure. Hence, performing scattering experiments with coherent light allows for reconstruction of the real space object. However, before reconstructing the image from coherent scattering and inverse Fourier transform one has to overcome an immense obstacle; neither the wave amplitude nor its phase can be measured. Only the intensity, i.e. the squared

modulus of the wave can be recorded. The phase information is lost in the intensity measurement. This well known phase problem makes it difficult to retrieve the real space object from its diffraction pattern. Fortunately, solutions to this problems have been found and it has been shown that the real space structure can be reconstructed from the measured intensity under certain conditions [37–39], therefore creating a novel measuring technique: soft x-ray magnetic holography [18].

In detail an experimental setup to apply this lensless technique first consists in a monocromator and a pinhole to provide coherent light with defined wavelength. With this one can obtain speckle patterns like the one shown in Fig. 2.12. The sample-mask unit is illuminated by the coherent beam and the diffraction pattern is recorded using a charged coupled device (CCD) camera. To be able to extract magnetic information

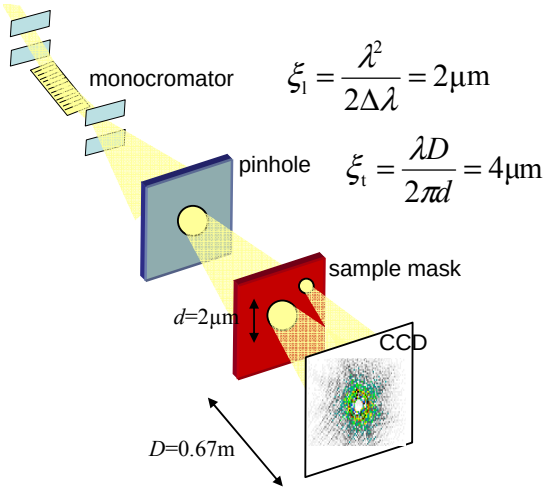

Figure 2.12: Schematics of an x-ray holography setup.

it is necessary to combine patterns obtained with opposite helicities, right and left circular. In Fig. 2.13 an example of two patterns as well as the subtraction is presented. Applying IFT to the combined diffraction pattern one obtains a real space structure where magnetic domains can be observed, as can be seen in the right part of the figure.

Three factors have to be taken into account concerning real space image resolution:

- the distance between the reference hole and sample hole (coherence)
- CCD camera – sample distance (largest detectable k values)

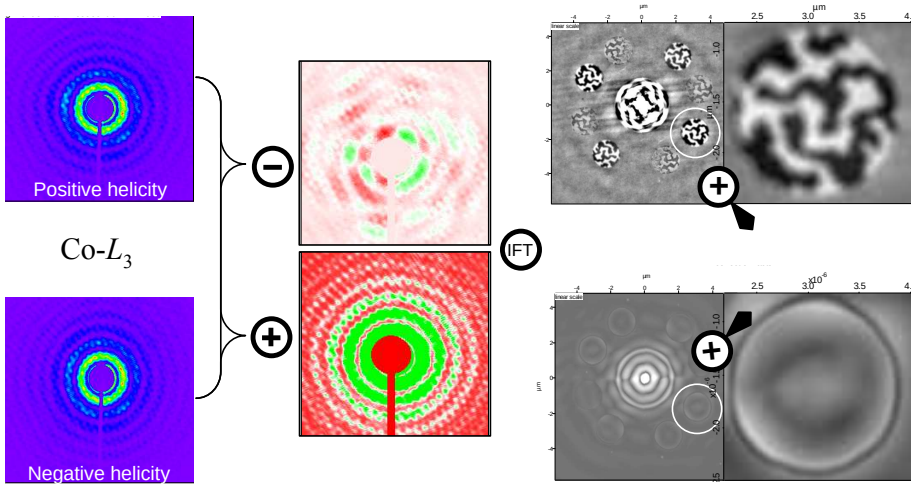

Figure 2.13: In experiment to holograms with opposite helicity are recorded (left). The difference image mainly contains the magnetic information (center). Using inverse Fourier transformation one receives the real space domain structure.

- the size of the reference hole (convolution)

For good magnetic contrast one additionally has to take into account the relative intensities of the light passing the pinhole with respect to the light passing the sample hole. For example, a typical mask with object and reference hole diameters of about 1.8 µm and 200 nm, respectively, has an intensity ratio of object and reference beam, before traversing the sample, of 80:1. Taking into account the absorption by the membrane and the sample structure, the intensity transmitted through the object beam is reduced and the ratio is slightly lowered. This gives an absorption-corrected intensity ratio of about 50 : 1 at the Co-L_3 absorption edge. A strong deviation in intensities reduces the effect of interference, which later on results in a reduced magnetic contrast. In contrary, while the ultimate spatial resolution of the reconstructed image is limited by the wavelength, the resolution of the reconstructed image in real space is given by the size of the reference pinhole [18]. In practice, the image is as if it was painted by a pencil of tip size similar to the size of the reference hole. Note, these to properties are somewhat in contradiction. On the one hand the pin hole must be that large that it gives the same intensity as the object hole, on the other hand it should be as small as possible to give optimal resolution.

Fig. 2.14 illustrates the aforementioned effects of the reference hole size on mag-

netic contrast and resolution. The magnetic images shown on top were retrieved from the magnetic hologram acquired at Co-L_3 absorption edge of a sample-mask structure with five reference holes of different size. For instance, the image retrieved from the largest reference aperture shows higher magnetic contrast but a blurred domain structure (top right image). In general, the contrast increases with the reference hole size while resolution diminishes. For more information on x-ray holography see for

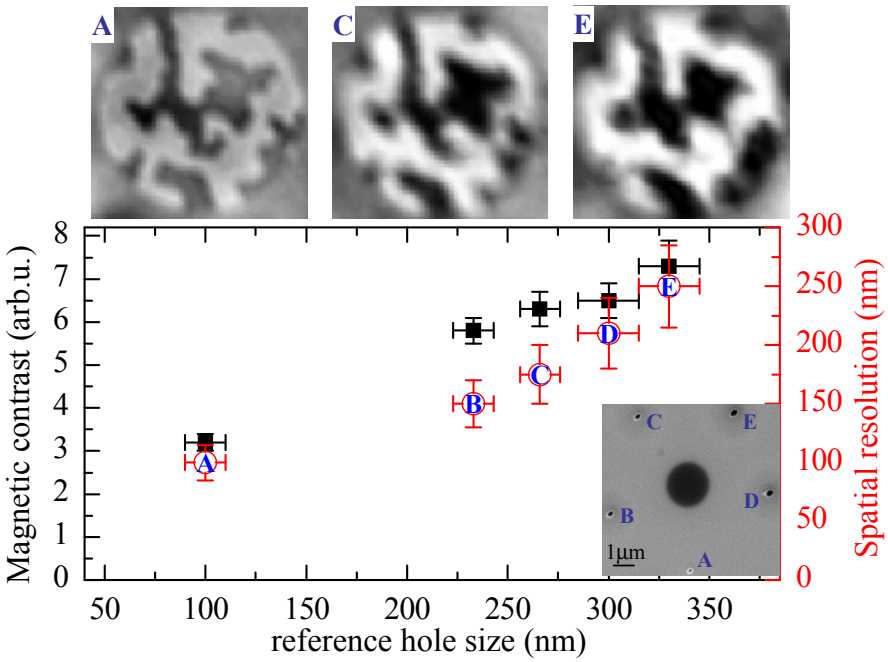

Figure 2.14: Effect of reference hole size on domain contrast (squares) and spatial resolution (circles) extracted from magnetic images (top) of a demagnetized $[Pt/Co]_8/10$ nm FeMn sample. The magnetic contrast is taken from the difference between the two prominent gray scale values of the magnetic images, which correspond to Co domains with opposite out-of-plane magnetization, whereas the resolution is given by the domain wall width from line scans taken through opposite magnetic domains. The reference hole size is estimated from the scanning electron microscopy image taken from the mask-side of the structure shown in the bottom right inset.

instance [20, 40].

2.3. Conclusions

Two setups have been presented in this chapter, which enable magnetic characterization and imaging. Both techniques can be used under magnetic fields as both are photon based.

The first setup is an extended magneto-optic Kerr effect setup that allows for the simultaneous measurement of two independent magnetization components. A data analysis has been developed to minimize non-linear effects. The simultaneous measurement of two in-plane magnetization components in combination with the full angular study gives a precise characterization of magnetic reversal processes and allows to detect exactly the orientation of the characteristic magnetization axes. Using this technique the magnetic properties of twofold, fourfold, and onefold symmetry system will be investigated in the following.

As a second setup lensless imaging using soft x-ray holography and circular dichroism has been developed. In chapter 5 the advantages of this technique are exploited. The combination of spectroscopy, i.e. the element selective quantification of magnetic moments, and imaging of buried interfaces allows to investigated the FM/AFM interfaces of exchange-biased systems under applied field.

References

[1] L. G. Parratt, Phys. Rev. **95**, 359 (1954).

[2] D. B. Williams and C. B. Carter, *Transmission Electron Microscopy: A Textbook for Materials Science* (Plenum Press, 1996).

[3] Y. Zhu, ed., *Modern Techniques for Characterizing Magnetic Materials* (Kluwer Academic Publisher, 2005).

[4] R. Wiesendanger, *Scanning probe microscopy: methods and applications* (Cambrigde University Press, 1994).

[5] H. Hopster and H. P. Oepen, eds., *Magnetic Microscopy of Nanostructures* (Springer, Berlin, 2004).

[6] J. A. C. Bland and B. Heinrich, *Ultrathin magnetic structures: An introduction to the electronic, magnetic structural properties* (Springer, Berlin, 2005).

[7] S. Foner, Rev. Sci. Instrum. **30**, 548 (1959).

[8] A. P. Guimaraes, *Principles of nanomagnetism* (Springer, Berlin, 2009).

[9] J. Kerr, Phil. Mag. S. 5 **3**, 321 (1877).

[10] R. M. A. Azzam and N. M. Bashara, *Ellipsometry and polarized light* (North-Holland Publishing Company, Amsterdam, 1977).

[11] Z. Q. Qiu and S. D. Bader, Rev. Sci. Instrum. **71**, 1243 (2000).

[12] C. R. Pike, A. P. Roberts, and K. L. Verosub, J. Appl. Phys. **85**, 6660 (1999).

[13] J. Zak, E. R. Moog, and S. D. Bader, Phys. Rev. B **43**, 6423 (1991), erratum, Phys. Rev. B **43**, 6423 (1991).

[14] H. F. Ding, S. Pütter, H. P. Oepen, and J. Kirschner, J. Magn. Magn. Mater. **212**, L5 (2000).

[15] A. L. Robinson, *Center for X-ray optics and Advanced Light Sources; X-ray Data booklet* (lawrence berkely national laboratory, University of california, 2009).

[16] J. Albillos, Master's thesis, Universidad de Zaragoza (2006).

[17] H. A. Dürr, T. Eimüller, H. J. Eimüller, S. Eisebitt, M. Farle, W. Kuch, F. Matthes, M. Martins, H. C. Mertins, P. M. Oppeneer, et al., IEEE TRANSACTIONS ON MAGNETICS **45**, 15 (2009).

[18] S. Eisebitt, J. Lüning, W. F. Schlotter, M. Lörgen, O. Hellwig, W. Eberhardt, and J. Stöhr, Nature **432**, 885 (2004).

[19] A. Scherz, W. F. Schlotter, K. Chen, R. Rick, J. Stöhr, J. Lüning, I. McNulty, C. Günther, F. Radu, W. Eberhardt, et al., Phy. Rev. B **76**, 214410 (2007).

[20] O. Hellwig, S. Eisebitt, W. Eberhardt, W. F. Schlotter, J. Lüning, and J. Stöhr, J. Appl. Phys. **99**, 08H307 (2006).

[21] D. Attwood, *Soft X-rays and Extreme Ultraviolet Radiation: Principles and Applications* (Cambridge University Press, 1999).

[22] G. Beutier, A. Marty, F. Livet, G. van der Laan, S. Stanescu, and P. Bencok, Rev. Sci. Instrum. **78**, 093901 (2007).

[23] J. L. Erskine and E. A. Stern, Phys. Rev. B **12**, 5016–5024 (1975).

[24] B. T. Thole, G. van der Laan, and G. A. Sawatzky, Phys. Rev. Lett. **55**, 2086–2088 (1985).

[25] M. Blume, J. Appl. Phys. **57**, 3615 (1985).

[26] M. Blume and D. Gibbs, Phys. Rev. B **37**, 1779–1789 (1988).

[27] G. van der Laan, B. T. Thole, G. A. Sawatzky, J. B. Goedkoop, J. C. Fuggle, J. M. Esteva, R. Karnatak, J. P. Remeika, and H. A. Dabkowska, Phys. Rev. B **34**, 6529–6531 (1986).

[28] G. Schütz, W. Wagner, W. Wilhelm, P. Kienle, R. Zeller, R. Frahm, and G. a. Materlik, Phys. Rev. Lett. **58**, 737–740 (1987).

[29] C. T. Chen, F. Sette, Y. Ma, and S. Modesti, Phys. Rev. B **42**, 7262–7265 (1990).

[30] B. T. Thole, P. Carra, F. Sette, and G. van der Laan, Phys. Rev. Lett. **68**, 1943–1946 (1992).

[31] P. Carra, B. T. Thole, M. Altarelli, and X. Wang, Phys. Rev. Lett. **70**, 694 (1993).

[32] C. T. Chen, Y. U. Idzerda, H. J. Lin, N. V. Smith, G. Meigs, E. Chaban, G. H. Ho, E. Pellegrin, and F. Sette, Phys. Rev. Lett. **75**, 152–155 (1995).

[33] J. Stöhr, Y. Wu, B. D. Hermsmeier, M. G. Samant, G. R. Harp, S. Koranda, D. Dunham, and B. P. Tonner, Science **259**, 658 (1993).

[34] J. Stöhr and H. C. Siegmann, *Magnetism, From Fundamentals to Nanoscale Dynamics* (Springer, Berlin, 2006).

[35] M. Born and E. Wolf, *Principles of Optics* (Pergamon Press, Oxford, 1959).

[36] J. W. Goodman, *Introduction to Fourier optics*, series in electrical and computer engineering (McGraw-Hill, New York, 1996), 2nd ed.

[37] R. Gerchberg and W. Saxton, Optik **35**, 237–246 (1972.).

[38] J. N. Cederquist, J. R. Fienup, J. C. Marron, and R. G. Paxman, Optics Letters **13**, 619–621 (1988).

[39] H. He, S. Marchesini, M. Howells, U. Weierstall, H. Chapman, S. Hau-Riege, A. Noy, and J. C. H. Spence, Phys. Rev. B **67**, 174114 (2003).

[40] S. Eisebitt, M. Lörgen, W. Eberhardt, J. Lüning, and J. Stöhr, Appl. Phys. A **80**, 921 (2005).

Chapter 3

The influence of Magnetic Anisotropy on model systems

Symmetry is what we see at a glance.

Blaise Pascal

The effect of the symmetry of the magnetic anisotropy on the magnetic properties has been investigated in several model nanostructures that present well defined magnetic anisotropies. Angular dependent vectorial-resolved Kerr magnetometry measurements have been performed in polycrystalline FM thin films with induced uniaxial anisotropy (twofold symmetry), epitaxial Fe (100) thin films (fourfold symmetry), and exchange-biased (onefold symmetry) FM/AFM bilayers with a priori collinear anisotropy configuration, i.e., with the interfacial-induced unidirectional anisotropy axis parallel to the intrinsic uniaxial FM anisotropy. The experimental data reveal a strong influence of the symmetry on the magnetic properties. This understanding open additional avenues to tailor the magnetic properties of future nanostrutures.

No matter what application one is interested in, a key property of a ferromagnetic sample is the preferred direction of its magnetization. Magnetic anisotropy is a key parameter in the design of all magnetic materials. In permanent magnets, this direction should be fixed rigidly to ensure proper functioning of the magnet. In sensing applications, such as in read heads, an easy rotation of the magnetization of a ferromagnetic layer in the faint stray field of a magnetized hard disk is, however, necessary. The

magnetic anisotropy is the quantity that determines the easy magnetization direction of a magnet and it is also decisive for the magnetization reversal in external fields.

In this chapter, the angular dependence of the magnetic properties of model magnetic nanostructures with well-defined anisotropy is presented. In particular, ferromagnetic (FM) systems with tailored uniaxial (twofold symmetry) and biaxial (fourfold) magnetic anisotropy will be studied. Furthermore, model exchange-biased ferromagnetic/antiferromagentic (FM/AFM) bilayers, which combine the intrinsic FM anisotropy and the induced-interfacial unidirectional anisotropy (twofold+onefold) with an intended collinear configuration.

(a). What is going to be measured

The most common way to represent the magnetic properties of ferromagnetic system is by plotting the magnetization against the applied magnetic field, as is shown in Fig. 3.1. The typical parameters used to define magnetic properties are as follows. The value of the magnetization, when fully aligned to the applied field, is called saturation magnetization, M_S. The value of the magnetization at zero applied field the rema-

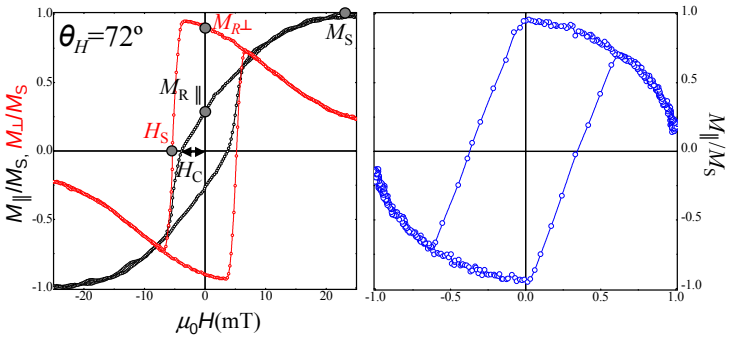

Figure 3.1: Hysteresis loop of a 6 nm permalloy film at selected angle ($\theta_H = 72°$) is shown. Longitudinal (black symbols) and transversal (red symbols) components of the hysteresis curves are displayed in the left panel, where characteristic values extract from both components, H_C, M_R and M_S are shown. In blue symbols $M_{\parallel}(M_{\perp})$ is plotted.

nence, M_R. As the vectorial Kerr measures the parallel as well as the perpendicular magnetization component one actually has to distinguish $M_{R,\parallel}$ and $M_{R,\perp}$. The switching field, H_S is the critical field necessary to change the sign of the $M_{\perp}$ component. The corresponding critical field to change sign of $M_{\parallel}$ is the coercive field H_C. In case of uniaxial anisotropy (see the following chapter) one additionally has the anisotropy field H_K, the field value at which the hard axis hysteresis saturates in figure 3.3.

3.1. Uniaxial Systems

Some metals present the simplest kind of anisotropy, only one characteristic direction. This is called uniaxial anisotropy. A very typical material is the FeNi alloy permalloy. Actually, the composition of Fe and Ni in permalloy is chosen in such a way that it should not present magnetic anisotropy and only a very weak magnetostriction. However, due to small residual fields during growth or, e.g., geometrical substrate properties, small uniaxial anisotropies are common.

3.1.1. Sample preparation

A thin magnetic permalloy film has been studied as model two-fold symmetry system. The film has been sputtered at room temperature (RT) onto a thermally oxidized Si substrate. The thickness of the FeNi film is 6 nm. A buffer layer of Ta has been deposited at oblique incidence to promote a uniaxial anisotropy, as depicted in Fig. 3.2. With this method the preferred direction of the magnetization is perpendicular to the plane of incidence of the sputtered Ta buffer layer [1].

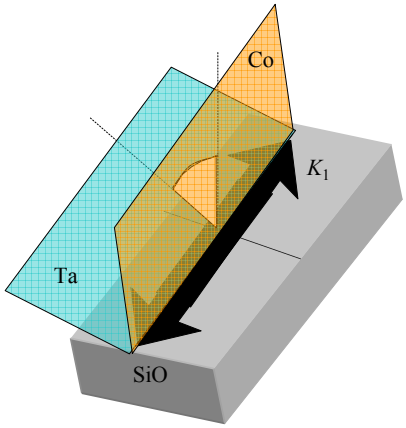

Figure 3.2: A buffer layer of Ta deposited at oblique incidence promote a uniaxial anisotropy. With this method the preferred direction of the magnetization is perpendicular to the plane of incidence of the sputtered Ta buffer layer.

This is the so-called easy axis (e.a.) of magnetization (left panel of Fig. 3.3). In contrast, the direction in the plane of incidence has the highest energy and the magnetization avoids to be oriented in this direction (right panel of Fig. 3.3). This is the so-called hard axis (h.a.), which is perpendicular to the e.a. in a uniaxial system.

In the left panel Fig. 3.3 a), $M_{\parallel}$ and $M_{\perp}$ are plotted for the case of $\theta_H = 0^\circ$ (e.a.). The graph for $M_{\parallel}$ (black line) presents a square loop while the graph for $M_{\perp}$ (red

[1] The 6 nm FeNi thin film has been grown by J. Sort

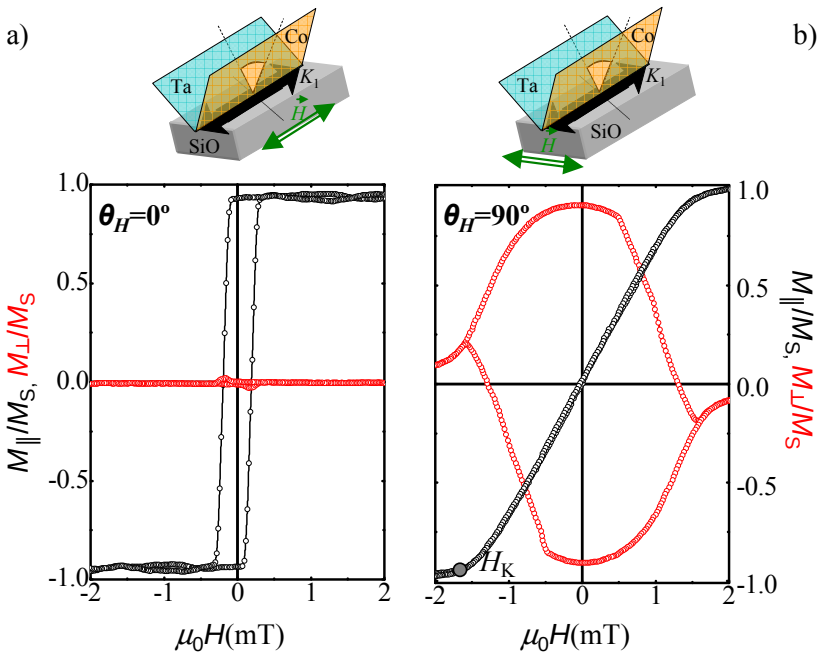

Figure 3.3: Longitudinal and transversal components of the hysteresis curves of a 6 nm permalloy film. The easy axes ($\theta_H = 0°$) and hard axes ($\theta_H = 90°$) direction is shown left and right, respectively. The upper panels show the relative orientation between the anisotropy, K_1 and the applied field.

line) is zero for all field values. Starting at a high positive field, magnetization and field are fully aligned. The system is saturated ($M_\parallel/M_S = 1$). The projection, $M_\parallel$, remains constant until the field is decreased to a critical negative value where $M_\parallel$ switches from $+M_S$ to $-M_S$ ($H_C = 2mT$). The backward branch of the hysteresis loop has a symmetric behavior. Increasing the field from negative saturation $M_\parallel$ remains constant until a critical positive value is reached. Here $M_\parallel$ jumps from $-M_S$ to $+M_S$. This critical field value has the same modulus as the critical field of the forward branch but opposite sign. The magnetization switches between the two possible equilibrium states of the system such that the magnetization is either parallel or anti-parallel to the field. Hence, $M_\perp$ is always zero.

For $\theta_H = 90°$ a non-hysteretic loop is found for $M_\parallel$, shown in panel Fig. 3.3 b). At high positive field the system is saturated in direction of the applied field, consequently $M_\perp$ is zero. Decreasing the field from high values $M_\parallel$ first remains constant. At the

certain positive field it starts to decrease linearly to zero with the slope that is inverse proportional to the anisotropy field, H_K. The linear behavior continues down to the critical field where $M_{\parallel}$ shows saturation $M_{\perp}$ is zero. In the linear region of $M_{\parallel}$ however $M_{\perp}$ is increasing and showing maximum at $H = 0$.

3.1.2. Magnetic characterization

The magnetic characterization has been performed in our artifact-free vectorial magneto-optic Kerr setup. Selected hysteresis curves measured around characteristic directions ($\theta = 0^{\circ}$ and $\theta = 90^{\circ}$) are shown in Fig. 3.4. Both components of the magnetization, $M_{\parallel}$ and $M_{\perp}$ are presented in black and red symbols, respectively. The squared hysteresis loop corresponds to the easy direction while a non-hysteretic loop is observed in h.a. direction.

(a). Magnetization Reversal processes

The vectorial-MOKE setup allows for detailed angular studies, i.e. the parallel and perpendicular components of magnetization are studied not only as a function of applied field but also as a function of applied field angle. Each sample is investigated varying the field angle in the full angular range from 0° to 360°, with a precision of 1° (A more complete angular study of the uniaxial system is presented in chapter A.1.1).

Selected hysteresis curves for angles close to characteristic direction, i.e. easy axis (e.a.) and hard axis (h.a.) are presented in figure 3.4. The left column corresponds to the angular region around the e.a. ($\theta_H = 0^{\circ}$). As has been described in figure 3.3, the e.a. presents a square loop in $M_{\parallel}$ and zero $M_{\perp}$. The top panel shows the hysteresis curve for $\theta_H = -18^{\circ}$. The curve presents smooth rotation in both branches of $M_{\parallel}$ as well as $M_{\perp}$ until a critical field is reached and switching takes place. At this field both $M_{\parallel}$ and $M_{\perp}$ change sign. For $M_{\parallel}$ and $M_{\perp}$ the backward and forward branch are point symmetric with respect to the origin. The bottom panel displays the hysteresis curves for $\theta_H = +18^{\circ}$, i.e. opposite to the top panel. Note that the curve for $M_{\parallel}$ is exactly the same. However the curve for $M_{\perp}$ is mirrored with respect to the field axis when compared to the case of $\theta_H = -18^{\circ}$.

The right column shows the angular region around the hard axis, $\theta_H = 90^{\circ}$, shown in the centered panel. Top and bottom panel deviate from this direction by $\mp 18^{\circ}$, respectively. As for the left column $M_{\parallel}$ is identical in the top and bottom panels, while $M_{\perp}$ again shows mirror symmetry. following chapter 3.1.3.

The experimental data qualitatively follows the prediction of the coherent rotation model (shown as continuous line in figure 3.4) by Stoner-Wohlfarth [1], which will be

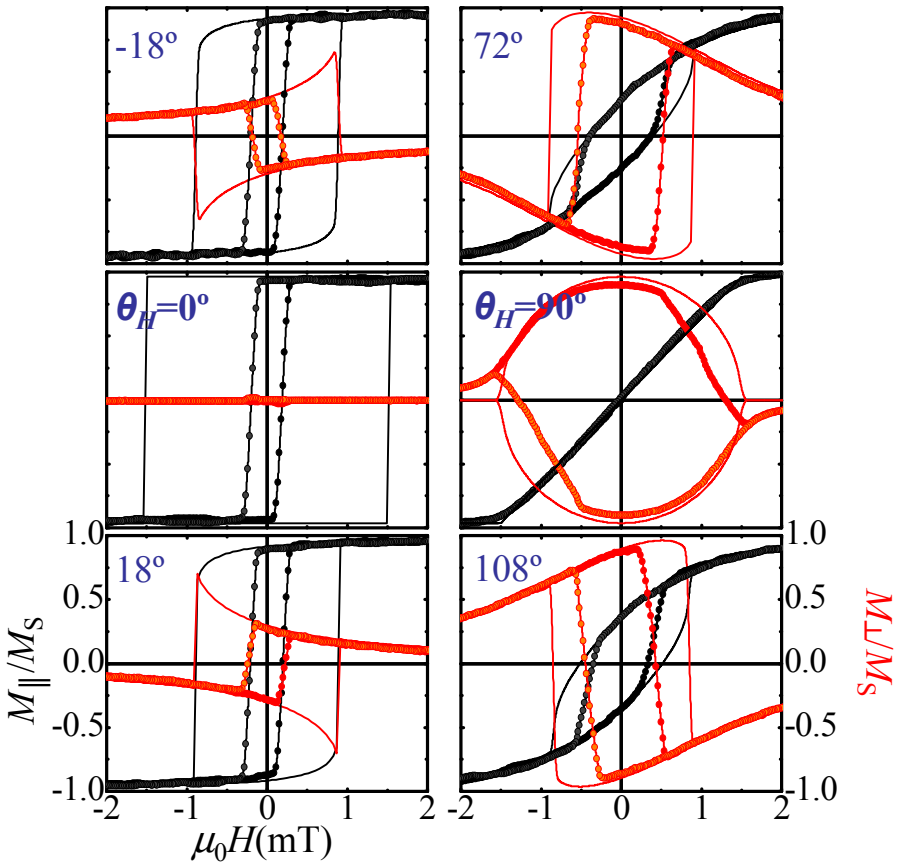

Figure 3.4: Selected hysteresis loops around e.a. and h.a. The measured data (6 nm FeNi) is compared to a theoretical uniaxial system. The figure shows the angular symmetry of the reversal processes with respect to the characteristic angles.

explained in the

However, there are quantitative deviations. The deviations appear due to the fact that the system not only shows coherent rotation but also domain wall nucleation and propagation. The presence of domains lowers the total magnetization such that the vectorial sum of $M_{\parallel}$ and $M_{\perp}$ does not add up to a vector of length M_S. This can be easily seen when presenting the data in the $M_{\parallel}$-$M_{\perp}$-plane. This has been done in figure 3.5. Plotting the data in the $M_{\parallel}$-$M_{\perp}$-plane as in figure 3.5 additionally allows to extract the angle of the domain wall, Ω. Domain walls start to occur when $M(H)$

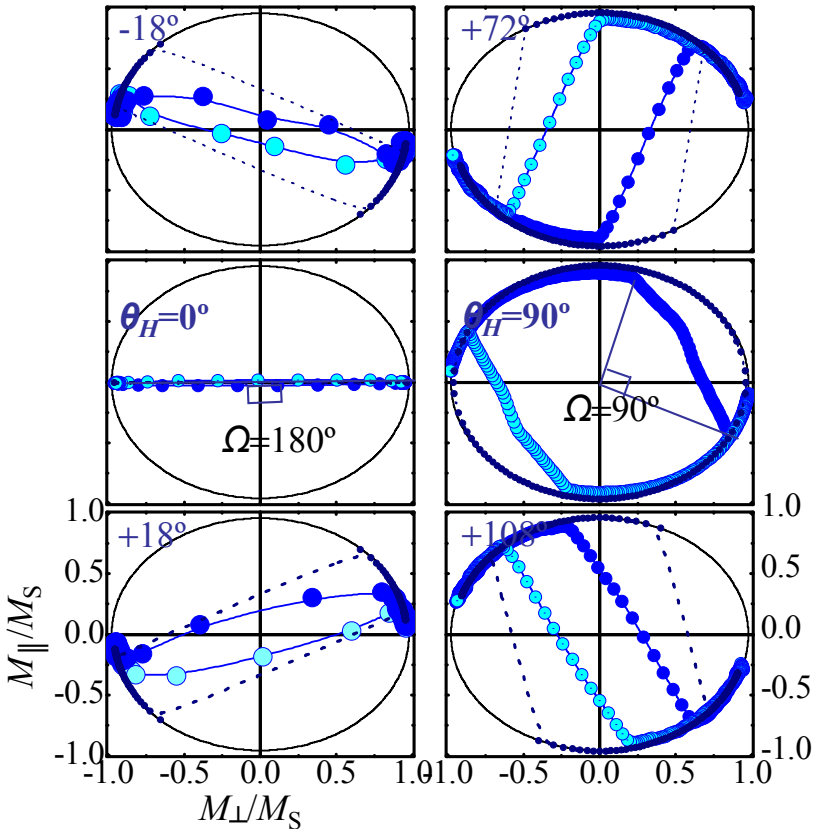

Figure 3.5: Hysteresis curves of a 6 nm permalloy thin films in parametric representation. In this representation it is obvious that around the e.a. mainly domain wall nucleation and propagation takes place. Near the h.a., however, many data points lie on the circle, implying the presence of coherent rotation processes. Within the SW-model the magnetization also jumps from one side of the circle to the other; this is shown as dashed lines. Within the SW-model, however, there are no states inside the circle.

leaves the circle and they disappear when $M(H)$ reaches the other side of the circle. The states on the secant are defined by nucleation and propagation of domain walls. Note, the direction of the magnetization of the decreasing domain is given by the point where the hysteresis curve leaves the circle, while the direction of the increasing domain is given by the point where the hysteresis curves returns to the circle. Hence, the angle of the domain wall (DW) is given by the mid point angle by the triangle defined by the center of the circle and the two intersections of the secant, e.g. $\Omega(\theta_H =$

$0°) = 180°$.

(b). Angular Dependences of M_R, H_C and H_S

The symmetry of the system, hence, the order of the anisotropy, can be easily recognized by the angular dependence of the remanence. In Fig. 3.6 is presented both

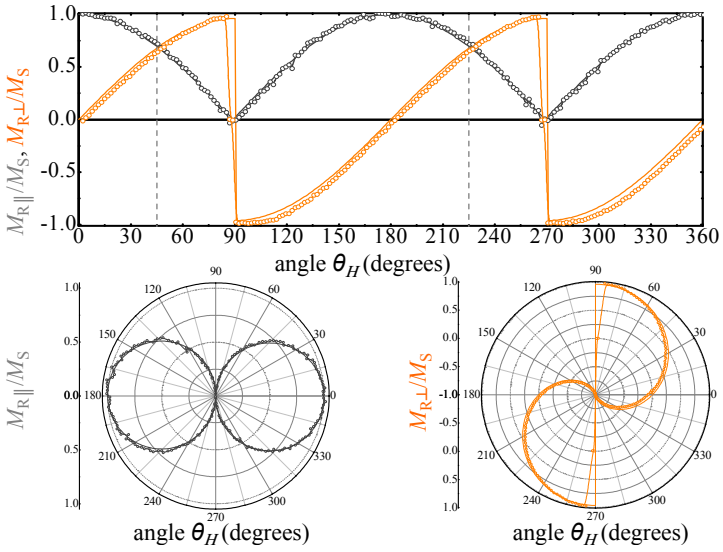

Figure 3.6: Angular evolution of the remanence for a 6 nm thin FeNi film. Two representation of both components of the magnetization ($M_{R,\parallel}$ and $M_{R,\perp}$, gray and orange, respectively) are shown: linear as a function of the angle of the applied field (upper panel) and two individual polar plots (lower panels). The SW-model (continuous lines) is in very good agreement with the experimental data (symbols).

remanence, $M_{R,\parallel}$ and $M_{R,\perp}$, dark gray and orange, respectively. The $M_{R,\parallel}$ component has a $|\sin\theta_H|$ behavior. It is positive semidefinite for all field directions. However, the $M_{R,\perp}$ component changes sign when crossing a characteristic angle (e.a. or h.a.), i.e. $M_{R,\perp}$ is sensitive to the characteristic axes. The polar-plot representation in the lower panel emphasizes the twofold symmetry. In continuous line is displayed the prediction of the SW-model.

In summary we see that the Stoner-Wohlfarth-model quantitatively predicts the remanence of $M_\parallel$ and $M_\perp$ for all the angular range. As this is a zero field property it actually does not depend strongly on the details of the model.

In contrast coercive and switching fields are described by the Stoner-Wohlfarth-model only near the h.a., as can be seen in figures 3.7 and 3.8, respectively.

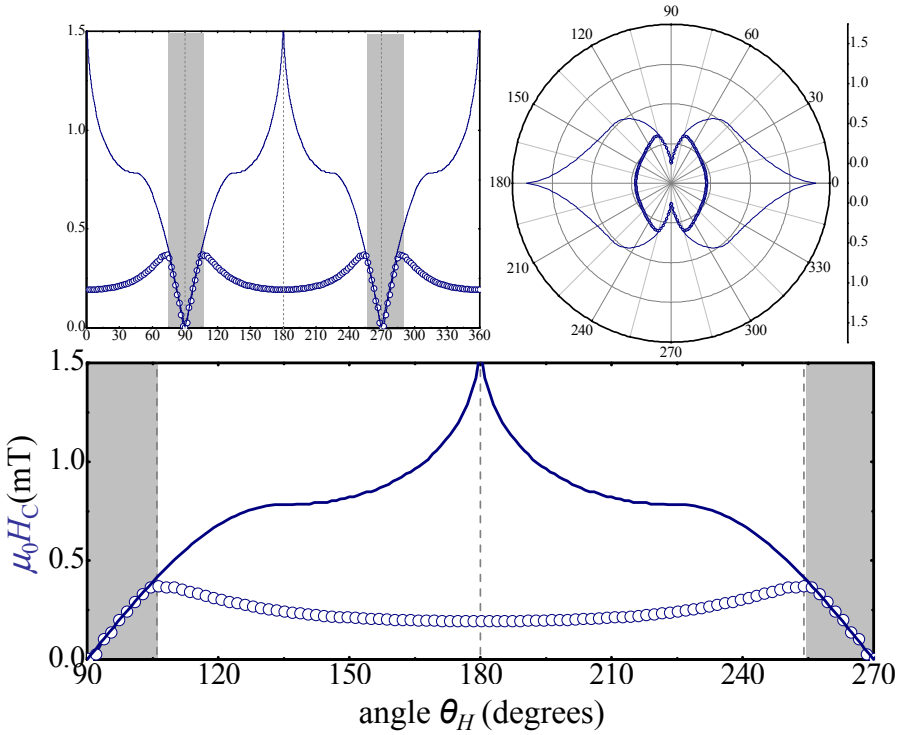

Figure 3.7: Angular evolution of the coercive field for a 6 nm permalloy film. The theoretical prediction of SW-model is plotted on top in continuous line.

The upper panels of both figures, Fig. 3.7 and 3.8 display the full angular dependence of coercive and switching fields, respectively. In the lower is presented a zoom around the e.a.

Near the e.a. nucleation and propagation of domains take place such that the Stoner-Wohlfarth-model, which was developed for single domain particles, must fails. Hence, to describe the coercivity and switching field near the e.a. a different model is needed. The first ideas were given by Givord and Kronüller [2, 3]. This corresponding model will be shortly introduced at the end of chapter 3.1.3.

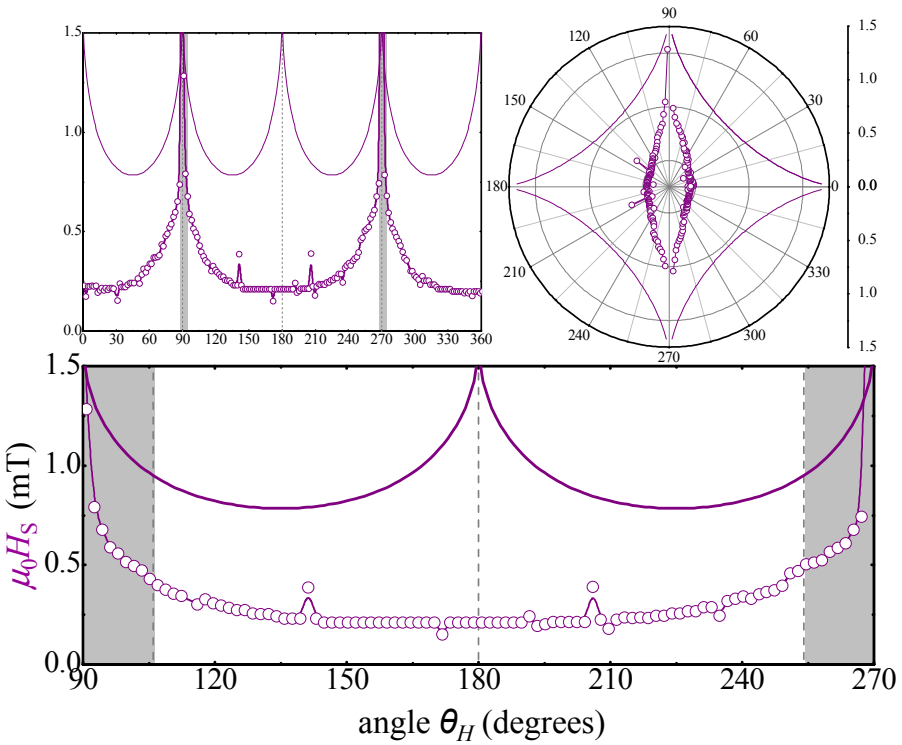

Figure 3.8: As in Fig. 3.7, but for the switching field.

3.1.3. Models of ideal systems

In the following two complementary models to describe hysteresis are discussed. The first one assumes a rotation of magnetization under applied fields, while the second presents exclusively domain wall nucleation and propagation. Comparing the results to the previously presented date reveals that both models predict the data, but in different angular regions.

(a). The coherent rotation model

In 1947 E. C. Stoner and E. P. Wolhfarth developed a model to described the mechanism of magnetic hysteresis in heterogeneous alloys [1]. In this model, the so-called SW-model, the authors consider an elliptic single domain particle. Due to its shape

the particle shows uniaxial anisotropy. When applying an external field there is only competition between the Zeeman energy and the anisotropy energy of the particle. The total energy is given by:

$$E_{\text{tot}} = K_1 \sin^2 \varphi - \mu_0 H M_S \cos(\varphi - \theta_H), \tag{3.1}$$

where φ is the angle between the anisotropy direction and the magnetization $\vec{M}$ whereas θ_H is the angle between applied field $\vec{H}$ and anisotropy direction (see figure 3.9). For each angle θ_H, the hysteresis loops can be simulated numerically by minimizing Eq. 3.1 with respect to φ, i.e. $\frac{\partial E_{\text{tot}}(H)}{\partial \varphi}\Big|_{\theta_H=\text{const}} = 0$. In the model the magnetization follows the local minimum via coherent rotation. For each applied field angle θ_H the magnetization hysteresis loops are derived by

$$\begin{aligned} \frac{M_\parallel(H)}{M_S} &= \cos(\theta_H - \varphi) \\ \frac{M_\perp(H)}{M_S} &= \sin(\theta_H - \varphi). \end{aligned} \tag{3.2}$$

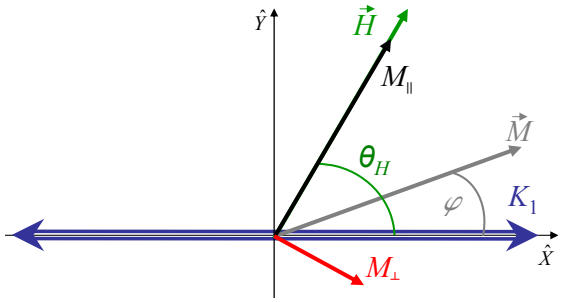

Figure 3.9: Scheme of relevant vectors and angles in a uniaxial system under applied field. Anisotropy K_1, magnetization, $\vec{M}$ and applied field, $\vec{H}$.

In figure 3.10 the SW-model is explained schematically. As within this model the magnetization is a vector of constant modulus, it is represented via gray vector rotating on a circle in the $M_\parallel$-$M_\perp$-plane. The projection of the magnetization onto $M_\parallel$ and $M_\perp$ are given by black and red arrows, respectively. The easy anisotropy direction is mark as blue double arrow. The applied field is shown as green arrow, its strength is represented as the vector's length. In the following six characteristics points of the hysteresis forward branch, shown at the central panel, are explained with help of the vector scheme. In point i) a strong field is applied. The magnetization is almost aligned with the field, such that $M_\parallel$ is almost saturated while $M_\perp$ is close to

zero. In point ii) the field has decreased. The magnetization has rotated towards the easy anisotropy direction and its projection on the $M_{\parallel}$-direction has decreased while the projection onto the $M_{\perp}$-direction has increased. In point iii) the applied field is

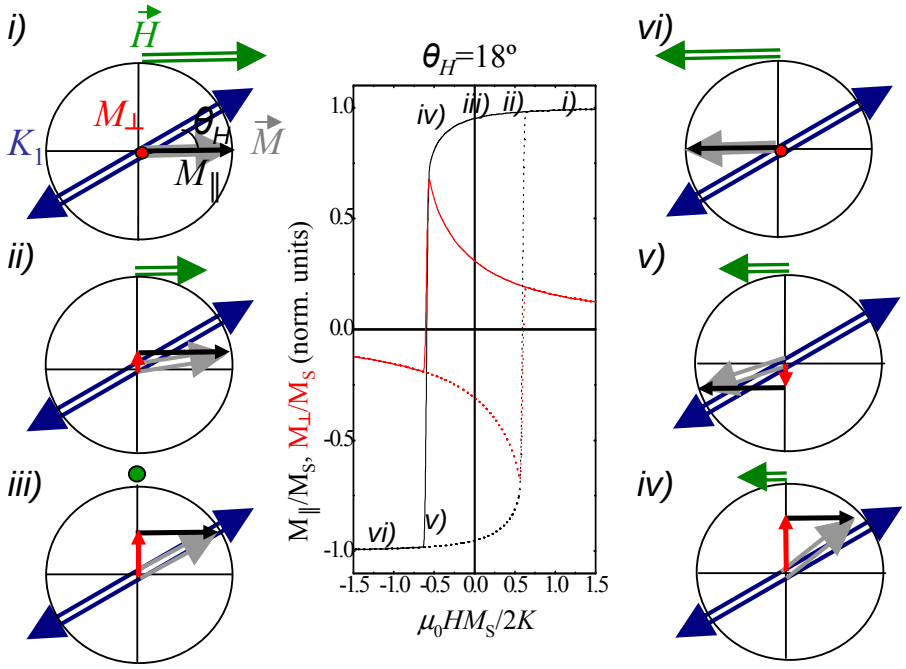

Figure 3.10: Vectorial resolved hysteresis curves predicted by the SW-model. The configuration of field, anisotropy, and magnetization at six characteristic points. For every characteristic point the applied magnetic field is shown as green arrow; its strength is represented as the vector's length. The magnetization, represented as gray vector, is a vector of constant modulus, which therefore moves on a circle. The projection of the magnetization onto $M_{\parallel}$ and $M_{\perp}$ are given by black and red arrows, respectively. The easy anisotropy direction is marked by a blue double arrow.

zero and the magnetization points in the easy anisotropy direction. Going to negative fields (point iv) the magnetization continues rotating, decreasing $M_{\parallel}$ and increasing $M_{\perp}$. At point v) the critical field has been past and the magnetization has switched to the other side of the circle. With further decrease of the field the magnetization rotates away from the anisotropy axes and towards of the applied field (point vi)). The same happens for the backward branch but in mirror symmetry.

Theoretical hysteresis loops of the SW-model for different applied field angles ($\theta_H = 0°$, 30°, 60° and 90°) are shown in figure 3.11. In the left and right panel (a) and (b) plot $M_\parallel$ and $M_\perp$ are plotted for the different angles θ_H.

The graph for $M_\parallel$ at $\theta_H = 0°$ presents a square loop while the graph for $M_\perp$ is zero for all field values. At $\theta_H = 90°$, the component $M_\parallel$ is fully reversibles. The angles in between present both soft and sharp transition, in $M_\parallel$. The signal of $M_\perp$ decrease when the magnetization is aligned with the applied field.

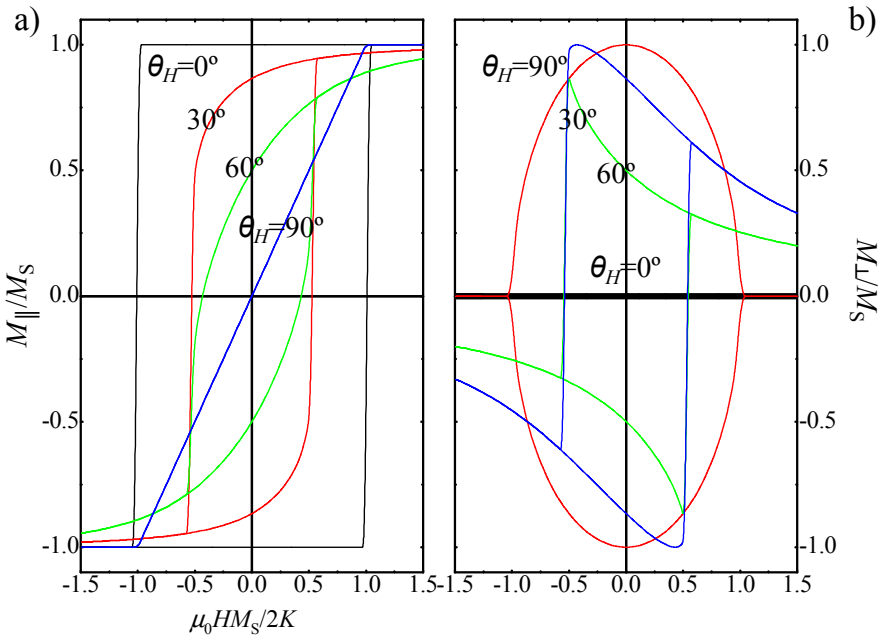

Figure 3.11: Selected hysteresis loops at different applied field angles $\theta_H = 0°$, 30°, 60°, and 90°. The curve corresponding to $\theta_H = 0°$ and 90° are fully saturated in two different states,$\pm M_S$. The 30° and 60°-loop shows soft changes and sharp jumps. The 90° curve presents a non-hysteretic loop.

Due to the vectorial character of the representation, complementary information can be extracted from the two components of $\vec{M}$. At high positives fields the magnetization is almost but not fully saturated at 30°, 60°.[2] Consequently, there is signal in the perpendicular component.

[2] In the SW-model full saturation is only possible for $\theta_H = 0°$ and $\theta_H = 90°$

Note, the angular evolutions predicted by the model, i.e. remanence, coercive and switching field, have been introduce in Fig. 3.6, Fig. 3.7 and Fig. 3.8, respectively, in continuous line.

(b). Energetic consideration

The energetics of a uniaxial model system is shown in figure 3.12 for three specific field angles. For each angle the situation of three different field strengths is presented. The largest field corresponds to the switching field. Each graph shows the anisotropy

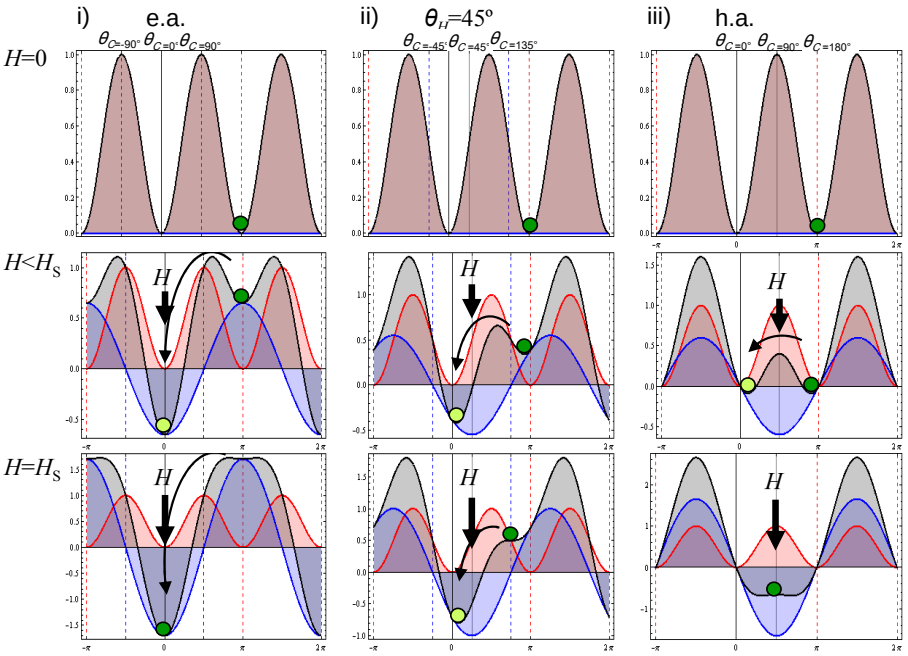

Figure 3.12: Energy landscape of a uniaxial system under applied magnetic fields. Three field directions are presented, i) $\theta_H = 0°$, ii) 45° and iii) 90°. The field strength increases from top toward the bottom. In the bottom row the situation of the critical field is depicted. Note, the local minimum that is occupied by the magnetization has transformed into a saddle point and vanishes. The magnetization has to move to the next minimum. This process is incoherent and not reversible, i.e. it results in magnetic hysteresis.

energy (red curve), the Zeeman energy (blue curve), as well as the sum of both (black curve). In the first row the applied field is zero ($H = 0$), such that the total energy

is equal to the anisotropy energy. Consequently, the magnetization symbolized by a dark green disk, points in e.a. direction (marked as red, dashed lines). The situation for small applied fields is shown in the second row. The direction of the applied field is shown as gray line. Due to the applied field the minimum that is occupied by the magnetization now only represent a local minimum. The new absolute minimum is marked with the light green disk. As local and absolute minimum are separated by an energy barrier, the magnetization stays in the local minimum. The third row displays the case of critical field, i.e. the point where the local minimum vanishes. Hence, the magnetization has switched to the absolute minimum. At the same time it passes the angle of 90° with respect to the field direction, shown in the blue dashed lines, such that the projection on the field direction changes sign. Hence, the field at which the magnetization passes the blue dashed line is equivalent to the coercive field.

There are two possible ways how the magnetization may pass the angle of 90° (blue, dashed line). For field directions close to the e.a. (<45°) the magnetization passes 90° as the local minimum vanishes at angles above 90°, while the absolute minimum is found below 90°. For field directions close the h.a. (>45°) the local minimum strongly changes its position as a function of field strength, such that it passes 90°, before it vanishes. Hence, in the first case switching field and coercive field are identical, while they have different values in the second case. The border line of these two cases is given by an applied field angle of 45° (see center column of figure 3.12). The situation for smaller and lager angles is shown in the left and right columns of figure 3.13, respectively.

Due to the variable field the total energy (3.1), i.e. the sum of Zeeman and potential energy, can present one or two minima. Hence, the system shows critical behavior at the point where the second minimum vanishes. At this critical field the total energy shows a saddle point. Therefore, the first ($\partial E/\partial\theta_H$) and the second derivative ($\partial^2 E/\partial\theta_H^2$) are zero. By rewriting equation 3.1 the free parameters H_x and H_y are introduced.

$$E = K\sin^2\theta_H - MH_x\cos\theta_H - MH_y\sin\theta_H = 0 \tag{3.3}$$

With this new form for the total energy, the condition $\partial E/\partial\theta_H = \partial^2 E/\partial\theta_H^2 = 0$ results in an implicit equation for H_x and H_y of the form [4]:

$$H_x^{2/3} + H_y^{2/3} = (2K/M)^{2/3} \tag{3.4}$$

The solutions to this equation is the astroid shown in figure 3.6 (purple line) In case of a uniaxial anisotropy it is also possible to give an explicit solution for the critical field

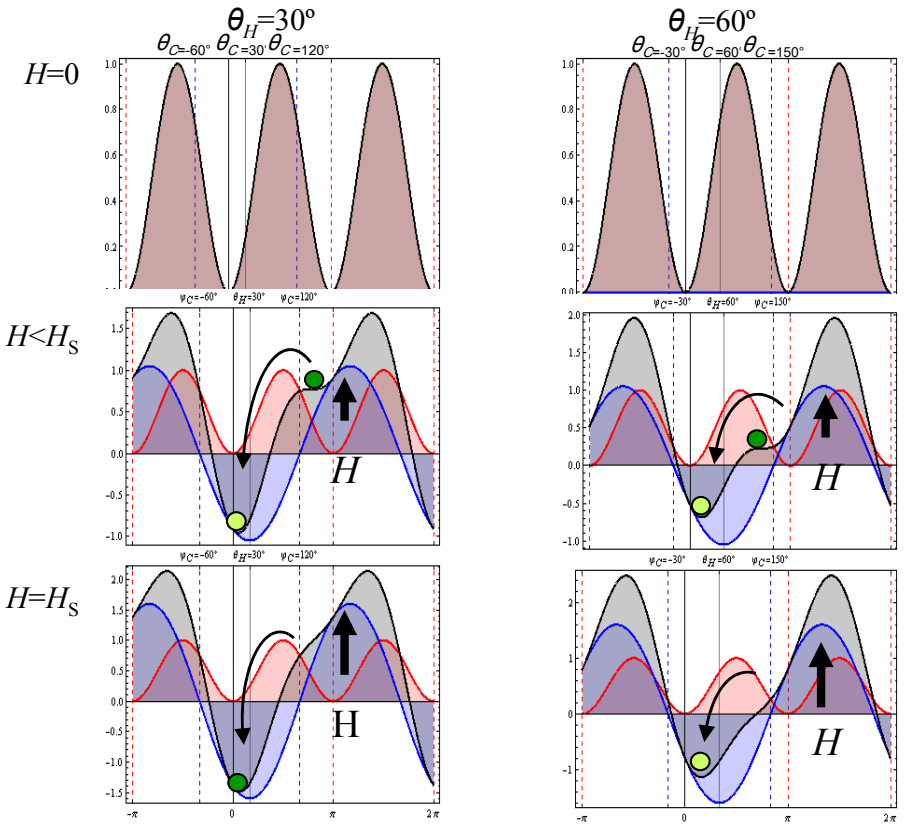

Figure 3.13: Energetic landscape of a uniaxial system with applied field to clarify the difference of H_C and H_S. For applied field angles below 45° ($\theta_H = 30°$) the local minimum, occupied by the magnetization, vanishes before crossing 90° with respect to the field direction. The 90° line is passed during the switching process such that $H_C = H_S$. For applied field angles above 45° ($\theta_H = 60°$) the local minimum vanishes after crossing 90° with respect to the field direction. The switching process takes place after crossing 90°, i.e. after a change of sign in $M_{\parallel}$, such that $H_C \neq H_S$.

at which the total energy shows a saddle point, the explicit solution is:

$$H_S = \frac{1}{(\cos^{2/3}\theta_H + \sin^{2/3}\theta_H)^{3/2}} \frac{2K}{\mu_0 M_S} \tag{3.5}$$

(c). Starting field theory

According to Givord switching always take place via nucleation and propagation of domain walls. This assumptions is in complete contrast to the coherent rotation model. To nucleate a domain the magnetization has to overcome an energy barrier, E_b. This energy barrier is due to defect sites as e.g. grain boundaries and usually much smaller than the anisotropy energy. The energy to overcame the barrier is due to the applied field i.e. Zeeman energy. At zero field the magnetization lies parallel to the e.a. direction similar to the SW-model. Increasing the field also increases the Zeeman energy, such that a volume V gains the energy

$$E(H) = -\mu_0 V \vec{M} \cdot \vec{H} \tag{3.6}$$

At the coercive field this energy equals E_b, i.e. the magnetization in the volume V has enough energy to overcome the energy barrier. Hence, in this volume the domain nucleates. The coercive field therefore fulfills

$$E_\mathrm{b} = -\mu_0 V M_\mathrm{S} H_\mathrm{C} \varphi(H_\mathrm{C}), \tag{3.7}$$

where $\varphi(H_\mathrm{C})$ is the angle between the applied field and magnetization. Equation 3.7 cannot be solved for H_C such that further assumption are required. As the energy barrier is supposed to be very small, nucleation take place at rather small fields. Hence, it can be assumed that the magnetization still is parallel to the e.a. direction. Therefore, φ is approximately the angle between applied field and e.a. direction, θ_H, and independent of H. With this assumptions it is possible to solve equation 3.7 for H_C, which then reads

$$H_\mathrm{C} = -\frac{E_\mathrm{b}}{\mu_0 V M_\mathrm{S} \cos\theta_H} = \frac{H_0}{\cos\theta_H}, \tag{3.8}$$

where H_0 is the coercive field at $\theta_H = 0$. Note, that H_C diverges when φ approaches 90° i.e. the h.a. This is a contradiction to the assumption of smalls field made above. Hence, the model fails near the h.a. The simple model by Givord was modified by Gao and Zhang [5]. Additionally to the nucleation process the authors also take into account the energy cost of the domain wall when increasing the domain after nucleation. As the domain wall completely surrounds the nucleus all magnetization direction are present, such that this energy is independent of the applied field angle, as a consequence $(\cos\theta_H)^{-1}$-law of Givord is modified by angle independent constant

summand. More detailed calculations [5] show that the coercive field follows

$$H_C \approx \left(0.61 + 0.39 \cdot \frac{1}{\cos\varphi}\right) H_0 \tag{3.9}$$

The extremely good agreement between this model and the measured data can be seen in figure 3.14.

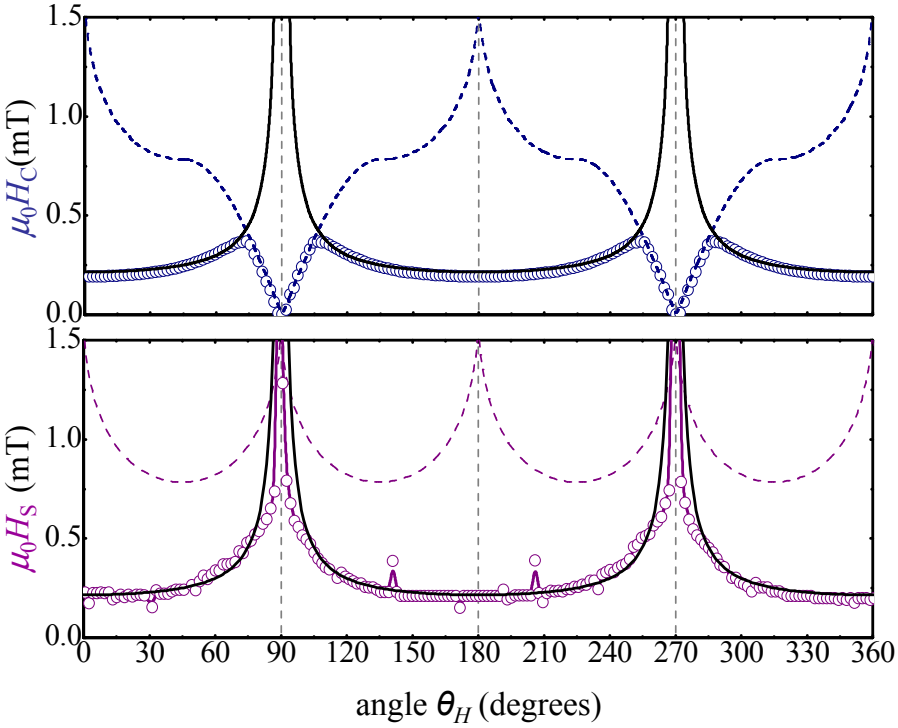

Figure 3.14: Angular evolution of the coercive and switching field, in the upper and lower panels, respectively, for a 6 nm permalloy film, display as symbols. Two theoretical models plotted, SW-model dashed line and starting field theory model in continuous line.

The coercive field follows the prediction by Gao and Zhang for large angular region around the e.a. Only near the h.a. where the prediction of H_C due to SW lies below this so-called starting field theory [5] H_C follows the coherent rotation model [1].

Due to the assumption that nucleation occurs when the magnetization is parallel

to the e.a. both models, the simple version of Givord as well as the modified version of Gao-Zhang have $H_C = H_S$ (see figure 3.14, in continuous line).

3.2. Biaxial Systems

Depending on the crystallographic structure, growth conditions, morphology, stresses, etc. systems can present different kinds of anisotropy. In case of iron with its bcc structure in bulk one observes a cubic anisotropy. In thin films with [100] orientation and with in-plane magnetization this simplifies to a in-plane fourfold anisotropy.

3.2.1. Sample preparation

To perform experiments on a system with four-fold anisotropy Fe films were grown in ultrahigh vacuum (UHV) with a base pressure of 3×10^{-8} Pa. The commercial substrate was first cleaned, in air, with acetone in ultra-sound during 10 minutes. After that it has been annealed at 450°C during 1 hour in UHV. During normal deposition via sputtering the system was held to room temperature.

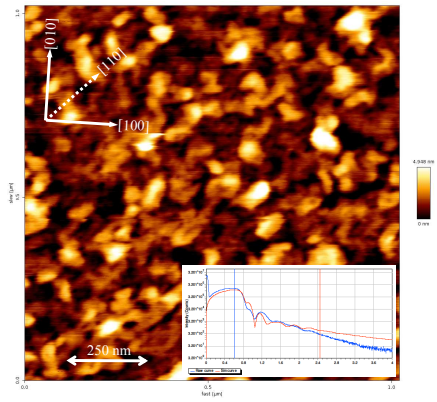

Figure 3.15: AFM image of a Fe/MgO(100) film with Al capping layer. The topographical image of 1×1 µm^2. Inset: XRD spectra gives the thickness of 20 nm Fe and 3 nm Al.

The Fe films have been grow according to the well-known Fe(100)[110]||MgO(100) epitaxial condition with a possible tetragonal distortion resulting from a relatively small lattice mismatch [6]. Finally, the sample has been capped by 3 nm of Al to prevent oxidation. The nominal thickness of 20 nm was measured in an ex-situ X-ray diffraction (XRD) system. [3] Additionally, atomic force

[3] The samples were grown and characterized by XRD in the group of Prof. Dr. K. Liu at University of California, Davis.

microscopy images have been recorded (see: figure 3.15).

The initial growth of Fe on MgO(100) occurs according the Volmer-Weber mechanism, due to the higher surface free energy of Fe(100) compared to MgO(100). With increasing Fe film thickness, the three-dimensional Fe island coalesce into a continuous layer [7]. For deposition at 360 °C, the Fe lattice parameter increases toward the MgO surface net spacing with increasing thickness in the 1–10 mono-layer coverage regime. It then relaxes back toward the bulk Fe lattice parameter at greater thicknesses. Consequently, thicker films will present a dislocation network.

3.2.2. Magnetic characterization

The iron thin films have been characterized magnetically utilizing the vectorial magneto-optic Kerr effect. In figure 3.16 characteristic hysteresis loops at $\theta_H = 0°, 45°$ and 90° are shown. symmetry the e.a. and h.a. are found every 45° (instead of

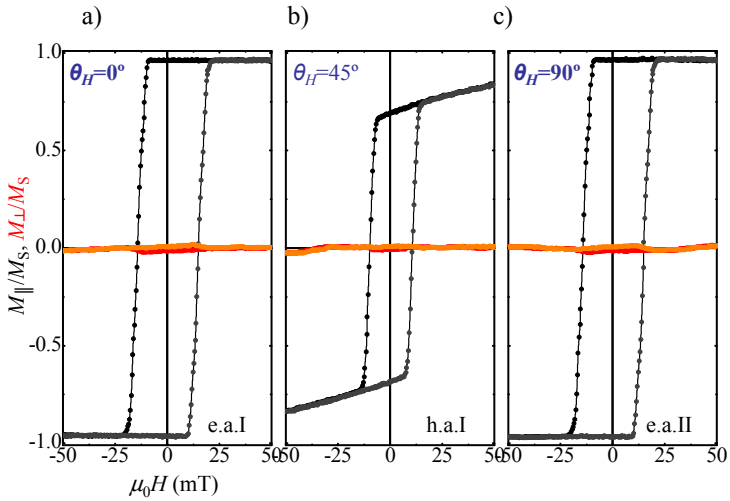

Figure 3.16: From the loops measured at the characteristics angles, $\theta_H = 0°$, e. a. I, $\theta = 45°$, h. a. I, $\theta_H = 90°$, e. a. II, and $\theta_H = 135°$, h. a. II, the fourfold symmetry of the BCC Fe system grown on MgO(100) becomes obvious. The SW-model (lines) only qualitatively fits the experimental data (symbols).

90° as for the twofold symmetry systems of section 3.1).

The easy axes, present the expected square loop at $M_\parallel$. In this system, however, the hard axes do not show fully reversible loops. This is due to the fact that there are

two equivalent minimums between two opposite h.a. directions, while there is only one in the uniaxial case.

Hence, the h.a. presents an open hysteresis with a remanence of $M_R = \cos 45° \approx 0.71$. As in zero field the magnetization is perfectly aligned with the e.a. directions, which show fourfold symmetry, the angular evolution of the remanence perfectly follows the prediction (Fig. 3.17), i.e. as a projection from the e.a. on the field direction. The parallel component shows a perfect 4-leaves clover (lower-left polar plot of Fig. 3.17), while the perpendicular component presents a 4-sail mill (lower-right polar plot of Fig. 3.17).

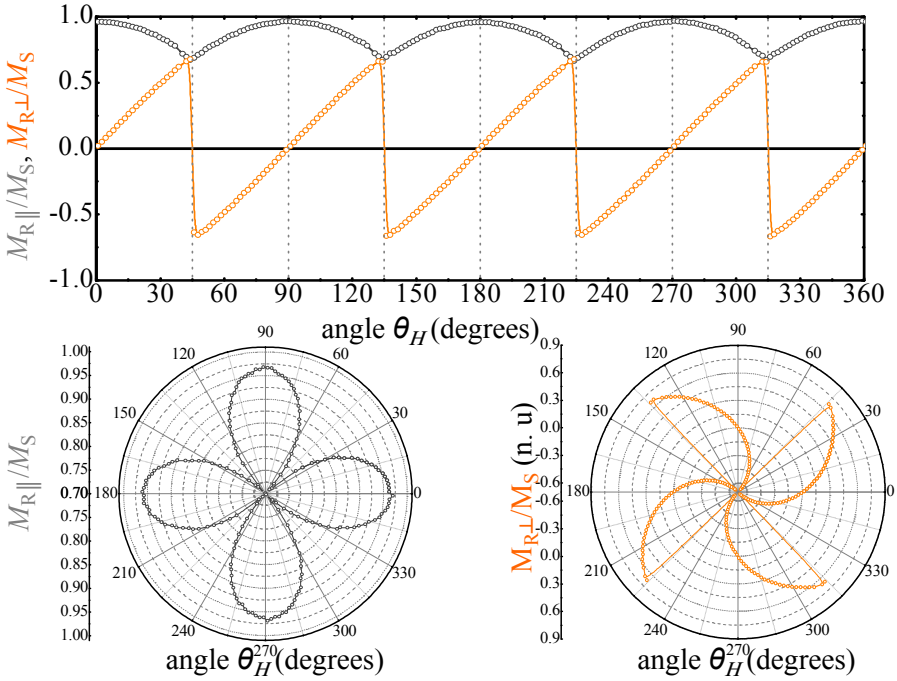

Figure 3.17: Angular evolution of the remanence of a 20 nm Fe film on MgO(100). The top panel shows $M_{R,\parallel}$ and $M_{R,\perp}$ (gray and orange, respectively) as a function of applied field angle while the lower panels show polar plots. The experimental data (symbols) is well described by the SW-model (continuous line).

(a). Magnetization Reversal processes

One must note that magnetization reversal processes take place not only with one jump, i.e. one sharp transition, but in a large angular range two jumps appear [8, 9]. For those angles where only one transition is found the magnetization switches by DW of 180°. The system exhibits DWs of 90° where two transitions occur. The presents of 90° DWs can be seen in Fig. 3.18. This figure shows representative hysteresis

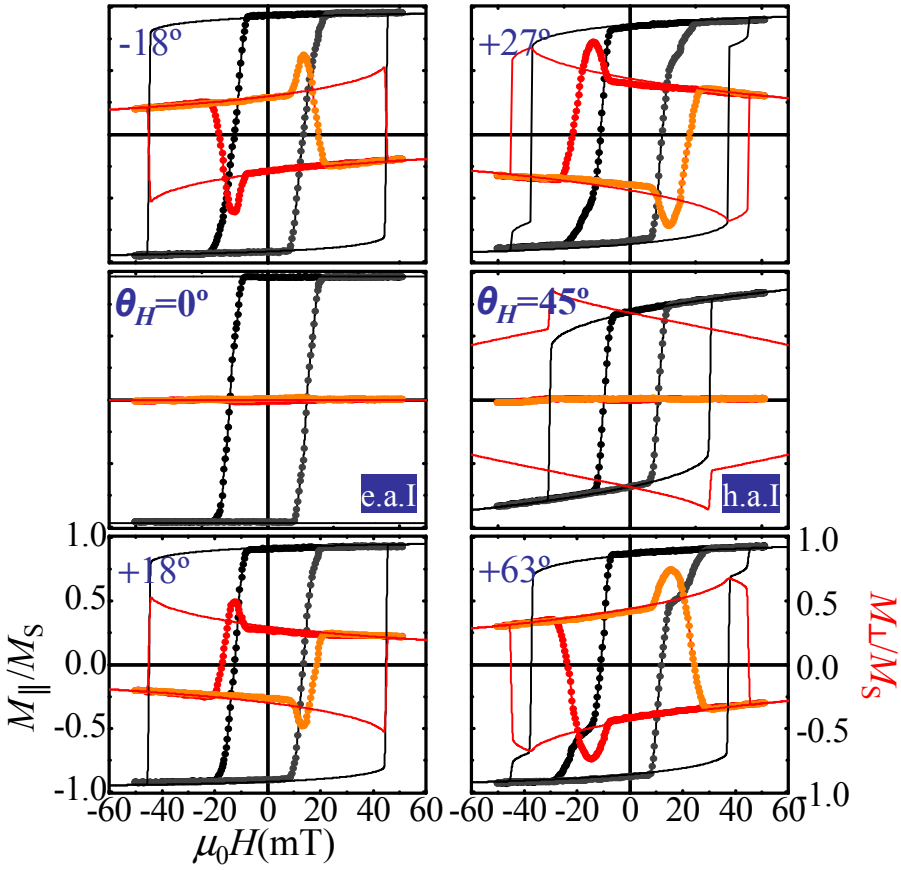

Figure 3.18: Hysteresis loops around the e.a. and h.a. The reversal processes via 2 transitions and the symmetry around the characteristic angles can be seen easily. While the SW-model (continuous lines) also predicts 2 transitions around the h.a. only 1 is found near the e.a., in contradiction to the experimental finding.

loops corresponding to $\pm 18^\circ$ angles around one of the e.a. and one of the h.a. As in a uniaxial systems (see section 3.1), both $M_{\parallel}$ and $M_{\perp}$ have the backward and forward branch point symmetric with respect to the origin. The hysteresis curves of $M_{\parallel}$ are qualitatively the same in the upper and lower panel. The loops for $M_{\perp}$, however, are mirrored with respect to the field easy axes. Two transitions are found in the angular region of $\pm 40^\circ$ around hard axes, while only one transition appears $\pm 5^\circ$ around easy axes.

The two kinds of transitions are also seen in Kerr-microscopy images in figure 3.19, corresponding to 90° DWs close to the h.a. and 180° DWs close to the e.a.

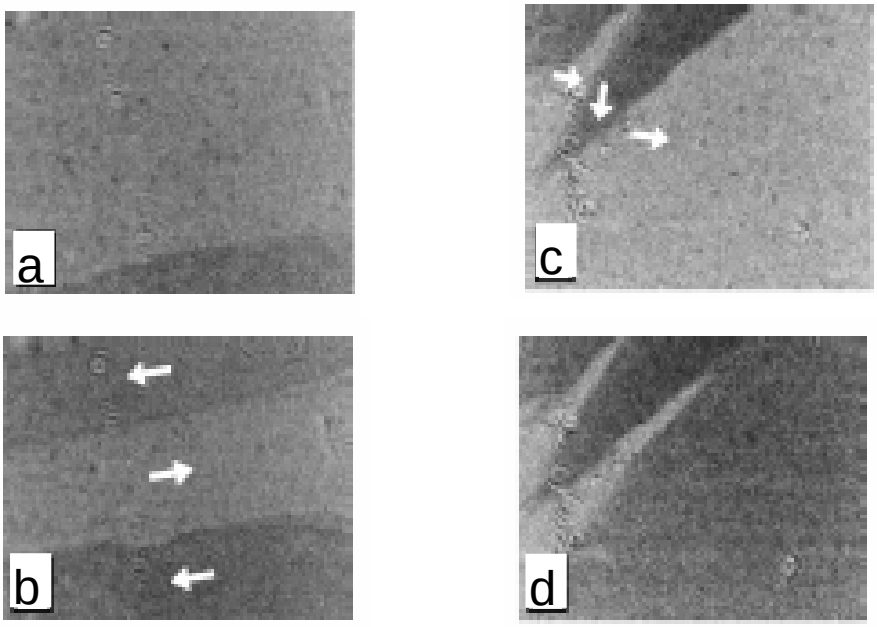

Figure 3.19: Left panel: experimental Moke images along easy axis at consecutiveness magnetic filed (a) 78 and b) 79 Oe. A large domain aligned field direction is present. A very small increase in field causes this domain to grow and cover the whole sample. In the right panel the filed is applied (a) 64 and b) 66 Oe)in an angle between easy and hard axis direction. The magnetization reversal takes place by means of 90° domain walls. (Images from [10])

Similar behavior is also predicted by the modified SW-model, where the twofold

anisotropy has been substituted by a fourfold one. The total energy in this case reads

$$E_{\text{tot}} = \frac{1}{4}K_2 \cos^2 2\theta_H - \mu_0 M_S H \cos(\varphi - \theta_H), \tag{3.10}$$

where K_2 is the fourfold anisotropy constant.

Within the SW-model a double transition appears if the local minimum of the magnetization vanishes while the second local minim of the fourfold anisotropy still exits [8]. The predicted angular range for this behavior is approximately $\pm 22.5^\circ$ around the hard axes, such that, the single transition is predicted $\pm 22.5^\circ$ around the easy axes. The angular range for the single transition is, however, much smaller in the experiment, see Fig. 3.20. The panels show the $M_\parallel$ and $M_\perp$ where one transition take place, shadow by light and dark gray for experimental and simulated data, respectively. This can be understood intuitively, when considering DW nucleation and propagation. Due to nucleation the magnetization leaves its local minim for smaller fields, such that the second minim is still present [8]. Hence, a new domain, rotated by 90° has been established. As this domain has a lower Zeeman energy, further increase of the external field is required to nucleate further 90° walls to switch into the final state. Measurements clearly show two transitions where the model predicts only one transitions. Only very close to the easy axes, the measurements present the single transition as predicted by the model. The angular range is, however, only $\pm 5^\circ$.

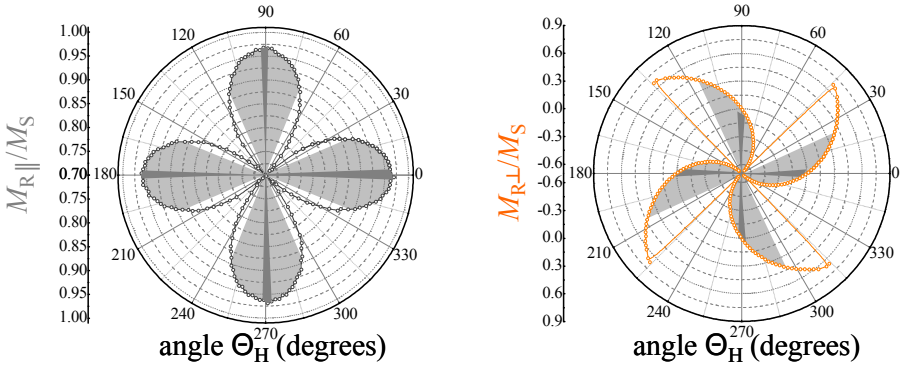

Figure 3.20: The panels show the $M_\parallel$ and $M_\perp$ where one transition take place, shadow by light and dark gray for experimental and simulated data, respectively.

Following the ideas of Cowburn et al. the angular and field dependence of the transitions can be understood in terms of nucleation and the propagation of DWs. The

important parameters are the depinning energies for 90° and 180° DWs, respectively. Assuming that the depinning takes place if the energy difference of the two domains overcomes the depinning energy the two critical fields are calculated as

$$H_{c1,c2} = \frac{\varepsilon_{90^\circ}}{\mu_0 M_S(\pm\cos\theta_H \pm \sin\theta_H)}, \tag{3.11}$$

where ε_{90° is the depinning energy of 90° DW. The important parameter for the single transition naturally is the depinning energy, ε_{180°, of the 180° DW. The angular and field dependence of the single transition again follows the $\cos^{-1}$ law, equivalent to the 180° DW of uniaxial system. According to Cowburn the single transition occurs whenever it predicts a lower coercive field. The simple model however, does not take

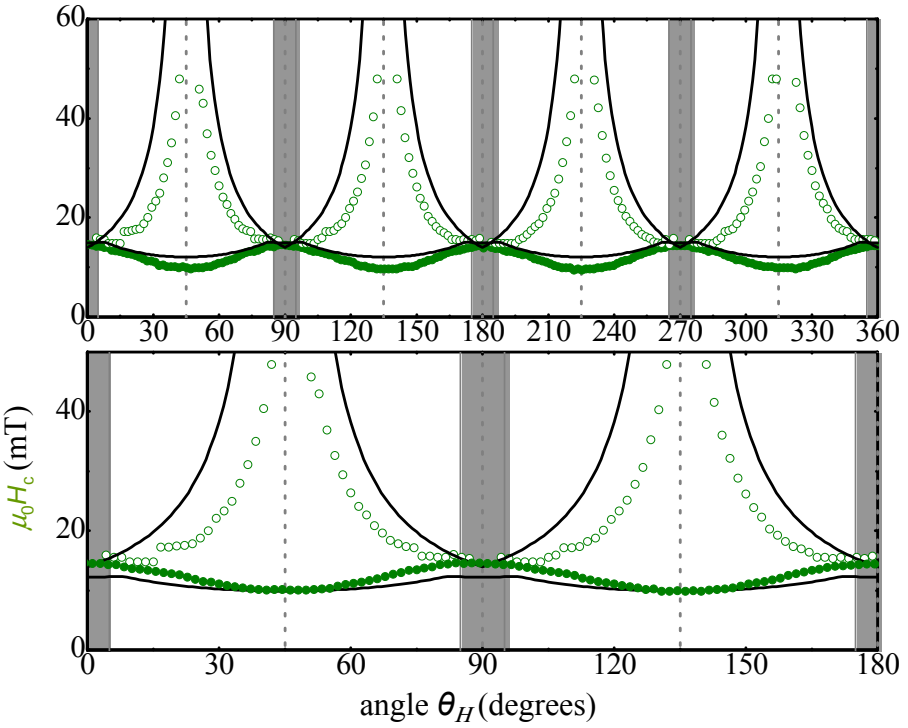

Figure 3.21: The experimentally determined critical fields (symbols), H_{C1} and H_{C2} of a 20 nm Fe/MgO(100) films, as a function of the angle of the applied magnetic field. The prediction of the modified pinning model [9] (continuous olive line) is plotted on top. The region where 1 transition is observed is shown in gray, while the white region present 2 transitions.

into account neither a nucleation barrier nor any rotation of the magnetization, due to the external applied field. Therefore, it probably underestimates the critical fields. The experimental data is compared to this model in Fig. 3.21.

Both critical fields—H_{C1} and H_{C2}—have been calculated from his model, taking into account 180° DW, for the regions where only one transition appears. This critical field follows the, already known, pinning law $(\cos\theta_H)^{-1}$. The 90° DW has been taking into account to reproduce the angular regions where two transitions are measured. The pinning model qualitatively reproduces the angular evolution of the critical fields in the full angular range.

In contrast the SW-model predicts peaks in the evolution of the critical fields that are not found in experiment. This model strongly overestimates the field in the whole angular range, as can be seen also from a detailed survey presented in Figs. A.3 and A.4.

3.3. Exchange-Bias systems

In the following chapter the previously discussed ideal systems of pure uniaxial anisotropy will be investigated with additional exchange-bias effect.

The spin arrangement at the interface in layered magnetic materials often is crucial for the understanding of their magnetic properties and has profound consequences for practical applications. Particularly important is the unidirectional coupling between the spins in an anti-ferromagnet (AFM) and those in an adjacent ferromagnet (FM), referred to as exchange-bias [11]. This effect is widely used to pin the magnetization of thin FM films in today's magnetic applications [12–16], such as magnetic recording, sensors, actuators, and spintronic devices. Future advances in fields such as ultrahigh-density recording and medical applications are also promoted by effectively increasing the magnetic stability of nanomagnets [17, 18]. A comprehensive description of the effect involves fundamental questions of surface and interface magnetism [19–23]. The most striking feature is the shift of the FM hysteresis loop along the magnetic field axes. Moreover, engineering fully adjustable magnetic hysteresis [24] as well as the use of nanostructures [25] or multifunctional materials [26] has been demonstrated recently in exchange coupled FM/AFM systems. In addition, there is a plethora of other magnetic phenomena associated to exchange coupled FM/AFM systems, such as coercivity enhancements [27, 28], magnetization reorientation [29, 30], modified antiferromagnetic spin structures [31–33], and asymmetric magnetization reversal [34, 35], which are still not fully understood [12–16]. These effects often manifest themselves very differently for various material combinations. Prospects for

controlling, tailoring, and enhancing of desirable effects depend on a clear understanding of the mechanisms governing exchange-bias.

3.3.1. The origin of exchange-bias

The combination of two different classes of magnetic materials, for instance FM and AFM materials result in a new effect known as exchange-bias (EB). This phenomenon was discovered in 1956 by Meiklejohn and Bean [11]. The exchange-bias effect, also known as unidirectional anisotropy was first studied in Co particles embedded in their anti-ferromagnetic oxide, CoO. The first observation was the clear displacement of the hysteresis curve from the origin of coordinates. In a first hypothesis it was concluded that the effect was due to the magnetic interaction across the common interface. Being recognized as an interface effect, which can also be verified easily from the measurements in Fig. 3.24, studies on EB have been performed mainly on thin films consisting of a FM layer in contact with an AFM one.

The basic underlying physics of exchange-bias was already described in the seminal work of Meiklejohn and Bean 50 years ago [11].

Exchange-bias can be understood phenomenologically by analyzing the microscopic magnetic state of the common interface, as is depicted in figure 3.22. The critical temperatures of the two different magnetic layers that are in close contact should satisfy the condition $T_C > T_N$, where T_C is the Curie temperature of the FM layer and T_N is the Néel temperature of the AFM layer.

At a temperature, which is higher than the Néel temperature of the AFM layer and lower than the Curie temperature of the FM ($T_N < T < T_C$), the FM spins align along the direction of an applied field (H), whereas the AFM spins are randomly oriented in a paramagnetic state, see Figure 3.22-i). In this high temperature situation the hysteresis curve of the ferromagnet is centered around zero, not being affected by the proximity of the AFM layer.

To obtain the EB effect the ferromagnet is saturated by applying a high enough external field H_{FC} and then, without changing the magnitude or direction of the applied field, the temperature is decreased to a finite value lower than T_N (field cooling procedure). Note, the order transition (diverging correlation length) of the AFM takes place under applied magnetic field. After field cooling the system, due to exchange interaction, the interface layer of the AFM will align parallel (antiparallel) to the FM spins. The rest of the AFM will establish antiferromagnetic order with respect to that layer (3.22-ii)). In a naive picture it is assumed that both the FM and the AFM are in a single domain state and that they will remain in this single domain state during the magnetization reversal process. When reversing the field, the FM spins will try to

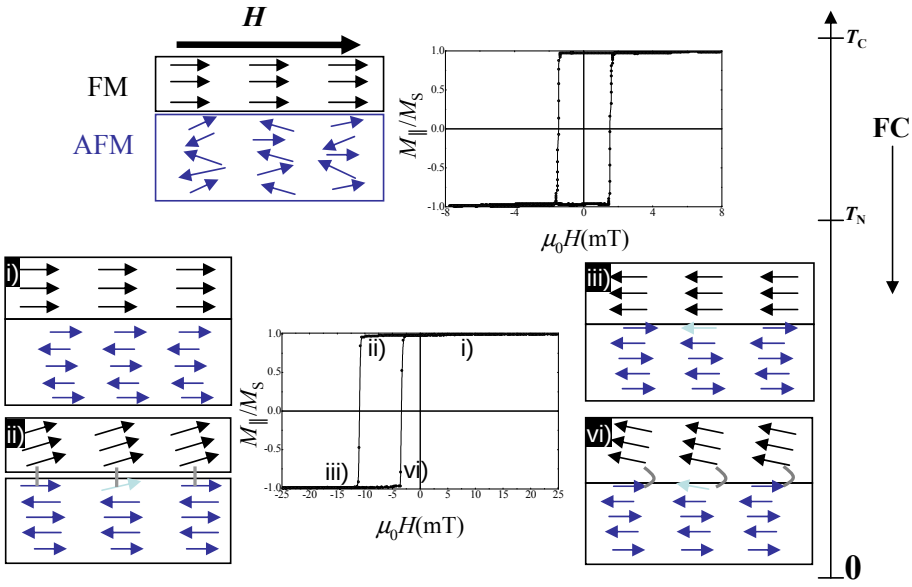

Figure 3.22: Scheme of a bilayer FM/AFM system at different temperatures and field. In a) the temperature is above the Néel but below the Curie temperature such that the AFM is disordered while the FM shows order. No exchange-bias is observed. Cooling the AFM to temperatures below the Néel temperature b) and in the presence of an applied field, the AFM becomes ordered and coupled to the FM. From now on applied fields only acts on the FM as the AFM has zero net magnetization. However, the field not only has to overcome forces due to the FM but also forces due the AFM, which is exchange coupled to the FM. This changes the magnetic signal, the hysteresis, from the FM layer compared to the uncoupled case.

rotate in-plane to the opposite direction. Being coupled to the AFM spins, this rotation takes a bigger force and therefore a stronger external field to overcome this coupling and to rotate the ferromagnetic spins. As a result, the first coercive field is higher than it used to be at $T > T_N$, where the interface interaction is not yet active (3.22-iii)). On the way back from negative saturation to positive field values, the ferromagnetic spins require a smaller external force in order to rotate back to the original direction. As a result, FM (AFM) interface coupling will shift the hysteresis loop in direction of negative (positives) field values. This displacement of the loop is called exchange-bias field (H_E). It should be noted that in this simple description the AFM spins are considered to be rigid and fixed to the field cooling direction during the entire reversal process. If, however, the AFM is not completely rigid the AFM spin can slightly rotate

during the magnetization reversal. The additional energy to rotate this spins results in an increase of the coercive field (3.22-iv)).

3.3.2. Properties of exchange-biased soft (FeNi) and hard (Co) magnetic thin films

Two material systems are studied, cobalt or permalloy in contact with antiferromagnetic iridium-manganese. The thickness of the ferromagnetic layer has been chosen as 12 nm while the antiferromanget has a thickness of only 5 nm. This choice ensures $T_C > T_N$.

(a). Sample preparation

A buffer layer of 5 nm Ta was employed to favor [111] texture. The Ta layer was deposited at oblique incidence to promote a uniaxial anisotropy in the FM layer that is grown on top. With this method the easy-axis of magnetization of the FM layers

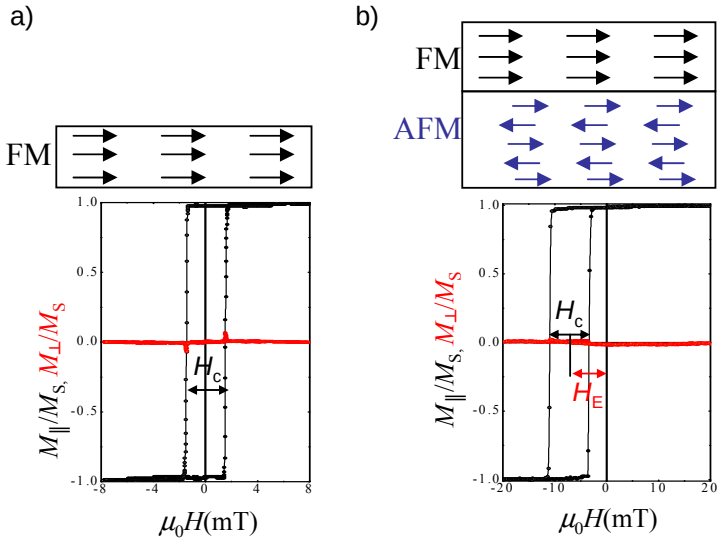

Figure 3.23: Two hysteresis loops from a 21 nm Co thin films are presented at $tH = 0°$. The panels show the different loops presented when the Co film is coupled to an AFM, in this case IrMn. Exchange-bias field is defined as the displacement of the loop from the origin.

is in the direction perpendicular to the incident plane of the sputtered Ta buffer layer.

Finally, the samples were capped by 2 nm of Ta to prevent oxidation.[4] In order to set the unidirectional anisotropy direction, the samples have been annealed at 420 K for 30 minutes and field cooled to RT in a 0.25 T external field. The field has been aligned in the direction of the FM anisotropy. Note that this procedure should, a priori, render samples with collinear uniaxial and unidirectional anisotropies, i.e., parallel K_U and K_E, as is shown in Fig. 3.23. Reference FM layers were sputtered at room temperature on thermally oxidized silicon substrates.

(b). Reference sample varying FM thickness

Two series of sample with varying the thickness have been grown. Thickness dependent properties of these series are presented in Fig. 3.24. The evolution of the exchange-bias field reveals the surface nature of this effect, while the uniaxial anisotropy evolves with the volume. The anisotropy energy density, K can be split into a volume term, K_V and surface term, K_S thus

$$K = K_V + K_S/t \quad \Longleftrightarrow \quad t \cdot K = t \cdot K_V + K_S \tag{3.12}$$

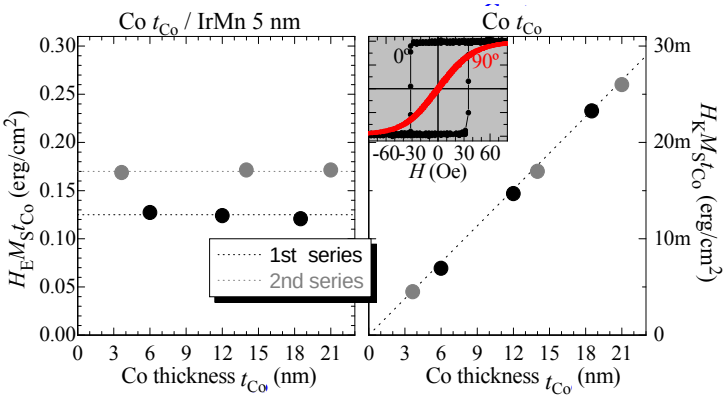

Figure 3.24: Thickness dependence of the exchange-bias (left) and anisotropy field (right) for two sample series (black and gray dots). The properties of the FM layer are well reproduced such that the data lies on the same line. The interface properties, however, differ between the two series, such that two different axis interceptions are found.

[4] The sample were grown by Dr. J. Sort in Grenoble.

Hence, plotting the product of thickness and anisotropy versus thickness reveals surface contributions as constant offset, whereas volume contributions result in a slope. Presenting the exchange bias field and the uniaxial anisotropy in this way in Fig. 3.24 shows for both series a constant value for $t \cdot H_{\mathrm{E}}$. The slope is, within the errors, zero. Consequently, the exchange-bias field can be attributed to the surface. On the other hand, the uniaxial anisotropy shows a clear linear behavior. Extrapolating the data to zero thickness gives a zero y-axis intercept. From this it can be concluded that the uniaxial anisotropy is a pure bulk effect and has negligible surface and interface contributions.

(c). Magnetic properties of FM layers

The magnetic characterization has been performed by high-resolution vectorial Kerr magnetometry, measuring simultaneous both components of the in-plane magnetization, $M_{\parallel}$ and $M_{\perp}$ (see Appendix A.1.3 for the full angular study).

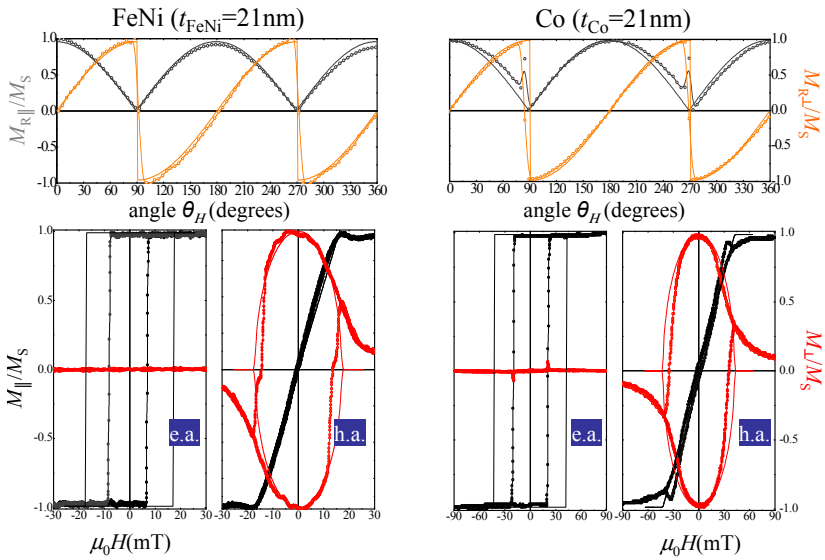

Figure 3.25: Magnetic properties of the Co and FeNi reference samples, i.e. the magnetic thin films without exchange-bias.

The characteristic hysteresis loops of the reference samples, i.e. without exchange-bias are shown in Fig. 3.25. For $\theta_H = 0^\circ$ the loops show easy axis behavior. The

hysteresis is square shaped with $M_{R,\parallel} = M_S$ and a sharp irreversible transition at the coercive field ($\mu_0 H_C(\text{FeNi}) = 7$ mT, $\mu_0 H_C(\text{Co}) = 0.3$ mT). The perpendicular component, $M_\perp(H)$, is zero during the reversal processes. At 90° the typical hard axis behavior is found, as discussed in the previous chapters. Note, that Co and FeNi films behave in the same way except that the critical fields are six times larger for Co. This indicates that the effective anisotropy for Co films is about one order of magnitude larger compared to FeNi films of similar thickness.

The large difference in FM anisotropy manifests itself in the hysteresis loops measured for the different FM/AFM bilayers. Fig. 3.27 shows representative magnetization loops measured along the field cooling direction, i.e. the easy-axis of magnetization, for hard Co/IrMn and soft FeNi/IrMn films. For $\theta_H = 0°$ (central rows), the magnetization reverses via a sharp irreversible transition, indicating that the reversal is mainly governed by nucleation and propagation of magnetic domains. For the Co/IrMn bilayer, $M_\perp = 0$ during the whole magnetization loop, which reflects that the magnetic domains are aligned parallel to the external field. On the contrary, a clear hysteresis is observed in $M_\perp$ for the FeNi/IrMn bilayer, indicating that the domains are not parallel to the easy axis of magnetization. This observation implies the presence of an additional non-collinear anisotropy and thus a reorientation of the effective FM anisotropy.

In case of $\theta_H \neq 0°$ both bilayers systems present magnetization reversal asymmetry. This means that the forward branch behaves differently compared to the backward branch. The asymmetry ζ is defined as the difference between the largest values of $M_\perp$ of the descending and ascending branches, i.e.

$$\zeta = \frac{M_\perp|^{\text{forward}}_{\text{max}} - M_\perp|^{\text{backward}}_{\text{max}}}{M_S} \tag{3.13}$$

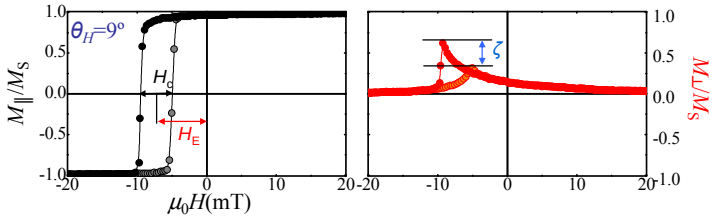

Figure 3.26: The addition of an unidirectional anisotropy introduce a symmetry breaking that can be detected easily in the transversal component. This asymmetry is defined as the different between of the absolute values of the transversal component, denoted by ς.

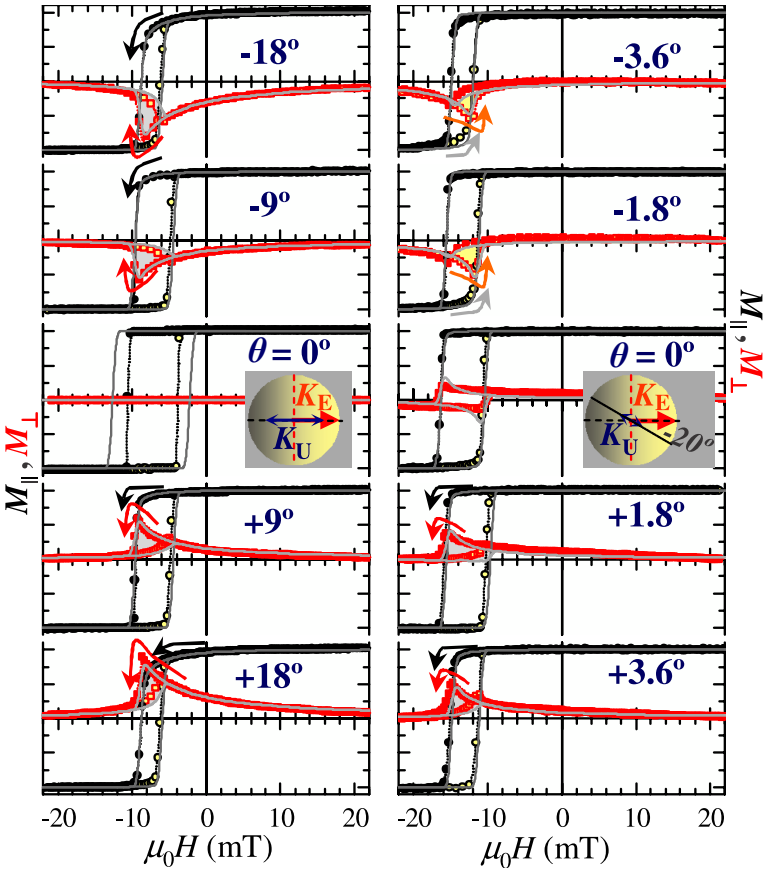

Figure 3.27: Hysteresis curves near the e.a. of exchange-biased Co/IrMg and FeNi/IrMg films (left and right, respectively). Both systems show almost square shaped loops. For presented angles with $\theta_H < 0°$ both branches of the transveral component are negative, for Co as well as for FeNi. Co shows the strongest transversal signal in the forward branch, while FeNi has the stronger signal in the backward branch. For positive θ_H the both transversal branches are negative, with the strongest Co signal still in the forward branch, while the strongest FeNi signal is in the backward branch. Moreover, for $\theta_H = 0°$ one would expect a vanishing transversal component, as it is also observed in pure uniaxial systems. However, the FeNi system shows an open hysteresis.

Namely, magnetization reversal via reversible rotation processes is more relevant in one branch of the hysteresis loop. This results in a larger $M_\perp$ values and rounded transitions in $M_\parallel$. However, the angular evolution of this asymmetry depends on the

FM material. In the (hard) Co case, the maximum $M_\perp$ is always found in the descending branch, i.e. when the field sweeps against the bias direction. This finding is independent of the field orientation angle (left panels of Fig. 3.27).

Remarkably, for the (soft) FeNi case the maximum $M_\perp$ value can be found in either descending or ascending branches of the hysteresis loop, depending on the sign of the applied magnetic field angle with respect to the easy axis.

For positive angles ($\theta_H > 0^\circ$, bottom right panels), it is found in the descending branch, i.e. when the field sweeps against the exchange bias direction. On the contrary, for negative angles ($\theta_H < 0^\circ$, top right panels) the maximum value is observed in the ascending branch, i.e. when the field sweeps along the bias direction.

(d). Angular dependence of coercive and bias field

The angular dependence of the exchange bias $H_\mathrm{E}(\theta_H)$, coercivity $H_\mathrm{C}(\theta_H)$, and asymmetry $\zeta(\theta_H)$ is shown in Fig. 3.28.

For Co/IrMn as well for FeNi/IrMn non-zero asymmetry is observed in the whole angular range of irreversible processes, i.e. $\pm\theta_\mathrm{C}$ around the e.a. of the ferromagnet. It is remarkable that the largest exchange-bias field is found at θ_C, if the easy axis of the FM is collinear with the FM direction. The critical angle θ_C increases as the anisotropy ratio $K_\mathrm{U}/K_\mathrm{E}$ increases.

Further investigation of Fig. 3.28 reveals that Co/IrMn and FeNi/IrMn do not behave the same way. ζ changes its sign around the easy axis for the Co/IrMn bilayer, it is always positive for the FeNi/IrMn bilayer. Additionally, the angular evolution of the exchange-bias is not symmetric around the e.a. for the FeNi/IrMn films.

The connection between θ_C, H_E and ratio of the anisotropies can be understood easily if the geometrical asteroid solution of the coherent rotation model is used (see Fig. 3.29 [34]). In the case of FeNi/IrMn, the intrinsic uniaxial magnetic anisotropy is small compared to the unidirectional anisotropy, thus, corresponds to smaller astroid, thus giving a smaller angle θ_C.

A unidirectional anisotropy displaces the asteroid critical curve from the origin. Therefore, if the applied field is not parallel to K_E, the field sweep line does not pass through the symmetry center of the critical curve. This results in inequivalent switching fields and consequently asymmetric ascending and descending branches of $M_\parallel$ and $M_\perp$. Irreversible transitions, i.e., hysteresis, are expected only when the magnetic sweep line passes through the asteroid (filled circles in Fig. 3.29). For larger angles, i.e., $\theta > \theta_\mathrm{C}$, the magnetization reversal becomes completely reversible, the field line lies outside the asteroid, and the asymmetry between the two reversals vanishes.

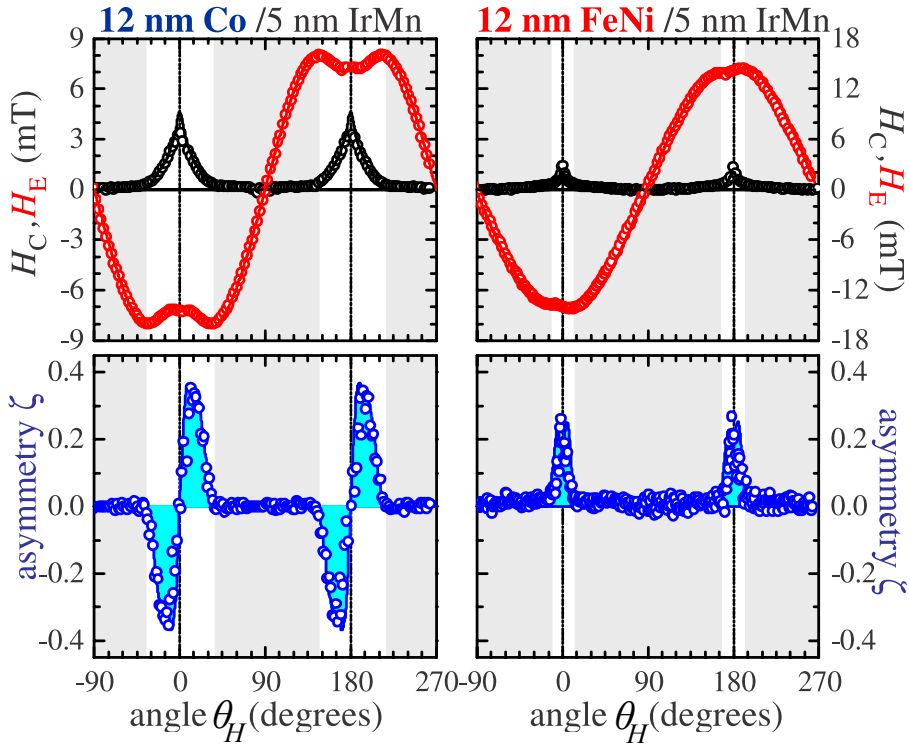

Figure 3.28: Angular evolution of coercivity, exchange-bias and asymmetry of exchange-coupled bilayers with different intrinsic FM anisotropy. Experimental values (symbols) derived from Kerr measurements such as those shown in Fig. 3.27, and fit curves (lines) obtained using the SW model including unidirectional K_E and uniaxial K_U anisotropy constants are shown. Collinear and non- collinear ($\theta_H = 20°$) anisotropies have been used for the Co/IrMn and FeNi/IrMn bilayers, respectively. The shadowed areas indicate the range of angles where only reversible processes take place during the reversal. Note that the occurrence of asymmetry is linked with the appearance of irreversibility, i.e. coercivity, and the maximum of the exchange bias. Moreover, the non-symmetric behavior of the reversal asymmetry found for the FeNi case is reflected by the angular dependence with only positive values.

Calculations based on a coherent rotation SW-model including K_U and K_E reproduce the experimental findings, as shown in Fig. 3.27 and Fig. 3.28.

The parameters K_U and K_E were determined from the experimental data of the reference FM films and the FM/AFM bilayers, respectively. The behavior observed

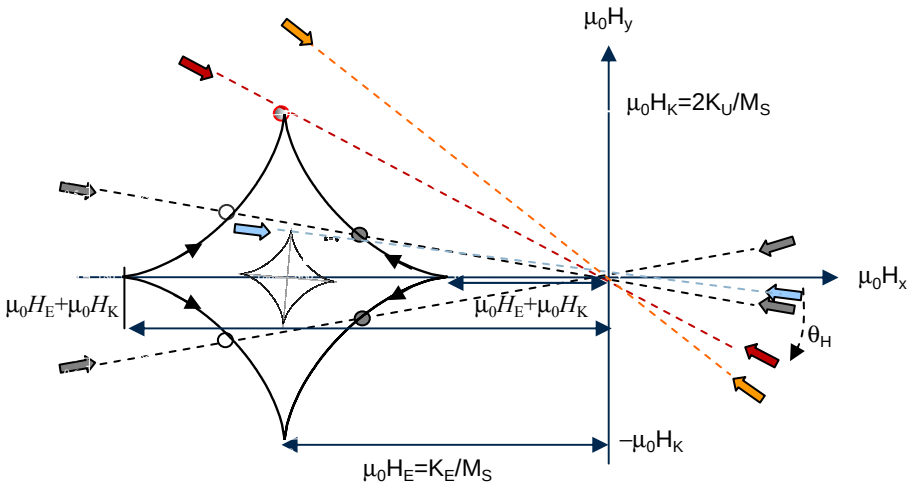

Figure 3.29: The astroid of a uniaxial system (compare to Fig. 3.7) with exchange bias. The astroid increases with increasing uniaxial anisotropy K_U, such that the angle θ_C also increases () SW-solution of switching field in an exchange bias system. The ordinate axis correspond to the anisotropy field whereas the shift in the abscissa axis correspond to the exchange-bias field. The θ_C increases as the anisotropy ratio K_U/K_E increases

for Co/IrMn is well reproduced by considering collinear anisotropies. Surprisingly, for the FeNi/IrMn bilayers, although the field cooling was performed with the external field oriented parallel to the easy axis of the original FeNi uniaxial anisotropy, non-collinear anisotropies [36–38] with a significant misalignment ($\beta = -20°$) have to be considered to reproduce the hysteresis loops.

These results explain the wide variety of conflicting experimental results for different FM/AFM materials combinations. Asymmetries in the magnetization reversal have been observed for many FM/AFM systems with both in-plane [34–48] and perpendicular [15, 49] anisotropy for the FM layer. In general, one branch shows more rotational processes than the other. In this branch also a larger density of domains is observed during the irreversible domain nucleation processes [15, 41, 42, 48, 49]. For some systems, rounded transitions in $M_{\parallel}$ and larger $M_{\perp}$ values are found in the descending branch [34, 35, 39–41, 47–49], where the field is applied parallel to the exchange bias direction, while other systems display the opposite behavior [35–38, 42–46, 48]. The results presented here indicate that this discrepancy is related to the difference between a collinear and a non-collinear anisotropy case.

A general explanation is depicted schematically in Fig. 3.30 on the basis of the ratio of magnetic anisotropies of FM and AFM materials and a new, non-collinear anisotropy contribution, which originates from the frustrated interactions at FM/AFM interfaces. Moreover, the nature of the anisotropy can be unambiguously deduced from the angular dependence of the hysteresis loops.

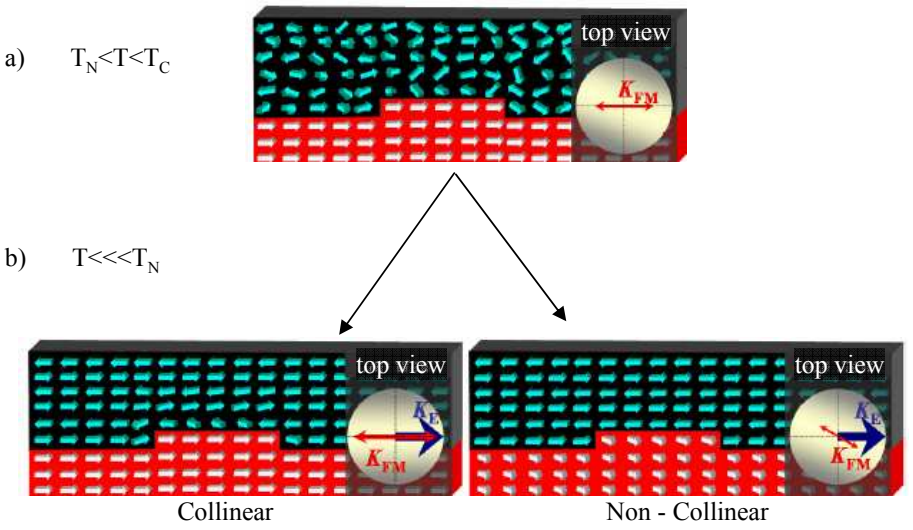

Figure 3.30: Asymmetries in the magnetization reversal in FM/AFM systems can be explain with the schematic idea of collinear and non-collinear anisotropies cases. The origin of relative orientation is found in the relationship between the anisotropies

In order to reach a better understanding of the surprisingly large misalignment of the anisotropy, we performed numerical simulations based on a three-dimensional cubic lattice of Heisenberg spins to investigate the spin configuration of the system. A randomly generated roughness was introduced at the FM/AFM interface to induce a magnetic frustration. Fig. 3.31 shows cross-section views of the magnetic configurations of the system in zero field for different anisotropy values. For $K_{FM} > K_{AFM}$, a partial spin realignment of the AFM layer at the interface is found (see Fig. 3.31, bottom), consistent with Refs. [45–48].

In the limit of an isotropic FM layer, i.e. $K_{FM} = 0$, the simulation results in an average perpendicular alignment between the FM magnetization and the spin lattice of the AFM layer (3.31, top). This scenario was observed experimentally for Fe/FeF_2 [50] and FeNi/NiO [31]. For both conditions, the existence of magnetic frustration at

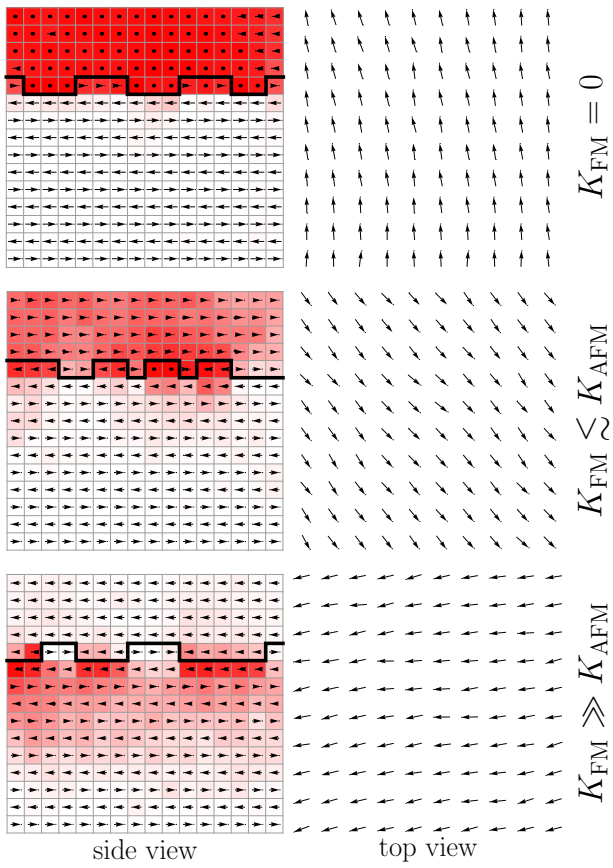

Figure 3.31: Cross-section views (left) from a 3D simulated spin configuration of FM/AFM bilayers with randomly generated interface roughness. The anisotropy of the ferromagnet increases from top to bottom. The right panels show the spin configuration of the topmost layer of the ferromagnet, i.e. a top view of the system. Note, due to frustration the ferromagnet with zero anisotropy turns 90° (red) to the AFM spin direction. With increasing anisotropy it turns into the easy axis direction (white), while the interface layers of the AFM turn out of the preferred direction. The anisotropy-angle relationship strongly depends on the surface roughness.

the FM/AFM interface implies that the system cannot satisfy all its magnetic bounds simultaneously, which can promote a spin reorientation either in the FM or AFM layer, depending on their anisotropy values. In the same way, for moderate K_{FM} different partial spin reorientations of the FM layer are obtained depending on the $K_{\mathrm{FM}}/K_{\mathrm{AFM}}$

ratio, as shown in the center graphs of Fig. 3.31, center). Although the model does not take into account all of the details of real samples, such as the frustration inside the AFM layer (grain boundaries) and chemical intermixing at the interfaces, the results agree qualitatively well. The magnetic frustration, intrinsic to any real sample, and the small K_U and K_E result in a reorientation of the FM anisotropy direction, as observed experimentally. In agreement with the experimental results, no such reorientation affects should take place for large K_U, as indicated by the Co/IrMg system.

References

[1] E. C. Stoner and E. P. Wolfarth, Phil. Trans. Roy. Soc. **A240**, 599 (1948).

[2] D. Givord, T. Tenaud, and T. Viadieu, J. Magn. Magn. Mater. **72**, 247 (1988).

[3] H. Kronmüller, K.-D. Durst, and G. Martinek, J. Magn. Magn. Mater. **69**, 149 (1987).

[4] J. C. Slonczewski, IEEE Trans. Mag. **45** (2009).

[5] R.-W. Gao and D.-H. Zhang, J. Appl. Phys. **35**, 4628 (1996).

[6] Toshio Urano and Toru Kanaji, J. Phys. Soc. Jpn. **57**, 3403 (1988).

[7] B. M. Lairson, A. P. Payne, S. Brennan, N. M. Rensing, B. J. Daniels, and B. M. Clemens, J. Appl. Phys. **78**, 4449 (1995).

[8] Q. Zhan, S. Vandezande, K. Temst, and C. Van Haesendonck, Phys. Rev. B **80**, 094416 (2009).

[9] R. P. Cowburn, S. J. Gray, J. Ferré, J. A. C. Bland, and J. Miltat, J. Appl. Phys. **78**, 7210 (1995).

[10] J. L. Costa-Krämer, D. M. Borsa, J. M. García-Martín, M. S. Martín-González, D. O. Boerma, and F. Briones, Phys. Rev. B **69**, 144402 (2004).

[11] W. H. Meiklejohn and C. P. Bean, Phys. Rev. **102**, 1413 (1956).

[12] J. Nogués and I. K. Schuller, J. Magn. Magn. Mater. **192**, 203 (1999).

[13] A. E. Berkowitz and K. Takano, J. Magn. Magn. Mater. (1999).

[14] M. Kiwi, J. Magn. Magn. Mater. **234**, 584 (2001).

[15] F. Romanens, S. Pizzini, F. Yokaichiya, M. Bonfim, Y. Pennec, J. Camarero, J. Vogel, J. Sort, F. Garcia, B. Rodmacq, et al., Phys. Rev. B **72**, 134410 (2005).

[16] F. Radu and H. Zabel, *Exchange Bias Effect of Ferro-/Antiferromagnetic Heterostructures* (Springer, Berlin, 2007).

[17] V. Skumryev, S. Stoyanov, Y. Zhang, G. Hadjipanayis, D. Givord, and J. Nogués, Nature **423**, 850 (2003).

[18] J. Eisenmenger and I. K. Schuller, Nature Materials **2**, 437 (2003).

[19] F. Nolting, A. Scholl, J. Stöhr, J. W. Seo, J. Fompeyrine, H. Siegwart, J. P. Locquet, S. Anders, J. Lüning, E. E. Fullerton, et al., Nature **405**, 767 (2000).

[20] H. Ohldag, A. Scholl, F. Nolting, E. Arenholz, S. Maat, A. T. Young, M. Carey, and J. Stöhr, Phys. Rev. Lett. **91**, 017203 (2003).

[21] H. Ohldag, A. Scholl, F. Nolting, S. Anders, F. U. Hillebrecht, and J. Stöhr, Phys. Rev. Lett. **86**, 2878 (2001).

[22] W. Kuch, L. I. Chelaru, F. Offi, J. Wang, M. Kotsugi, and J. Kirschner, Nature Materials **5**, 128 (2006).

[23] M. Bode, E. Y. Vedmedenko, K. von Bergmann, A. Kubetzka, P. Ferriani, S. Heinze, and R. Wiesendanger, Nature Materials **5**, 477 (2006).

[24] S. Brück, J. Sort, V. Baltz, S. Suriñach, J. S. Muñoz, B. Dieny, M. D. Baró, and J. Nogués, Adv. Mater. **17**, 2978 (2005).

[25] J. Nogués, J. Sort, V. Langlais, V. Skumryev, S. Suriñach, J. S. Muñoz, and M. D. Baró, Phys. Rep. **422**, 65 (2005).

[26] H. Béa, M. Bibes, F. Ott, B. Dupé, X.-H. Zhu, S. Petit, S. Fusil, C. Deranlot, K. Bouzehouane, and A. Barthélémy, Phy. Rev. Lett. **100**, 017204 (2008).

[27] C. Leighton, J. Nogués, B. J. Jonsson-Akerman, and I. K. Schuller, Phys. Rev. Lett. **84**, 3466 (2000).

[28] J. Camarero, Y. Pennec, J. Vogel, S. Pizzini, M. Cartier, F. Fettar, F. Ernult, A. Tagliaferri, N. B. Brookes, and B. Dieny, Phy. Rev. B **67**, 020413 (2003).

[29] W. Kuch, F. Offi, L. I. Chelaru, M. Kotsugi, K. Fukumoto, and J. Kirschner, Phys. Rev. B **65**, 140408 (2002).

[30] W. A. A. Macedo, B. Sahoo, V. Kuncser, J. Eisenmenger, I. Felner, J. Nogués, K. Liu, W. Keune, and S. I. K., Phys. Rev. B **70**, 224414 (2004).

[31] J. Camarero, Y. Pennec, J. Vogel, M. Bonfim, S. Pizzini, F. Ernult, F. Fettar, F. Garcia, F. Lançon, L. Billard, et al., Phys. Rev. Lett. **91**, 027201 (2003).

[32] M. Finazzi, A. Brambilla, P. Biagioni, J. Graf, G.-H. Gweon, A. Scholl, A. Lanzara, and L. Duo, Phys. Rev. Lett. **97**, 097202 (2006).

[33] A. Hoffmann, Phys. Rev. Lett. **93**, 097203 (2004).

[34] J. Camarero, J. Sort, A. Hoffmann, J. M. García-Martín, B. Dieny, R. Miranda, and J. Nogués, Phys. Rev. Lett. **95**, 057204 (2005).

[35] A. Tillmanns, S. Oertker, B. Beschoten, G. Güntherodt, J. Eisenmenger, and I. K. Schuller, Phys. Rev. B **78**, 012401 (2008).

[36] H. Xi and R. M. White, J. Appl. Phys. **86**, 5169 (1999).

[37] F. Radu, A. Westphalen, K. Theis-Bröhl, and H. Zabel, J. Phys.: Condens. Matter **18**, L29 (2006).

[38] M. J. M. Pires, R. B. de Oliveira Jr., M. D. Martins, J. D. Ardisson, and W. A. A. Macedo, J. Phys. Chem. Solids **68**, 2398 (2007).

[39] J. McCord, C. Hamann, R. Schäfer, L. Schultz, and R. Mattheis, Phys. Rev. B **78**, 094419 (2008).

[40] V. I. Nikitenko, V. S. Gornakov, A. J. Shapiro, R. D. Shull, K. Liu, S. M. Zhou, and C. L. Chien, Phys. Rev. Lett. **84**, 765 (2000).

[41] M. R. Fitzsimmons, P. Yashar, C. Leighton, I. K. Schuller, J. Nogués, C. F. Majkrzak, and J. A. Dura, Phys. Rev. Lett. **84**, 3986 (2000).

[42] A. Kirilyuk, T. Rasing, H. Jaffres, D. Lacour, and F. Nguyen Van Dau, J. Appl. Phys. **91**, 7745 (2002).

[43] J. McCord, R. Schafer, R. Mattheis, and K. U. Barholz, J. Appl. Phys. **93**, 5491 (2003).

[44] P. Blomqvist, K. M. Krishnan, and H. Ohldag, Phys. Rev. Lett. **94**, 107203 (2005).

[45] Z. P. Li, O. Petracic, R. Morales, J. Olamit, X. Batlle, K. Liu, and I. V. Schuller, Phys. Rev. Lett. **96**, 217205 (2006).

[46] J. Olamit and K. Liu, J. Appl. Phys. **101**, 2694378 (2007).

[47] S. Brems, K. Temst, and C. Van Haesendonck, Phys. Rev. Lett. **99**, 067201 (2007).

[48] T. R. Gao, D. Z. Yang, and S. M. Zhou, Phys. Rev. Lett. **99**, 057201 (2007).

[49] J. Camarero, J. Miguel, J. Goedkoop, J. Vogel, F. Garcia, F. Romanens, S. Pizzini, N. B. Brookes, J. Sort, and B. Dieny, Appl. Phys. Lett. **89**, 232507 (2006).

[50] T. J. Moran, J. Nogués, D. Lederman, and I. K. Schuller, Appl. Phys. Lett. **72**, 120823 (1997).

Chapter 4

Tailoring Magnetic Properties by breaking symmetry

What I cannot create, I do not understand.

Richard P. Feynman

Prospects for controlling and designing desirable magnetic behavior of thin films and bilayers systems depend on a clear understanding of the key parameters (anisotropies) that govern the magnetization reversal processes.

The properties of magnetic systems can be tuned up to a certain point by properly inducing an extrinsic anisotropy or controlling the relative orientation and strength of anisotropies with different symmetry. The anisotropies are studied by means of vectorial-MOKE. The study of the angular evolution of the critical fields sheds light onto the relative strength of the contributing anisotropies.

By means of a FC procedure it is possible to tailor the magnetic properties of exchange-bias bilayers. This allows precise control of system properties additional to other parameters as e.g. intrinsic interfacial frustration [1].

The findings reveal the importance of the anisotropy configuration in order to properly account for the effects on reversal processes.

Up to now systems with single symmetry have been investigated. These were onefold, twofold and fourfold, i.e. exchange bias,[1] uniaxial and biaxial anisotropy, respec-

[1] Note, exchange bias is an ferromagnet-antiferromagnet interface effect, such that it requires the pres-

tively. As the anisotropy has direct influence on the magnetization reversal processes, one needs to control these three basic ingredients as the key to tailor desired material properties.

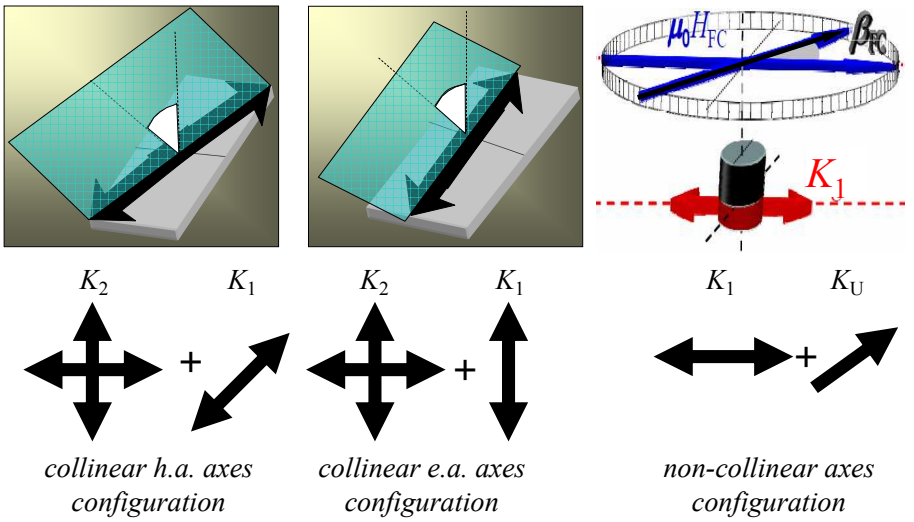

Figure 4.1: The presence of extra anisotropies can be induced by coincidence or on purpose. The anisotropies investigated in this chapter have been induced by angle of growing deposition a) and field cooling procedures b), tunning the relative strength and orientation between the them.

In the following chapter it is first shown how to combine uni- and biaxial anisotropies. This includes controlling not only the relative strength[2] but also the relative orientation of these two ingredients.

As is shown in the Fig. 4.1 the relative orientation between uniaxial and biaxial anisotropies is control by polar angle of deposition. This procedure allows to obtain either the so call *collinear e.a. configuration*, where both e.a. from the uni- and biaxial anisotropies are oriented parallel, or *collinear h.a. configuration*, where both h.a. from the uni- and biaxial anisotropies are oriented parallel.

Furthermore, it is shown that it is also possible to control the exchange-bias direction by using the field cooling procedure, therefore, introducing different behavior

ence of two systems, i.e. the ferro- and the antiferromagnet. It is, therefore, somewhat different to the pure single layer anisotropy systems.

[2]The relative strength of uni- and biaxial anisotropy is always referring to equation 4.1 unless mentioned otherwise

in forward and backward branch of the hysteresis loops (third panel of Fig.4.1, *non-collinear axes configuration*)

4.1. Uniaxial-Biaxial systems with collinear hard axes

As has been shown in chapter 3 uniaxial and biaxial anisotropy systems have different magnetization reversal processes and show different behavior for different angular ranges of applied fields; for instance there are angles for which biaxial systems show two transitions while uniaxial systems always show only one. Hence, the properties of the magnetic system can be tuned up to certain point by properly combining uni- and biaxial anisotropies. One way of doing so would be by choosing the relative angles, between the two anisotropy direction. However, in many cases this angle is given by material properties and cannot be chosen freely. A second option is to control the relative strength of the anisotropy energies, e.g. by choosing a proper step density for vicinal surface substrates [2]. In the following the system γ'Fe_4N/Cu(100) is investigated.

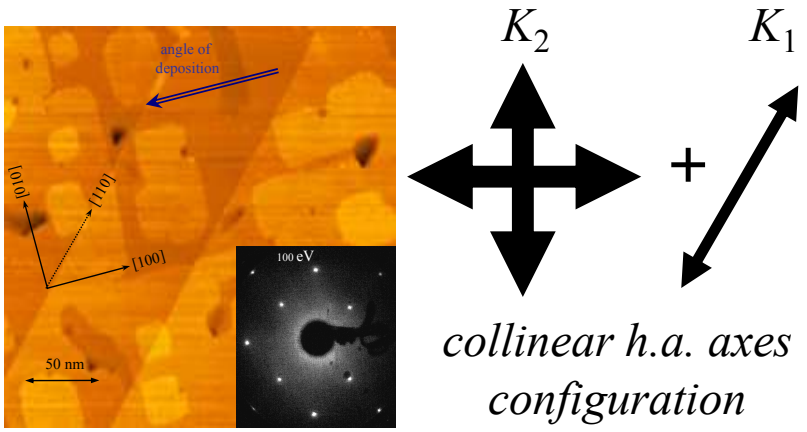

Figure 4.2: STM image of 20 ML thick iron nitride film grown on Cu(100). The angle of deposition and the crystallographic direction are indicated. The inset shows the corresponding LEED pattern. In the left schematic representation of the relative orientation between the involve anisotropies

The iron nitride films were grown in an ultra-high vacuum (UHV) chamber with a base pressure in the range of 10^8 Pa, equipped with a home-made scanning tunneling microscope (STM) and a rear-view low-energy electron diffraction (LEED)

optics. The main chamber was connected to an independently pumped, home-built radio-frequency (RF) plasma discharge source. The Cu(100) substrate was cleaned by cycles of sputtering and annealing at 900 K. In order to grow Fe_4N films, during the deposition of Fe, the sample was simultaneously exposed to a flux of atomic N (actually a mixture of N and H) generated by the RF source. The Fe and N atom flux sources were oriented at -45° and $+45^\circ$ with respect to the surface normal, respectively. After cooling the sample to 300 K, the films were characterized in situ by STM and LEED (see Fig. 4.2). The Fe deposition rate was calibrated without N flux. The calibration was done by means of STM for submonolayer coverage. For the ex situ measurements, the films were capped with a 3 nm thick Cu film to avoid oxidation.

Magnetic characterization

Representative Kerr hysteresis loops for γ'Fe_4N/Cu(100) thin films recorded at selected angles θ_H between the magnetic field and the crystallographic axes are shown in figure 4.3, in particular, around the easy and hard axes of magnetization. $\theta_H = 0^\circ$ is taken when the external field is aligned parallel to the [110] in-plane crystallographic direction. Both easy and hard axes are located precisely by looking for the change of sign of the $M_\perp$ loops when these characteristic directions are crossed. The 2 left-middle graphs of figure 4.3 show two easy axes slightly displaced with respect to the $\langle 100 \rangle$ crystallographic directions (-40.5° (e.a. I) and $+40.5^\circ$ (e.a. II)) [3].

The easy axes are thus not orthogonal to each other, as was found in epitaxial magnetic semiconductors compounds with broken symmetry,[4, 5] but they form an angle $\alpha = 81^\circ$. On the contrary, the hard axes are mutually orthogonal (see 2 right-central graph of Fig. 4.3b)) at 0° (h.a. I) and 90° (h.a. II), i.e. along the [110] and $[\bar{1}10]$ crystal direction, respectively.

The two easy-axes loops displayed in the central graphs are similar, but the behavior of the reversal is non-symmetric for positive and negative angles around the easy axes. For instance, for $\theta_H = -58^\circ$, i.e. below e.a., the $M_\perp$ loop presents two transitions (denoted by arrows), whereas only one transition is present above it, e.g. at $\theta_H = -22^\circ$. The opposite case is found around e.a. II, i.e. one (two) transition for applied field angles below (above) e.a. II. In turn, the hard axes $M_\parallel$ loops for $\theta_H = 0^\circ$ and 90° are clearly different in the squareness of the loops as well as in the coercive field (see right-central graphs of Fig. 4.3b])). The remanence and coercive field values are smaller in h.a. II. Additionally, a different reversal behavior is observe between the two hard axes. Around h.a. II two transitions are clearly observed in the $M_\perp$ loops, against only one around h.a. I.

This non-symmetric reversal behavior is more clear when the angular evolution

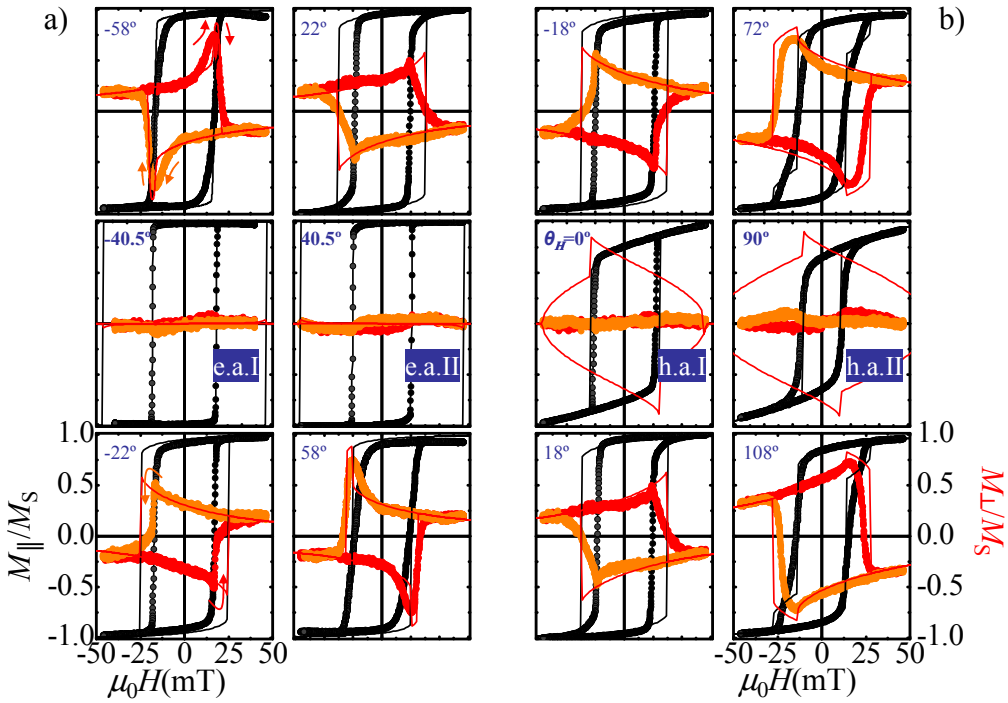

Figure 4.3: Magnetization reversal processes of 100 ML thick γ'Fe4N(100) film around the two easy axes (a) and around the two hard axes (b) of magnetization. The corresponding applied field angles $H(\theta)$ are indicated in the graphs. The experimental $M_\parallel(H)$ and $M_\perp(H)$ loops are given by black and red circles, respectively. The two branches of the hysteresis are depicted with filled and empty symbols for increasing and decreasing fields, respectively. The lines are the corresponding simulated loops using the model described in the text.

of the reduced remanences, i.e. $M_{R,\parallel}/M_S$ and $M_{R,\perp}/M_S$, is plotted in Figure 4.4. In principle, cubic-symmetry system should display fourfold symmetry, i.e. a behavior repeated every 90°. In this case two different behaviors are observed with a periodicity of 180°.

A butterfly shape is found, instead of the characteristic "four-leaves clover" expected from the cubic symmetry of the film (see section 3.2). The h.a. of the uniaxial anisotropy is parallel to one of the h.a. of the biaxial anisotropy. This kind of system will be refereed to as *collinear hard axes configuration*.

The experimental data are well fit by the simulated data, as has been shown in

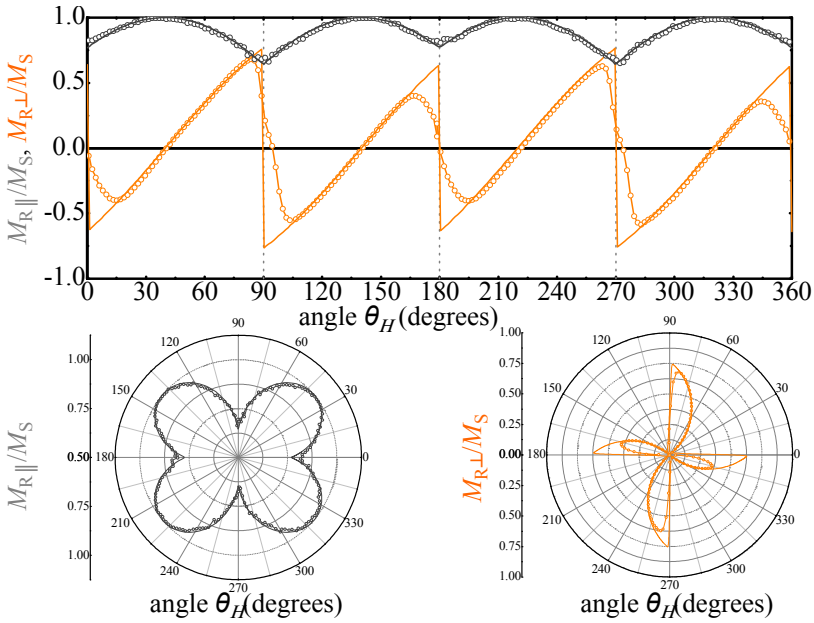

Figure 4.4: Angular dependence of the reduced remanence $M_{\parallel}$ (gray symbols) and $M_{\perp}$ (orange symbols) as a function of the angle of the applied field θ_H for a 100 ML thick γ'Fe4N(100) film. The lines are the simulation of the experimental data (symbols) using the model described in the text. Lower panels: polar plots of $M_{\parallel}$ and $M_{\perp}$. Note that the broken symmetry results in a characteristic butterfly shape behavior of the parallel remanence with non-orthogonal easy axes, but at an angle $\theta_H = 81^{\circ}$.

Fig. 4.5. The simulation describe the butterfly shape eventhough overestimated the angular range where to transitions are found, see Fig. 4.5. In this figure the experimental data are dark gray area while the simulated date are in light gray.

In order to reproduce the experiment have been performed numerical simulations based on a coherent rotation model which includes fourfold K_2 (biaxial) and twofold K_1 (uniaxial) anisotropy contributions. K_1 is taken with its easy axis along the (110) crystal direction, i.e. aligned with one of the hard axes of the biaxial anisotropy *collinear hard axes configuration*, according to the morphological characterization.

In an external field H, the total energy reads:

$$E_{\text{tot}} = K_1 \sin^2 \theta_H + \frac{1}{4} K_2 \cos^2 2\theta_H - \mu_0 M_S H \cos(\varphi - \theta_H) \tag{4.1}$$

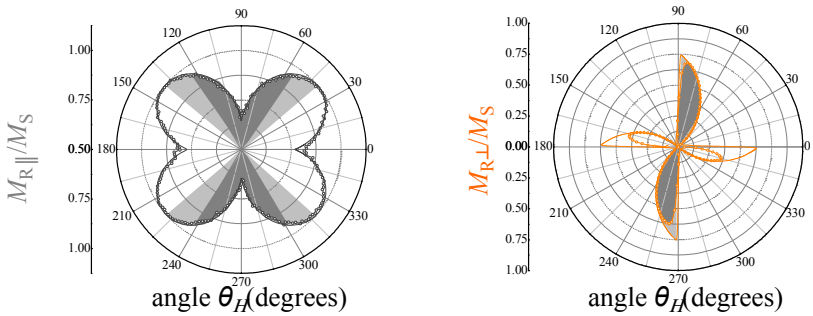

Figure 4.5: Angular dependence of the reduced remanence $M_{\parallel}$ (gray symbols) and $M_{\perp}$ (orange symbols) as a function of the angle of the applied field θ_H for a 100 ML thick γ'Fe4N(100) film. The lines are the simulation of the experimental data (symbols) using the model described in the text. The angular range where the reversals proceed via 1 transition are marked as shaded areas. Brighter gray indicates the angles predicted by the model and dark gray is the angular range present at experiment. The reversal proceeds via one irreversible transition around h. a. II. Lower panels: polar plots of $M_{\parallel}$ and $M_{\perp}$. Note that the broken symmetry results in a characteristic butterfly shape behavior of the parallel remanence with non-orthogonal easy axes, but at an angle $\theta_H = 81°$.

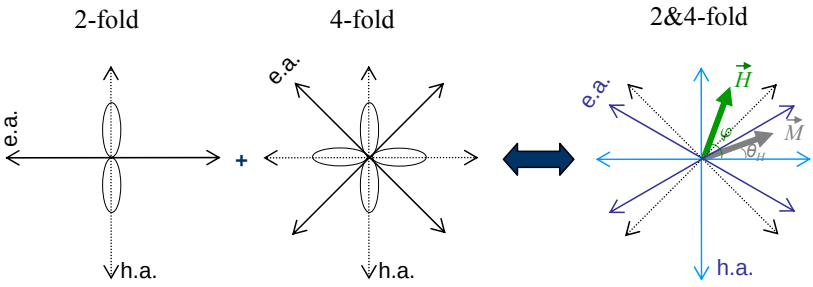

Figure 4.6: Energy scheme of relevant anisotropy system and their characteristic easy and hard direction.

If $K_1 \geq K_2$ the system becomes truly uniaxial such that the following considerations are restricted to $K_1 < K_2$ where the system still shows biaxial character. It is further more possible to restrict K_1 to positives values as negative values correspond to a system rotation of 90°. Hence, this does not change the underlying physics.

Due to the relative orientation of the anisotropy contributions the directions of the h.a. are not altered. However, the orientations of the e.a change (see: scheme 4.6a)). This is due to the fact that the uniaxial anisotropy hardens one and weakens the other hard axis of the fourfold anisotropy such that the e.a. move towards the weakened h.a. As a consequence the two h.a. are found at a relative angle of 90° while the angle between the two e.a. deviates from 90° (see: scheme 4.6b)).

Naturally, the deviation increases with increasing twofold anisotropy (K_2), while it vanishes for $K_1 = 0$.

To find the equilibrium angle of equation 4.1 it is necessary to find the minimum zeros of the first derivative. As one can factor out either $\sin\theta_H$ or $\cos\theta_H$, i.e. the hard axes solution, a third order equation remains(cite)).

For $\bar{H} = 0$ the equilibrium angle is

$$\alpha = \arccos\frac{K_1}{K_2} \tag{4.2}$$

Hence, by measuring the angle of the two easy axes one can determined the relative strength of first and second order anisotropy. Additionally, it is possible to access the values of K_1 and K_2 with the help of the two hard axes loops. A Tailor series (cite)with respect to $\bar{H}$ for the hard axes provides

$$\left.\frac{M_\parallel}{M_\mathrm{S}}\right|_{\bar{H}=0} = \sqrt{\frac{1 \pm \frac{K_1}{K_2}}{2}} + \frac{\mu_0 M_\mathrm{S}}{4(K_2 \pm K_1)} H + \mathcal{O}(H^2), \tag{4.3}$$

where the $+$ and $-$ sign refers to the two different h.a. Obviously the relative strength of the anisotropies constant can also be obtained by the two different remanences, M_R^+ and M_R^-, of the two different h.a. Furthermore, the slopes, κ^+ and κ^-, allow to extract K_1 and K_2 independently, figure 4.7. One eventually gets

$$\begin{aligned} M_\mathrm{S}^2 \frac{K_1}{K_2} &= (M_\mathrm{R}^+)^2 - (M_\mathrm{R}^-)^2 \\ K_1 &= \frac{\mu_0 M_\mathrm{S}}{8}\left(\frac{1}{\kappa^+} - \frac{1}{\kappa^-}\right) \\ K_2 &= \frac{\mu_0 M_\mathrm{S}}{8}\left(\frac{1}{\kappa^+} + \frac{1}{\kappa^-}\right) \end{aligned} \tag{4.4}$$

Therefore, even in the presents of nucleations and propagation, which influences coercive and switching fields, one can extract the anisotropy constant with help of SW-model.

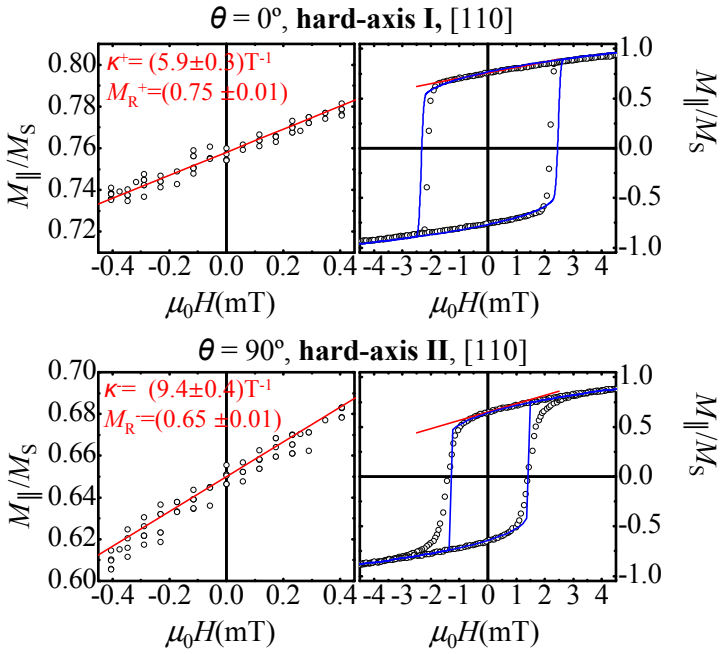

Figure 4.7: Hard axes $M_{\parallel}$ hysteresis loops of the symmetry breaking system of γ'Fe4N(100). The symbols are the experimental data. The left graph are zoom in to clearly see the fit of the hard-axes loops in the neighborhood of $H = 0$. The slopes are given in $1/T$, then μ_0 has to be removed from Eq. 4.4. From both slopes and remanence values we extract $K_2 = (4.5 \pm 0.3 \times 10^4)$ J/m^3 and $K1/K2 = 0.15 \pm 0.02$. These values are used to calculate the magnetization curves, depicted with blue lines in the right graphs.

Figure Fig. 4.9 shows that there is an excellent agreement between Eq. 4.2 and the values extracted from the angular dependence reported for other symmetry breaking epitaxial cubic systems, including metals [6, 7], semiconductors [5] and insulating [8] magnetic materials. Therefore, the anisotropy balance determines the angle between the easy axes independently of the system. Moreover, it is not even necessary to change the system; it is sufficient to change temperature to observe that the competition between anisotropies determines the angle between easy axes [5]. Figure 4.9 shows the angular dependence of the reduced remanence components calculated with the model for several anisotropy ratios. The top graph displays the evolution of the parallel component. For increasing K_1/K_2 values, the maximum value of $M_{\mathrm{R},\parallel}/M_S$ (which gives the easy axis) moves toward $\theta_H = 0°$, breaking the orthogonality of the

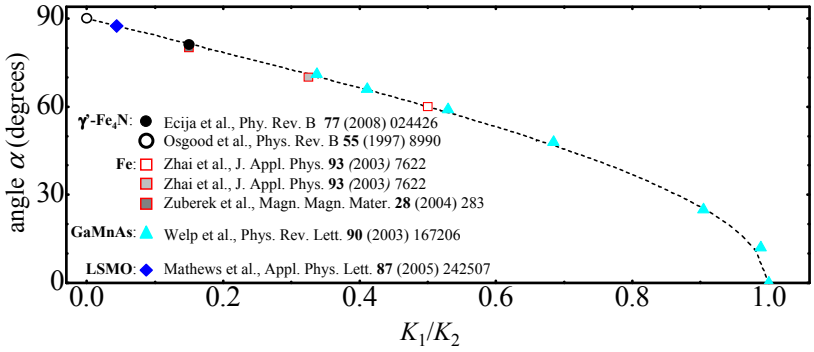

Figure 4.8: Angle between the easy axes, α, as a function of the anisotropy ratio K_1/K_2. The dashed line is given by Eq. 4.2. The symbols are extracted from angular dependence studies performed in other symmetry breaking systems.

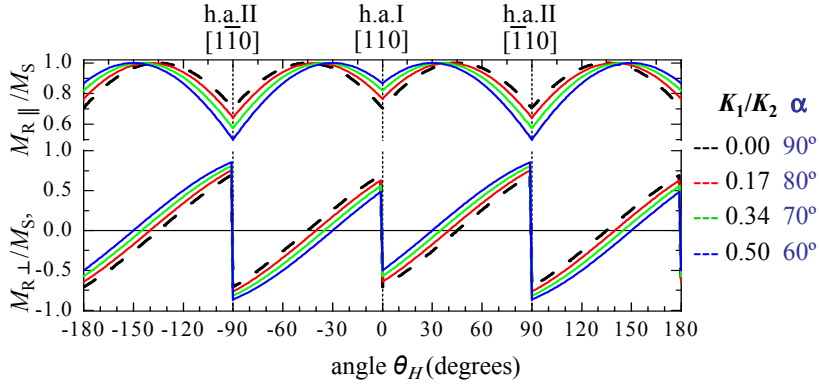

Figure 4.9: Calculated reduced remanence magnetization components as a function of the angle for the indicated anisotropy ratios. The corresponding α angles are also indicated

easy axes, and the remanence at the two hard axes becomes increasingly different. The former is difficult to detect experimentally due to the sinusoidal behavior of $M_{\mathrm{R},\parallel}/M_S$ around the easy axes.

This might explain why the nonorthogonality of the easy axes has not been noticed in experimental studies where only $M_{\mathrm{R},\parallel}$ is measured. In fact, nonorthogonal easy axes have been resolved only in epitaxial magnetic semiconductor compounds by means of magnetic imaging techniques [5]. The difference between the remanence

values at the hard axes is, however, easier to observe and, in fact, can be found for several other epitaxial cubic symmetry breaking systems where hard-axis hysteresis loops are shown [2, 5, 8–14]. Note that the anisotropy ratio, and consequently the angle α between easy axes by using Eq. 4.2, can be estimated from the remanence values of the parallel component at both hard axes (Eq. 4.4). In turn, the perpendicular component $M_{R,\perp}/M_S$ is also affected by the symmetry breaking (see Fig. 4.9). For increasing K_1/K_2 values, the zero crossing at the easy axes shifts toward 0° and the remanence at the two hard axes becomes increasingly different. Both are easy to observe experimentally, and the zero crossing provides the direct measurement of the angle between easy axes. Finally, has to be stressed that the peculiar magnetization reversal behaviors found in our system, i.e., non-symmetric reversal around the e.a. directions and different hard axis reversal pathways, should take place in the other symmetry breaking epitaxial cubic systems.

4.2. Uniaxial-Biaxial systems with collinear easy axes

After discussing the combination of uni- and biaxial anisotropies with collinear hard axes (*collinear hard axes configuration*), now the opposite extreme case, i.e. collinear easy axes will be presented. This kind of system will be refereed to as *collinear easy axes configuration*. Additionally, the strength of the uniaxial anisotropy will be controlled thus creating different systems, one with dominant biaxial and two with dominant uniaxial anisotropy. All of them exhibit different reversal processes.

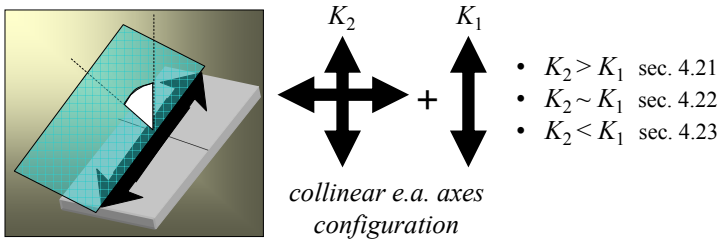

Figure 4.10: The relative ratio between uniaxial and biaxial anisotropies is controlled by angle deposition. It has been chose three different cases, $K_2 > K_1$, K_2 K_1 and $K_2 < K_1$.

4.2.1. Properties of systems with dominant biaxial anisotropy

In the following section a biaxial system with a tailored uniaxial anisotropy is investigated. The uniaxial anisotropy is induced by grazing incident deposition of Fe onto MgO(100). Hence, this allows to control the direction of the anisotropy via the azimuthal angle of incidence, while the polar angle influences the strength. Here the uniaxial anisotropy is chosen to be smaller than the biaxial anisotropy. The uniaxial easy axis is set to be collinear with one of the biaxial easy axes, *collinear easy axes configuration*. Note, this is the opposite case of the previous section where the hard axes have been aligned (*collinear hard axes configuration*).

The system with the collinear anisotropy configuration presents the reversal processes shown in Figure 4.11. As a consequence of the modifications of the intrinsic biaxial anisotropy of the thin film by the induced twofold symmetry, the magnetization reversal at the two easy directions ($\theta_H = 0^\circ$ and 90°) are clearly different. Hence, the biaxial easy axis at 90° (e.a. II) is hardened by the uniaxial anisotropy. The $M_\parallel(\theta_H = 0^\circ)$ loop (super-easy axis, e.a. I), presents the expected squared curve with only one sharp transition, whereas two transitions are present in e.a. II, see central panels of figure 4.11 a). The reversal takes place by two (one) irreversible transition, related to nucleation and propagation of 90° (180°) domain walls, when the applied field is close to the e.a. II and the hard axes (e.a. I). Due to the collinear e.a. the two h.a. are similar, but the behavior of the reversal processes are non-symmetric for positives and negative angles, i.e. either in direction of e.a. I or e.a. II (see central panels of figure 4.11b)). Both hard axes present double transition due to the dominant biaxial anisotropy. However, these double transitions are observed only when going in direction of the hardened easy axis, while only one transition is found when going into the direction of the super easy axis. The coercive field is smaller in e.a. II. In the angular region near it, two transitions are clearly observed in the $M_\perp$ loops. In contrast, only one transition is found in the region around e.a. I (super-easy axes).

This non-symmetric reversal behavior is hidden in the angular evolution of the reduced remanences, i.e. $M_{R,\parallel}/M_S$ and $M_{R,\perp}/M_S$, as plotted in figure 4.12. Furthermore, the applied field has not be sufficient to fully saturate the magnetization in the h.a. directions. This results in an extra feature in the $M_{R,\perp}$(h.a.)/M_S. Hence, the curve does not present a single jump in h.a. direction. As a consequence one cannot detect the small deviation that exists in these characteristic directions, predicted by the coherent model (see continuous orange line, $M_{R,\perp}/M_S$). Vertical dashed lines indicate $\theta_H = 45^\circ$, 135°, 235° and 310° corresponding to h.a. of a pure biaxial anisotropy system.

Note, this is similar to the discussion in section 4.1 where the *collinear hard axes*

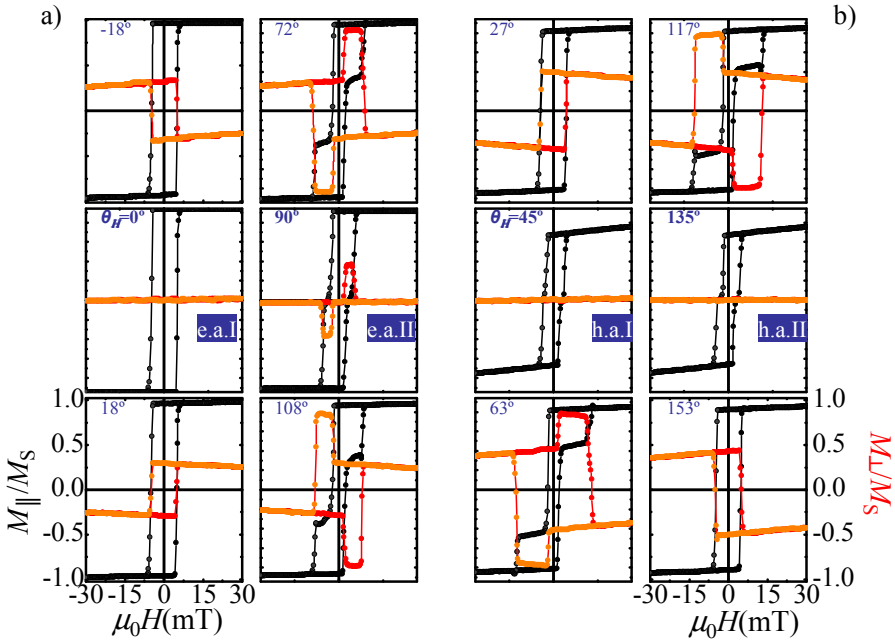

Figure 4.11: Magnetization reversal processes study of 20 nm Fe/MgO(100) thin film around the two easy axis (a) and around the two hard axis (b) of magnetization. The corresponding applied field angles θ_H are indicated in the graphs. The experimental $M_{\parallel}(H)$ and $M_{\perp}(H)$ loops are given by black and red circles, respectively. The two branches of the hysteresis are depicted with filled and empty symbols for increasing and decreasing fields, respectively. 1 or 2 transitions are measured around the easy axes, e.a. I and e.a. II, respectively, whereas 1 and 2 are found in both hard axes (h.a. I and h.a. II)

configuration has been presented. Magnetization reversal processes of both configuration can be summarized as follow. One transition is present around the amplified anisotropy-axis (super e.a. or super h.a.), while two transitions are found around the diminished-axis (hardened e.a. or softened h.a.). The angular evolution around these axes show symmetric behavior, i.e. for nearby angles 1 and 2 transition are found, respectively. On the other hand, non-symmetric reversal has been measured around the others characteristic axes—the non-collinear axes—where different angular regions with 1 or 2 transitions are present.

The critical fields of the *collinear easy axes configuration* are compared to the SW-solution in figure 4.13. Naturally, the SW-model strongly overestimates the critical

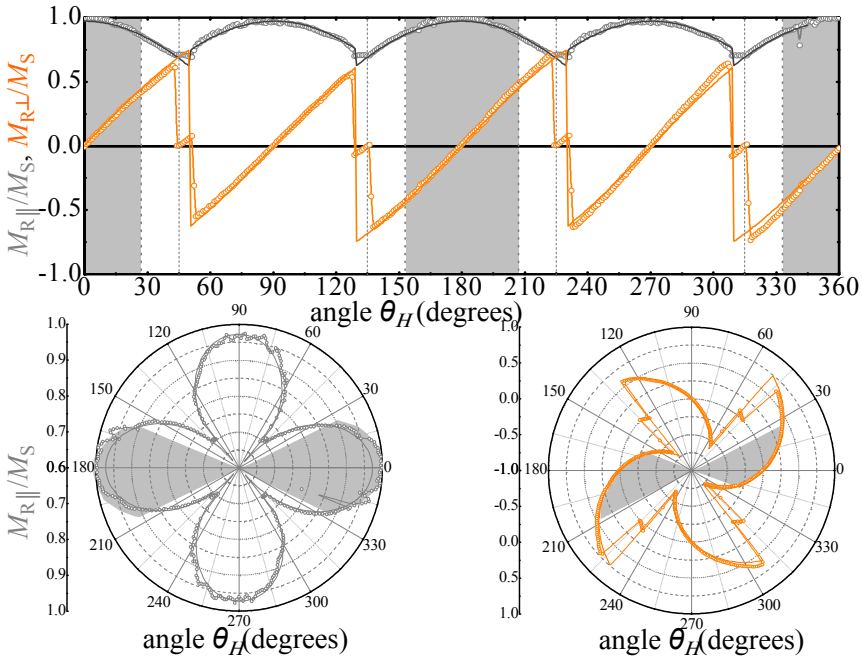

Figure 4.12: Angular dependence of the reduced remanence $M_{\parallel}$ (gray symbols) and $M_{\perp}$ (orange symbols) as a function of the applied angle θ_H for a 20 nm Fe/MgO(100) thin film. The range of angles where the reversal proceeds by one irreversible transition (around e.a. I, super-easy axis) are marked by gray shaded areas. The cracked presented around both h.a. at $M_{\parallel}$ is due to not all the magnetization is fully saturated at this field direction thus large applied field are needed. Lower panels, polar plots of $M_{\parallel}$ and $M_{\perp}$. Note, the crack is more clear at $M_{\perp}$ in polar representation. The continuous lines are the simulation values obtain from the ratio $K_1/K_2 = 0.18/1$.

fields near the e.a. especially the super e.a. (e.a. I). On the other hand, the behavior near the h.a. is well reproduced. Although the SW-model (see lower panel of Figure 4.13) overestimates the coercive field around e.a. regions, the angular evolution is reproduced qualitatively. The typical failure of the SW-model, however, results in a peak at the e.a. I that is not present in the data. Interestingly, both, data and model, show a peak at the e.a. II ($\theta_H = 90^\circ$ and 270°, marked by vertical dashed lines). The region of two transitions found in the experiment is slightly larger than predicted by SW-model.

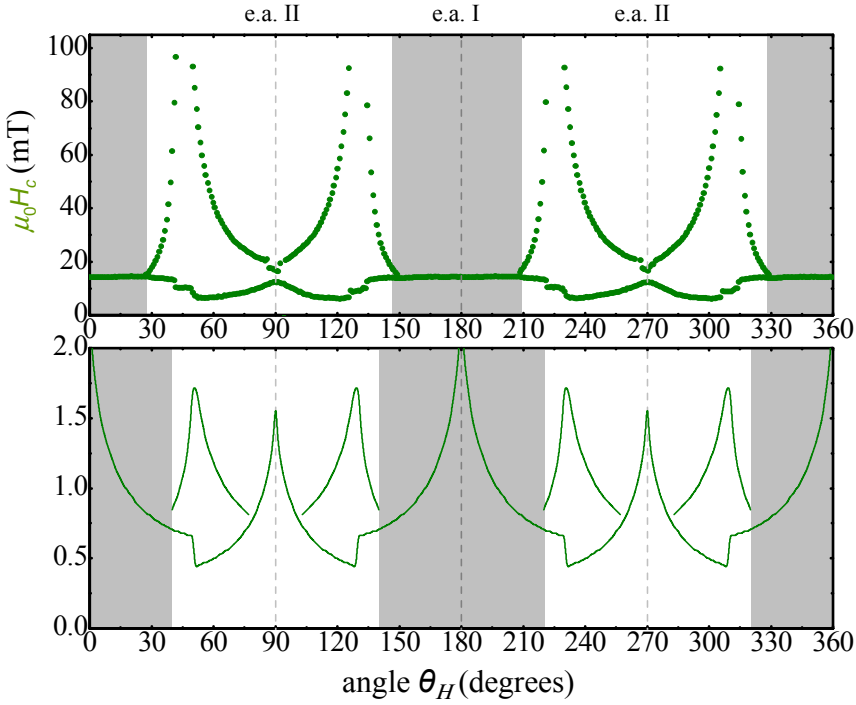

Figure 4.13: Angular dependence of critical fields (fields where discontinuities appear) from *collinear easy axes configuration* are presented in upper and lower panels, measured and theoretical data respectively. The simulation reproduces qualitatively the experimental evolution, dashed lines and symbols, respectively. Only the regions where coherent rotation are predominant the model is well fitted, as around the hard axes and e.a. II.

4.2.2. Properties of virtually uniaxial systems with large biaxial anisotropy

Non-ideal fourfold symmetry systems, as the two presented in the previous sections 4.1 and 4.2 have been studied to understand and characterize the different reversal processes that can occur in systems where uniaxial anisotropy has been introduced on purpose or by coincidence.

The following results present the ability to determine and tailor the reversal processes by varying the strength, K_1/K_2 of the two involved anisotropies to obtain a large range of features, combinations of 1 and 2 or even 3 transitions at the magnetization

reversal processes, super-axis either easy or hard, butterfly shape like in remanence angular evolution and so on.

Within the framework of coherent rotation nn additional transition is observed when the ratio between the anisotropies is $0.2 < K_2/K_1 < 1$. In this case a so-called field driven spin reorientation occurs [15]. For instance, the system 5 nm Fe/MgO(100) seems to exhibit this behavior. The main feature of this sample is the angular dependence of the remanence repeated every 180° i.e. reproducing twofold symmetry, as is shown in Figure 4.14. The detailed angular study of the hysteresis

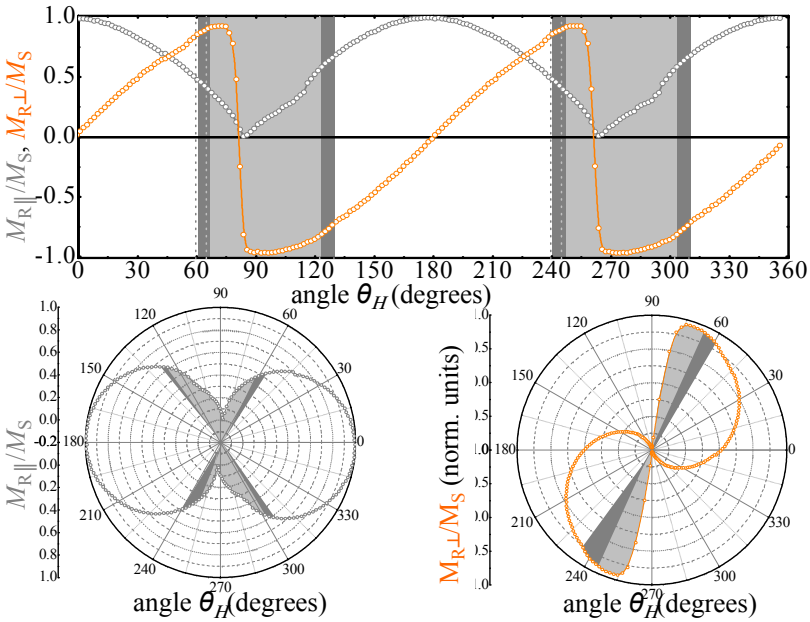

Figure 4.14: Angular dependence of the reduced remanence $M_\parallel/M_S$ (gray symbols) and $M_\perp/M_S$ (orange symbols) as a function of the angle of the applied field, θ_H for a 5 nm Fe/MgO(100) thin film. The main feature of this fourfold symmetry system with induce twofold symmetry is the predominant uniaxial evolution in the remanences. The magnetization reversal processes take place by 1, 2 or 3 transitions as is remarked in the graphics by areas in white, light gray and dark gray, respectively. The lower panels show the polar plots of the remanence. As the remanence show biaxial character, the fourfold contribution is usually not clear. However, in this case there is a small misalignment such that the zero-crossings of $M_{R,\perp}$ are not at 90°and 270°. The misalignment is not identical to the deviation from the expected characteristic axis, but can be, especially for $K_1 \approx K_2$ significantly smaller. Hence, even very small misalignments easily result in notable effects.

curves shows reversal processes via 1 transition around the e.a. and 2 and 3 around the apparently h.a. as can be seen in figure 4.15.

The center-left panel presents the characteristic angle, e.a. with a well defined squared

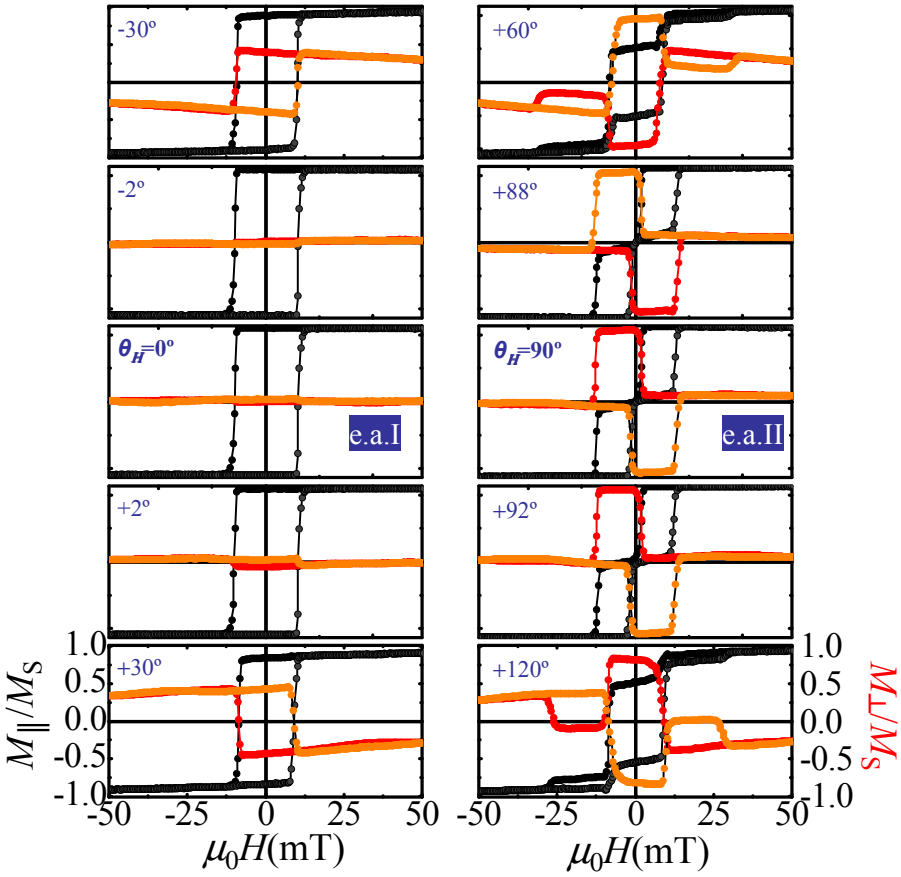

Figure 4.15: Selected hysteresis loops around e.a. and h.a. from 5 nm Fe/MgO(100)). The figure shows the symmetric reversal processes around the characteristic angles. Around the e.a. only a sharp transition due to magnetization reversal via 180° domain walls take place, while the peculiar h.a. presents two sharp transitions and a remanence of zero. Three transitions are found in a narrow angular region near 45°, marked in the angular evolution of the remanence and critical fields (Figures 4.14 and 4.16).

loop in the $M_{\parallel}$ as is expected from a biaxial system. The nearby angles show only 1

transition and the $M_\perp$ component changes sign when crossing the characteristic direction. The center-right panel displays the h.a. While only small deviations from a twofold symmetry system are found when looking at the angular evolution of the remanence a detailed analysis of the corresponding hysteresis loops reveals strong differences. The h.a. is a non-reversible curve, presenting two transitions, a feature associated with fourfold symmetry systems. Only for a small angular range the magnetization reversal proceeds via 2 or even 3 jumps. Three jumps are only observed near 45°, 135° etc. which in contrast tries to establishes a minimum. At this point the transversal component becomes very important, as it reveals a change of sign also around 45° and the corresponding angles. Hence, the transversal component changes the sign 8 times instead of 4, which would be expected from a twofold system. Note, four changes of sign are expected in a SW-system, even in the presence of a field driven spin reorientation. (Nevertheless, a transition in positive fields is observed. In the angular evolution of the critical fields this additional transition—field driven spin reorientation—is shown as negative values in Fig. 4.16. By doing so one can distinguish between the transitions that also take place in pure systems and field driven spin reorientation transitions. Shadowed areas mark the angular range where two and three transitions are found, light and dark gray, respectively. Note, all previous pure systems do not show transitions in this region as only coherent rotation is expected. Hence, this transition must be a field driven spin reorientation. However, this term is typically used in cases where the applied field creates additional minimums that are not present in zero field. Hence, applied fields are required to reveal the influence of the additional fourfold anisotropy. In the present case, however, $M_\perp$ reveals that we have a truly fourfold system, as the magnetization changes from CW to CCW rotation 8 times. The dominant fourfold symmetry becomes completely obvious when plotting the integrated modulus of $M_\perp$ as a function of field angle, i.e.

$$I_M^\perp(\theta_H) = \int_{-H_{\max}}^{H_{\max}} \mathrm{d}H \; |M_\perp(\theta_H)|, \tag{4.5}$$

which somewhat reproduces the anisotropy energy landscape. This is due to the fact the $M_\perp$ vanishes in case of an easy axis, while it has strong signal at hard axes, where the anisotropy energy presents a minimum and a maximum, respectively. By plotting the data, maximums correspond to the hard axis, which then can be identified as in Fig. 4.17 .

In the present system an non-collinearity of 107° is found. With the energy function

$$E_{\mathrm{tot}} = K_1 \sin^2\varphi + \frac{1}{4}K_2 \sin^2(2\varphi) - \mu_0 M_S H \cos(\varphi - \theta_H), \tag{4.6}$$

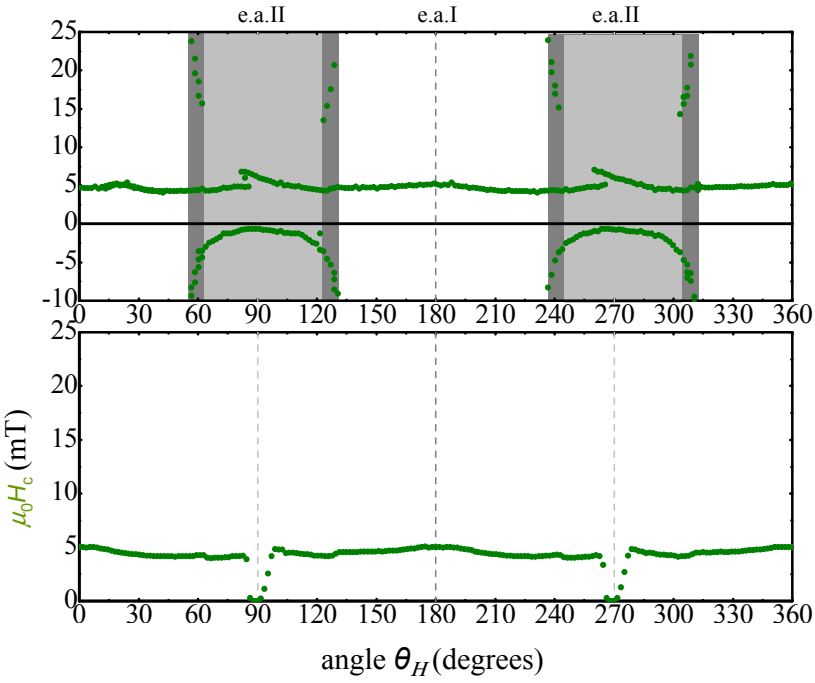

Figure 4.16: Critical fields, extract form the experimental hysteresis loops (top). The light gray shadowed areas is the angular range where the magnetization reversal proceeds via 2 transition, while dark gray area corresponds to angles where 3 transitions are found. Coercive field of $M_{\parallel}$ (bottom).

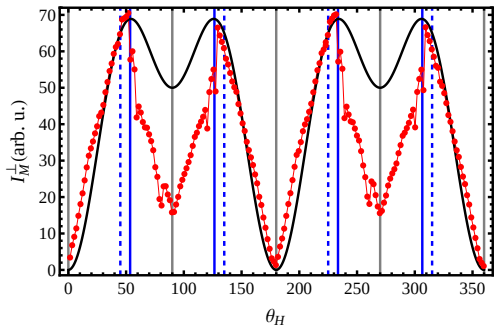

Figure 4.17: Angular evolution of the integrated modulus of $M_{\perp}$ (red). Gray lines show the easy axis of a collinear easy axis fourfold while the blue lines corrspond to the non-collinear hard axis. The dashed blue lines correspond to the hard axis of a pure fourfold system. The maximums and minimums agree very well with the anisotropy energy landscape of a collinear easy axes system with $K_2/K_1 = 3.4$.

which—in case of $K_2 > K_1$—gives an opening angle α between the hard axes of

$$\alpha = \arccos(-\frac{K_1}{K_2}), \tag{4.7}$$

one calculates $K_2/K_1 = 3.4$, which is actually biaxial dominated.

The reason why the $M_{\parallel}$-component seems to be twofold is purely due to domain wall nucleation and propagation. The energy of the local minimum at 90° at $H = 0$ is so high compared to the energy of the global minimum at 0° and 180° that already in positive fields nucleation and propagation takes place. Hence, the 90° easy axis domain decays into 0° and 180° domains. Consequently, the system is dominated by nucleation and propagation. While in previous cases the SW-model could describe the data at least qualitatively, this is not possible here. In the previous cases domain wall nucleation and propagation only shifted the field values at which critical transitions took place. Here the nucleation processes introduce transitions that are completely unpredicted by the SW-model.

4.2.3. Properties of uniaxial systems with small biaxial contribution

For a sample of approximately 5 nm Fe/MgO the anisotropy ratio K_1/K_2 has been set to$1/0.8$. In this case still one finds regions with 1, 2 or 3 jumps. Compared to the previous chapter, however, the angular range where these jumps are found is much smaller. Selected hysteresis loops are shown in Fig. 4.18. As in the previous system, due to the small value of the biaxial anisotropy the total symmetry is twofold. The two characteristics angles are displayed in the central row of Fig. 4.18. The easy axis presents a well squared hysteresis loop at the $M_{\parallel}$ component. For nearby angles $M_{\perp}$ changes sign displaying only one transition. On the other hand, the hard axis presents a seemingly reversal curve at the $M_{\parallel}$ component, but with presence of three transitions, due to the weak influence from the biaxial contribution. The biaxial anisotropy cannot be detected by quick inspection of the angular evolution of the remanence, as is depicted at Fig. 4.19. The presences of the fourfold symmetry, however, is obvious in the angular evolution of the critical fields, as can be seen in Fig. 4.20 (upper and lower panels are experimental and simulated data, respectively). In a narrow angular range around $\theta_H = 90°$ and 270° one observes 2 and 3 transitions. This feature is not found in twofold symmetry systems. Note that the angular evolution shows a peak (marked as dashed gray line) at the e.a. ($\theta_H = 0°$ and 180°) that is also predicted by the model, even though much larger in the model (lower panel). In a pure twofold

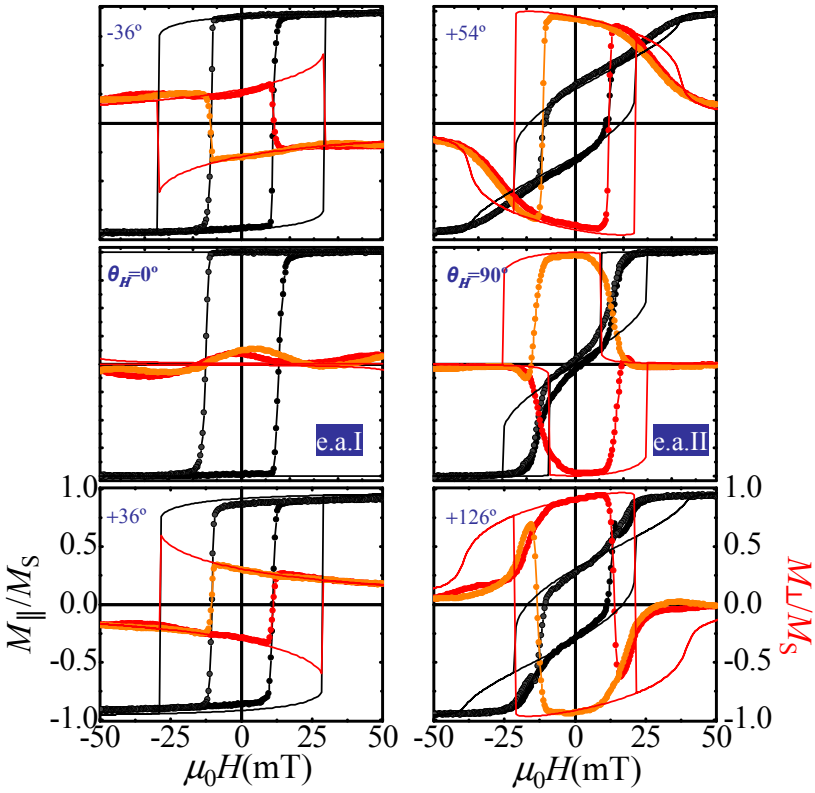

Figure 4.18: Selected hysteresis loops around e.a. and h.a. from a Fe/MgO(100)) thin film with thickness less than 5 nm. The figure shows the symmetric reversal processes around the characteristic angles. Around e.a. only a sharp transition do to magnetization reversal via 180° domain walls whilst peculiar h.a. with two transitions and a remanence of zero. Symmetric behavior of $M_{\perp}$ is found around the h.a.

system this region would present the flat plateau, predicted by the pinning model (see chapter (c)). Hence, the peak indicates coherent rotation processes that do not take place in pure twofold symmetry systems. Note, in a pure twofold symmetry system the region close to e.a. present a flat angular evolution of critical fields (see section 3.2 Fig. 3.21).

Using Eq. 4.6 it is possible to simulate the data presented in this chapter. Equation 4.6 allows a continuous change from pure uniaxial to pure biaxial behavior. The evolution of M_R/M_S with changing K_1/K_2 is shown in Fig. 4.21 Looking at $M_{R,\parallel}/M_S$ one sees

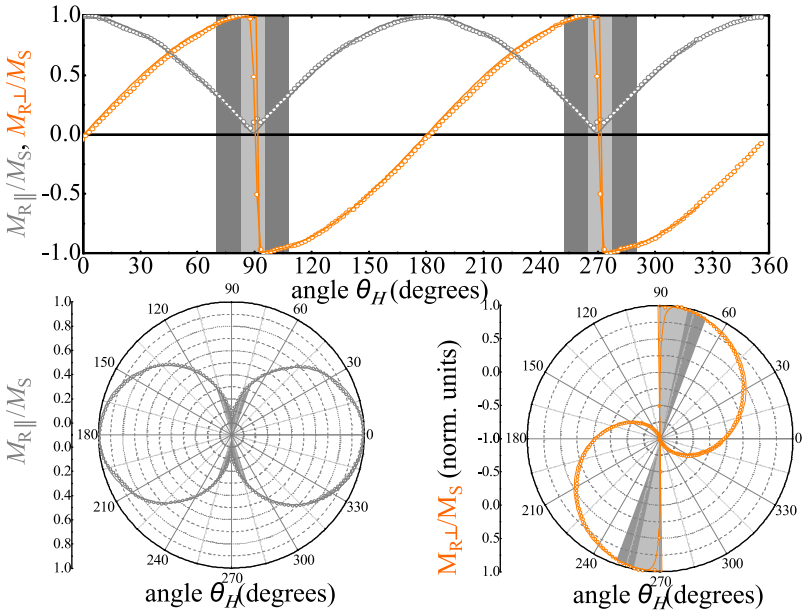

Figure 4.19: Angular dependence of the reduced remanence $M_{\parallel}$ (gray symbols) and $M_{\perp}$ (orange symbols) as a function of the angle of the applied field θ_H for less than 5 nm Fe/MgO(100) thin film. The fourfold symmetry of the system is hidden by the twofold symmetry in the angular evolution of the remanences. The magnetization reversal processes take place by 1, 2, or 3 transitions as is remarked in the graphics by areas in white light gray and dark gray, respectively. The lower panel show the polar plots of the remanence can induced to confusion of the involved anisotropies.

that there are only minor deviations from a pure fourfold system. Due to softening effects that easily take place in experiment, these deviations can be washed out. Hence, on basis of $M_{R,\parallel}/M_S$, the system might incorrectly be identified as pure fourfold. Only the additional information of $M_{R,\perp}/M_S$ reveals the true character of the sample, i.e. the mixture of uni- and biaxial anisotropies. However, one has to be careful not to confuse the additional transitions in $M_{R,\perp}/M_S$ with the effect of non-saturated systems, as shown in Fig. 4.12

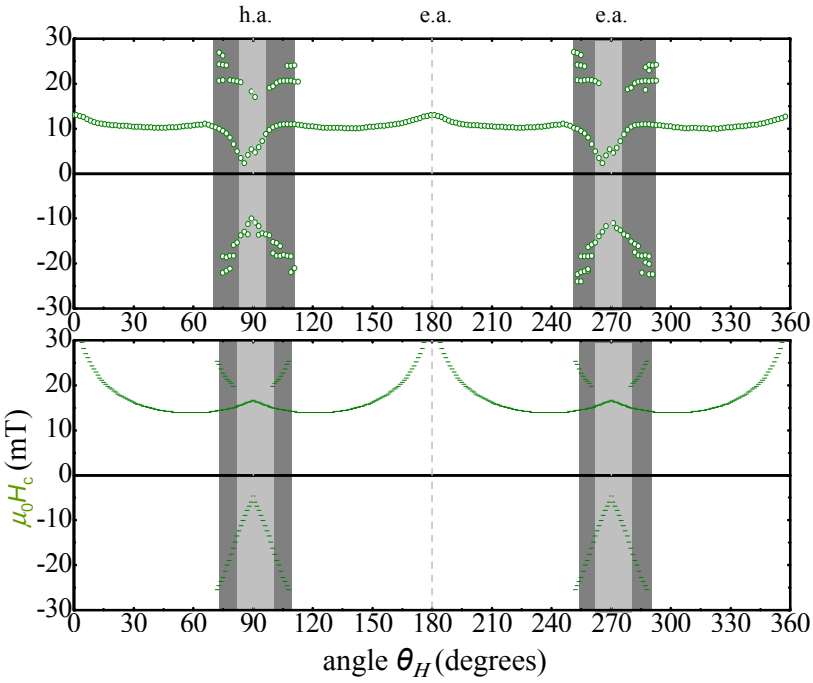

Figure 4.20: Critical fields, extracted form the experimental hysteresis loops are shown in the upper panel of this figure. The light gray shadowed areas are the angular range where the magnetization reversal proceeds via 2 transition, while the dark gray areas correspond to angles where 3 transitions are found in one branch of the hysteresis loops. The lower panel shows the angular dependence of critical field simulated with coherent model where two anisotropies uniaxial and biaxial are collinear with ratio of $K_1/K_2 = 0.8$. The correspondence between experiment and theory is enterprisingly good.

4.3. Properties of Exchange-Bias Systems

In low dimensional magnetic systems the broken symmetry at surfaces and/or interfaces and the lateral dimensions alter the magnetic behavior. As a consequence new or additional anisotropies appear, which induce new reversal processes, as has been shown in the previous chapters. Those anisotropies can be uniaxial due to angle of deposition, stress, diffusion or due to the shape i.e. magnetostatics (see section 4.1 and 4.2). Some important interfacial "effects" are e.g. the coupling of Co-layers via Pt layers (hybridization, see chapter 5)) or the unidirectional anisotropy due to direct

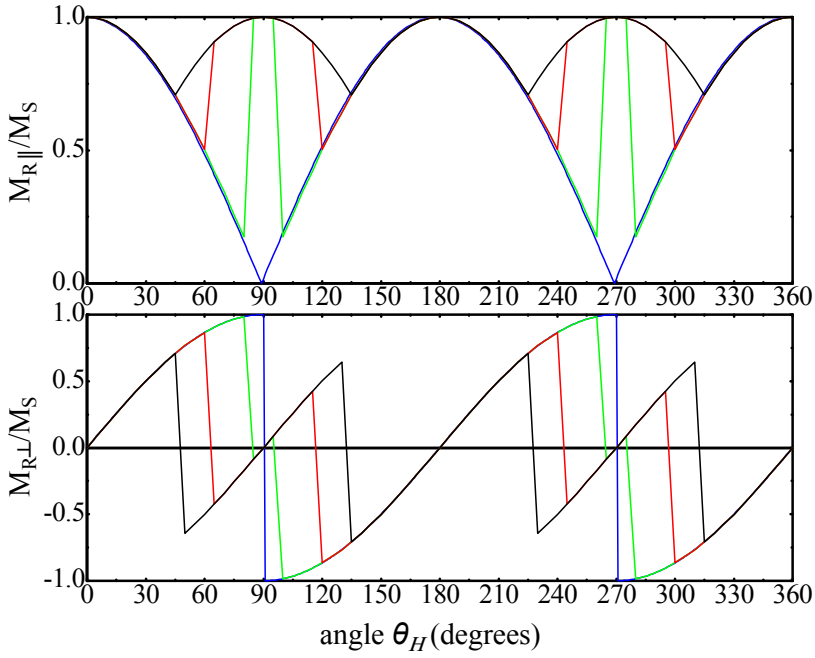

Figure 4.21: Simulation of angular evolution of M_R/M_S changing K_1/K_2 from pure uniaxial to pure biaxial behavior (blue and black continuous lines, respectively).

exchange (see chapter 3.3).

Different intrinsic parameters (such as chemical composition, thicknesses and shape) as well as reversible extrinsic ones (such as a field cooling procedure) have been explored to understand the exchange coupling phenomena in FM/AFM systems [16], aiming to control the behavior of tailored magnetic devices. In general, the interfacial exchange coupling effects depends on the strength of the anisotropies [4] as well as their relative orientation [17], exhibiting a complex phase diagram of different reversal modes. Different field cooling (FC) procedures, varying both strength [18, 19] and FC angle [17, 20], and/or interfacial magnetic frustration [21, 22] are at the origin of the relative orientation between the intrinsic FM anisotropy and the induced interfacial unidirectional anisotropy.

In this section the asymmetries measured at the magnetization reversal processes of soft FM/AFM (FeNi/IrMn; see chapter 3.3) systems are investigated in detail. In a next step the non-symmetric processes and angular evolutions (such as, H_C, H_E

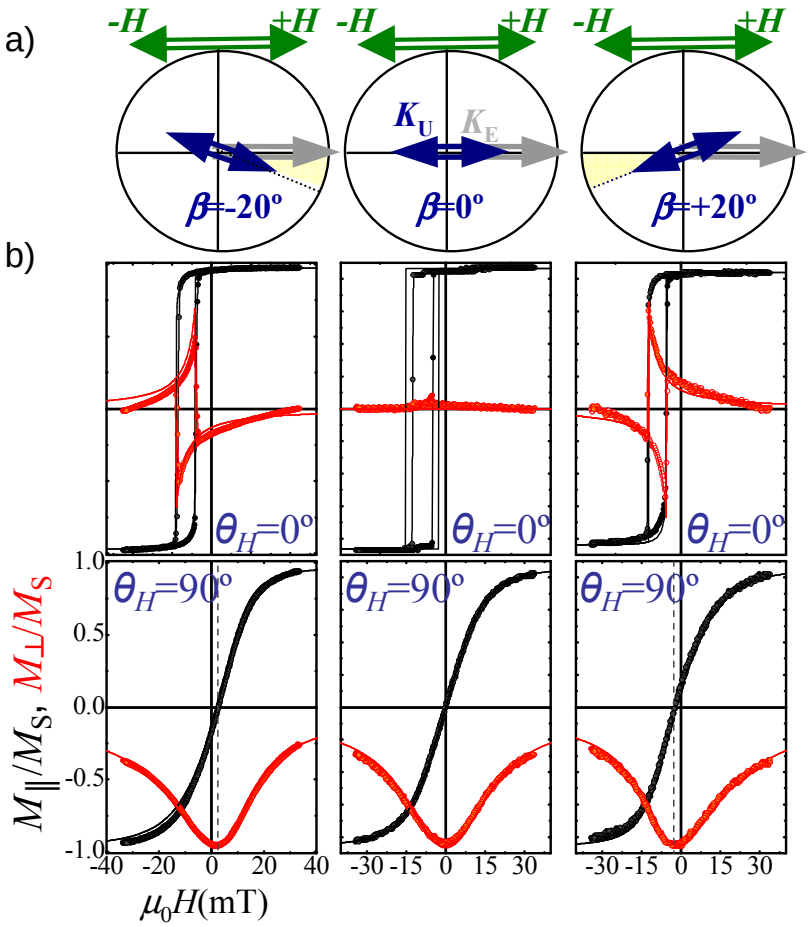

Figure 4.22: Magnetization reversal of a Co/IrMn bilayer for different FC angles $\pm\beta_{FC}$ with respect to the FM anisotropy axis. (a) Schematic representation of the anisotropy configuration after the FC procedures. The size of the arrows is scaled to the experimental values of K_U and K_E. (b) Hysteresis loops $M_\parallel$ (black symbols) and $M_\perp$ (red symbols) at selected field angles θ_H, parallel (top panels) and perpendicular (bottom) to the FC direction. The $M_\perp$ at $+\beta_{FC}$ is point symmetric to the one at $-\beta_{FC}$ for the $\theta_H = 0°$. In case of the $\theta_H = 90°$ the loop is biased to right at $-\beta_{FC}$ while is shifted to left at $+\beta_{FC}$. The solid lines are the simulated curves obtained using the SW model with the anisotropy configurations depicted in (a).

and so on) are tailored in hard FM/AFM Co/IrMn thin films. Non-collinear uniaxial K_U and unidirectional K_E anisotropy configuration are induced via a FC procedure.

This non-collinear exchange coupling results in peculiar non-symmetric magnetic features, including reversal modes, exchange bias field and coercivity. This coupling is achieved after annealing a polycrystalline Co/IrMn bilayer at 420 K for 30 minutes and field cooled to room temperature (RT) in a 0.3 T external field by misaligned angles $\beta_{FC} \neq 0^\circ$ with respect to the easy magnetization direction of the FM layer. High resolution vectorial Kerr magnetometry measurements have been performed to study the dependence of the reversal, of both parallel ($M_\parallel$) and transverse ($M_\perp$) magnetization components, with respect to the external field angle (θ_H). $\theta_H = 0^\circ$ is defined when the magnetic field is aligned parallel to the FC direction.

In Fig. 4.22 in-plane resolved magnetization hysteresis loops are compared at selected field angles θ_H for the collinear ($\beta_{FC} = 0^\circ$) and non-collinear ($\beta_{FC} = \pm 20^\circ$) exchange coupling configurations, as depicted Fig. 4.22a). For $\theta_H = 0^\circ$, parallel to the FC direction, the left-top graphs of Fig. 4.22 b) shows that both induced exchange bias and coercivity are similar and the magnetization behaves symmetrically whether the field sweeps along (increasing field branch) or against (decreasing field branch) the FC direction. However, the reversal takes place in a different fashion. In both cases, $M_\parallel$ reverses mainly via a sharp irreversible transition, indicating that the reversal is mainly governed by nucleation and propagation of magnetic domains. For the collinear configuration $M_\perp(\theta_H = 0) = 0$ in the whole field loop, whereas for the non-collinear case a clear hysteresis with both smooth reversible and sharp irreversible transitions are observed. This indicates that during the sharp transitions the nucleated magnetic domains are aligned parallel and non-parallel to the external field for the collinear and non-collinear coupling configurations, respectively. For $\theta_H = 90^\circ$, perpendicular to the FC direction, smooth reversible transitions are observed in both $M_\parallel$ and $M_\perp$ hysteresis loops for both coupling configurations (lower graphs of Fig. 4.22 b)), indicating that magnetization rotation is the relevant process during reversal. Remarkable is the noticeable negative field shift of the $M_\parallel$ hysteresis loop found for the non-collinear case ($\beta_{FC} > 0$), which is indicative of the non-collinear anisotropy configuration (marked by a vertical dashed line in the right bottom graph of Fig. 4.22 b)).

Positive field shift of the $M_\parallel$ hysteresis loop is measured when the the FC angle is negative ($\beta_{FC} = -20^\circ$) (see Fig. 4.22 b)). In easy axis direction ($\theta_H = 0^\circ$) the non-collinearity manifests itself in a open $M_\perp$-loop. In the case of negative β_{FC} the $M_\perp(\theta_H = 0^\circ)$ component is point symmetric to $M_\perp$ for the corresponding positive β_{FC}. A peculiar asymmetric magnetization reversal behavior is found for the non-collinear coupled FM/AFM bilayers, for instance, $\beta_{FC} = 20^\circ$. The right and left panels of Fig. 4.23 show the hysteresis loops acquired around the FC direction for negative and positive θ_H values, respectively. In general, both irreversible sharp transitions

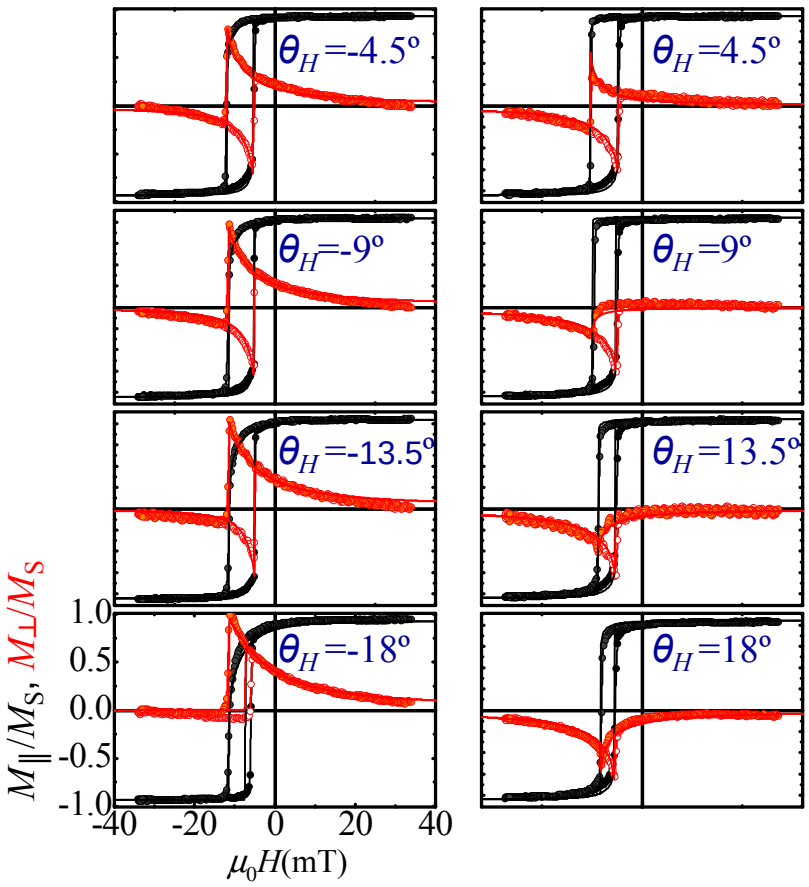

Figure 4.23: In-plane hysteresis loops (at $\beta_{FC} = 20°$), $M_{\parallel}$ (black symbols) and $M_{\perp}$ (red symbols), of the non-collinear coupled Co/IrMn bilayer at the labeled field angles θ_H. The two panels show measurements acquired at symmetric angles around the FC direction. To clarify the evolution of the magnetization, the two branches of the experimental loops have been depicted with different filled symbols. The solid lines are the simulated curves obtained using the SW model with the anisotropy configurations depicted in Fig. 4.22 (a).

and reversible smooth transition are observed in both components of magnetization, indicating rotation and nucleation and further propagation of magnetic domains, respectively. The asymmetric reversal behavior is found by the different rounded $M_{\parallel}$ transitions and different maximum values of $M_{\perp}$ observed in the decreasing and in-

creasing field branches of the hysteresis loop. Similar features were also observed in collinear coupled FM/AFM systems [23]. On the contrary, several remarkably differences are found in the present study. For the non-collinear coupled bilayer, and depending of the field angle, $M_\perp$ can reverse either in one semicircle or in both semicircles, whereas for the collinear case $M_\perp$ only reverses in one semicircle. Moreover, the angular range where $M_\perp$ reverses in both semicircles is not symmetric around the FC direction. For instance, $M_\perp$ reverses in both semicircles at $\theta_H = -9^\circ$ whereas only in one at $\theta_H = 9^\circ$. Hence, the reversal asymmetry is not symmetric around the FC direction in the non-collinear case. Magnetization reversal via rotation processes is not always more relevant in the same field branch but can be found in either descending or ascending branches of the hysteresis loop, depending on the sign of the applied magnetic field angle with respect to the FC direction.

The non-symmetric reversal around the FC direction, where the reversal takes place in one or both semicircle is found for different positives FC direction, as is shown in the Fig. 4.24. Selected angles around the e.a. for different FC directions are displayed in columns. The angular range where the asymmetry is detected decreases with increasing the FC angle. Note, at $\beta_{\mathrm{FC}} = 82^\circ$ (and larger FC angles) and $\theta_H \pm 9^\circ$ the reversal only take place in one semicircle, only in short angular range the $M_\perp$ rotates in both semicircles. The $M_\perp$ component clearly shows the effect of non-collinearity. Furthermore, it is sensitive to the applied field direction. Hence, it allows to measured the critical angle, at which the FC angle is orthogonal to the FM anisotropy, as is it shown in the change of sign in $M_\perp$ at $\theta_H = 0^\circ$ for $\beta_{\mathrm{FC}} = 82^\circ$ and $\beta_{\mathrm{FC}} = 95^\circ$. To stress the point, $M_\perp$ for $\theta_H = 0^\circ$ and $\beta_{\mathrm{FC}} = 82^\circ$ is rotating CCW while it is rotating CW for $\beta_{\mathrm{FC}} = 95^\circ$. The coercive field at $\theta_H = 0^\circ$ decreases with increasing β_{FC}. The asymmetries measured at the hysteresis loops are clearly described by the astroid picture as has been introduced in previous chapters. The astroid describes the fields were sharp transition take place, in case of an uniaxial anisotropy it displays an astroid centered at the origin (see 3.1.3 (a)). The switching field of a more complex system, as exchange-bias, are well described by an astroid biased from the origin (see **??**. The different reversal processes produced at non-collinear exchange-biased system are understood rotating the biased astroid by β_{FC} as is shown in Fig. 4.25. The different reversal processes measured at the hysteresis loops are shown in the Fig. 4.25. The exchange-bias field is realized by shifting the astroid ($\mu_0 H_{\mathrm{E}}$) the β_{FC} correspond to the rotation of the astroid. Due to the rotation, each gray line cuts the astroid in two non-equivalent points. This is already true for the non-rotated astroid. Hence, this corresponds to the asymmetry in forward and backward branch. Due to the additional rotation of the astroid it is obvious that now the two gray lines cut the astroid in four

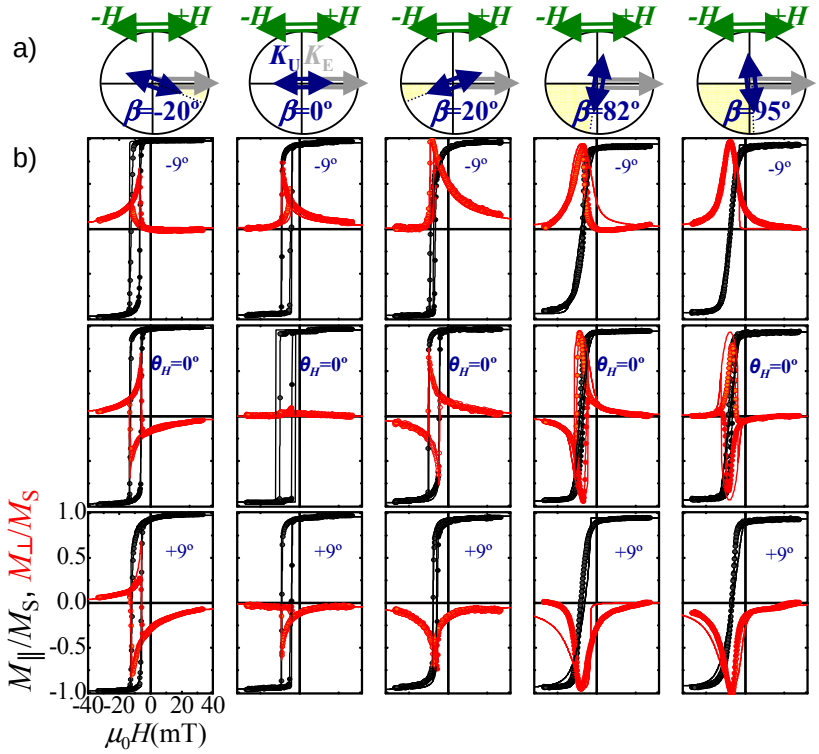

Figure 4.24: Selected hysteresis loops of a Co/IrMn bilayer for different FC angles $\pm\beta_{\rm FC}$ with respect to the FM anisotropy axis. (a) Schematic representation of the anisotropy configuration after the FC procedures. (b) At $\theta_H = 0^\circ$ the $M_\perp$ (squares) increases the signal while the $\beta_{\rm FC}$ increases or decreases. The opposite behavior is found in $M_\parallel$ at $\theta_H = 0^\circ$, the $H_{\rm C}$ decreases while the $\beta_{\rm FC}$ increases. At positives and negatives θ_H around each $\beta_{\rm FC}$ (columns) the $M_\perp$ component rotates in opposite direction. mirror symmetry is found in the $M_\perp$ around the $\beta_{\rm FC} = 0^\circ$ (rows). The solid lines are the simulated curves obtained using the SW model with the anisotropy configurations depicted in (a)

different points. This corresponds to the asymmetric behavior in the angular evolution. In case of only one contact point with the astroid (red line), a sharp transition would be measured in the hysteresis loop symmetric for both branches, forward and backward. All the other angles (blue line) are reversible hysteresis loops.

The symmetry breaking of the non-collinear coupling is also reflected in the angular dependence of both exchange bias and coercivity (see Fig. 4.26). For example, $H_{\rm E} = 0$ is not found perpendicular to the FC direction, but at $\theta_H = -81^\circ$ and $+99^\circ$.

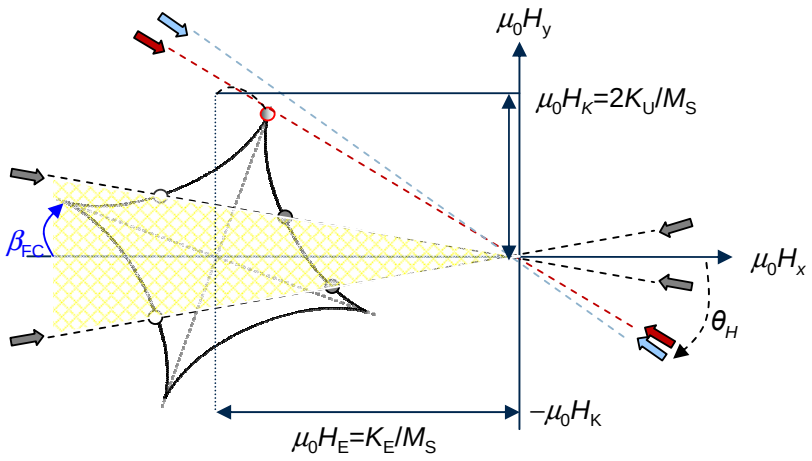

Figure 4.25: Switching field for SW-solution for exchange-bias system where the uniaxial anisotropy has an angle to respect the unidirectional one (β_{FC}).

Both coercivity and exchange bias are not symmetric around the FC direction, i.e. $H_C(\theta_H) \neq H_C(-\theta_H)$ and $H_E(\theta_H) \neq H_E(-\theta_H)$. Around the FC direction, i.e. $\theta_H = 0°$, the coercivity is non-zero and displays a plateau. This region of almost no variation in H_C coincides with $M_\perp$ reversing in both semicircles (see the area highlighted around $\theta_H = 0°$ in Fig. 4.26). Furthermore, in this angular range $M_\perp$ shows different behavior for positive and negative applied field angles with respect to the FC direction. Hence, it is possible to assign two critical angles at $\sim -25°$ and $\sim +40°$. Within the angular region limited by these angles one observes non zero coercivity and magnetization reversal in both semicircles, while outside this region the coercivity is zero and magnetization reversal take place in only one semicircle. The maximum exchange bias value is found near the FC direction, but does not coincide. Moreover, zero exchange-biased is not found perpendicular to the FC direction. This behavior is general for all β_{FC} directions, as is depicted in Fig. 4.24 Due to symmetry one observes the following properties. The exchange-bias evolution for $+\beta_{FC}$ is point symmetric to $-\beta_{FC}$. Hence, if the maximum exchange-bias for $+\beta_{FC}$ is found at $\theta_H = 180° - \delta$, the evolution for $-\beta_{FC}$ shows its maximum at $\theta_H = 180° + \delta$ (assuming no other parameters change). The angle at which zero bias is found behaves in a similar way, due to symmetry zero exchange-bias is found at $\theta_H = 90°$ only if $\beta_{FC} = 0°$ or $90°$. However, it approaches the high symmetry direction with increasing K_E. While the magnetization reverses in only one semicircle for $\beta_{FC} = 0°$, with increasing non-collinearity the

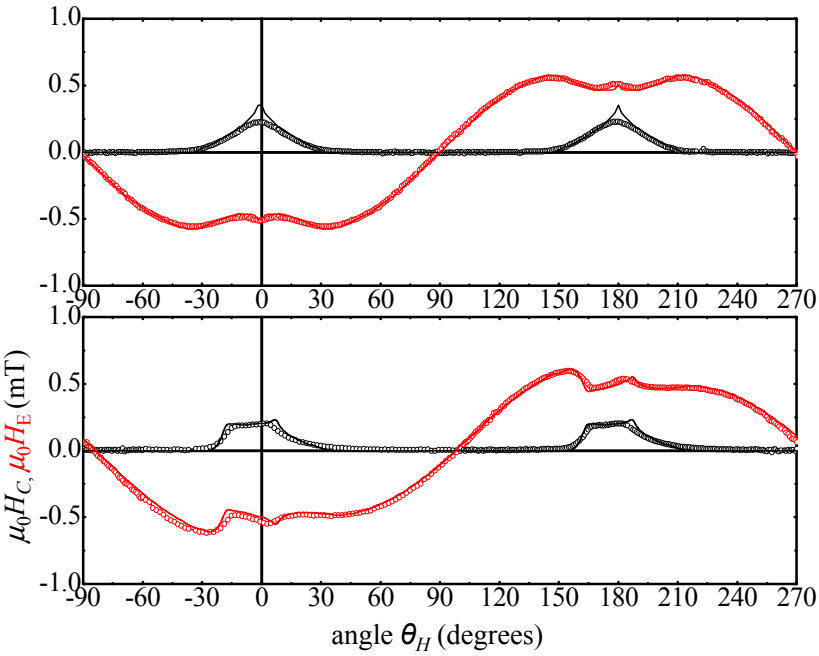

Figure 4.26: Angular dependence of exchange bias, $\mu_0 H_E$, and coercivity, $\mu_0 H_C$, for the (a) non-collinear and (b) collinear coupled Co/IrMn bilayer. The range of angles where only reversible processes take place during the reversal are marked by gray shadowed areas. The angular range around the FC direction where $M_\perp$ reverses in both semicircles is also highlighted in light yellow. The symbols are the experimental values derived from Kerr measurements as those shown in Fig. 2. Continuous lines are the simulated curves obtained using the SW model with the anisotropy configurations depicted in Fig. 4.22 (a).

region where the magnetization reverses in both semicircles also increases. This coincides with an increasing plateau in the angular evolution of coercivity. This increasing behavior reaches a maximum that in detail depends on K_E/K_U and decreases again towards $\beta_{FC} = 90°$, where the plateau vanishes again and reversal takes place in only one semicircle (see Fig. 4.27).

All the non-symmetric magnetic behaviors found experimentally in the non-collinear exchange coupled FM/AFM bilayer are well reproduced without any parameters with a simple coherent rotation SW-model including K_U and K_E misaligned β_{FC}, i.e. the FC angle with respect to the FM anisotropy direction, shown as solid lines in the Figures. The values K_U and K_E were extracted from the experimental data of the

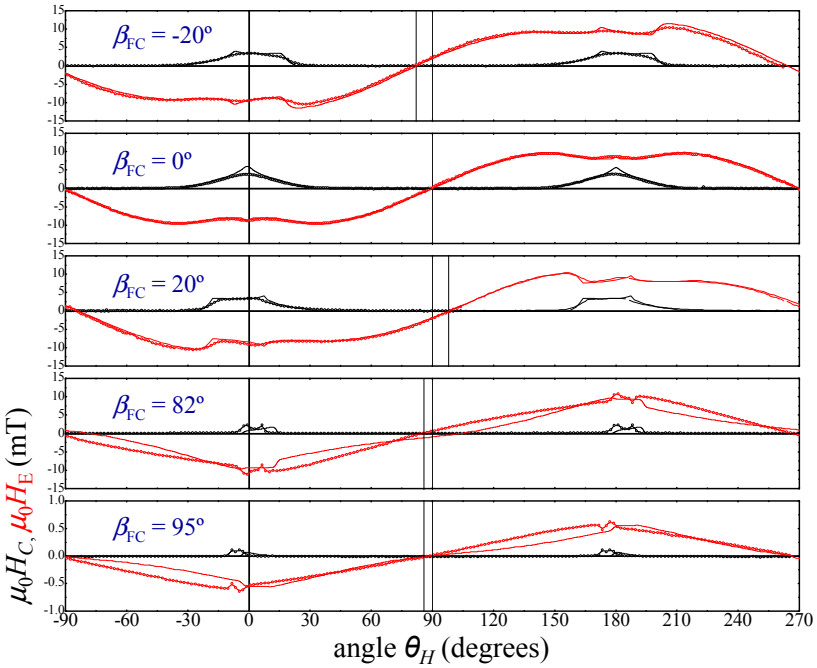

Figure 4.27: Angular dependence of exchange-bias, $\mu_0 H_E$, and coercivity, $\mu_0 H_C$, for non-collinear and collinear coupled Co/IrMn bilayer. The range of angles where only reversible processes take place during the reversal are marked by gray shadowed areas. The angular range around the FC direction where $M_\perp$ reverses in both semicircles is also highlighted in light yellow. The symbols are the experimental values derived from Kerr measurements. Symmetric behavior around the $\beta_{FC} = 0^\circ$ is found in both H_E and H_C. The exchange-bias field, H_E, crosses zero at different $\theta_H = 90^\circ$ depending the anisotropy configuration. Continuous lines are the simulated curves obtained using the SW-model with the anisotropy configurations depicted in Fig.4.22 (a).

reference FM film and the FM/AFM bilayers. The same anisotropy values were used to simulated the behavior of bilayer with collinear anisotropies, i.e. $\beta_{FC} = 0^\circ$, shown in Fig. 4.22.

4.4. Conclusions

To fully control the magnetic properties it is fundamental to perform detailed angular studies of remanences, critical fields and reversal processes. It has been shown

that even small anisotropy contributions can reorient the characteristic axes (butterfly shape) and drastically change the magnetization reversal behavior in very narrow angular regions, i.e. the change from 1 to 2, or even 3 sharp transitions. While pure system are qualitatively reproduced by the SW-model—i.e. the number of transitions is identical and only their angular position is shifted—mixed anisotropy systems can present transitions unpredicted by the SW-model. They only emerge due to a specific energy landscape in combination with domain wall nucleation and propagation. A detailed analysis of this type of systems strongly requires the additional measurement of the $M_{\perp}$-component. This once more emphasizes the relevance of the vectorial-Kerr setup.

The determination of the involved anisotropies, their relative orientation and strength are essential to determine the magnetic properties. In FM thin films non-collinear anisotropy can be tailored via deposition conditions (i.e., oblique *vs.* normal incidence) or substrate structure (i.e., polycrystal *vs.* single-crystal). In exchange-bias systems it is also possible to apply field cooling procedure with the external magnetic field misaligned with respect to the easy magnetization direction of the FM.

To gain a deeper insight into the exchange-bias the microscopic interface is studied, in the next chapter, by means of soft x-ray holography. The capability of element-selectivity and the accessibility to buried layers allows to investigated the coupling between FM/AFM at the interface level and to image the uncompensated moments of the AFM pinned to the FM layer.

References

[1] E. Jiménez, J. Camarero, J. Sort, J. Nogués, N. Mikuszeit, J. M. García-Martín, A. Hoffmann, B. Dieny, and R. Miranda, Phys. Rev. B **80**, 014415 (2009).

[2] S. Van Dijken, G. Di Santo, and B. Poelsema, Phys. Rev. B. **63**, 104431 (2001).

[3] D. Ecija, E. Jiménez, J. Camarero, J. M. Gallego, J. Vogel, N. Mikuszeit, N. Sacristán, and R. Miranda, Phy. Rev. B **77**, 024426 (2008).

[4] J. Camarero, J. Sort, A. Hoffmann, J. M. García-Martín, B. Dieny, R. Miranda, and J. Nogués, Phys. Rev. Lett. **95**, 057204 (2005).

[5] U. Welp, V. K. Vlasko-Vlasov, X. Liu, J. K. Furdyna, and T. Wojtowicz, Phys. Rev. Lett. **90**, 167206 (2003).

[6] Y. Zhai, L. Shi, W. Zhang, Y. X. Xu, M. Lu, H. R. Zhai, W. X. Tang, X. F. Jin, Y. B. Xu, and J. A. C. Bland, J. Appl. Phys. **93**, 7622 (2003).

[7] R. Zuberek, K. Fronc, W. Paszkowicz, and H. Szymczak, J. Magn. Mag. Mat. **283**, 28 (2004).

[8] M. Mathews, F. M. Postma, J. C. Lodder, R. Jansen, G. Rijnders, and D. H. A. Blanka, Appl. Phys. Lett. **87**, 242507 (2005).

[9] R. K. Kawakami, E. J. Escorcia-Aparicio, and Z. Q. Qiu, Phys. Rev. Lett. **77**, 2570–2573 (1996).

[10] Y. B. Xu, D. J. Freeland, M. Tselepi, and J. A. C. Bland, Phys. Rev. B **62**, 1167–1170 (2000).

[11] O. Thomas, Q. Shen, P. Schieffer, N. Tournerie, and B. Lépine, Phys. Rev. Lett. **90**, 017205 (2003).

[12] K.-Y. Wang, M. Sawicki, K. W. Edmonds, R. P. Campion, S. Maat, C. T. Foxon, B. L. Gallagher, and T. Dietl, Phys. Rev. Lett. **95**, 217204 (2005).

[13] X. Liu and J. K. Furdyna, J. Phys. Condens. Matter **18**, R245 (2006).

[14] F. Bisio, R. Moroni, F. Buatier de Mongeot, and L. Canepa, M.and Mattera, Phys. Rev. Lett. **96**, 057204 (2006).

[15] Y. T. Millev, H. P. Oepen, and J. Kirschner, Phy. Rev. B. **57**, 5848 (1997).

[16] J. Nogués and I. K. Schuller, J. Magn. Magn. Mater. **192**, 203 (1999).

[17] A. Tillmanns, S. Oertker, B. Beschoten, G. Güntherodt, J. Eisenmenger, and I. K. Schuller, Phys. Rev. B **78**, 012401 (2008).

[18] J. Nogués, D. Lederman, T. J. Moran, and I. K. Schuller, Phys. Rev. Lett. **76**, 4624 (1996).

[19] P. Miltényi, M. Gierlings, M. Bamming, U. May, G. Güntherodt, J. Nogués, M. Gruyters, C. Leighton, and I. K. Schuller, Appl. Phys. Lett. **75**, 124998 (1999).

[20] J. Nogués, T. J. Moran, D. Lederman, and I. K. Schuller, Phys. Rev. B **59**, 6984 (1999).

[21] J. Olamit, Z. P. Li, I. K. Schuller, and K. Liu, Phys. Rev. B **73**, 024413 (2006).

[22] S. H. Chung, A. Hoffmann, and M. Grimsditch, Phys. Rev. B **71**, 214430 (2005).

[23] J. Camarero, Y. Pennec, J. Vogel, S. Pizzini, M. Cartier, F. Fettar, F. Ernult, A. Tagliaferri, N. B. Brookes, and B. Dieny, Phy. Rev. B **67**, 020413 (2003).

Chapter 5

Imaging and quantifying the perpendicular exchange bias phenomena

A picture is worth a thousand words.

The perpendicular exchange coupling in FM/AFM systems is investigated by combining soft x-ray magnetic spectroscopy and magnetic holography measurements. Ferromagnetic $[Co/Pt]_n$ multilayers with perpendicular magnetic anisotropy exchange coupled to antiferromagnetic IrMn to FeMn films have been prepared in specially designed sample-mask structures. The element specificity and the ability to measure in applied magnetic fields have been exploited in order to quantify and to image the phenomena. The holography experiments allow the visualization of both FM and uncompensated AFM magnetic structures, showing that they replicate to each other during magnetization reversal. These results provide new microscopic insights into the exchange coupling phenomena and explore the sensitivity limits of the technique.

This Chapter presents element-selective microscopic magnetization reversal studies of room temperature perpendicular exchange coupled $[Co/Pt]_n$/AFM systems by means of the new experimental set-up developed for both soft x-ray spectroscopy and holography imaging purposes, as described in Chapter 2. In the first Section

is briefly introduced the exchange coupling phenomena in perpendicular magnetic anisotropy systems. The second Section gives the details on the preparation of the sample-mask structures as well the previous magnetic characterizations performed with standard (no element specific) techniques. The third Section introduces the different element-specific measurements that have been performed. The fourth and fifth Sections show the element-specific experimental results obtained in two different systems, i.e. $[Co/Pt]_n$/IrMn and $[Co/Pt]_n$/FeMn systems. The summary and the general conclusions on the perpendicular exchange coupling phenomena are given in last section.

5.1. Introduction

The interfacial exchange coupling phenomenon in ferromagnetic/antiferromagnetic (FM/AFM) systems was discovered almost half a century ago [1], but despite extensive research, there are still ongoing controversies about the underlying basic mechanism [2]. The most notable changes in the FM hysteresis loops in FM/AFM systems are a displacement away from the zero field axis, referred as exchange bias H_E, an enhanced coercivity H_C , and an asymmetric behavior in the magnetization reversal (see Chapters 3 and 4). The formers features are actually used in advanced magnetic in-plane spintronic devices [3, 4], by pinning the harder reference layer in spin valve heads and magnetic random access memory circuits, and will play an important role in future nanometer-sized magnetic in-plane or out-of-plane information storage media [5], by effectively increasing the stability of small magnetic particles, and in magnetic out-of-plane data-storage devices.

Most of the studies on FM/AFM systems have focused on systems where the magnetization of the ferromagnetic layer is confined to the film plane. In-plane exchange coupling effects have been found in single- and poly-crystalline FM/AFM structures [3], including those in which the AFM layer presents a compensated spin structure at the surface, where the effects are induced by atomic-level roughness features [6]. It has already been found that pinned (non pinned) uncompensated AFM spins at the interface are correlated with H_E [7] (H_C [8, 9]), and that the competition between anisotropies determines the asymmetric behavior of the magnetization reversal [10], which depends on the angle of the applied field. In the previous chapters it has been shown that also the configuration between the involved anisotropies is a key parameter to understand the peculiar magnetic behavior of in-plane exchange biased systems [11–13].

The study of exchange-bias phenomena in perpendicular magnetic anisotropy

(PMA) systems is a very recent issue. Perpendicular exchange bias effects in FM/AFM systems were firstly reported in 2000 below room temperature [13–14], and one year later above room temperature [14, 15]. The latter was an important breakthrough opening the way for building up new sensors and magneto storage devices based in exchange biased PMA systems. The fundamental study of the exchange bias in systems with PMA is interesting because significant differences may be expected with the magnetic properties of systems with in-plane mangetic anisotropy. From a more applied point of view, this offers the possibility to make spin-valves or tunnel junctions with perpendicular-to-plane magnetization that can be quite useful for magnetic field sensors, especially integrated planar sensors, or for magnetic random-access memory devices.

Perpendicular exchange-coupling effects have been found in several FM/AFM systems [14–29]. From a basic research point of view, the study of this phenomenon is interesting to elucidate both similarities and differences in the micromagnetic and dynamical properties between systems with in-plane and with perpendicular-to-plane anisotropy. Technologically these studies are also important because perpendicular exchange coupling offers the possibility of preparing spin valves or tunnel junctions with perpendicular magnetization [15, 18, 19]. So far, different PMA systems, i.e., [Pt/Co] [15–19, 28] [Pt/FeCo] [14], Ni[20], or $[Pd/Co]_n$ [21] multilayers based systems, have been successfully perpendicularly exchange-coupled with several AFM films, such as FeF_2 [16], CoO [15, 17, 22, 23], FeMn [14, 18, 19, 21, 24, 25, 29], NiO [20], IrMn [26, 29], NiMn [29]. Note that all of them are AFM systems that also have been used to pin FM layers in the film plane. This indicates that the simple picture of a coplanar AFM spin structure is not correct but a 3D AFM spin structure with components both in the film plane and normal to the film plane is present [30, 31]. This 3D spin structure leads in-plane or perpendicular exchange coupling depending on the anisotropy direction of the FM layer [17], and on its magnitude compare with the FM/AFM exchange anisotropy [28]. Perpendicular exchange coupling persists well above room temperature for FM/AFM systems with metallic AFM, like for the in-plane exchange coupled systems. The crucial key to obtain perpendicular exchange coupling is thus to have strong PMA in the FM layer to avoid the in-plane reorientation attempt exerted by the AFM layer at the interface.

The basic description of the perpendicular exchange-coupling in FM/AFM systems is illustrate in Fig. 5.1 For temperatures above the AFM ordering temperature (T_N), the spin structure of the AFM layer is disordered. Upon cooling down trough T_N with the FM layer saturated along the perpendicular direction, the AFM spins close to the interface couple and align with the interfacial FM spins, yielding the energeti-

cally stable situation for the coupling at the interface. To reverse the FM layer in the opposite direction, and assuming that the AFM spins are not affected by the external field, the FM layer must overcome this interfacial exchange energy in addition to its intrinsic anisotropy energy. In contrast, the interfacial coupling , would help the FM layer to reverse to its original direction. This results in an hysteretic reversal behavior shifted from the zero field a bias field H_E, which must be proportional to the interfacial exchange energy and inversely proportional to the FM thickness, since it is an interface phenomena. Similarly to in-plane biased systems, the existence of unpinned AFM spins that are dragged by the torque exerted by the FM layer during reversal, would promote an enhanced coercivity.

This simple description will be analyze by studying the element-selective magnetic properties obtained from soft x-ray magnetic spectroscopy and holography measurements performed in perpendicular exchange coupled $[Pt/Co]_n$/AFM systems.

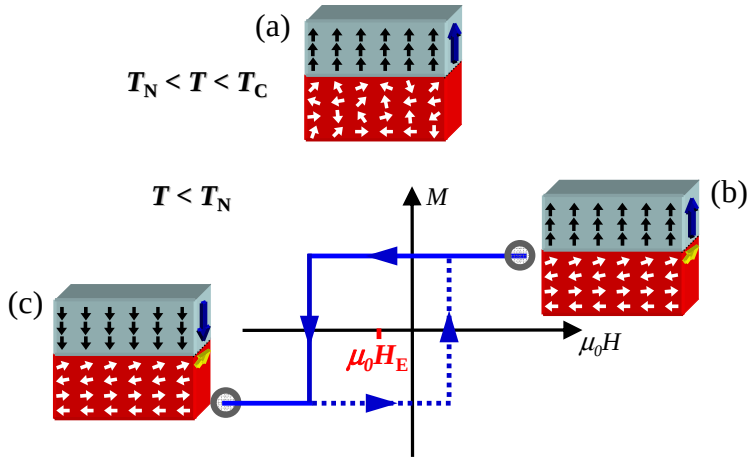

Figure 5.1: Schematic representation of the perpendicular exchange coupling phenomenon showing the spin configuration of an FM/AFM system at different stages: (a) above the AFM ordering temperature T_N; b) upon cooling with the FM layer saturated along the perpendicular direction, the AFM spins at the interface couple and align with the FM spins; c) when the applied magnetic field reverses the FM layer, while the AFM spins are not directly affected. The middle graph illustrate the corresponding hysteresis loop.

5.2. Sample-mask preparation

Specially designed sample-mask structures for the holography purposes were prepared at SPINTEC, Grenoble, France. The sample-mask structure is schematically shown in Fig. 5.9. The samples were grown by sputtering [1.8 nm Pt/0.6 nm Co]$_n$/AFM, with n=8 and 4, onto a 100 nm thick Si_3N_4 membrane, to facilitate x-ray transmission measurements. The membranes were first precovered with a 1.2 nm Pt buffer layer to promote [111] texture. Different AFM layers have been used, 10 nm FeMn and 5 nm IrMn, in order to get exchange coupling effects at room temperature [15, 26]. The AFM film was then capped with 3 nm Al to prevent oxidation. Reference FM/AFM samples grown onto opaque Si/SiO_2 substrates were prepared in the same run in order to check the magnetic properties of the samples grown on transparent substrates in comparison with the ones grown on standard opaque substrates [15, 26]. The base pressure was 2×10^{-8} torr, whereas the Ar pressure during deposition was 2.5×10^{-3} mbar. All depositions were performed at room temperature with deposition rates of ~ 0.1 nm/s. During deposition the magnetron sputter source produced a significant stray field (~ 5 mT) perpendicular to the surface plane. The AFM layers were hence grown on [Pt/Co] multilayers that were nearly magnetically saturated. In any case, the sample-mask structures were field-cooled in a +0.2 T perpendicular magnetic field.

The back-side of the membrane supports an opaque sputtered [100 nm Au/10 nm Cr]$_{10}$ multilayer with a 1.8 μm diameter aperture for the field of view (object hole). Five smaller apertures around the object hole, each guiding a reference beam [32], were milled through the whole structure (see Fig. 5.9). The 1.1 μm thick [Au/Cr] mask guarantees that the x-ray beam is transmitted only through the object and reference holes. The diameter of the reference holes is in the range of $150 - 250$ nm, which determines the spatial resolution of the reconstructed images [33]. Note that the area defined by the object-reference apertures, i.e. $\pi(3.7\ \mu\text{m})^2$, is much smaller than the coherence area provided at ID08, of about ($17\ \mu\text{m} \times 307\ \mu\text{m}$) [34].

An extensive review of the structural characterization of the FM/AFM samples can be found in [15], for [Pt/Co]$_n$/FeMn, and [26], in the case of [Pt/Co]$_n$/IrMn, but the most important aspects are summarized in the next for the sake of completeness. The growth procedure results in very low roughness films with a fcc-[111] crystal texture, as indicate the low-angle x-ray reflectivity (see Fig. 5.3.a) and large-angle x-ray diffraction measurements (Fig. 5.3.b).

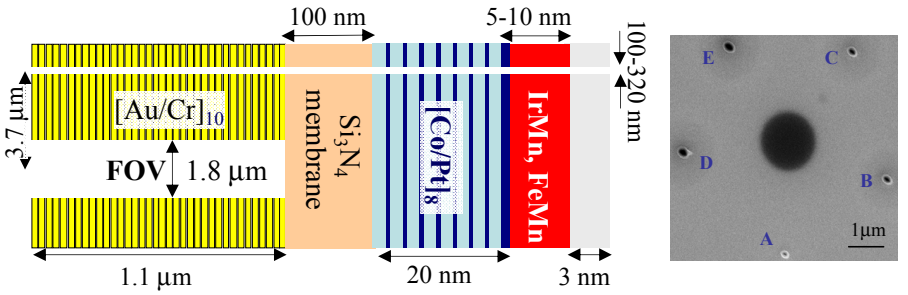

Figure 5.2: Sample-mask structure cross-section showing the aperture for the field of view and one aperture of the reference beam. A SEM image of the membrane showing the sample hole and the 5 reference holes is added on the right side.

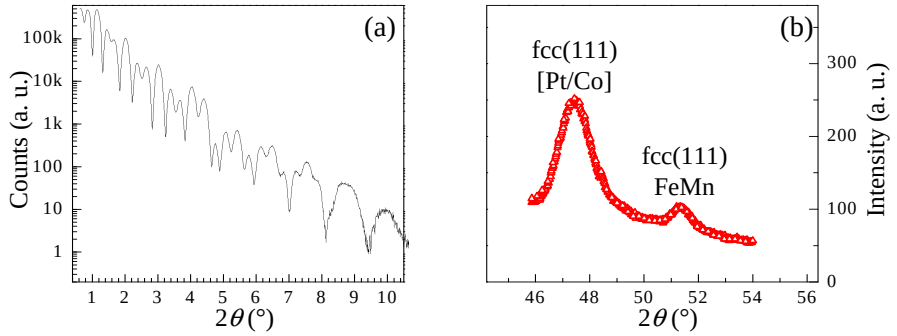

Figure 5.3: (a) Low-angle x-ray reflectivity of the $[Pt/Co]_4$/FeMn/Pt film grown with the procedure described in text. The observation of well-defined kiessing fringes indicates a very low roughness (RMS$<$ 0.2 nm). (b) Corresponding large-angle x-ray diffraction spectrum. The intensity peaks reflect the fcc-[111] texture of both FeMn and Pt/Co layers.

5.2.1. Kerr characterization

The magnetic characterization of the sample-mask structures and their magnetic homogeneity have been checked by using standard magnetometry techniques (without element specificity). Fig. 5.4 displays representative room temperature (RT) polar Kerr magnetization loops acquired by illuminating a $[Pt/Co]_8$/IrMn sample-mask structure from the top (IrMn side) and the bottom (Au side) with a 50 μm spotsize He-Ne laser beam. These Kerr loops probe the whole magnetic film deposited on

the membrane (mainly frame, similar to the TEY experiments) and the actual sample region in the object hole explored in the x-ray transmission experiments (because of the opacity of the Au mask to the laser beam), respectively. The measurements were carried out with the field applied perpendicular to the plane of the sample. Note that there is no difference between both Kerr loops, which reflects the large homogeneity of the FM/AFM structure. The hysteresis loop shows the usual effects of FM/AFM systems. The coercive field H_C=31 mT is enhanced with respect to a similar FM system, of about 2 mT, and an exchange bias field H_E of -5 mT is observed. In addition, the shape of the Kerr loops is identical to the one acquired in the x-ray transmission experiments, which excludes any impact on the exchange coupling properties during the x-ray measurements.

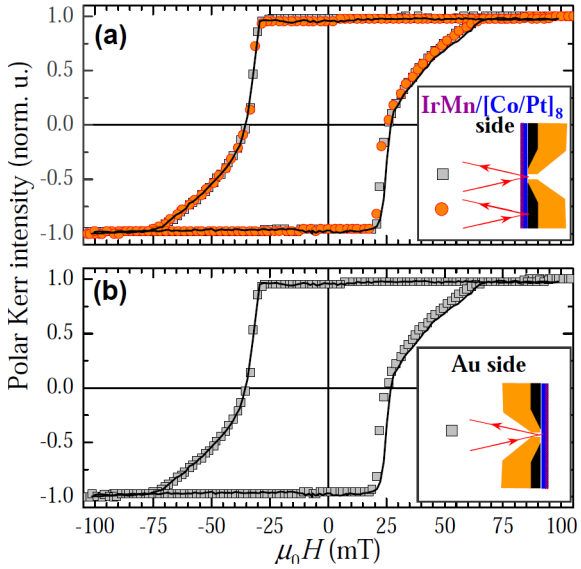

Figure 5.4: Polar Kerr hysteresis loops acquired by illuminating the $[Pt/Co]_8$/IrMn sample-mask structure from the IrMn (a) and Au (b) sides, as indicated in the insets. The symbols are the corresponding Kerr data. The solid line is the hysteresis loop recorded in transmission at the Co L_3 edge in the x-ray transmission experiment.

The hysteresis loop is similar, i.e. same shape and coercivity, compared to the one of a reference FM/AFM system grown on Si with the exception that the exchange bias is reduced [25]. Fig. 5.5 compares the RT polar Kerr loops measured on a [1.8 nm Pt/0.6 nm $Co]_8$/5 nm IrMn reference sample deposited onto an opaque Si/SiO_2 sub-

strate and onto the Si_3N_4 membrane, i.e. the sample studied with x-rays. Both samples were grown by magnetron sputtering in the same run using similar buffer and capping layers and field cooling (FC) procedure (described in the body of the manuscript). Both samples show similar coercive fields, $\mu_0 H_C$= 31 mT, and hysteresis curve shapes, indicative of a magnetization reversal by nucleation, propagation, and annihilation processes, as expected in perpendicular anisotropy systems when the magnetostatic interactions becomes important. On the contrary, the exchange bias value of the reference sample is three times larger, similar to the ones of [26], indicative of stronger interfacial coupling effect in the sample deposited onto a Si/SiO_2 substrate. This difference could be related to the different substrates used, e.g. different stress, but the opacity of the reference sample makes it not suitable for the x-ray experiments in transmission geometry. In any case, as discussed above, perpendicular exchange coupling effects are still observed in the transparent sample-mask structure needed for the soft x-ray transmission measurements.

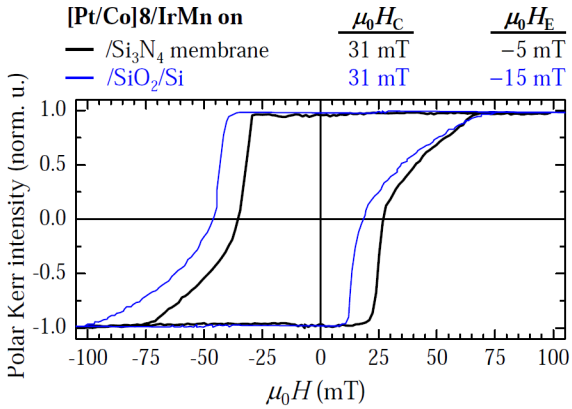

Figure 5.5: Hysteresis loop acquired from the sample-mask structure (black line) used for the soft x-ray holography measurements and in a reference sample deposited onto an *opaque* Si/SiO_2 substrate (blue line). Coercive field and exchange bias values are indicated.

5.3. Element-selective magnetic measurements

To understand the mechanisms that govern microscopically the magnetization reversal processes of perpendicular exchange-coupled anisotropy systems as well as to give direct evidences of the role of the interfacial coupling strength on it, we have used

a unique experimental set-up combining soft x-ray magnetic spectroscopy and holography capabilities, which provide quantitatively element(layer), spatial, and magnetic sensitivities that are not affected by external magnetic fields.

The basis of these measurements were already introduced in Chapter 2. The experiments were carried out at beamline ID08 of the European Synchrotron Radiation Facility (ESRF) which provides 100% circularly polarized light in the soft x-ray region. In this Section are detailed the experimental set-up, after the last pin-hole which defines the incoming synchrotron beam (see Fig. 2.11), and the different operation modes used in order to both quantify and image the magnetic properties of the whole system with element selectivity and in external applied fields.

5.4. Experimental setup

The experimental layout is schematically shown in Fig. 5.6. This set-up enables both quantifying magnetic properties of the whole system by spectroscopic means and imaging magnetic domains with element selectivity and in external applied fields.

The sample-mask structures were mounted in a high-vacuum chamber and the field applied perpendicular to the film surface was generated by an electromagnet mounted outside. The x-ray beam was incident along the surface normal (transmission geometry). Both, x-ray absorption and holography measurements were performed at room temperature (RT). The x-ray absorption spectra (XAS) were obtained by recording simultaneously the total electron yield (TEY), from the sample photocurrent measured with a picoamperemeter, and the transmitted photon intensity, by using a movable photodiode (see Fig. 5.1). Magnetic information is obtained from the x-ray magnetic circular dichroism spectra (XMCD), which is obtained from the difference of two XAS spectra acquired with opposite photon helicities, one taken with left circularly polarized light, and one with right circularly polarized light.

Holograms were recorded by removing the movable photodiode and by using a 16-bit back-illuminated charge-coupled device with 1300×1340 pixels, placed at a distance of 45 cm from the sample-mask position. The direct transmitted beam was blocked by a beam stop of 0.5 mm diameter, in order to avoid the high intense the straight-through beam. Holograms were acquired for opposite photon helicities at the corresponding L_3 absorption edges. Direct Fourier inversion of the difference pattern, i.e. magnetic hologram, yields an image of the magnetic domain structure within the object hole, as shown in Fig. 2.12

Due to its versatility in energy and polarization synchrotron radiation is used as light source. The coherence is achieved by means of a monochromator grating as well

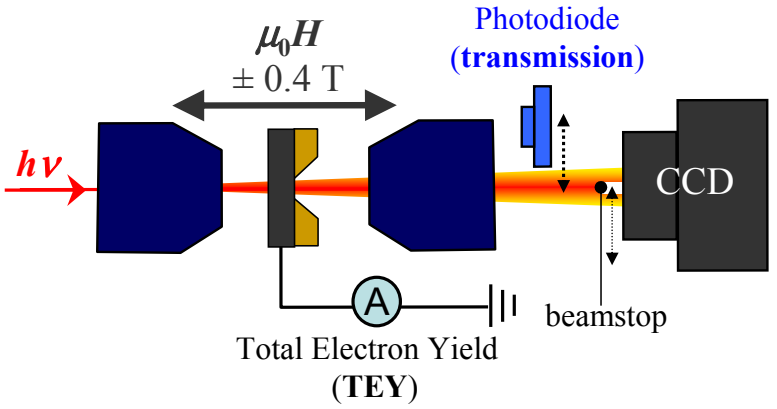

Figure 5.6: The difference in signal strength for TEY and transmission for the two possibilities of mounting the sample. Note that in the left panel the transmission signal contains Mn as well as Co information, while the right lower panel only shows a peak for Co.

as a pinhole (longitudinal and transversal coherence, respectively). These are the first parts of the beam line setup outside of the synchrotron ring. The sample is place in the vacuum chamber at the end of the beam line. At the sample position it is possible to apply magnetic fields via an electromagnet. The diffraction pattern is recorded with a CCD camera 45 cm away from the sample.In the spectroscopy configuration the CCD is replaced by a photodiode. In this way transmission and absorption spectra as well as the diffraction pattern images can be recorded(see section 2.2).

The sample can be mounted in two different ways, either with the gold-mask or the magnetic layers facing to the beam. The two different ways of mounting the sample give different signal-noise ratios, as depicted in Fig. 5.7. Especially for probing the FM/AFM interface higher quality is achieved by first illuminating the magnetic structure before passing the gold-mask. In the other orientation the light has first to pass all magnetic layers hence, the number of photons reaching the interface is significantly reduced.

Both measurements, total electron yield (TEY) and transmission spectra are taken in both sample orientation, 5.7 a), the gold-mask is facing the beam, in b) the magnetic part faces the beam. In both orientations the Mn $L_{2,3}$-edges are clearly visible in TEY. However, for imaging the interface it is necessary to see a dichroic signal in transmission. Note, no dichroic signal is observed when the gold-mask is facing the beam, while the other orientation gives a dichroic signal, although very small, see

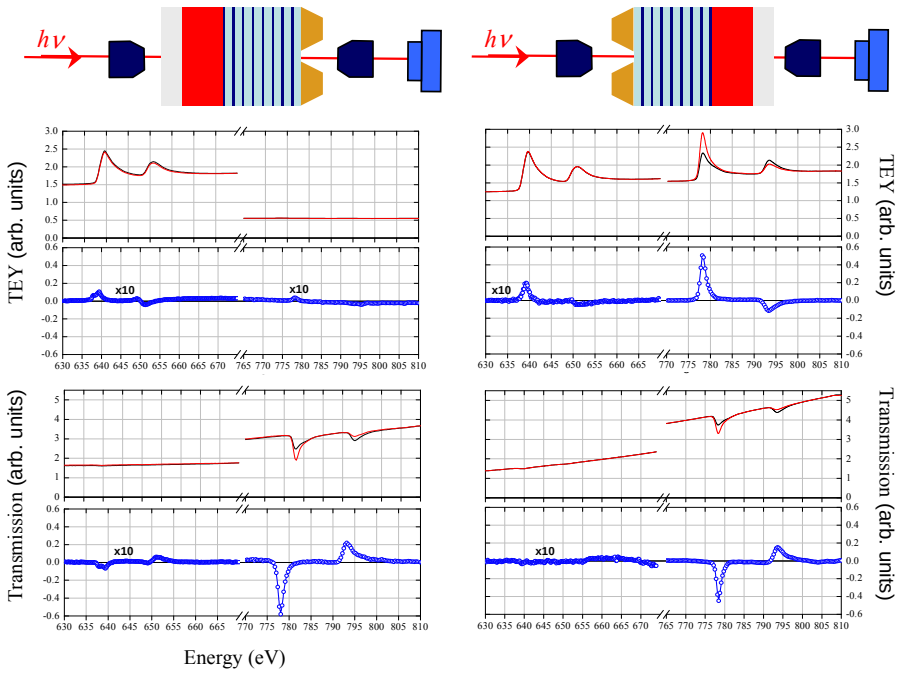

Figure 5.7: The difference in signal strength for TEY and transmission for the two possibilities of mounting the sample. Note that in the left panel the transmission signal contains Mn as well as Co information, while the right lower panel only shows a peak for Co.

Fig. 5.7b). As is shown in the following section this setup will allow to image the magnetic moments as well as the corresponding hysteresis loops.

Measuring the x-ray transmission as a function of applied field one can record hysteresis curves. The possibility to extract a hysteresis loop even from very small signals is shown in Fig. 5.8 (lower graph). The left panel of Fig. 5.8 shows the signal obtained from several (52 measurements) hysteresis loops. It seams that these loops do not contain any useful magnetic information; one might interpret them as noise. However, averaging all of them results in the hysteresis loop displayed in the right panel of Fig. 5.8. To properly center the hysteresis loops it is necessary to measure up to positive and negative saturation. From the saturated state one can calculate the total magnetic moment using the sum rules [35]. As expected cobalt shows the same moment for positive and negative saturation. The hysteresis loops obtained from the Co signal is shown in Fig. 5.8.

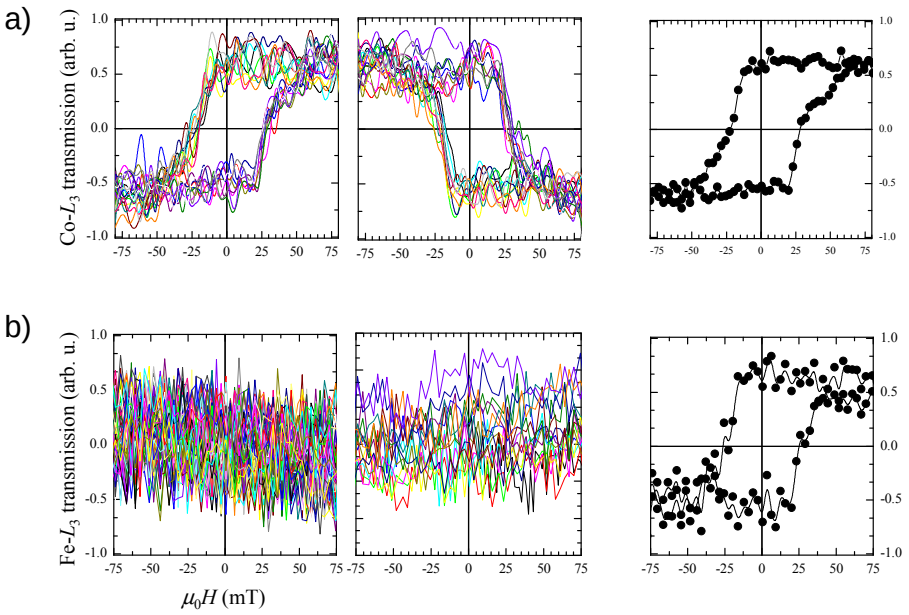

Figure 5.8: Hysteresis curves obtained by transmission. While a single measurement already presents clear hysteresis in case of Co (upper left panels), the signal of iron needs an averaging process.

5.5. The properties of CoPt Multilayers on IrMn

In this section magnetic soft x-ray holography is used as main technique to quantify the uncompensated moments of FM/AFM systems and to find their position at the interface. The reversal processes in the FM layer are imaged. We have studied $[Co/Pt]_n$/IrMn, $n = 8$ and $n = 4$, systems with an equivalent Co thickness of only 4.8 nm and 2.4 nm, respectively. The sample-mask structure was prepared by sputtering [1.8 nm Pt/0.6 nm Co]$_8$/5 nm $Ir_{20}Mn_{80}$ onto a 100 nm thick Si_3N_4 membrane, which was precovered with a 1.2 nm Pt buffer layer. The IrMn film was then capped with 3 nm Al to prevent oxidation. The back-side of the membrane supports an opaque [100 nm Au/10 nm Cr]$_{10}$ multilayer with a 1.8 µm diameter aperture for the field of view (object hole). Five smaller apertures around the object hole, each guiding a reference beam [32], were milled through the whole structure (see Fig. 5.9). The 1.1 μm thick [Au/Cr] mask guarantees that the x-ray beam is transmitted only through the object and reference holes. The diameter of the reference holes is in the range of

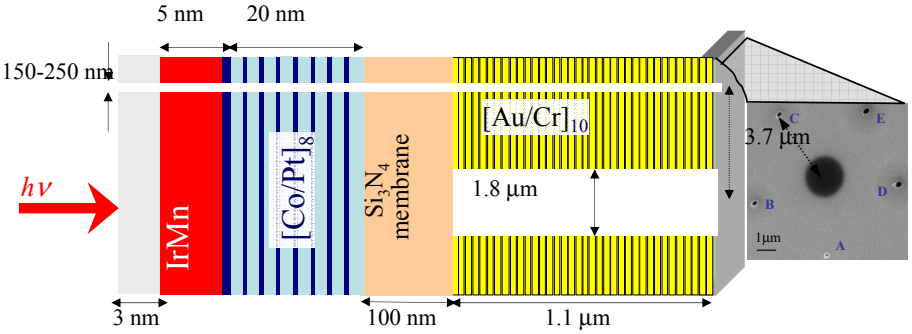

Figure 5.9: Sample-mask structure cross-section showing the aperture for the field of view and aperture of the reference beam. On the right an SEM image of the membrane showing the sample hole and the 5 reference holes is added.

150-250 nm, which determines the spatial resolution of the reconstructed images [33]. Note that the area defined by the object-reference apertures, i.e., $\pi(3.7\ \mu m)^2$, is much smaller than the coherence area provided at ID08, of about (17 µm×307 µm) [34].

The sample-mask structure was field-cooled in a +0.2 T perpendicular magnetic field and mounted in a high-vacuum chamber. The x-ray beam was incident along the surface normal with the IrMn film facing the beam. An electromagnet mounted outside allows to apply external magnetic fields perpendicular to the film surface, i.e., parallel to the x-ray beam. Both, x-ray absorption and holography measurements were performed at room temperature (RT). The absorption measurements were obtained by recording simultaneously the TEY, from the sample photocurrent measured with a picoamperemeter, and the transmitted photon intensity, by using a movable photodiode.

Element-selective magnetic quantification is achieved from the XMCD spectra obtained from the difference of the x-ray absorption spectra recorded with positive and negative photon helicities at the Mn and Co $L_{2,3}$-edges.

Fig. 5.10 shows absorption spectra at the Mn and Co $L_{2,3}$-edges recorded with positive and negative photon helicities (black and red continuous line, respectively), and the corresponding XMCD spectra (blue line). The obvious difference between the XMCD spectra can be understood by considering the different information depths of both detection modes. In the TEY detection mode the information depth is limited to about 2 nm, which corresponds to the electron escape depth [36]. On the other hand the photon penetration length is about 50 times larger at the absorption edges. Thus

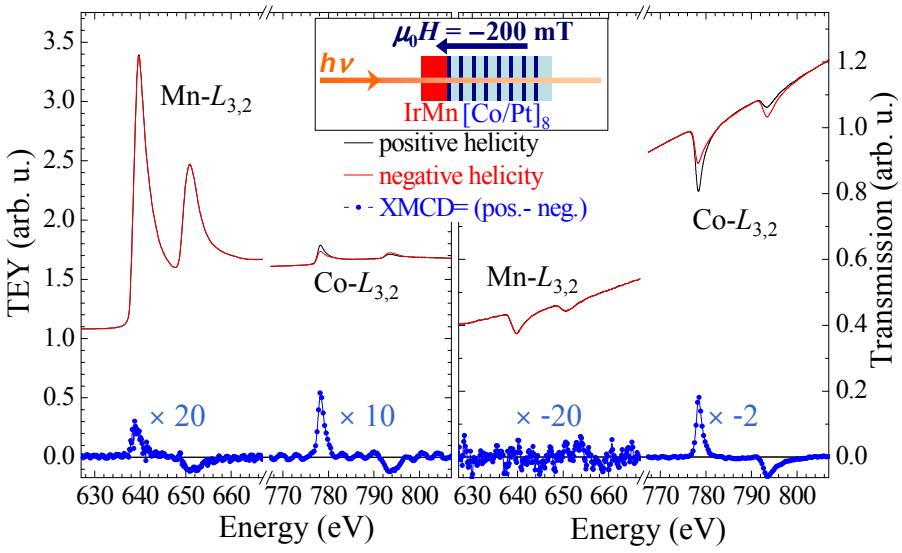

Figure 5.10: Absorption and XMCD spectra at the Mn-L and Co-L edges of the [Pt/Co]$_8$/IrMn sample recorded by the detection of the TEY signal (left) and the transmitted photon intensity (right). The sample is placed with the IrMn layer facing the incoming light in a external field of $\mu_0 H = -200$ mT, as the inset shows. The x-axis of the graphs is split for clarity. The spectral differences in both detection modes result from different probing depth and different background contributions (see text). Note that the small dichroism signal at the Mn-L edges is only seen by TEY detection.

TEY measurements are more sensitive to the topmost part of the IrMn layer while transmission measurements probe the whole AFM/FM system. The surface sensitivity of the TEY detection explains the larger Mn absorption signal in comparison to the Co absorption signal. The difference in probing depth is also the origin of the larger Co signal in the transmission spectra.

In addition to the different probing depths, there is also a difference in the background properties of both absorption spectra as a result of the presence of the reference holes. The photon intensity passing the reference holes gives a significant offset in the transmission spectra but has no effect on the TEY spectra. This is the reason for the small Mn absorption in the transmission spectrum compared to the TEY spectrum.

Fig. 5.11 shows the XMCD spectra, normalized to the corresponding absorption L_3 peak, acquired at both saturation states. The clear Mn-$L_{2,3}$ XMCD signals in the spectra shows the existence of a net Mn moment in the AFM layer. The same

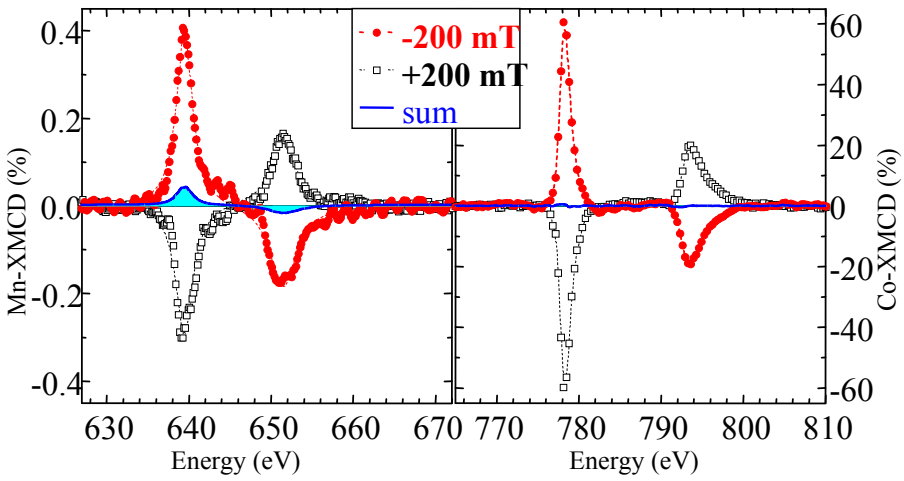

Figure 5.11: Normalized TEY-XMCD spectra acquired at the Mn-*L* (left) and Co-*L* (right) edges in negative (filled circles) and positive (empty squares) saturation. The solid line is the sum of the averaged XMCD spectra. The clear non-zero sum spectra at the Mn-*L* edge is related to the amount of uncompensated AFM moments which are fixed (pinned) during FM reversal, and its positive sign indicates that they are oriented opposite to the field cooling direction.

sign of both Mn and Co XMCD signals reveals a parallel alignment between the FM and the net (uncompensated) AFM moments. At negative saturation, the normalized XMCD at the Mn L_3 and Co L_3 edge corresponds to 0.4% and 60% of the polarization-averaged absorption signal, respectively. The size of the magnetic moment corresponding to uncompensated Mn spins was estimated by using sum rule analysis to be 0.05 μ_B, which is less than 2% of the magnetic moment of Mn (2.6 μ_B) in bulk $Ir_{20}Mn_{80}$ alloys [37]. We estimate an effective thickness of uncompensated Mn moments of (1.4 ± 0.5) monolayers (ML) assuming that they are localized at the AFM/FM interface. Similar values were found in perpendicular exchange biased $[Pt/Co]_n$/FeMn systems, [38] and smaller values in in-plane exchange biased FM/IrMn systems (~ 0.5 ML) [39].

Switching the magnetization to positive saturation, against the exchange bias field direction, led to a reversal of both Mn and Co XMCD signals, but a noticeable smaller XMCD signal is found at the Mn edge (see Fig. 5.11). This indicates that while some uncompensated AFM moments rotate during FM reversal (i.e. they are unpinned), a few of them are fixed (pinned), as concluded from the non-zero sum curve (blue line in Fig. 5.11). It has been widely accepted that the pinned (unpinned) AFM moments

are responsible for the exchange bias (coercivity enhancement). From the magnitude of the sum curve we quantify that only 10% of the uncompensated AFM moments are pinned, and from its sign we conclude that the pinned moments are oriented in the direction of the exchange bias field, i.e., opposite to the field cooling direction. This indicates a preferred antiparallel alignment between the FM and the pinned AFM moments, which suggests an antiferromagnetic coupling across the interface between them. This direct evidence confirms recent reports of antiparallel (parallel) alignment between the FM and the pinned (unpinned) AFM moments for both in-plane [40] and perpendicular [41] exchange biased FM/IrMn systems. Holograms were recorded by a 16-bit back-illuminated charge-coupled device (CCD), with 1300×1340 pixels, placed at a distance of 45 cm from the sample-mask position. Holograms were acquired for opposite photon helicities at the L_3 absorption edges. Direct Fourier inversion of the difference pattern, i.e., magnetic hologram, yields an image of the magnetic domain structure within the object hole. [33]

The magnetic imaging capability of the set-up is shown in Fig. 5.12. In the figure

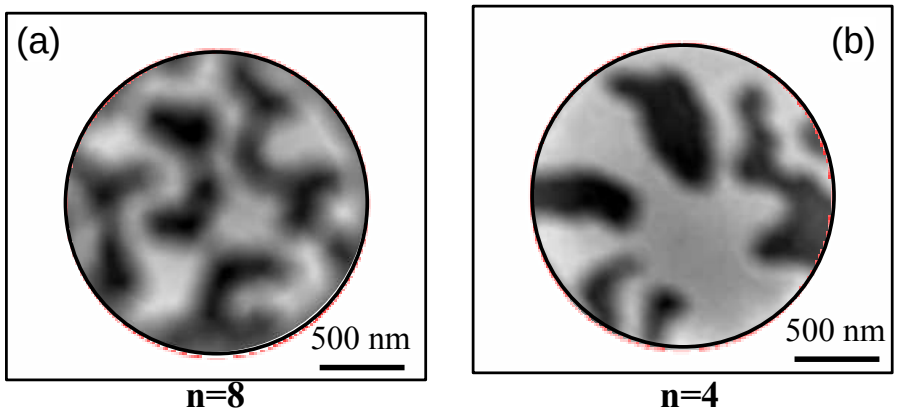

Figure 5.12: Co magnetic domain images of $[Pt/Co]_n/5$ nm IrMn films with $n = 8$(a) and $n = 4$(b) in their demagnetized states. The images are retrieved from the spatial Fourier transformation of magnetic holograms acquired at the Co-L_3 absorption edge, as described in the text. The derived domain periodicity (reference hole size) are of about 500 nm (150 nm) and 700 nm (100 nm) for the film with $n = 8$ and $n = 4$, respectively.

is compared the magnetic domain structure of the FM layer of $[Pt/Co]_n$/(5 nm) IrMn samples, with $n = 8$ and $n = 4$, which correspond with an equivalent Co thickness of 4.8 nm and 2.4 nm, respectively, acquired in zero field after demagnetizing the sample

in an alternating magnetic field with a decreasing amplitude. The sample with more Co ($n = 8$) shows a more blurred image because the size of its reference hole (150 nm) is only 3.3 times smaller than its domain periodicity (of about 500 nm), whereas the image corresponding to $n = 4$ (100 nm) has a reference hole 7 times smaller than its domain periodicity (of about 700 nm). The images show random magnetic domain structures with periodicities at least one order of magnitude smaller than in similar perpendicular anisotropy FM systems, as expected for FM/AFM systems. This originates from the low dimensionality and the minimization of dipolar effects in perpendicular anisotropy systems. The domain size is determined by the balance between the magnetostatic energy, which reduces upon domain formation, and the domain wall energy. Hence, the difference in domain size is likely to be due to the larger total magnetization [42], and therefore dipolar interaction, for the $n = 8$ sample.[1]

We also tried to image the uncompensated moments in the IrMn layer by soft x-ray holography but we could not observe any magnetic contrast at the Mn L_3 edge. This can be understood by the small amount of uncompensated AFM moments, as described above, and the strong background intensity in the transmission spectra, Fig. 5.10) which result in the vanishing Mn XMCD signal.

The element-selective hysteresis loop obtained from transmission measurements at the Co L_3 edge also shows the usual effects of FM/AFM systems (see central panel of Fig. 5.13). The coercive field $\mu_0 H_C = 31$ mT is enhanced with respect to a similar FM system (of about 2 mT), and an exchange bias field $\mu_0 H_E$ of -5 mT is observed.

The evolution of the magnetic domain structure of the FM layer along the whole hysteresis loop of the $[Pt/Co]_8/5$ nm IrMn sample is shown in Fig. 5.13. The images show that the magnetization reversal is characterized by nucleation of magnetic domains and domain wall propagation processes. Different magnetic domain configurations were also found in the increasing and decreasing field branches of the hysteresis loop, i.e., asymmetric reversal. This showed for the first time that holography experiments allow imaging the magnetization reversal of an exchange-biased FM layer with an equivalent Co thickness bellow 5 nm in real space and in external magnetic fields.

In this section the capabilities of the magnetic soft x-ray holography have been explored to study the properties of $[Co/Pt]_n/5$ nm IrMn multilayers ($n = 8$ and $n = 4$). Hysteresis loops obtained at the Co-edge have been measured and uncompensated moments at the FM/AFM interface have been quantified via absorption spectra. However, the uncompensated moments could not be imaged due to the small signal; in the following section this inconvenience is solved by changing the thickness of the AFM as well as its composition.

[1] The domain size is predicted to decrease with increasing film thickness in the ultrathin limit, only [42].

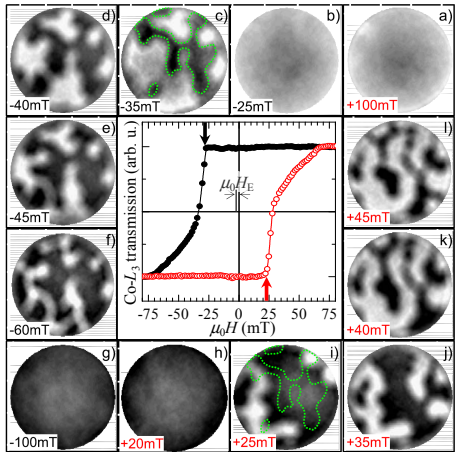

Figure 5.13: Evolution of the magnetic domain structure of the FM layer along the hysteresis loop. The images were recorded at the Co-L_3 edge. The magnetic field values are given in each image. Center: element selective hysteresis loop recorded in transmission at the Co L_3 edge. The exchange bias field and the nucleation fields (arrows) in both branches are indicated. The domain structure close to the nucleation point of the descending branch (c) is superimposed on the image recorded close to the nucleation field of the ascending branch (i).

5.6. The properties of CoPt Multilayers on FeMn

Macroscopically both FM/FeMn and FM/IrMn systems behave similarly, but different transmission sensitivities have been found regarding the capability to image the uncompensated AFM domain structure.

As in the previous paragraphs the experiments were carried out at beamline ID08 of the European Synchrotron Radiation Facility (ESRF), which provides almost 100 % circularly polarized light in the soft x-ray region. The experimental layout and the sample-mask structure are the same as in the previous section; the scheme is shown in Fig. 5.9. In the present case the AFM is FeMn, 10 nm thick. The diameter of the reference holes is in the range of $150-250$ nm, and the distance to the object aperture is 3.7µm, i.e. smaller than the transverse coherence length of the light (ξ_t). The latter depends on the wavelength of the photons (λ), the size of the source (d) and its distance from the sample (D), as explained in chapter 2.2. Here we placed a 50 µm diameter pinhole (secondary source) at 1.5 m from the sample. Then, at the Co-L_3 absorption edge, the transverse coherence is $\xi_t = \lambda D/2\pi d > 7$ µm ($\xi_l \simeq 300$ µm [34]).

The analysis carried out in section **??** concluded the exchange-bias phenomena as

interfacial effect. The technique, magnetic soft x-ray holography, allows to image the uncompensated moments responsible for this effect.

The analysis of the soft x-ray absorption spectra collected simultaneously by recording both the TEY and the transmitted photon intensity, provides valuable (quantified) information about the magnetic properties of the exchange-coupled FM/AFM systems, about their location in depth, as well as about the possibility to exploit dichroism in the transmitted beam intensity for imaging, as has been shown in the previous section.

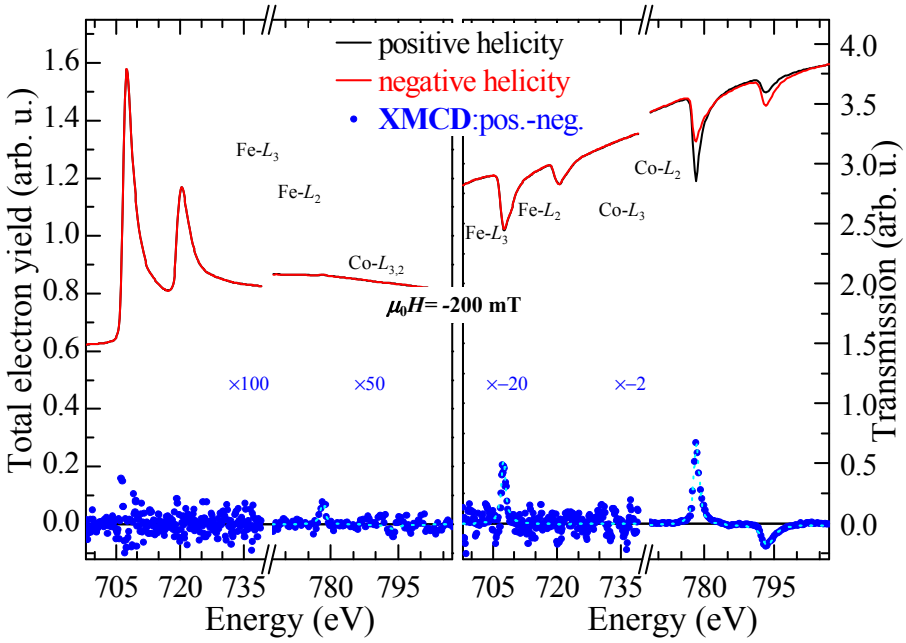

Figure 5.14: Absorption and XMCD spectra at the Fe-L and Co-L edges of a $[Pt/Co]_8$/10 nm FeMn sample recorded by the detection of the TEY signal (left) and the transmitted photon intensity (right). The sample is placed with the FeMn layer facing the incoming x-ray beam in a external field of $\mu_0 H = -200$ mT. The x-axis of the graphs is split for clarity. The spectral differences in both detection modes result from different probing depth and different background contributions (see text). Note that the small dichroism signal at the Fe-L edges is only seen by transmission detection.

Element-selective magnetic quantification of the FM/AFM systems can be achieved from XMCD spectra (see Fig. 5.14), and from element-selective hysteresis

loops recorded at selected L_3 absorption edges (Fig. 5.15). The latter shows a coercive field $\mu_0 H_C = 75$ mT and a clear non-zero exchange bias field $\mu_0 H_E = -10.5$ mT.

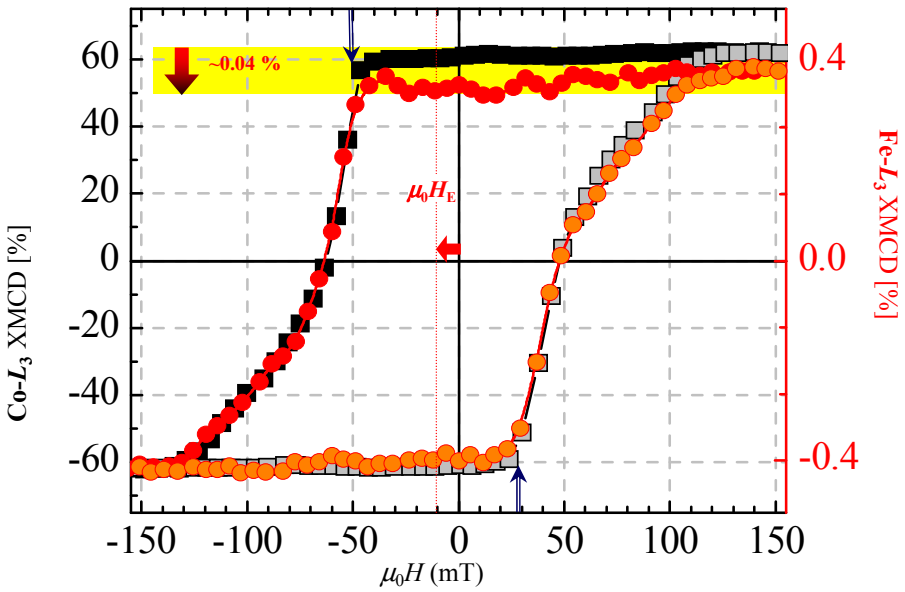

Figure 5.15: Element-selective XMCD hysteresis loops of a [1.8 nm Pt/0.6 nm Co]$_8$/10 nm FeMn sample acquired in transmission geometry. The symbols show the evolution of the XMCD signal with the external field recorded at the Co-L_3 (filled symbols, left y-axis) and Fe-L_3 (open symbols, right y-axis) edges, which reflect the hysteresis loop of the FM and the unpinned AFM moments, respectively. XMCD data are normalized to their corresponding absorption L_3 peaks.

Fig. 5.14 shows raw XAS spectra (top) at the Fe and Co $L_{2,3}$ absorption edges of the [Pt/Co]$_8$/10 nm FeMn sample recorded at negative saturation with positive and negative photon helicities, and the corresponding XMCD spectra (bottom). As explained before, the obvious difference between the absorption spectra can be understood by considering the different information depths of both detection modes. In the TEY detection mode the information depth is limited to about 2 nm, which corresponds to the electron escape depth [36]. On the other hand, the photon penetration length is about 50 times larger at the absorption edges. Thus TEY measurements are more sensitive to the topmost part of the FeMn layer while transmission measurements probe the whole system. The surface sensitivity of the TEY detection explains

the larger Fe absorption signal in comparison to the Co absorption signal. The difference in probing depth is also the origin of the larger absorption Co signal in the transmission spectra.

Note that the amount of uncompensated AFM moments derived from the spectroscopy analysis is similar for both $[Pt/Co]_8$/AFM systems. Different detection modes needed to be used as the Fe-XMCD signal is just found in transmission mode for FM/10 nm FeMn, while the Mn-XMCD signal is just found in the TEY mode for FM/5 nm IrMn (5.10). In both cases the top AFM surface was faced to the incoming x-ray beam. This apparent discrepancy can be ascribed to the difference in both probing depths (thinner AFM IrMn layer), photon flux (lower at the Mn edge), and absorption properties (slightly larger at the Mn edge). For instance, the vanishing Fe-XMCD signal in TEY measurements for the FM/FeMn system indicates that the uncompensated moments are deeply buried, as discussed above. On the other hand, the photon intensity passing the reference holes gives a significant offset in the transmission spectra, which makes it more difficult to detect tiny dichroic signals related to the uncompensated AFM moments (ca. 1% of the total absorption). In addition, the size of the reference hole of the FM/IrMn sample-mask structure was 1.5 times larger than the one of FM/FeMn, which resulted in larger transmitted intensity backgrounds at the absorption edges. All this results in a vanishing Mn-XMCD signal in transmission measurements for the FM/IrMn system. Hence, for the present samples, the possibility to exploit the dichroism in transmission measurements for imaging the domain structure of the uncompensated AFM moments was only possible for the FM/FeMn system.

The smaller domain periodicity found for the thicker sample (n=8) has been also found in perpendicular exchange-biased $[Pt/Co]_n$/FeMn systems by means of soft x-ray magnetic scattering measurements [38]. Here we show for the first time the magnetic structure of the uncompensated AFM moments during FM reversal. Fig. 5.16 displays element-selective magnetic images taken at positive saturation (right images) and during the decreasing field branch (left) of the hysteresis loop. The small but significant total integrated XMCD signal in transmission at the Fe-L_3 edge (30 times smaller than the signal at the Co-L_3 edge, as Fig. **??** shows) implies that long acquisition times had to be used for imaging the uncompensated AFM moments, i.e., fifteen times longer than for the Co images (for which we used 1 min). At positive saturation, the element-selective magnetic images show just bright gray scale values, whereas during the decreasing field branch several magnetic domains (dark) are observed. This reveals that the uncompensated AFM moments replicate the magnetic domain structure of the FM layer, proving that the FM moments *locally* drag the unpinned AFM

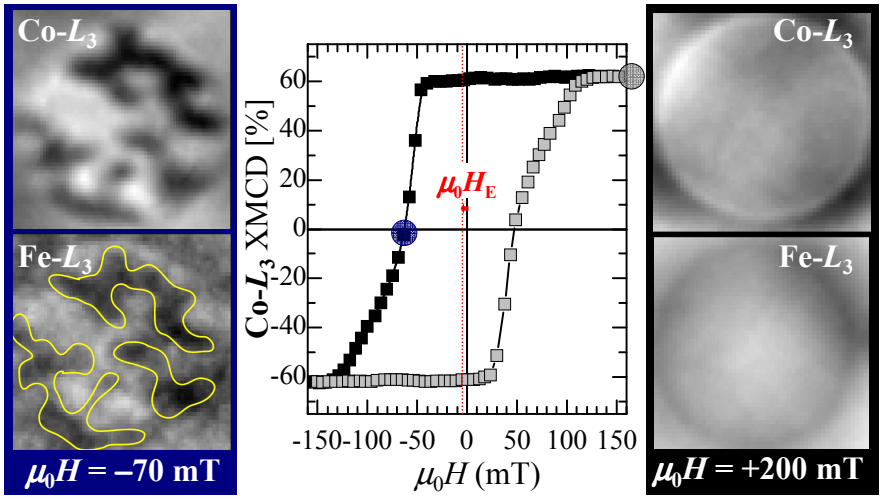

Figure 5.16: The XMCD hysteresis of Co in CoPt/FeMn (center panel). The outer panels show domain images obtained from the Co and Fe edge in the staurated and demagnetized state. Both, Fe and Co, obviously show the same structure.

moments during magnetization reversal. The energy cost to do that would explain the coercivity enhancement found in FM/AFM systems.

A complete element-selected hysteresis loop is presented in Fig. 5.17 and 5.18, Co and Fe, respectively. The images correspond to the central hysteresis loop.

At positive saturation (190 mA) both layers, FM and AFM, are saturated presenting dark contrast without any magnetic domain, decreasing the field (at 120 mA) nucleation phenomena has already started and the sample in both layers is broken into domains, as has been extract from the spectroscopy the domains from the AFM are dragged by the FM layer, the uncompensated unpinned moments at the interface are parallels to the FM layer. The annihilation process is present aroun 70 mA, the density of dark domains decrease in favor of the bright one. Finally, at 40 mA only one dark domain is present, before achieve bright saturation. In the ascending branch the unpinned moments from the interface are dragged by the FM layer, as can be seen in the images.

The asymmetry present in the hysteresis loop is well identified in the images, as can be seen at $\pm$60 mA, positive field image display a well defined are where only one bright domain is present whilst at negative field the dark domains are homogeneously

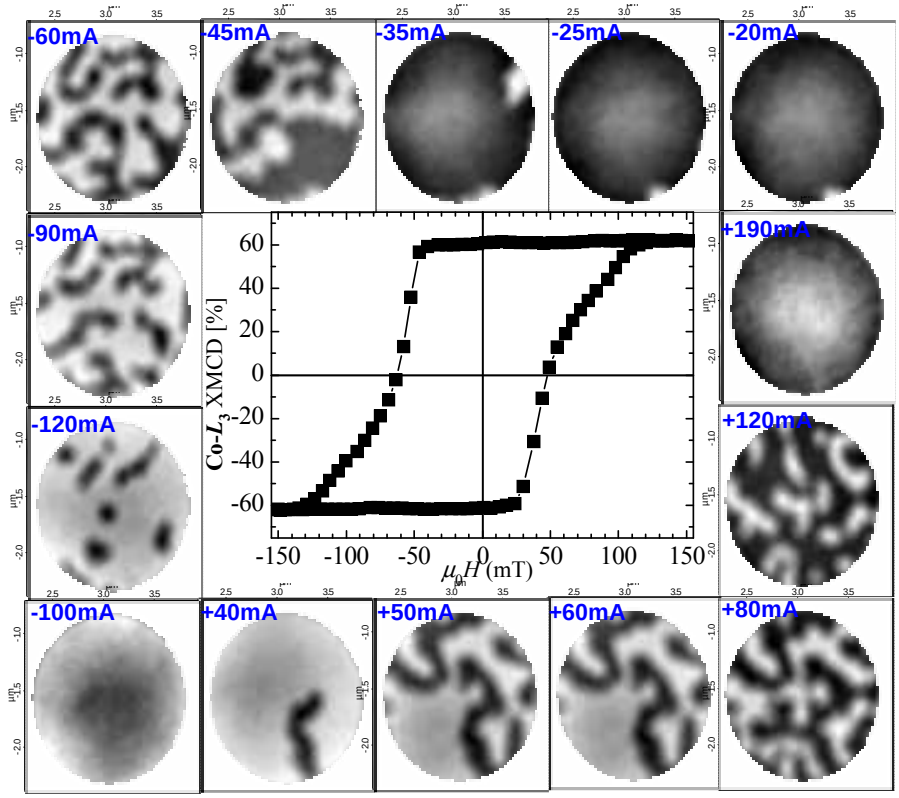

Figure 5.17: XMCD hysteresis loops from Co edge in CoPt/FeMn. For several field values also XMCD-holography images where taken. The asymmetry present in the hysteresis loop is well identified in the images, as can be seen at ± 60 mA.

distributed over all the sample, hence both layer, FM and AFM, present the same distribution.

5.7. conclusion

The holography imaging experiments allow visualizing the magnetization reversal processes of buried layers under external magnetic fields and quantify the magnetic moments. Two types of uncompensated AFM moments have been identified at the

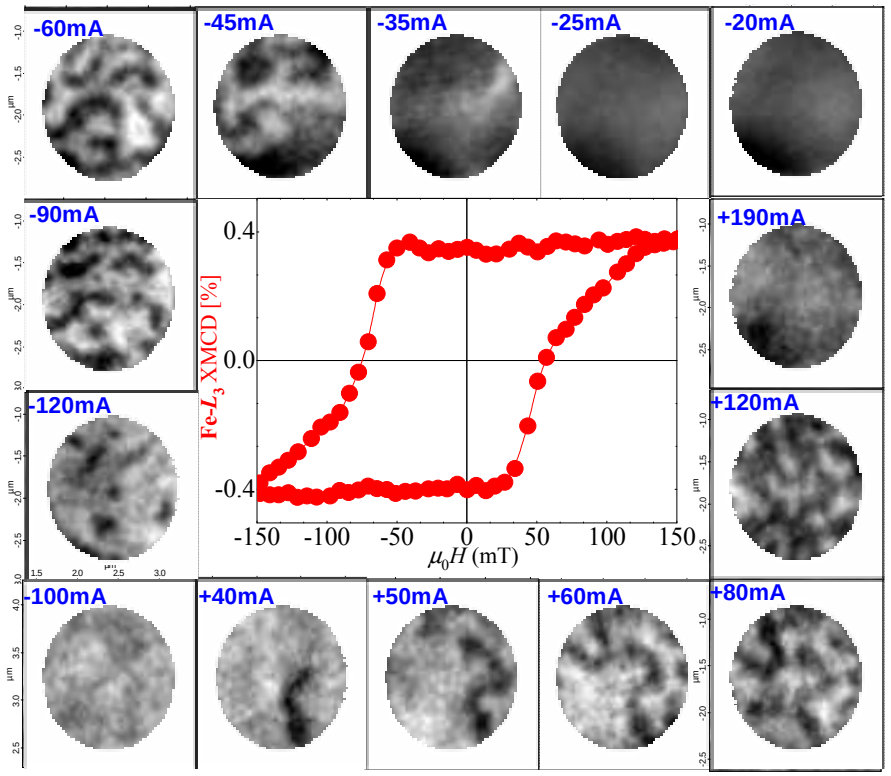

Figure 5.18: XMCD hysteresis loops from the Fe edge in CoPt/FeMn. For several field values also XMCD-holography images where taken. Although the Fe signal is much smaller than the Co signal, one can easily see that the domain structures are similar. Note, the reconstructed real space images have different size due to the different wavelength. Cutting the images with the same mask results in less information for the lower energy (larger wavelength), i.e. Fe.

FM/AFM interface. Uncompensated AFM moments rotate during FM reversal (i.e., they are unpinned), which are associated to the enhanced coercivity, while a few of them kept fixed (pinned), responsible of the exchange bias field. The unpinned Fe spins in CoPt/FeMn have been imaged, revealing that they replicate the FM domain structure.

References

[1] W. H. Meiklejohn and C. P. Bean, Phys. Rev. **102**, 1413 (1956).

[2] J. Nogués, T. J. Moran, D. Lederman, and I. K. Schuller, Phys. Rev. B **59**, 6984 (1999).

[3] J. Nogués and I. K. Schuller, J. Magn. Magn. Mater. **192**, 203 (1999).

[4] S. A. Wolf, R. A. Awschalom, D. D.and Buhrman, J. M. Daughton, S. von Molnár, A. Y. Roukes, M. L.and Chtchelkanova, and D. M. Treger, Science **249**, 1488 (2001).

[5] V. Skumryev, S. Stoyanov, Y. Zhang, G. Hadjipanayis, D. Givord, and J. Nogués, Nature **423**, 850 (2003).

[6] W. Kuch, L. I. Chelaru, F. Offi, J. Wang, M. Kotsugi, and J. Kirschner, Nature Materials **5**, 128 (2006).

[7] H. Ohldag, A. Scholl, F. Nolting, E. Arenholz, S. Maat, A. T. Young, M. Carey, and J. Stöhr, Phys. Rev. Lett. **91**, 017203 (2003).

[8] H. Ohldag, T. J. Regan, J. Stöhr, A. Scholl, F. Nolting, J. Lüning, C. Stamm, S. Anders, and R. L. White, Phys. Rev. Lett. **87**, 247201 (2001).

[9] J. Camarero, Y. Pennec, J. Vogel, S. Pizzini, M. Cartier, F. Fettar, F. Ernult, A. Tagliaferri, N. B. Brookes, and B. Dieny, Phy. Rev. B **67**, 020413 (2003).

[10] J. Camarero, J. Sort, A. Hoffmann, J. M. García-Martín, B. Dieny, R. Miranda, and J. Nogués, Phys. Rev. Lett. **95**, 057204 (2005).

[11] E. Jiménez, J. Camarero, J. Sort, J. Nogués, N. Mikuszeit, J. M. García-Martín, A. Hoffmann, B. Dieny, and R. Miranda, Phys. Rev. B **80**, 014415 (2009).

[12] E. Jiménez, J. Camarero, P. Perna, N. Mikuszeit, F. J. Terán, J. Sort, J. Nogués, J. M. García-Martín, A. Hoffmann, B. Dieny, et al., J. Appl. Phys. **109**, 07D730 (2011).

[13] E. Jiménez, J. Camarero, J. Sort, J. Nogués, A. Hoffmann, F. J. Teran, P. Perna, J. M. García-Martín, B. Dieny, and R. Miranda, Appl. Phys. Lett. **95**, 122508 (2009).

[14] F. Garcia, G. Casali, S. Auffret, B. Rodmacq, and B. Dieny, J. Appl. Phys. **91**, 6905 (2002).

[15] F. Garcia, J. Moritz, F. Ernult, S. Aufret, B. Rodmacq, B. Dieny, J. Camarero, Y. Pennec, S. Pizzini, and J. Vogel, IEEE Trans. Magn. **38**, 2730 (2002).

[16] B. . Kagerer, C. . Binek, and W. Kleemann, J. Mag. Magn. Mat. **217**, 139 (2000).

[17] S. Maat, K. Takano, S. S. P. Parkin, and E. E. Fullerton, Phys. Rev. Lett. **87**, 087202 (2001).

[18] O. Hellwig, S. Maat, J. B. Kortright, and E. E. Fullerton, Phys. Rev. B **65**, 144418 (2002).

[19] F. Garcia, J. Sort, B. Rodmacq, S. Auffret, and B. Dieny, Appl. Phys. Lett. **83**, 3537 (2003).

[20] Z. Y. Liu and S. Adenwalla, J. Appl. Phys. **94**, 1105 (2003).

[21] C. H. Marrows, Phys. Rev. B **68**, 012405 (2003).

[22] P. Kappenberger, S. Martin, Y. Pellmont, H. J. Hug, J. B. Kortright, and E. E. Hellwig, O.and Fullerton, Phys. Rev. Lett. **91**, 267202 (2003).

[23] S. M. Zhou, L. Sun, P. C. Searson, and C. L. Chien, Phys. Rev. B **69**, 024408 (2004).

[24] J. Sort, B. Dieny, M. Fraune, C. Koenig, B. Lunnebach, F.and Beschoten, and G. Güuntherodt, J. Appl. Phys. **84**, 3697 (2003).

[25] F. Romanens, S. Pizzini, F. Yokaichiya, M. Bonfim, Y. Pennec, J. Camarero, J. Vogel, J. Sort, F. Garcia, B. Rodmacq, et al., E. Phy. J. B **45**, 185 (2005).

[26] J. Sort, V. Baltz, F. Garcia, B. Rodmacq, and B. Dieny, Phys. Rev. B **71**, 054411 (2005).

[27] F. Romanens, S. Pizzini, F. Yokaichiya, M. Bonfim, Y. Pennec, J. Camarero, J. Vogel, J. Sort, F. Garcia, B. Rodmacq, et al., Phys. Rev. B **72**, 134410 (2005).

[28] S. van Dijken, J. Moritz, and J. M. D. Coey, J. Appl. Phys. **97**, 063907 (2005).

[29] S. van Dijken and J. M. D. Coey, J. Mag. Magn. mat. **290-291**, 1290 (2004).

[30] S. Altieri, M. Finazzi, H. H. Hsieh, H. J. Lin, C. T. Chen, T. Hibma, S. Valeri, and G. A. Sawatzky, Phys. Rev. Lett. **91**, 137201 (2003).

[31] W. Kuch, L. I. Chelaru, F. Offi, J. Wang, M. Kotsugi, and J. Kirschner, Phys. Rev. Lett. **92**, 017201 (2004).

[32] W. F. Schlotter, R. Rick, K. Chen, A. Scherz, J. Stöhr, J. Lüning, S. Eisebitt, C. Günther, W. Eberhardt, O. Hellwig, et al., Appl. Phys. Lett. **89**, 163112 (2006).

[33] S. Eisebitt, J. Lüning, W. F. Schlotter, M. Lörgen, O. Hellwig, W. Eberhardt, and J. Stöhr, Nature **432**, 885 (2004).

[34] G. Beutier, A. Marty, F. Livet, G. van der Laan, S. Stanescu, and P. Bencok, Rev. Sci. Instrum. **78**, 093901 (2007).

[35] B. T. Thole, P. Carra, F. Sette, and G. van der Laan, Phys. Rev. Lett. **68**, 1943–1946 (1992).

[36] R. Nakajima, J. Stöhr, and Y. U. Idzerda, Phys. Rev. B **59**, 6421 (1999).

[37] T. Yamaoka, M. Mekata, and H. Takaki, J. Phys. Soc. Jpn. **36**, 438 (1974).

[38] J. Camarero, J. Miguel, J. Goedkoop, J. Vogel, F. Garcia, F. Romanens, S. Pizzini, N. B. Brookes, J. Sort, and B. Dieny, Appl. Phys. Lett. **89**, 232507 (2006).

[39] M. Tsunoda, T. Nakamura, M. Naka, S. Yoshitaki, C. Mitsumata, and M. Takahashi, Appl. Phys. Lett. **97**, 072501 (2010).

[40] S. Doi, N. Awaji, K. Nomura, T. Hirono, T. Nakamura, and H. Kimura, Appl. Phys. Lett. **94**, 232504 (2009).

[41] P. Schmid, I. adn Kappenberger, O. Hellwig, M. J. Carey, E. E. Fullerton, and H. J. Hug, and Europhys. Lett. **81**, **17001** (2008).

[42] B. Kaplan and G. A. Gehring, J. Magn. Magn. Mater. **128**, 111 (1993).

Summary

> The whole is more than the sum of its parts.
>
> Aristotle

This thesis focus on selected modern aspects of artificial magnetic layered nanostructures involving different magnetic anisotropy contributions. For this purpose, two specific photon-based experimental tools have been developed. The experiments reveal that the symmetry of the (tailored) magnetic anisotropy in single FM layers and FM/AFM bilayers has a strong influence on their magnetic properties providing, in addition, new fundamental insights into the exchange bias phenomenon. The different magnetic features are reproduced with a model without any free parameter, disclosing the key parameters that control these effects. This knowledge will certainly open additional avenues to develop future advanced magnetic devices based on anisotropy-tailored magnetic nanostructures. Future perspectives are also discussed.

This thesis reports a systematic study on the angular dependence of the magnetic properties of both model and complex magnetic nanostructures with well-defined (tailored) magnetic anisotropy. These have been classified according to their symmetry, including twofold (uniaxial anisotropy), fourfold (biaxial), and onefold (unidirectional) symmetries, and for the systems combining two anisotropies according to the configuration between them, including collinear and non-collinear cases.

This work has been devoted to technical development as well as fundamental understanding. From the technical point of view, two new experimental tools have been developed in parallel:

- An artefact-free vectorial-Kerr magnetometer for angular-dependent magnetic measurements;

- A unique setup combining soft x-ray magnetic spectroscopy and holography measurements, which allows both to quantify and to image buried magnetic nanostructures with element(layer)-selectivity.

Both techniques are pure photon-based (photon-in/photon-out), allowing the determination of the magnetic properties under applied magnetic fields.

From the fundamental point of view, several general experimental observations have been found in all magnetic anisotropy symmetries investigated:

- The angular dependence of the magnetic properties reveals the symmetry of the magnetic anisotropy.

- The relevant magnetization reversal processes depends on the orientation of the external magnetic field with respect to the characteristic axis, θ_H:

  - In general, irreversible (nucleation of magnetic domains and further propagation of magnetic domain walls) and reversible (rotation of magnetization) transitions takes place during magnetization reversal.
  - Irreversible transitions are more relevant close to the e.a. directions whereas reversible ones are observed close to the h.a. directions.

Numerical simulations based on a modified Stoner-Wohlfarth model reproduce satisfactorily the experimental data, even so when the model just considers coherent reversal processes, i.e., magnetic domain formation is not taken into account (single particle approximation). In particular:

- The angular dependence of the magnetization remanence of both components, i.e., $M_{\mathrm{R},\parallel}(\theta_H)$ and $M_{\mathrm{R},\perp}(\theta_H)$ are well reproduced with the model in the whole angular range,

- The reversal fields, i.e., $\mu_0 H_{\mathrm{C}}$ and $\mu_0 H_{\mathrm{S}}$, are well predicted close to the h.a. directions while they are overestimated close to the e.a. directions.

From the comparison between experimental data and numerical simulations, several conclusions can be pointed out for all magnetic symmetries investigated:

- The similarities and differences between model and experimental data are related with the relevant mechanism during magnetization reversal. The model reproduces well the experiments if the magnetization reversal is governed by reversible processes (magnetization rotation).

- The model confirms that the key parameters that control the magnetic properties are the ratio between the involve anisotropies (relative strength) and the effective symmetry configuration.

The specific findings concerning the different anisotropy symmetries are schematically presented in Tab. 5.1 and 5.2. Among the partial conclusions described in each chapter, several scientific highlights are indicated in the next:

- Single FM films combining uniaxial (twofold) and biaxial (fourfold) magnetic anisotropy contributions with a *collinear h.a. configuration* (i.e., with the hard axes directions oriented parallel) results in a highly asymmetric magnetic behavior with non-orthogonal easy axes directions. This property can be tailored by controlling the ratio between anisotropies.

- Single FM films combining uniaxial (twofold) and biaxial (fourfold) magnetic anisotropy contributions with a *collinear e.a. configuration* (i.e., with the easy axes directions oriented parallel) present one, two, or three irreversible magnetic transitions, depending on θ_H. The angular range for the different behaviors can be tailored by controlling the ratio between anisotropies.

- At the interface of a ferromagnet (FM) and an antiferromagnet (AFM) at a real FM/AFM interface the unavoidable frustration of the exchange coupling between the FM and the AFM gives rise to a non-collinear anisotropy, which becomes important for ferromagnets with negligible intrinsic anisotropy.

- A non-collinear anisotropy configuration in exchange-biased FM/AFM bilayers is achieved by a field cooling procedure with the magnetic field reoriented with respect to the easy magnetization direction of the FM layer.

- The magnetic properties of perpendicular exchange-biased FM/AFM systems have been quantified and imaged with element (layer) selectivity, spatial resolution, and in presence of external fields. Remarkably, magnetic images of buried interfaces with effective thicknesses as small as one monolayer have been shown.

- Two types of uncompensated AFM moments located close to the FM/AFM interface have been identified. Uncompensated AFM moments rotate during FM reversal (i.e., they are unpinned), which are associated to the enhanced coercivity, while a few of them kept fixed (pinned), responsible of the exchange bias field.

- Direct evidence of antiparallel (parallel) alignment between the FM moments and the pinned (unpinned) uncompensated AFM moments have been found. This suggests an antiferromagnetic (ferromagentic) coupling across the interface between them.

- The magnetization reversal of the unpinned AFM moments has been imaged for the first time, showing that the magnetic structures of both FM and unpinned uncompensated AFM magnetic structures replicate each other during magnetization reversal.

5.8. Perspectives

Future perspectives include further investigations on the angular-dependence of the magnetic properties of other magnetic nanostructures as well as the development of new specific experimental tools. Artificial multilayers would include metallic, insulating, and semiconducting magnetic systems as well as multiferroic materials. The studies would be accomplished in both extended and lithographed systems. Future scientific tasks will be related with temperature, electric current, time-resolved, and single-shot experiments performed in both perpendicular and in-plane magnetic anisotropy systems.
In addition, future aims would be related with the improvement of the developed experimental tools. For instance, in the vectorial-Kerr magnetometer setup one can implemented several additional capabilities:

- Variable-temperature capability. The temperature dependence of the magnetic properties is crucial for the fundamental understanding of the magnetic phenomena at the nanoscale [1]. Among others, magnetic order, magnetic anisotropy, and magnetization reversal processes are thermally activated properties. However, there are not systematic angular studies including temperature dependence.

- Magnetoresistance detection will allow to study simultaneously both magnetization reversal mechanisms and magnetoresistive responses in multilayer structures to further determine the relationship between them. Large magnetoresistance (MR) effects observed in ferromagnetic (FM) layers separated by nonmagnetic (NM) spacers have attracted sustained interest over the past decades for both fundamental and technological reasons [2]. Even though it is commonly assumed that the MR depends on the magnetic anisotropy of the multilayer structure, a clear experimental proof of the direct relationship between

the magnetoresistive behavior and the magnetization reversal processes, which determine the magnetic configuration of the FM layers, is still lacking.

There is certainly scope for further improvement of the magnetic holography setup regarding higher spatial resolution and magnetic sensitivity as well as the capability to image in-plane magnetic anisotropy systems. For instance,

- Better spatial resolution can be achieved by using smaller reference holes or/and by using extended references, i.e., straight lines, by using the HERALDO (holography with extended reference by autocorrelation linear differential operation) concept [3]].
- Nondestructive resonant magnetic scattering measurements using single pulses from a free electron laser source can probe elementary magnetization dynamics in the femtosecond regime [4].
- The combination of off-normal geometry measurements (e.g., with the sample rotated by 45° with respect to the beam) with sample-mask structures with straight line reference apertures close to the object hole can provide in-plane magnetic sensitivity [5].

References

[1] P. Poulopoulos and K. Baberschke, J. Phys. Condens. Matter **11**, 9495–9515 (1999).

[2] A. Fert, Ange. Chem. Inter. Ed. **47**, 5956 (2008).

[3] D. Zhu, M. Guizar-Sicairos, B. Wu, A. Scherz, Y. Acremann, T. Tyliszczak, P. Fischer, N. Friedenberger, K. Ollefs, M. Farle, et al., Phys. Rev. Lett. **105**, 043901 (2010).

[4] C. Gutt, S. Streit-Nierobisch, L. M. Stadler, B. Pfau, C. M. Günther, R. Könnecke, R. Frömter, A. Kobs, D. Stickler, H. P. Oepen, et al., Phys. Rev. B **81**, 100401 (2010).

[5] C. Tieg, R. Frömter, D. Stickler, S. Hankemeier, A. Kobs, S. Streit-Nierobisch, C. Gutt, G. Grübel, and H. P. Oepen, Opt. Exp. **18**, 27251 (2010).

Table 5.1: Magnetic properties of model magnetic anisotropies

Magnetic Anisotropy		Characteristic Axes		$M_R(\theta_H)$	$H_C(\theta_H)H_S(\theta_H)$	Reversal processes	
		e.a. ($M_{\parallel,\perp}$)	h.a. ($M_{\parallel,\perp}$)	$M_{R_\parallel}$ $M_{R_\perp}$	$H_{C_i}(\theta_H)$	Jumps	Domain Wall (DW)
K_1						1	180° DW all angular range
K_2						1 2	180° DW around ±2° e.a. 90° DW around ±43° h.a.
K_1+K_2 h.a(K_1) ∥ h.a(K_2) $K_1/K_2 = 1/6.7$						1 2	180° DW around ±13° h.a. 90° DW around ±32° super h.a.
K_1+K_2 e.a(K_1) ∥ e.a(K_2) $K_1/K_2 = 1/3$						1 2	180° DW around ±27° e.a. 90° DW around ±16° super e.a.
K_1+K_2 e.a(K_1) ∥ e.a(K_2) $K_1/K_2 = 1/1$						1 3 2	180° DW around ±27° e.a. 90°*and*180° DW in ±+6° 90° DW around ±57° h.a.
K_1+K_2 e.a(K_1) ∥ e.a(K_2) $K_1/K_2 = 1/0.8$						1 2	180° DW around ±54° e.a. 90° DW around ±36° h.a.

Table 5.2: Magnetic properties of exchange bias anisotropies

Magnetic Anisotropy	Characteristic Axes		$M_{R_\parallel}(\theta_H)$	$H_C(\theta_H)H_E(\theta_H)$	Reversal processes	
	e.a. ($M_{\parallel,\perp}$)	h.a. ($M_{\parallel,\perp}$)			Rotation of $M_\perp$	Angular range
$\beta(K_1,K_U) = -20°$					2 semicircle	36° around e.a.
$\beta(K_1,K_U) = 0°$					1 semicircle	360°
$\beta(K_1,K_U) = +18°$					2 semicircle	43° around e.a.
$\beta(K_1,K_U) = +82°$					2 semicircle	22° around e.a.
$\beta(K_1,K_U) = +95°$					2 semicircle	11° around e.a.

Conclusions

The experimental studies presented in this thesis illustrate how versatile the magnetic properties at the nanoscale are. Factors like deposition conditions (i.e., oblique *vs.* normal incidence), substrate structure (i.e., polycrystal *vs.* single-crystal), artificial interfaces (including in-plane, perpendicular, and exchange-biased anisotropy systems), or like magnetic history (i.e., field-cooling procedures) have been shown to drastically affect the symmetry of the effective magnetic anisotropy of single FM systems (Co, FeNi and Fe ultrathin films) or exchange-biased FM/AFM systems. As a consequence, magnetic properties such as characteristic axes, reversal fields, magnetic stability, and magnetization reversal processes can be strongly altered. These facts immediately emphasize the need to control such factors and also the possibility to tailor the structure, morphology and magnetic properties of magnetic nanostructures according to a specific purpose.

These results provide new insights into the fundamental understanding of magnetic nanostructures and highlight the importance of performing detailed angular dependence measurements, including magnetization reversal studies, in order to properly account for their magnetic properties. In addition, the relationships found between the different factors described above and the symmetry of the magnetic anisotropy is fundamental to enable the preparation of anisotropy-tailored magnetic nanostructures. This knowledge will certainly open additional avenues to develop future advanced magnetic devices.

Conclusiones

El estudio experimental presentado en esta tesis demuestra la versatibilidad de las propiedades magnéticas a escala nanométrica. Factores como las condiciones de deposición (oblicua vs. incidencia normal), estructura del substrato (policristalina vs. monocristal), superficies artificiales (incluyendo sistemas con anisotropía en el plano, perpendicular y de polarización de canje (bicapas FM/AFM)) o la historia magnética (procedimientos de enfriamiento bajo campo) muestran un drástico efecto sobre la simetría de la anisotropía efectiva en láminas delgadas FM (Co, FeNi y Fe) así como en sistemas bicapas FM/AFM. En consecuencia, las propiedades magnéticas como los ejes característicos, campos de inversión, estabilidad magnética y los procesos de inversión de imanación se pueden alteradas drásticamente. Este hecho enfatiza la necesidad de controlar estos factores así como la posibilidad de diseñar a voluntad la estructura, morfología y las propiedades magnéticas de las nanoestructuras.

Los resultados revelan una nueva perspectiva, a nivel fundamental, de la propiedades magnéticas de las nanoestructuras y resaltan la importancia de realizar medidas detalladas de la depencia angular, incluyendo los estudios de inversión de la imanación para poder controlar las propiedades magnéticas. Además, la relación entre los diferentes factores descritos y la simetría de la anisotropía magnética es fundamental para el diseño de la anisotropía de las nanoestructuras. Este conocimiento, sin duda, habre la posibilidad de nuevas avenidas para el desarrollo de futuros dispositivos magnéticos.

Appendix A

Angular Kerr studies

In this appendix additional information—namely full angular Kerr studies—on the investigated systems is presented.

A.1. Full angular studies on models systems

In the following additional results to chapter 3 are shown.

A.1.1. Angular study of pure uniaxial permalloy

The angular evolution of the magnetic properties are extracted from the hysteresis loops measured with a precision of 1°. An example study is shown in Fig. A.1. Hysteresis loops from a 6 nm permalloy film are presented every 9°. Additionally, the theoretical prediction of the SW-model is plotted as continuous lines. If the applied magnetic filed would only cause coherent magnetization rotation, the SW-model would fit the data in the whole angular range. However, the nucleation and propagation of domains leads to noticeable deviations, especially near the e.a. Presenting the data in the $M_{\parallel}$-$M_{\perp}$-plane (Fig. A.2) many points are found inside the circle with radius M_S, the closer to the e.a. the more data points inside the circle (see figure A.2).

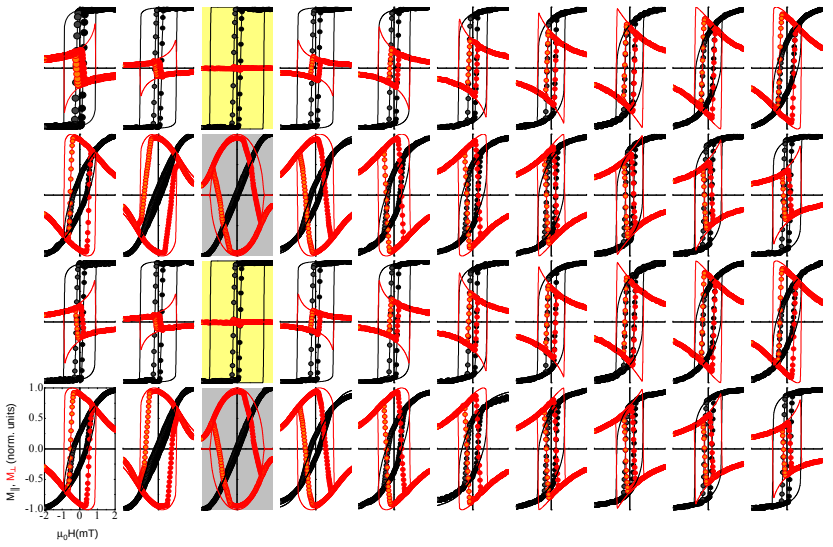

Figure A.1: An angular study of the hysteresis loops of a uniaxial FeNi thin film (6 nm). Loops are shown every 9°. The characteristics axis are highlighted (e.a. yellow, h.a. gray). Continuous lines correspond to solutions of the SW-model.

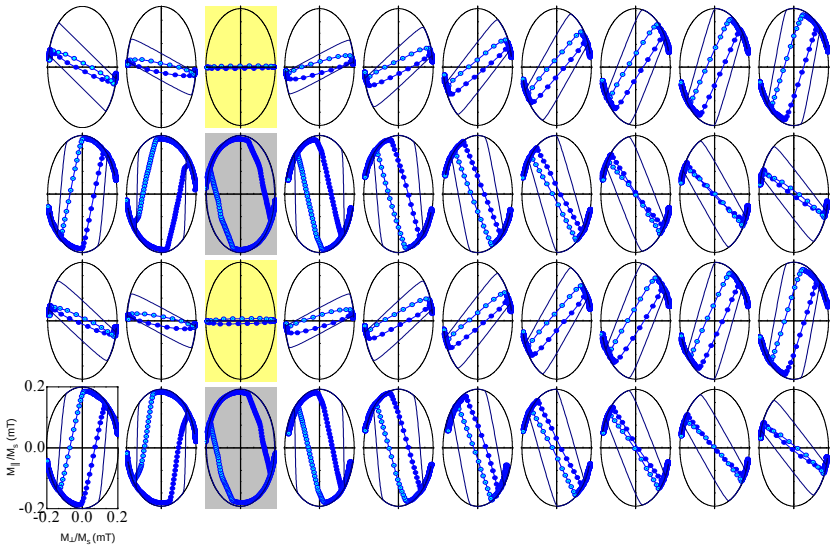

Figure A.2: . The complete angular study of the polar plots of the uniaxial FeN thin film. Measurements over 360° every 9° are shown in the $M_{\parallel}$-$M_{\perp}$-plane. The graphs highlighted in yellow are the 0° and 180° easy axes, while the gray background corresponds to the 90° and 270° hard axes. Continuous lines are predictions from the SW-model.

A.1.2. Angular study of pure biaxial iron

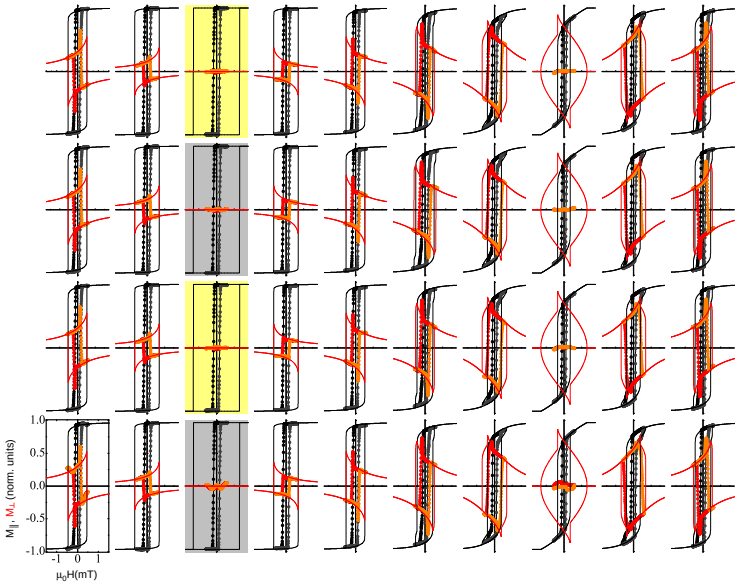

Figure A.3: Angular study of the hysteresis loops of biaxial a Fe/MgO(100)thin film (20 nm). Loops every 9° are displayed. The characteristics axis are highlighted (e.a. yellow, h.a. gray). Continuous lines correspond to solutions of the SW-model.

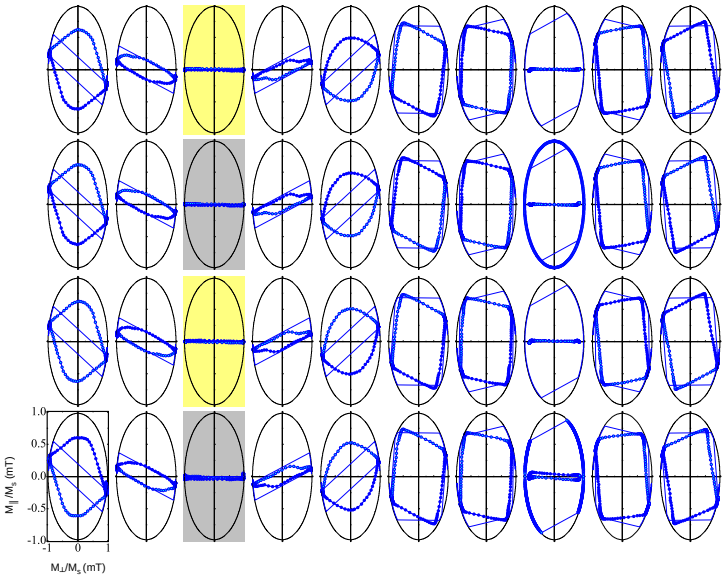

Figure A.4: The complete angular study of the polar plots of biaxial system, Fe/MgO(100), is represent in the graphic every 9°. The graphs in yellow background are the 0° and 90° corresponding to the easy axes and the gray background the 45° and 270° correspond to the hard axes of the system, as is predicted by the SW model for uniaxial anisotropic systems 270° off the easy axes

A.1.3. Angular study of exchange-biased uniaxial thin films

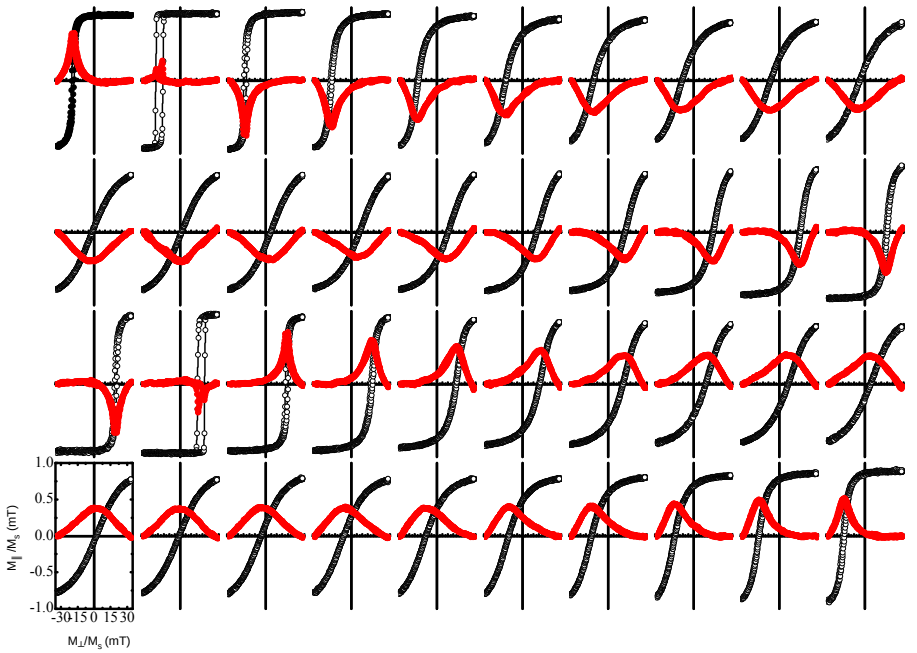

Figure A.5: The complete angular study of the hysteresis loops of the uniaxial system, FeNi, is represent in the graphic every 9°. The graphs in yellow background are the 0° and 180° corresponding to the easy axes and the gray background the 90° and 270° correspond to the hard axes of the system, as is predicted by the SW-model for uniaxial anisotropic systems 90° off the easy axes

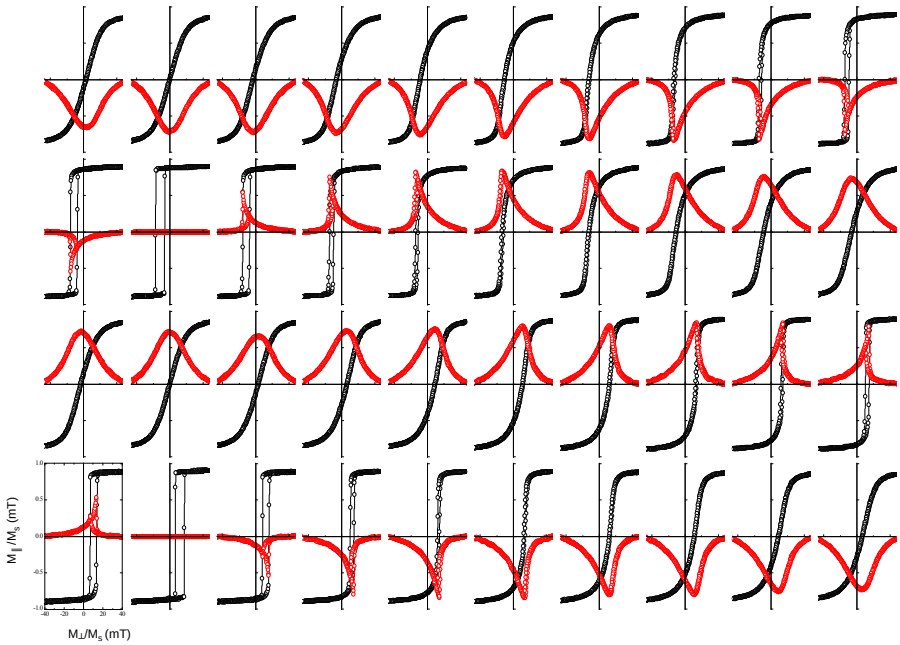

Figure A.6: The complete angular study of the hysteresis loops of the uniaxial system, Co, is represent in the graphic every 9°. The graphs in yellow background are the 0° and 180° corresponding to the easy axes and the gray background the 90° and 270° correspond to the hard axes of the system, as is predicted by the SW-model for uniaxial anisotropic systems 90° off the easy axes

Appendix B

Acronyms

AFM	Antiferromagnet
	Atomic Force Microscopy
CCD	Charge Coupled Device
DW	Domain Wall
e.a.	Easy Axes
ESRF	European Synchrotron Radiation Facility
FC	Field Cooling
FM	Ferromagnet
FOV	Field Of View
h.a.	Hard Axes
IGC	Inert Gas Condensation
LASUAM	Laboratorio de Superficies de la Universidad Autónoma de Madrid
LEED	Low Energy Electron Diffraction
MBE	Molecular Beam Epitaxy
MFM	Magnetic Force Microscopy
MOKE	Magneto-Optic Kerr Effect
M-MOKE	Magneto-Optic Kerr-Effect Microscopy
NIL	NanoImprint Lithography
PLD	Pulsed Laser Deposition
PMA	Perpendicular Magnetic Anisotropy
PVD	Plasma Vapor Deposition

SAM	Self-Assemble Monolayers
SAS	Small Angle Scattering
SEM	Scanning Electron Microscopy
SPM	Scanning Probe Microscopy
STM	Scanning Tunneling Microscopy
SW	Stoner-Wohlfarth
TEY	Total Electron Yield
v-Moke	vectorial Magneto-Optic Kerr-Effect
VSM	Vibrating Sample Magnetometry
XAFS	X-ray Absorption Fine Structure
XMCD	X-ray Circular Dichroism
XPS	X-ray Photoelectron Spectroscopy

Appendix C

Symbols

a	1-1-component of the Jones reflection matrix
$\mathbf{A}_{i,f,m}$	boundary matrix for initial, final, and magnetic medium
$\alpha_{1,2,3}$	angular alignment errors of optical components
$b_{1,2}$	M_y and M_z dependent parts of the 1-2- and 2-1-component of the Jones reflection matrix
β_{FC}	field cooling angle
$\vec{B}$	magnetic flux density
c	magnetization independent part of the 2-2-component of the Jones reflection matrix
d	M_x dependent part of the 2-2-component of the Jones reflection matrix
d	diameter
D	distance
$\mathbf{D}_{i,f,m}$	propagation matrix for initial, final, and magnetic medium
E_{p}	p-component of the electric field vector
E_{s}	s-component of the electric field vector
E	energy
E_{b}	energy barrier

E_{tot}	total energy
ε_{K}	Kerr ellipticity
$\mathbf{G}$	2×2 submatrix of the boundary condition matrix
H_{LS}	spin-orbit Hamilton operator
$\mathbf{H}$	2×2 submatrix of the boundary condition matrix
$\vec{H}$	magnetic field
H_{C}	coercive field
H_{E}	exchange-bias field
H_K	anisotropy field
H_{S}	switching field
$\mathbf{I}$	2×2 submatrix of the boundary condition matrix
I_0	intensity if initial beam
I_{p}	intensity of p-wave
I_{s}	intensity of s-wave
I_Δ	difference intensity of p- and s-wave
I_Σ	sum intensity of p- and s-wave
φ	angle of the magnetization with respect to the anisotropy easy axis
$\mathbf{J}$	2×2 submatrix of the boundary condition matrix
J	total angular momentum $(L+S)$
k	wave-vector
K	x-ray absorption edge
K_1	uniaxial anisotropy constant
K_2	biaxial anisotropy constant
K_{AFM}	("uniaxial") anisotropy of an antiferromagnet
K_{E}	unidirectional anisotropy constant
K_{FM}	("uniaxial") anisotropy of an antiferromagnet
K_{U}	Uniaxial anisotropy constant
$\vec{M}$	Magnetization vector
λ	wavelength
L	x-ray absorption edge

L	orbital angular momentum
$\mathbf{L}_2$	Jones matrix of a retarder
μ_0	permeability of free space
$\mathbf{M}$	boundary condition matrix (4×4)
M	x-ray absorption edge
$M_{\parallel}$	parallel component of the in-plane magnetization
$M_{\perp}$	transversal component of the in-plane magnetization
$M_{x,y,z}$	x, y, and z component of the magnetization
M_{S}	magnetization of saturation
M_{R}	magnetization of remanence
P_{I}	plane of incidence
P_{R}	plane of reflection
Q	Voigt constant
R_{ss}	reflectivity for s-polarized light into s-polarized light
R_{pp}	reflectivity for p-polarized light into p-polarized light
$\mathbf{r}$	Jones reflection matrix
$r_{\mathrm{ss,sp,ps,pp}}$	reflection coefficients for s-polarized light originating from s-polarized light, etc.
S	spin
t	thickness
t	time
T	temperature
T_{C}	Curie temperature
T_{N}	Néel temperature
$t_{\mathrm{ss,sp,ps,pp}}$	transmission coefficients for s-polarized light originating from s-polarized light, etc.
Θ	divergence angle of a wave
Θ_{K}	Kerr rotation
θ_H	in-plane angle of applied field

ξ	reversal asymmetry
$\xi_{l,t}$	longitudinal and transversal coherence length

List of Publications

[**1**] E. Jiménez *et al.*, *Imaging magnetization reversal of interfacial uncompensated AFM moments in exchange-biased FM/AFM systems*, in progress.

[**2**] E. Jiménez *et al.*, *Towards tailoring magnetic properties in exchange-biased systems*, in progress.

[**3**] E. Jiménez *et al.*, *On the road to custom-designed epitaxial thin films by controlled magnetic anisotropy symmetry breaking*, in progress.

[**4**] E. Jiménez *et al.*, *Artefact-free vectorial-Kerr magnetometry for the determination of magnetization reversal processes of magnetic nanostructures*, in progress.

[**5**] J. Camarero, E. Jiménez, J. Vogel, C. Tieg, P. Perna, A. Bollero, F. Yakhou-Harris, C. Arm, B. Rodmacq, E. Gautier, S. Auffret, B. Delaup, G. Gaudin, B. Dieny, and R. Miranda, J. Appl. Phys. **109**, 07D357 (2011).

[**6**] E. Jiménez, J. Camarero, P. Perna, N. Mikuszeit, F. J. Terán, J. Sort, J. Nogués, J. M. García-Martín, A. Hoffmann, B. Dieny, and R. Miranda, J. Appl. Phys. **109**, 07D730 (2011).

[**7**] C. Tieg, E. Jiménez, J. Camarero, J. Vogel, C. Arm, B. Rodmacq, E. Gautier, S. Auffret, B. Delaup, G. Gaudin, B. Dieny, and R. Miranda, Appl. Phys. Lett. **96** , 072503 (2010).

[**8**] E. Jiménez, J. Camarero, J. Sort, J. Nogués, A. Hoffmann, F. J. Terán, P. Perna, J. M. García-Martín, B. Dieny, and R. Miranda, Appl. Phys. Lett. **95**, 122508 (2009).

[**9**] E. Jiménez, J. Camarero, J. Sort, J. Nogués, N. Mikuszeit, J. M. García-Martín, A. Hoffmann, B. Dieny, and R. Miranda, Phys. Rev. B **80**, 014415 (2009).

[**10**] D. Ecija, E. Jiménez, J. Camarero, J. M. Gallego, J. Vogel, N. Mikuszeit, N. Sacristán, and R. Miranda, Phy. Rev. B **77**, 024426 (2008).

[**11**] P. Prieto, J. Camarero, J. F. Marco, E. Jiménez, J. M. Benayas, and J. M. Sanz, IEEE Trans. Mag. **44**, 3913 (2008).

[**12**] P. Prieto, K. R. Pirota, J. M. Sanz, E. Jiménez, J. Camarero, F. Maccherozzi, and F. G. Panaccione, Appl. Phys. Lett. **90**, 032505 (2007).

[**13**] D. Ecija, E. Jiménez, J. Camarero, J. M. Gallego, J. Vogel, N. Mikuszeit, N. Sacristán, and R. Miranda, J. Magn. Magn. Mater. **316**, 321 (2007).

[**14**] E. Jiménez, J. Camarero, J. Sort, A. Hoffmann, J. M. García-Martín, B. Dieny, and R. Miranda, *Role of anisotropies on magnetization reversal behavior in exchange-biased systems (Magnetic Nanostructures for Micro-Electromechanical Systems and Spintronic Applications*, NATO Adv. Sci. Inst., (2006), ISBN: 88 – 8296 – 209 – 1.

The following papers are not included in this thesis and go beyond of its scope:

[**15**] P. Perna, C. Rodrigo, E. Jiménez, F. J. Terán, N. Mikuszeit, L. Méchin, J. Camarero, and R. Miranda, J. Appl. Phys. **110**, 013919 (2011).

[**16**] V. Uhlír, S. Pizzini, N. Rougemaille, V. Cros, E. Jiménez, L. Ranno, O. Fruchart, M. Urbánek, G. Gaudin, J. Camarero, C. Tieg, F. Sirotti, and J. Vogel, Phys. Rev. B **83**, 020406 (2011).

[**17**] P. Perna, C. Rodrigo, E. Jiménez, N. Mikuszeit, F. J. Terán, L. Méchin, J. Camarero, and R. Miranda, J. Appl. Phys. **109**, 07B107 (2011).

[**18**] V. Uhlír, S. Pizzini, N. Rougemaille, J. Novotný, V. Cros, E. JimØnez, G. Faini, L. Heyne, F. Sirotti, C. Tieg, A. Bendounan, F. Maccherozotti, R. Belkhou, J. Grollier, A. Anane, and J. Vogel Phys. Rev. B **81**, 224418 (2010).

[**19**] P. Perna, E. Jiménez, F. J. Terán, L. Méchin, J. Camarero, and R. Miranda, Mater. Res. Soc. Symp. Proc. Vol. 1198, E01-04 (2010).

[**20**] S. Pizzini, J. Vogel, V. Uhlír, E. Bonet, N. Rougemaille, S. Laribi, F. Petroff, V. Cros, E. Jiménez, J. Camarero, C. Ulysse, G. Faini, and C. Tieg, ESRF Highlights 2008, 89-90 (European Synchrotron Radiation Facility, ESRF, Grenoble, 2009, Editor: G. Admans)

[**21**] S. Pizzini, V. Uhlír, J. Vogel, N. Rougemaille, S. Laribi, V. Cros, E. Jiménez, J. Camarero, C. Tieg, E. Bonet, M. Bonfim, R. Mattana, C. Deranlot, F. Petroff, C. Ulysse, G. Faini, and A. Fert, Appl. Phys. Express **2**, 023003 (2009).

Patents Inventors: C. Teichert, C. Hofer, M. A. Niño, J. Camarero, E. Jimenéz,J. J de Miguel, R. Miranda, N. Mikuszeit, L. Gridneva, D. Arvanitis, A. Persson, and T. Bobek

Title: **Nanomagnet Array and Method of Forming the same**
Application number: 1107008974
Awarding date: 24/07/2007
Patent number:1215
Priority country: Austria
Type of protection: Europa
Titular Entity: Montanuniversität Leoben, et al.
Ext.: Spain, Germany, Sweden

List of Figures

List of Tables

Acknowledgement

Son muchas las personas a las que quiero agradecer que, de una manera u otra, hayan hecho posible este trabajo.

En primer lugar, quiero expresar mi agradecimiento al Dr. Julio Camarero por haberme dado la oportunidad de desarrollar esta tesis doctoral bajo su direción, por brindarme su capacidad y su experiencia científicas y contagiarme la pasión por el conocimiento y por los nuevos retos. También le agradezco que me haya facilitado la asistencia a congresos internacionales y escuelas de magnetismo, así como que haya compartido su gran experiencia en sincrotrones.

Al profesor Rodolfo Miranda por abrirme las puertas a la gran familia del C-III.

Quiero resaltar mi cariño al Dr. Juan José Hinarejos quien siempre ha tenido tiempo para escuchar y dar buenos consejos y por ser un excelente compañero.

Me gustaría reconocer mi gratitud por la labor de los técnicos del C-III, Jose Rodríguez, José Luis Romera, Santiago Marquéz, Andrés Buendía, Rosa Díez y a Juan Benayas. Y por supuesto a Elsa, secretaria del departamento e Isabel, Marije y Jose Luis, personal de IMDEA, de quienes he recibido siempre la máxima atención y predisposición.

I want to thank to Prof. Kai Liu for giving me the opportunity to collaborate in his group during my stay in his laboratory, and Randy Dumas and Peter Green to take care of my accommodation and friendly help in the lab.

I am specially grateful to Prof. Dr. H. P. Open for giving me the opportunity to visit his laboratory and enjoy working in his group specially the close cooperation with Dr. R. Frömter and Daniel Sticker and the nice stay in Hamburg.

Quiero mostrar mi agradecimiento al Prof. Dr. J. de Miguel, Prof. Dr. W. Kuch y Prof. Dr. V. Cros por la positiva valoración de mi trabajo, su disponibilidad, atención y amabilidad.

A Jan Vogel y Stefania Pizzini de los que he aprendido muchísimo y quienes me han hecho disfrutar de los tiempos de sincrotrón.

Al equipo magnético que ha crecido muy rápidamente, con la incorporación de Paolo, Fran, Nikolai, José Luis, Cecilia, Alberto y desde hace unos pocos meses de Cintia. Quiero resaltar el esfuerzo que ha realizado Nikolai para completar esta tesis, dedicándome su tiempo en forma de horas de discusión diarias, simulaciones teóricas y continuas correcciones del manuscrito.

A mis compañeros-amigos, quienes me acogieron con los brazos abiertos cuando aterricé en la quinta planta. Cristina y Sara, Daniel Barredo, Pablo y David Écija (quienes siguen ayudándome desde Alemania), Lukcasz, Ewelina, Marta, Christian, Jesús, Víctor y Fabián, Nikoleta, Katrin, Dagmar. A Marina, Jonathan y Luigi, Flavio a Juan Benayas porque nos lo pasamos muy bien dentro y fuera del labo.

A las chicas: Manuela, Cecilia, Jose, Fabiola y Bogdana, por su amistad. A Cecilia, Manuela y Jose a las que debo mis últimos atisbos de raciocinio... que sería de nosotras sin esas fiestas de chicas. ¡Hay que repetirlo!

Quiero agradecer a Cecilia su ayuda durante estos años tanto dentro como fuera del laboratorio. Gracias a sus incómodas preguntas, exigiéndome respuestas claras y sus correcciones a mi ortografıa y vocabulario castelán me han ayuda a mejorar. Pero sobre todo por las risas y los buenos momentos y porque de vieja quiero ser como ella.

A manuela quiero agradecer que haya soportado estoicamente la continua repetición de TODAS mis charlas. Por seguirme la corriente, dejándose convencer de que los ciclos de histéresis son bonitos y por sentender los sistemas de exchange-bias. Por darme siempre una visión positiva de las trabas que me han surgido durante los años que nos conocemos, y por las horas compartidas.

A Jose, porque quedarse hasta tarde en el labo no sería lo mismo sin ella. Por enseñarme a mirar las moleculillas. Pero sobre todo por recordarme que hay vida fuera del labo. Por cuidar de Flix y mis plantas cuando tengo que salir y por estar dispuesta a ayudar en lo que sea.

A Anais y Roberto con quienes he compartido los últimos momentos de estrés y desesperación. Gracias por escucharme y comprenderme. Benito por poder contar con él, tanto para un viaje como para ensayar una charla.

A los amigos que me ha proporcionado el privilegio de viajar, entre los que quiero resaltar a mis compañeros Herculianos, Maria, Maria Angeles, Vera, Fei, Jorge y Holger.

A la Montse qui sempre m'espera a la cantonada del Zara del centre per fer el café i petar la xerrada. A partir d'ara els podrem fer més "amenut" o això espero. A Laura Abad con quien he compartido buenos momentos des de que nos conocimos en la guardería. A la Laura Román, perqué sempre va bé tenir una amiga mes boja que jo.

A mi abuelo por enseñarme el respeto hacia los demás y el amor al campo. A mi abuela por querer compartir su tiempo, experiencia y saber conmigo, por estar siempre a mi lado, por desearme lo mejor y escucharme en todo momento.

Al incondicional apoyo de mis tíos, Inma y Jose, que me han tratado como a una hija, ayudándome en los malos momentos y compartiendo los buenos. A mis primos, Diego y Paula, a los que quiero como hermanos por hacerme reír en todo momento y por demostrarme su cariño en toda ocasión.

A Diana por aguantar los partidos de basquet y las largas veladas delante de las monedas y junto a Edu por darme a mis dos sobrinas, Elena y Alba. Los bichos mas divertidos y maravillosos que me llaman Tieta.

A Agustín, Maripaz, Sergi y Ivan de los que recibo el apoyo que la distancia permite. A mi tía Julia, quien siempre me recibe con una sonrisa y los brazos abiertos.

A Flix, por estar a mi lado des de que empecé, por escucharme, tranquilizarme y dejarme que la cuide.

A mi madre por ser mi amiga y consejera, por contagiarme sus ganas de disfrutar y por su optimismo ante la vida. Por darme los ánimos que muchas veces he necesitado para continuar. A mi padre por dedicarme su tiempo libre enseñandome a estudiar, llevándome a todas mis actividades y dejándome discutir con él. Por estar cerca de mi. En fin, por dedicarme su vida y quererme como soy, grácies pares.

A Nikolai mi compañero dentro y fuera del laboratorio por soportarme 24 horas al dia, 7 dias a la semana y 365 dias al año, especialmente estos últimos meses. Por su paciencia, comprensión y amor.